Improving the Fatigue Life Prediction of Automotive Components Using Simulated Strain Signal Methods

Von der Fakultät für Ingenieurwissenschaften, Abteilung Maschinenbau und Verfahrenstechnik

der

Universität Duisburg-Essen

zur Erlangung des akademischen Grades

eines

Doktors der Ingenieurwissenschaften

Dr.-Ing.

genehmigte Dissertation

von

Teuku Edisah Putra
aus
Aceh, Indonesia

Gutachter: Prof. Dr.-Ing. Dieter Schramm
Prof. Ir. Dr. Shahrum Abdullah
Tag der mündlichen Prüfung: 03.05.2016

DECLARATION

I hereby declare that the work in this thesis is my own except for quotations and summaries which have been duly acknowledged.

3rd May 2016

TEUKU EDISAH PUTRA
P62603

ACKNOWLEDGEMENTS

In the name of Allah SWT, the most gracious and most merciful, all praises and glories to Allah SWT, the Almighty who allows this doctoral thesis to be accomplished. I feel honoured and privileged to glorify His name in the sincerest way through this accomplishment and ask Him to accept my efforts. My peace and salutations are always given to our prophet Muhammad SAW, who has guided us from darkness to lightness, from stupidity to cleverness and from the Jahiliah era to the Islamiah era, namely Islamic religion that we love. So by his guidance, we are able to differentiate the good and the bad, the right way and the wrong way in order to enter God paradise.

This doctoral thesis is the results of effort from many people, who have directly or indirectly collaborated with me. After four years, however, it is very difficult to remember all of them. Therefore, I apologise in advance for not including in these lines people who really also deserve mention. In the first place, I would like to convey my greatest gratitude to Prof. Ir. Dr. Shahrum Abdullah, for the sake of his wide view, optimism and guidance, this thesis was born and kept alive. Secondly, I would like to express my gratitude to Prof. Dr.-Ing. Dieter Schramm, who from the beginning trusted in my knowledge and accompanied me during the study period. Furthermore, my gratitude to Assoc. Prof. Dr. Mohd. Zaki Nuawi and Dr.-Ing. Tobias Bruckmann for supervising me towards the completion of the Ph.D. programme. My gratitude also to Prof. Dr.-Ing. Dr. h.c. (UKM) Axel Hunger who trusted in my responsibility and ability to participate in the Programme for International Studies in Engineering (PromISE) between Universiti Kebangsaan Malaysia, Malaysia, and Universität Duisburg-Essen, Germany.

These special gratitudes are also dedicated to the Ministry of Research and Technology of the Republic of Indonesia, Universiti Kebangsaan Malaysia and Deutscher Akademischer Austausch Dienst (DAAD) for sponsoring me during this double degree doctoral programme. My thanks also to the PromISE, Perusahaan Otomobil Nasional (Proton) Sdn. Bhd., APM Automotive Holdings Bhd., Universitas Syiah Kuala, Department of Mechanical and Materials Engineering Universiti Kebangsaan Malaysia, Departmental Chair of Mechatronics Universität Duisburg-Essen and to all my colleagues for their contributions and supports. Special thanks are dedicated to my father, Teuku Muchtaryuddin, and my mother, Cut Mariana, for their everlasting love. A most special thanks is dedicated to my lovely wife, Lisa Agustina, for her love, patience and supports during the period of my study. Finally, thank you to all my brothers and sisters in Indonesia.

ABSTRACT

This study aims to determine a suitable approach for generating strain signal leading to fatigue damage estimation using a significant acceleration model. It was hypothesised that the simulated model could reproduce a characteristic strain signal in similar to the actual strain signal. Three strain signals, all at 120 seconds, measured at the McPherson frontal coil spring of a Proton sedan had been used as a case study. The strain signals were acquired from a data acquisition involving car movements on various types of road surfaces at different speeds. The strains were caused by accelerations of the tyre while the car was being driven on rough road surfaces. Using a mathematical expression that was developed for car movements, the measured strain signals yielded acceleration signals usually used to describe the bumpiness of road surfaces. Furthermore, the fatigue-based acceleration signals were considered as disturbances acting on the automotive suspension system. These disturbances on the car body had an effect on generating strain signals via computer-based simulation, as responses of the coil spring, in the form of strains. Based on the simulations, all the simulated strain signals showed similar patterns to the actual strain signals. The simulated results also gave low fatigue damage deviations, which were less than 7.5 % for all the strain signals, with a root-mean square error of 0.011 % and a coefficient of determination of 0.9995. Furthermore, the extractions of higher amplitude cycle based on the energy of the wavelet transform were performed. From the extraction results, it was found that the wavelet transform was able to shorten the strain signal time up to 95.3 % and that 96.1 % of lower amplitude cycles were reduced, which these cycles theoretically contribute to a minimum fatigue damage. Thus, maintenance of fatigue damage by more than 92.7 % was produced. The segments that resulted from the extraction processes had been clustered using the Fuzzy *C*-means. The clustering results showed that the simulated strain signals had a significant coefficient of determination to the actual strain signals, reaching 0.8904 with a root-mean square error of only 0.5 %. Based on the cyclic testing results, the fatigue lives were distributed in a range of 1:2 or 2:1 correlation with a significant coefficient of determination of 0.9056. The testing time was successfully reduced by more than 85.1 % using the edited actual strain signals. In addition, using the edited simulated strain signals reduced the testing time up to 95.1 %. Indirectly, the use of modified strain signals could reduce device operating costs. The current study results are believed to provide a new knowledge towards generating simulated strain signals. Thus, the results bring greater meaning to the field of fatigue research. This work helps engineers in automotive industries involved in collecting road surface profiles, which are the main input for vehicle structures.

PENAMBAHBAIKAN RAMALAN HAYAT LESU KOMPONEN AUTOMOTIF BERASASKAN KAEDAH ISYARAT TERIKAN SIMULASI

ABSTRAK

Kajian ini bertujuan untuk menentukan kaedah yang sesuai digunakan bagi menjana isyarat terikan secara model pecutan yang membawa kepada pengiraan kerosakan lesu. Hipotesis kajian ini bahawa simulasi dalam model tersebut menghasilkan semula ciri-ciri isyarat terikan dalam persekitaran simulasi yang realistik seperti isyarat terikan sebenar. Tiga isyarat terikan sepanjang 120 saat yang dicerap pada pegas gegelung depan McPherson daripada sedan Proton digunakan sebagai kajian kes. Isyarat terikan diperoleh daripada satu pencerapan data yang melibatkan pergerakan kereta di atas pelbagai jenis permukaan jalan pada kelajuan yang berbeza. Isyarat terikan yang dicerap adalah disebabkan oleh pecutan tayar ketika kereta melalui permukaan jalan kasar. Dengan menggunakan ungkapan matematik yang dibangunkan untuk pergerakan kereta, isyarat terikan yang dicerap menghasilkan isyarat pecutan yang biasanya digunakan untuk menerangkan lekak daripada profil permukaan jalan. Seterusnya, isyarat pecutan berdasarkan lesu tersebut dianggap sebagai gangguan yang bertindak pada sistem ampaian automotif. Gangguan ke struktur kereta ini mempunyai kesan dalam menjana isyarat terikan, sebagai tindak balas pegas gegelung dalam bentuk terikan melalui simulasi komputer. Berdasarkan simulasi tersebut, semua isyarat terikan simulasi menunjukkan corak yang sama seperti isyarat terikan sebenar. Hasil simulasi juga memberikan perbezaan kerosakan lesu yang rendah, iaitu kurang daripada 7.5 % bagi semua isyarat terikan, dengan kesalahan punca min kuasa dua sebanyak 0.011 % dan pekali penentu sebanyak 0.9995. Seterusnya, pengekstrakan kitaran beramplitud tinggi berasaskan kepada tenaga penjelmaan anak-gelombang dilakukan. Daripada keputusan pengekstrakan yang diperoleh, didapati bahawa penjelmaan anak-gelombang tersebut mampu memendekkan tempoh isyarat terikan sehingga 95.3 % dan juga sebanyak 96.1 % kitaran beramplitud rendah dikurangkan, yang mana kitaran ini menyumbang kepada kerosakan lesu minimum. Justeru, pengekalan kerosakan lesu lebih daripada 92.7 % diperoleh. Segmen-segmen yang melalui proses pengekstrakan telah dikelompokkan dengan menggunakan Fuzzy *C*-means. Dapatan daripada pengelompokan tersebut menunjukkan bahawa isyarat terikan simulasi mempunyai korelasi yang signifikan dengan isyarat terikan sebenar, yang mencapai 0.8904 dan hanya memberi kesalahan punca min kuasa dua sebanyak 0.5 % sahaja. Berdasarkan kepada keputusan ujian kitaran, didapati bahawa kesemua hayat lesu berada dalam julat korelasi 1:2 atau 2:1 dengan pekali penentu yang signifikan, iaitu sebanyak 0.9056. Masa ujikaji berhasil dikurangkan lebih daripada 85.1 % dengan menggunakan isyarat terikan sebenar yang disunting. Ia bahkan menjimatkan masa ujikaji sehingga 95.1 % dengan menggunakan isyarat terikan simulasi yang disunting. Secara tidak langsung, penggunaan isyarat terikan terubahsuia boleh mengurangkan kos pengoperasian. Keputusan kajian ini dijangkakan memberikan sumbangan ilmiah baharu dalam menjana isyarat terikan. Justeru, keputusan ini membawa makna yang besar kepada bidang penyelidikan lesu. Kerja ini membantu jurutera industri automotif yang terbabit dalam pencerapan profil permukaan jalan, yang merupakan masukan utama bagi struktur kenderaan.

VERBESSERUNG DER LEBENSDAUERVORHERSAGE VON FAHRZEUGKOMPONENTEN AUF BASIS SIMULIERTER DEHNUNGSMESSMETHODEN

ZUSAMMENFASSUNG

Die vorliegende Arbeit zielt darauf ab, einen geeigneten Ansatz zu bestimmen, um mithilfe eines Beschleunigungsmodells Dehnungssignale zu erzeugen, die sich zur Vorhersage von Ermüdungsbrüchen eignen. Dabei wird angenommen, dass das Simulationsmodell charakteristische Dehnungssignale reproduzieren kann, die ähnlich zu den realen Dehnungssignalen sind. Als Fallstudie wurden drei 120-Sekunden-Dehnungsimpulse an einer vorderen McPherson-Aufbaufeder einer Proton-Limousine gemessen. Die Dehnungsmesswerte wurden auf Basis einer Datenerfassung aufgenommen, welche durch Fahrzeugbewegungen auf verschiedenen Arten von Straßenoberflächen mit unterschiedlichen Geschwindigkeiten gewonnen wurde. Die Dehnungen wurden durch die Beschleunigungen des Reifens verursacht, während das Fahrzeug über unebene Fahrbahnoberflächen fuhr. Mithilfe einer mathematischen Beschreibung der Fahrzeugbewegung lieferten die Dehnungsmessungen die Beschleunigungssignale, die zur Beschreibung der Unebenheit der Straßenoberfläche dienen. Weiterhin wurden die ermüdungsbasierten Beschleunigungssignale als Störung aufgefasst, die auf die Radaufhängung einwirkt. Aus dieser Anregung der Karosserie wurden zur Verifikation mit Hilfe einer Computersimulation Dehnungssignale in der Aufbaufeder erzeugt. Im Ergebnis zeigten alle simulierten Dehnungssignale ähnliche Muster wie die eigentlichen Dehnungsmessungen. Die Ergebnisse ergaben auch niedrige Abweichungen bei den Ermüdungsschäden, deren Anteil weniger als 7,5 % für alle Dehnungssignale einnahm. Weiterhin lagen die Fehler bei den quadratischen Mittelwerten bei 0,011 % während das Bestimmtheitsmass 0,9995 betrug. Darüber hinaus wurde die Extraktion von Zyklen mit höherer Amplitude basierend auf der Energie der Wavelet-Transformation durchgeführt. Aus den Ergebnissen wurde geschlossen, dass der Wavelet-Transformation eine Verkürzung des Signals bis zu 95,3 % gestatteten. Außerdem wurden 96,1 % der Zyklen mit niedriger Amplitude eingespart, die theoretisch nur zu minimalen Ermüdungsschäden beitragen können. Damit konnten mehr als 92,7 % der Ermüdungsschäden erfasst werden. Die Segmente, die aus dem Extraktionsprozess resultierten, wurden mit einem Fuzzy *C*-means Algorithmus geclustert. Die Ergebnisse zeigten, dass die simulierten Dehnungssignale einem signifikanten Bestimmungsmass mit den tatsächlichen Dehnungsmessungen von 0,8904 erreicht haben, wobei Fehlern der quadratischen Mittelwerten -Fehler von nur 0,5 % auftraten. Auf der Grundlage der zyklischen Testergebnisse wurde die Ermüdungslebensdauer in 1:2- oder 2:1-Korrelation verteilt, mit einem signifikanten Bestimmungsmass von 0,9056. Die Testzeit konnte unter Verwendung der bearbeiteten tatsächlichen Dehnungssignale um mehr als 85,1 % reduziert werden. Darüber hinaus reduzierte dies die Testzeit durch die bearbeiteten simulierten Dehnungssignale um bis zu 95,1 %. Indirekt kann die Verwendung der modifizierten Dehnungssignale die Gerätebetriebskosten erheblich verringern. Daher können die Ergebnisse der vorgelegten Studie als neuer Beitrag zur Forschung in Richtung simulierter Dehnungssignale gewertet werden. Auf diese Weise erhalten die Ergebnisse eine große Bedeutung für den Bereich der Ermüdungsforschung. Diese Forschung kann den Ingenieuren der Automobilindustrie bei der Erhebung Straßenoberflächenprofile helfen, die Hauptanregung für die Fahrzeugstrukturen sind.

CONTENTS

LIST OF TABLES

LIST OF FIGURES

LIST OF SYMBOLS

a	crack length
A_0	original unloaded cross-sectional area
B	coefficient factor of the material properties
b	fatigue strength exponent
C	number of clusters
c	fatigue ductile exponent
$\hat{c}$	confidence coefficient
cA	approximate coefficient
cD	detailed coefficient
CF	crest factor
CI	confidence interval
D	cumulative fatigue damage
d	damping coefficient
DF	degree of freedom
D_i	fatigue damage for each loading cycle
$D_{\max}$	maximum cumulative fatigue damage
$D_{\text{normalised}}$	normalised cumulative fatigue damage
D_0	original unloaded diameter
E	Young modulus or material modulus of elasticity
e	exponential factor of the material properties
EGV	energy gate value
E_{i}	expected value
$\bar{e}$	wavelet-based signal internal energy
$\bar{e}_{\max}$	maximum wavelet-based signal internal energy
$\bar{e}_{\text{normalised}}$	normalised wavelet-based signal internal energy
F_{j}	signal amplitude or data value
F_{jmax}	maximum signal amplitude or data value
f	frequency
f_0	frequency at the center of the mother wavelet
F_1	vector of true value

F_2	vector of n prediction
F_{ANOVA}	ANOVA coefficient
FT	Fourier transform
G	Gaussian distribution
g	gravity
$\dot{g}$	weighted exponent that is a fixed number greater than one
h	multiplicative factor
J	objective function
j	dilation factor which is the inverse of the frequency
J_2	second deviatoric stress invariant
K	kurtosis
k	spring stiffness
K'	cyclic strength coefficient
$K_{\max}$	maximum kurtosis
$\check{K}_{\max}$	maximum stress intensity factor
$\check{K}_{\min}$	minimum stress intensity factor
$K_{\mathrm{normalised}}$	normalised kurtosis
m	mass of object
MSE	mean squared error
MS_{E}	mean sum of squares due to error
MS_{T}	mean sum of squares due to treatment
N	number of variability
n	number of data
n'	cyclic strain hardening exponent
N_{E}	number of variability for error
N_f	number of cycles to failure for a particular stress range and mean
n_i	number of applied cycles at a particular stress level for each block loading
N_{T}	number of variability for treatment
O	observed value
P	applied force
p	scale index which is a reciprocal of frequency
P_{d}	damping force

P_i	inertial force
P_s	spring force
PSD	power spectral density
q	time shifting or translation
R^2	coefficient of determination
$r.m.s.$	root-mean square
$r.m.s._{max}$	maximum root-mean square
$r.m.s._{normalised}$	normalised root-mean square
$RMSE$	root-mean square error
SD	standard deviation
SD_{max}	maximum standard deviation
$SD_{normalised}$	normalised standard deviation
$Skew$	skewness
ST	S-transform
$STFT$	short-time Fourier transform
t	time
t'	time at the center of the window
$\check{T}$	treatment effect
U	Fuzzy c-partition
u	S-transform coefficient
v	vector of centers
W	Weibull distribution
w	window function
WC	wavelet coefficient
wm	positive-definite weight matrix
x	displacement
$\dot{x}$	velocity
$\ddot{x}$	acceleration
X^2	chi square
$\bar{x}$	mean value of the quantity
y	observation
α	location parameter
β	shape parameter

λ	scale parameter
θ	confidence limit
θ_1	lower confidence limit
θ_2	upper confidence limit
ω	angular frequency
Ψ	mother wavelet
ζ	damping ratio
μ	overall mean
γ	shear strain
ε	strain amplitude
ε_{e}	elastic strain amplitude
$\varepsilon_{\mathrm{normalised}}$	normalised strain amplitude
ε_{p}	plastic strain amplitude
ε'_f	fatigue ductile coefficient
ϵ	random error component that incorporates all other sources of variability in the experiment
σ	stress amplitude
σ_{limit}	fatigue limit
σ_{max}	maximum stress amplitude
σ_{mean}	mean stress amplitude
σ_{min}	minimum stress amplitude
σ_p	yield stress of material in pure shear
σ_{r}	stress ratio
σ_{uts}	ultimate tensile strength
σ_v	von Mises yield criterion
σ_{yield}	yield strength
σ'_f	fatigue strength coefficient
$\Delta\check{K}$	range of the stress intensity factor
$\Delta\sigma$	stress range

LIST OF ABBREVIATIONS

ANOVA	analysis of variance
CAD	computer aided design
CAL	constant amplitude loading
CDF	cumulative distribution function
CWT	continuous wavelet transform
DFT	discrete Fourier transform
DWT	discrete wavelet transform
Dymola	dynamic modeling language
EGV	energy gate value
FCM	Fuzzy *C*-means
FDE	fatigue data editing
FEA	finite element analysis
FEM	finite element method
FFT	fast Fourier transform
IDFT	inverse discrete Fourier transform
IFFT	inverse fast Fourier transform
MATLAB	matrix laboratory
MBD	multi-body dynamic
MSE	mean squared error
PDF	probability density function
PSD	power spectral density
r.m.s.	root-mean square
RMSE	root-mean square error
SAE	Society of Automotive Engineers
SD	standard deviation
STFT	short-time Fourier transform
SWT	Smith-Watson-Topper
UTS	ultimate tensile strength
VAL	variable amplitude loading

CHAPTER I

INTRODUCTION

1.1 HISTORY OF FATIGUE FAILURE

In engineering fields, there is one type of failure caused by various amplitude loadings. This type of failure is known as fatigue. In such a case, loads applied to any component never reach a sufficient level to cause failure in a single application (Memon et al. 2002). However, these continuous loads, after thousands, even millions of times, either constant or variable, cause loss of ductility and thus develop into cracks, leading to failure of components (Cui 2002). This failure occurs locally, permanently and gradually, depending on repeated and dynamic stresses suffered by critical areas, where stresses subjected are less than the ultimate tensile strength (UTS) and static yield strength (Aykan & Celik 2009; Beaurepaire & Schuëller 2011; Ye et al. 2014).

According to Chen (2007), Cini (2012) and Ye et al. (2014), preliminary understanding of fatigue failure was first noticed during the Industrial Revolution in nineteenth-century Europe. It was German mining engineer, W.A.J. Albert, who in 1829 reported a correlation between repeated lower amplitude loads and durability of a metal. The word “fatigue”, however, had originally been mentioned ten years later by J.-V. Poncelet in his book titled *introduction à la mécanique industrielle* (introduction to industrial mechanics). In 1842, one rail disaster occurred when a heavy duty locomotive axle failed under cyclic loads. Examination of the broken axle showed that it had brittle cracking across its diameter. W.J. Rankine, a British railway engineer, recognised the distinctive features of fatigue fracture and understood the effect of stress concentrations in a mechanical design.

Methods for characterising the fatigue life were based on the works performed by A. Wöhler between the years 1850 and 1870. He produced various laboratory experiments focused on the failure of railway axles. In order to determine the fatigue life parameters, smooth specimens with cylindrical gauge lengths were normally tested under constant conditions. The results of the cyclic tests performed at various stress levels were plotted to obtain a stress-life curve. His experiments are considered as the first in fatigue failure research. After his research, design engineers have tried to avoid using sharp edges in their mechanical designs because these stress concentration areas cause and accelerate fatigue failure.

In 1874, W. Geber developed a method for predicting the mean stress level effect of fatigue life, which was then modified by Goodman (1914) and C.R. Soderberg in 1930. In 1886, cyclic stress-strain behaviour of a material was reported by J. Bauschinger. The Bauschinger effect, which identifies the occurrence of cyclic strain softening and hardening, is the basis for the Coffin-Manson model (Manson 1954). In 1910, O.H. Basquin demonstrated the linear relation between stress amplitudes and number of cycles. This relation contributed to the Morrow and Smith-Watson-Topper (SWT) mean stress correction models developed in 1968 and 1970, respectively. Fracture mechanics took place with the works of Griffith (1921), who investigated cracks in brittle glass. This promoted greater understanding of fatigue since concepts of fracture mechanics are essentially involved in fatigue crack characteristics. Paris et al. (1961) proposed a method for predicting the rate of growth of individual fatigue cracks. In 1968, M. Matsuishi and T. Endo devised the rain flow counting algorithm to enable the application of the Palmgren-Miner linear cumulative fatigue damage rule, developed in 1945, to random loadings.

Fatigue is a major pattern of failure in engineering structures (Jiang & Zhao 2012) involving a large economic effect, as well as accidents that claim lives. Until now, more than half of all mechanical structural failures occur through the mechanism of fatigue crack growth (Beaurepaire & Schuëller 2011; Ye et al. 2014). Globally, a total of 306 fatal accidents was identified since 1934, resulting in more than 1,800 deaths, which was an alarming figure (Bhat & Patibandla 2011). Structural failures, with metal fatigue as the related cause, indicate that the current level of achievement remains far from perfection. The conditions above lead to a motivation for succeeding comprehensive fatigue analyses.

Extensive efforts have been made for fatigue analysis in modern structural designs based on theoretical models. Such models have provided an improved analysis of specific materials (Taheri et al. 2003). A consistent model, however, is still under development (Cui 2002). It has proven difficult to incorporate fatigue analysis for general use. This situation is caused by the complexity of fatigue phenomena (Ottosen et al. 2008; Ye et al. 2014). Many automotive components, which are often subjected to variable driving conditions, can be associated with failure caused by fatigue during their operations.

1.2 FATIGUE LIFE FOR AUTOMOTIVE SUSPENSION SYSTEM

Corrosion, improper heat treatment and surface finishing are the factors accelerating fatigue failure of a car component (Prawoto et al. 2008; Zhu et al. 2014). Aside from these factors, the physical conditions of road surfaces and the different velocities of the car are also main factors contributing to failure (Ottosen et al. 2008). The control and stability of a car entirely depend on the collision and the friction between road surfaces and tyres (Ferreira et al. 2009; Yang et al. 2009; Lajqi & Pehan 2012), which are uncertain and can change quickly and extremely. This dynamic interaction gives a certain amount of vibration causing problems with respect to car components and the ride quality. This vibration acts as a catalyst to speed up the crack initiation interfacing the function of the components and give a great impact on the performance of the car; contributing to mechanical failure due to fatigue; as the components are exposed to cyclic loads.

In such a case, vibrations are unavoidable and their isolation advantageous (Priyandoko et al. 2009). The reduction of vibrations is not only to provide comfort to passenger(s), but also as important, to help in reducing the probability of fatigue failure at car components; which results in less cost and reduces possibility of a fatal accident from occurring. Thus, a system absorbing vibrations of the vertically accelerated wheel is needed. The best system to resolve this problem is the suspension system. The suspension system is a mechanical device in which its main function is to minimise vertical displacements and accelerations (Tandel et al. 2014), and maximise tractions between road surfaces and tyres to provide steering stability (Singh 2013). It permits the control arm and wheel to move up and down. It operates under multi-axial service loadings, identified as the existence of more than one principal stress.

The car body supports the weight of the engine and the passenger(s), while the car body itself is supported by a suspension system on each tyre (Scuracchio et al. 2013). The weight of the car body and the loads it carries give the initial compressive forces to the suspension system. The compressive forces increase if the car goes through an uneven road surface at higher speeds. When the tyres experience shock, it increases the displacement of the tyres and the car body. At the same time, the vibrations transmitted to the car body are increased. The vibrations result in high stresses because the forces subjected are large.

Vibrations are absorbed by the tyres, the springs in a seat and the coil spring in a suspension system. The tyres and seat springs absorb a little vibration, while the coil spring does the rest in order to provide convenience to passenger(s) and ensure driving safety. Passenger(s), however, will still feel a little vibration at a certain level. In this case, the coil spring has a forced vibration, which occurs when energy is continuously added to the component by applying the oscillatory force at some forcing frequency. A significant amount of shock affects the coil spring, and at higher rates than other car components. Thus, coil springs play a vital role in the failure of car structures since they withstand the majority of resulting vibrations from road surfaces; contributing to fatigue failure. Problems that may occur to a coil spring are because of stiffness and low fatigue life (Abidin et al. 2013).

According to Zhu et al. (2014), compressive springs often fracture at the transition position from the bearing coil to the first active coil. It is caused by bending stresses because of no gap or a small gap between the bearing coil and the first active coil. According to Das et al. (2007), the existence of residual stresses on a component affects its durability. If the resulted stresses are repeated in a certain period, they increase the probability of fatigue failure for the component. A better way to access durability on a component is through service loads (Aykan & Celik 2009; Ye et al. 2014). Durability analysis requires knowledge of service loads since these loads are used for the laboratory testing of a component in engineering practices. Thus, early in the product development process, engineers need to predict stress and strain histories for the purpose of modelling and designing for mechanical fatigue (Ayoub et al. 2011).

Some strain signal acquisitions have been performed to monitor dynamic structural responses. For example, Oh (2001) measured a strain signal using a strain gauge on a light railway train for evaluating a fatigue data editing (FDE) technique. A train ran on a rail with a maximum speed of 80 km/h along a distance of 2.4 km. Furthermore, Haiba et al. (2003) collected strain signals at a lower suspension arm to investigate the effects of different assessment strategies on fatigue life. A car was driven at a constant speed of 34 km/h over a virtual pavé durability track. Strain gauges were also used by Ilic (2006) to measure service loads applied to the output shaft of automatic transmission systems for evaluating a novel methodology of data reduction. A car was driven on different road surfaces. For the minor road section, the length was 50 km with an average speed of 43 km/h for 70 minutes. For the highway section, the length was also 50 km with an average speed of 86 km/h for 35 minutes. For the winding road section, the length was 72 km with an average speed of 72 km/h for 60 minutes. For the last type of road surface, the car was driven on the built-up section with a length of 20 km and an average speed of 17 km/h for 70 minutes.

Abdullah et al. (2006) also used a strain gauge to measure a strain signal at a lower suspension arm for the purpose of the wavelet bump extraction validation. A vehicle travelled at 34 km/h over a pavé track. A strain signal at the end beam of a freight car bogie was measured by Baek et al. (2008), using a strain gauge to predict the fatigue life based on the rain flow cycle counting method. The load history was measured through 60 km/h over 25 minutes from starting to braking. Similar procedure was also performed by He et al. (2010), measuring strain signals at an automobile damper spring tower on different road surface conditions.

Strain signals were not only measured at small components, but also at big components. Alaoui et al. (2009) collected strain signals at a ship structure to analyse the influence of loading conditions on the short crack behaviour and to assess the fatigue crack life. The ship was subjected to variable loadings due to various sea states, wind and waves. Xia et al. (2012), Ye et al. (2012a) and Ye et al. (2012b) installed more than 100 strain gauges to measure dynamic strain responses at bridge deck sections from the effects of highway traffic, railway traffic, monsoon, typhoon and temperature. The strain signals were continuously acquired for one year. All those

strain signal acquisition processes, however, are very expensive, intrusive, time consumption, not error-free and require high levels of skill and training (Motra et al. 2014; Ye et al. 2014).

1.3 PROBLEM STATEMENT

For obtaining random fatigue loading histories on relevant parameters at a coil spring, a strain signal acquisition typically entails numerous sets of instrumentations. After all these, there is still a possibility for the measurement to show that the desired results cannot be obtained, thus making the whole measurement a waste of resources, causing much financial loss (Rao 2009). Because of the weaknesses of measuring equipment used, the accuracy and reliability of a strain signal are reduced and are often in question, as the magnitude of strains is often small (Motra et al. 2014). The existence of errors directly affects the results, leading to inappropriate judgments and even wrong conclusions (Jiang et al. 2011).

Because the strain signal at a coil spring cannot be measured directly with a high degree of accuracy, especially during normal driving, it was desirable to develop a simulation for generating strain signals. The acceleration signals caused by road surfaces were considered as a disturbance in the developed simulation. The simulated strain signals were compared to the actual strain signals for validation purposes, especially in terms of their durability. To the best of the author's knowledge, no such simulation was previously proposed. Thus, the simulation is expected to bring greater meaning in automotive industries involving strain signal acquisitions.

1.4 RESEARCH OBJECTIVES

To help eliminate particular difficulties in experimentations, automotive industries nowadays rely heavily on computer simulations to study the general trends before investing in actual tests. To alleviate the expenses associated, a model is first created and simulations are run on it to make sure that the trend shows improvement and that one may indeed go ahead and invest in actual experimentations. It makes it possible to do essential assessments before a system is built, it can alleviate the need for expensive experiments and it can provide support in all stages of a project from conceptual design, through commissioning and operations.

Thus, the main objective of the current study is to propose techniques to develop fatigue-based strain signals by utilising computer-based simulation with consideration of road surface profiles that may lead to fatigue failure. Several secondary objectives needed to be completed in order to achieve the main objective, namely:

1. To investigate the acceleration trends for a coil spring, driven on different road surfaces identified for strain signal collection.
2. To determine the strain signals of the coil spring subjected to fatigue-based acceleration signals, by performing a dynamic simulation based on a mathematical expression.
3. To validate the simulated strain signals through simulated and experimental procedures to show that the generation of the simulated strain signals saves time as well as minimises life estimation errors.

1.5 SCOPE OF RESEARCH

The study focuses on strain signal development at the coil spring of a passenger car due to the effect of road surface profiles. A computer aided design (CAD) software for engineering was used for the component modelling, while a finite element analysis (FEA) software was utilised to determine the stress distributions of the component. Furthermore, actual strain signals were utilised to generate acceleration signals using a programming language software, and simulated strain signals were yielded using a multi-body dynamic (MBD) software. For the strain signal validation purposes, the programming language software was also utilised to develop algorithms for extracting and clustering potential damaging segments, and then developed strain signal correlations. Moreover, to identify the strain signal behaviour, a crack growth software was used to determine statistical parameters and fatigue damage. Finally, uni-axial cyclic tests were performed according to ASTM E606-92 (1998). Based on the validations, the accuracy of the simulated strain signals could be judged.

1.6 RESEARCH HYPOTHESES

Several hypotheses had been identified through the research, namely:

1. The acceleration signals demonstrate a variable amplitude pattern with time known as variable amplitude loading (VAL). Smooth road surfaces give small vibrations to the coil spring, while rough road surfaces are the largest contributor to the occurrence of vibrations and are considered to contribute substantially to fatigue failure.
2. The dynamic simulation should be able to produce strain signals showing similar patterns to the actual strain signals. The simulation will be developed based on the equation of motion for an automotive coil spring, with the main input is accelerations being accepted by the component when being driven on road surfaces.
3. Both the actual and simulated strain signals are predicted to give a minimum fatigue damage deviation. The performed simulation considers road surface profiles and the simulated strain signals are validated using many methods to make sure that they are as realistic as possible. Using the MBD simulation for developing strain signals, the time can be reduced, the errors can be minimised and the high levels of skill to operate the simulation are not required.

1.7 SIGNIFICANCE OF RESEARCH

Durability analysis of the component is needed since it withstands the majority of resulting vibrations from road surfaces. The experimental expenses and the presences of error have seriously inhibited the general use of a strain signal in fatigue studies. The limitations of strain signal acquisition cause most fatigue tests to be performed using a constant amplitude loading (CAL). Thus, an MBD simulation for generating strain signals was developed in the study. The accelerations measured at a coil spring affected by road surfaces were the input for the simulation. The work simulated the durability behaviour at the coil spring considering that the car suspension component was subjected to a number of effective shocks. Using the simulation, the traditional ways for a strain signal measurement involving a lot of time and costs and not error-free can be abandoned.

In addition, the current study introduced a new wavelet-based FDE. The wavelet transform was used as a tool for accelerating durability tests by identifying and extracting segments that support fatigue damage in an original strain signal. Wavelet-based energy is more sensitive to amplitude changes based on localised time-frequency concept, so it can be applied to detect the locations that have high fatigue damage. Damaging segments were combined to produce a shorter modified strain signal while maintaining its original characteristics. Maintaining the original characteristics, the FDE could produce more accurate modified strain signals for the purpose of laboratory experiments. With this technique, where the results from the MBD simulation and the FDE are combined, the economic effects may be reduced and the durability testing time is saved. These methods are necessary since they effectively give significant contributions to future durability and fatigue failure assessments.

CHAPTER II

LITERATURE OVERVIEW

2.1 AUTOMOTIVE SUSPENSION SYSTEM

2.1.1 Types of Automotive Suspension Systems

Most automotive suspension systems operate similarly. The main difference is the location and the arrangement of basic components, such as links connecting the car body and the tyres, shock absorbers, control arms and springs (Lajqi & Pehan 2012). The suspension system can be broadly classified into two sub-groups, namely non-independent and independent, referring to the ability of opposite wheels to move independently of one other. Non-independent or solid axle suspension systems have both the right and left tyres attached to the same solid axle. When one tyre hits a bump, it is moved upwards, causing a slight tilt to the other tyre. It must be stable so that the tyres are aligned. Each axle must be adapted to the situation at high speed braking. It is able to support the vehicle weight and can also provide resistance to stresses occurring when braking. The non-independent suspension system, as shown in Figure 2.1, is commonly used at the front of vans and trucks.

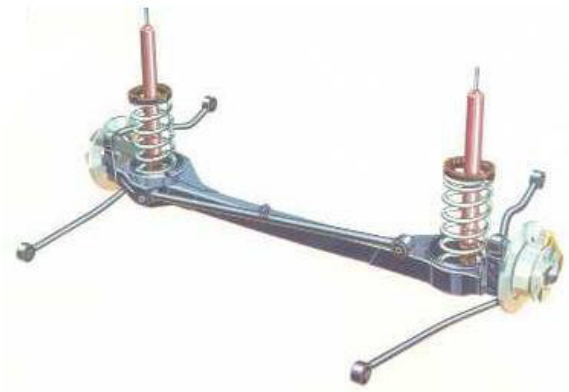

Figure 2.1 Design of non-independent suspension system

Source: Longhurst 1994

In an independent suspension system, the tyres are installed separately. When a tyre is driven on a road surface, vibrations are not transferred to the other tyre, while car structural distortions and steering vibrations can be reduced. It can reduce the elasticity of springs so that the car can be driven with ease. This type of suspension system allows one tyre to move up and down with minimal effect on the other. Today, nearly all passenger cars and light trucks use independent frontal suspensions for better resistance to vibrations (Singh 2013). Among the independent suspension system types are McPherson strut, double-A and multi-link, as shown in Figure 2.2.

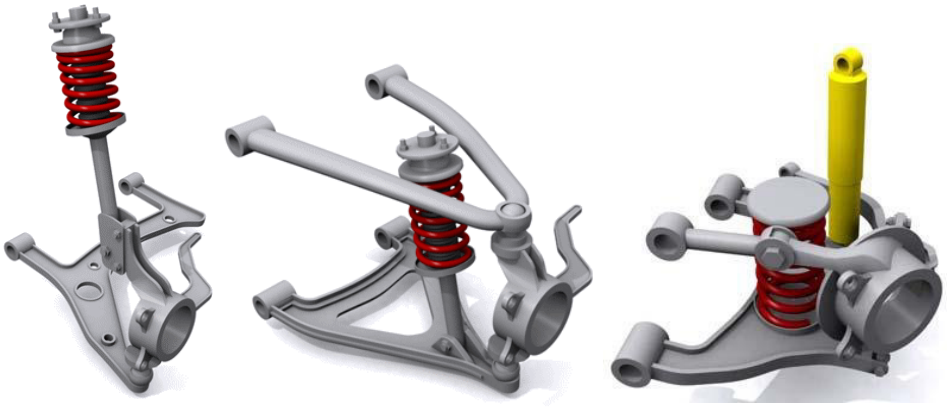

(a) (b) (c)

Figure 2.2 Design of independent suspension system: (a) McPherson strut, (b) double-A, (c) multi-link

Source: Longhurst 1994

According to the external power input to the system, suspension systems can be categorised as passive, semi-active and active (Goga & Kľúčik 2012; Lajqi & Pehan 2012; Alvarez-Sánchez 2013; Qazi et al. 2013). A passive suspension system consists of a spring and shock absorber damper without control, where the movement is being determined entirely by road surfaces. A semi-active suspension system has the same elements but utilises controlled dampers and uses varying damping force as a control force. Active suspension systems differ from semi-active suspension systems in that the control force is produced using separate actuators to literally raise and lower the car body independently at each wheel.

Many automotive manufactures perform extensive tests to modify suspension designs in order to provide the best combination of ride quality, directional control, ease of handling, safety, stability and service life (Priyandoko et al. 2009; Qazi et al.

2013). Four important performance parameters that require optimisation are (Miller 1988): (1) ride comfort related to the acceleration sensed by passenger(s) when a car is driven on a rough road surface, (2) body motion associated with the pitch and roll of the sprung mass created primarily for cornering and braking manoeuvres, (3) road handling related to the contact force between tyres and road surfaces, and (4) suspension deflection referring to the relative displacement between sprung and unsprung masses. With such behaviour patterns, the performance of automotive suspension systems is greatly increased throughout the years due to the increase of car capabilities.

2.1.2 Mechanism of Automotive Suspension System

The coil spring, also known as the helical spring, is the most common type of spring found in modern cars (Lee 2007). The coil spring is a torsion type spring designed to offer resistance to external applied pressures. Torsion refers to the twisting action of the coils where the effect of the torque can be observed on its stiffness. A coil spring must be strong enough to withstand the resulting vibrations and ideally isolates the car body from the vibrations or shaking effects associated with turning, braking and acceleration (Singh 2013). At the same time, the coil spring should be soft enough, whereas for good road handling capability, it requires a stiff coil spring.

The Hooke law, developed by R. Hooke in 1660, states that the displacement x of an elastic object, such as coil spring, is directly proportional to the spring force P_s applied to it. That is:

$$P_s = kx \tag{2.1}$$

where k is the spring stiffness. Assuming the elastic limit is not exceeded, a graph of force against extension produces a straight line that passes through the origin. The gradient of the line is the spring stiffness. While carrying out an experiment, the spring stiffness is found to be different depending on the objects and materials. The greater the spring stiffness, the stiffer the spring. The softer the spring and the greater the mass, the longer the period of vibration (Thite 2012; Tandel et al. 2014).

The spring deflects an amount proportional to the force required to accelerate the spring system. The spring stiffness provides a restoring force to move the mass back to equilibrium, and dampers oppose any displacement away from equilibrium. Damping is usually the result of viscous or frictional effects. If such force is also proportional to velocity, the damping force P_d may be related to the velocity $\dot{x}$ by:

$$P_d = d\dot{x} \tag{2.2}$$

and the damping coefficient d is expressed by:

$$d = 2\zeta\sqrt{km} \tag{2.3}$$

where m is the mass and ζ is the damping ratio.

Conceptually, the damping ratio is the amount of damping allowing the deflected system to just return to its equilibrium position with no oscillation. When $\zeta = 0$; the system is undamped, when $0 < \zeta < 1$; it is called an under damped system, when $\zeta = 1$; it is called critical damping, and when $\zeta > 1$; it is an over damped system. An under damped system oscillates when it is deflected and released, while an over damped system never returns to its equilibrium position. In a critical damping case, the system never executes a full cycle. The damping force is just sufficient to dissipate the energy within one cycle of motion. A system with critical damping returns to equilibrium the fastest without oscillation (Kelly 2012; Magrab 2012). Damping removes kinetic and potential energies from a mass-spring-damper system. A higher damping coefficient in the system causes the amplitudes of free vibration to decrease over time (Thite 2012; Tandel et al. 2014) and also limits the peak transmissibility in forced vibration.

2.1.3 Vibration at Coil Spring

Vibrations are caused by imperfections, especially involving movement of the car tyres through rough road surfaces (Eski & Yildirim 2009). Since the vibration is defined as oscillatory motion resulted from varying force to a structure, it involves a

change of position or displacement. Velocity is the rate of change in displacement with respect to time that can be described as the slope of the displacement curve. Similarly, acceleration is the rate of change of velocity with respect to time, or the slope of the velocity curve (MSC NASTRAN 2012). Displacement, velocity and acceleration are also referred to as a shock or vibration, depending on the waveform of the forcing function that causes the acceleration. A forcing function that is periodic in nature generally results in an acceleration that is analysed as a vibration. On the other hand, a force input having a short duration and a large amplitude would be classified as a shock load (Figliola & Beasley 2011).

A method that has been used to classify a vibration is based on its degree of freedom, which is the number of independent kinematic variables to describe the movement of a system. A mass-spring-damper system with single degree of freedom can be characterised by Figure 2.3. A single degree of freedom system was considered in the study assuming the vibration act in each suspension without affecting other suspension. This shows the relationship among four basic components of the dynamic system, which are mass, resistance (spring), energy dissipation (damper) and applied force (Kelly 2012; MSC NASTRAN 2012).

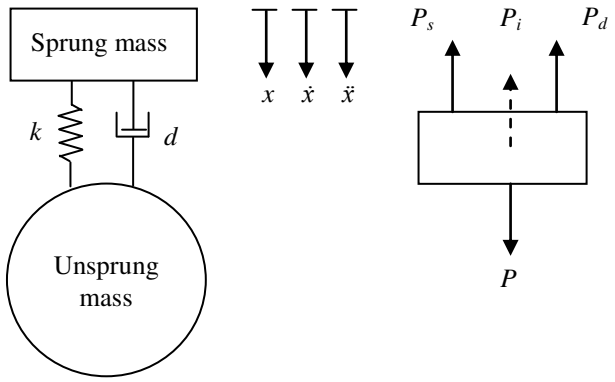

Figure 2.3 A mass-spring-damper system and its free body diagram
Source: Tandel et al. 2014

According to the Newton second law of motion, all forces have both magnitude and direction. As the mass-spring-damper system moves in response to an applied force, forces induced are a function of both the applied force and the motion in

the individual components. The governing equation of this system can be derived from the law as:

$$P_i + P_d + P_s = P \tag{2.4}$$

where P is the applied force and P_i is the inertial force, which is a force opposite in direction to an accelerating force acting on a component, and is equal to (Kreyszig 2011; Juvinall & Marshek 2012):

$$P_i = m\ddot{x} \tag{2.5}$$

where $\ddot{x}$ is the acceleration. Submitting Equations (2.1), (2.2) and (2.5) into (2.4), the equation of motion may then be expressed as (Kelly 2012; Magrab 2012):

$$m\ddot{x} + d\dot{x} + kx = P \tag{2.6}$$

Each overdot denotes a time derivative. The equation describes the behaviour of a physical system of its motion as a function of time. The spring and the damping forces are proportional to the displacement and velocity, respectively, whereas the inertial force is dependent on the acceleration. Considering the free-body diagram in Figure 2.3, the spring and the damping forces must balance the inertial force for the mass (Figliola & Beasley 2011).

Many problems rising in automotive areas have been solved by simulating the dynamic behaviour of structural components on which dynamic forces are acting. Based on Equation (2.6), some studies have modified suspension designs in order to increase the capabilities of a suspension system. According to Goga & Kľúčik (2012), passive suspension systems are not ideal to achieve good driving stability and passengers' comfort. Thus, a passive suspension system was optimised, showing a significant decrease of amplitudes and faster stabilisation of measured quantities against results of the model with the original parameters. A similar study also had been performed by Lajqi & Pehan (2012) introducing an optimisation procedure for active and semi-active suspension systems. When a vehicle equipped with an active or

semi-active suspension system drove over a road bump, the driving comfort and the driving safety were acceptable. However, when the vehicle was equipped with a passive suspension system, the accelerations and the dynamic forces exceeded the limit. These excess values caused driving discomfort and had negative influences on safety.

In order to avoid the induced road variations over the car body, Alvarez-Sánchez (2013) presented a linear mathematical model to design a sliding mode controller. Tandel et al. (2014) also implemented a controller for decreasing the body acceleration of an active suspension system to almost half of a passive suspension system, and the ride comfort of passenger(s) could therefore be improved. The results also showed that the body acceleration increased with the increase in spring stiffness and decreased with the increase in damping coefficient. Amplitudes of the body acceleration of the active and passive suspension systems were similar, but the body acceleration of the passive suspension system took more time to dissipate in the simulation. Finally, Zhang et al. (2014) discussed a stabilisation problem to enhance the vehicle handling considering time varying velocity. The designed controller could achieve much smaller sideslip angle and the yaw rate was closer to the desired yaw rate from a reference model. Vibrations subjected to a component increase strains. Then, the strains give rise to stress concentration of the component.

2.1.4 Stress Concentration

Considering the elongation of a component that occurs as a result of the applied force P, the true stress σ at fracture can be mathematically defined as the following expression:

$$\sigma = \frac{P}{A_0} \tag{2.7}$$

where A_0 is the original unloaded cross-sectional area. The equation is always correct as an expression for the mean stress in any cross section, only if: (1) the load is uniformly distributed over the cross section, (2) the section being considered is well

removed from the loaded ends, (3) the component is perfect, with no holes, notches, threads, internal imperfections, or even surface scratches rising to stress concentration, (4) the component is totally free of stress when the external loads are removed, (5) the component comes to stable equilibrium when loaded, and (6) the component is homogeneous. Unless several important requirements are fulfilled, errors can occur assuming that the equation also give greater maximum stress in the section, perhaps by several hundred percents (Juvinall & Marshek 2012).

The stress σ and the strain ε are connected by a linear relationship, known as the Hooke law, as reported by Callister & Rethwisch (2012) and Juvinall & Marshek (2012). In an equation form, the Hooke law is described as:

$$\sigma = E\varepsilon \tag{2.8}$$

where E is the material modulus of elasticity. This equation works as long as the elastic limit is not exceeded. If a component is stretched too much, it does not return to its original length when the applied load is removed.

Ramberg & Osgood (1943) suggested an equation for describing the non-linear relationship between the stress σ and the strain ε. The Ramberg-Osgood model establishes a relation among damage, plastic strain, the cyclic strength coefficient K' and the cyclic strain hardening exponent n' which could be derived using stress-strain parameters. In its original form, the equation is described as:

$$\varepsilon = \frac{\sigma}{E} + K'\left(\frac{\sigma}{E}\right)^{n'} \tag{2.9}$$

The first term on the right side is equal to the elastic part of the strain, while the second term accounts for the plastic part. According to Upadhyaya & Sridhara (2012), the plastic strain is mainly responsible for damage growth, where damage initiates only after the accumulation of threshold plastic strain. The model could be used to predict stress distributions (Wei & Elgindi 2013); it showed a very good agreement to deterministic or random inputs (Sireteanu et al. 2014).

In 1913, R.E. von Mises suggested the yield criterion σ_v, as reported by Stephens et al. (2001), Lee et al. (2005) and Rösler et al. (2007), that can be expressed as:

$$\sigma_v = \sqrt{3}\sigma_p \tag{2.10}$$

The yielding of materials begins when the second deviatoric stress invariant J_2 reaches the yield stress in pure shear σ_p, that can be formulated as:

$$J_2 = \sigma_p^2 \tag{2.11}$$

Then,

$$\sigma_v = \sqrt{3J_2} \tag{2.12}$$

or:

$$\sigma_v^2 = 3J_2 \tag{2.13}$$

The equation assumes that (Donato & Bianchi 2012): (1) material is isotropic and homogeneous, (2) deformation takes place under constant volume, (3) tensile and compressive yield strengths are equal, and (4) the yielding phenomenon is not influenced by the hydrostatic component of the stress state. It gave better results compared to principal stress criterion, and could be used for a fatigue design optimisation (Klimkeit et al. 2011). It was recommended in the case of multi-axial stresses and ductile materials (Aygül et al. 2012).

Although it was developed more than one hundred years ago, the majority of FEA software still applies the von Mises yield criterion for stress analysis on metal components. Some studies had proved its robustness and efficiency, such as for a car suspension system ball joint (Ossa et al. 2011), steel column (Ban et al. 2012), cardiovascular stent (dos Santos et al. 2012), leaf spring (Karthik et al. 2012a; 2012b),

cylinder (Brünnet et al. 2014) and crane shaft (Zambrano et al. 2014). A coil spring might be strong enough to withstand a single applied load, but what happens when the component operates repeatedly? To predict component failure in such a case requires what is called durability analysis.

2.2 DURABILITY ASSOCIATED TO FATIGUE FAILURE

2.2.1 Durability Analysis

Many fatigue failures result in the loss of human life and in environmental pollution. Thus, automotive manufacturers have made large investments in fatigue area so as to achieve products which meet a specified fatigue life target (Al-Asady et al. 2009). One of the essential elements to achieve this target is durability. Durability is the ability of a component to withstand loadings without failure in an appropriate time. Components that have a good durability can reduce maintenance costs and material changes, as well as prevent failures and optimise component designs (He et al. 2010).

According to Bishop et al. (2000), there are several main engineering activities to complement the durability analysis, namely computer modelling, laboratory experiments and component testing. The computer modelling uses a software estimating the fatigue life of a component based on component geometry, material properties and service load. Figure 2.4 shows the relationship between the elements involved in the durability analysis. The component geometry is required for fabrication purposes to ensure that the component is properly placed in a testing machine. The material properties are used in conjunction with the component geometry and the service load. The main purpose of the laboratory experiment is to determine the deformation and the fatigue life of a component subjected to a particular service load. Next, the results of the fatigue life obtained from the computer modelling and the laboratory experiment can be compared. In automotive applications, the component testing can be performed by driving the component on a road surface in order to obtain a fatigue loading. The fatigue loading, also known as fatigue signal, typically consists of a set of variables taken at equally spaced intervals of time.

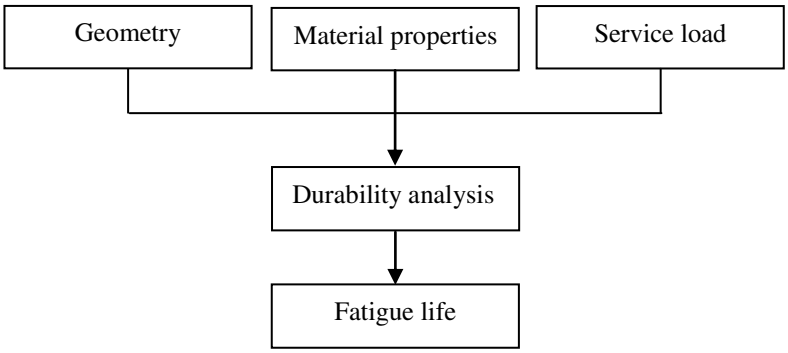

Figure 2.4 A conventional view of durability activities
Source: Karthik et al. 2012a

2.2.2 Types of Strain Signals

Signal is a form of information coming from many sources obtained by measuring and using some recording methods as a time function. According to Figliola & Beasley (2011), it may be categorised as analog, discrete time or digital. Many signals occurring in the environment or during a measurement carried out are analog signal, before converting to discrete time or digital. Analog signal is a smooth and continuous signal that is close to the natural state, which cannot be represented by a specific numerical equation. Among the advantages of the signal is that information transmitted is easily understood by its receiver, so misunderstanding can be inevitable. The weakness of the signal is that errors easily occur during information transmission and requires large storage space, time and cost to store and updates the information. A signal information becomes a problem if it is sent to the system that does not use analog signal in its application.

Contrast to this continuous signal is a discrete time signal, for which information about the magnitude of the signal is available only at discrete points in time. Because of that, some assumptions must be made when information is not available. Clearly, as the time between samples is reduced, the difference between the discrete variable and the continuous signal representations decreases. Discrete signals may appear to be quite different in terms of the information contained in the analog signal. Important information, however, can be well explained by such a discrete series. The accuracy of this representation depends on the frequency content of the signal, the interval between each discrete number and the total of measuring period sampling.

Digital signals are obtained in the form of readings at specific times, such as a certain time every hour. Digital signals have two important characteristics: (1) they exist at discrete values in time, and (2) the magnitude can have only certain discrete values, determined by a process known as quantisation at each discrete point in time. Quantisation assigns a single number to represent the range of magnitudes of a continuous signal. Thus, a digital signal provides a quantised magnitude at discrete times. Figure 2.5a shows digital and analog forms of the same signal. The waveform that would result from assuming that the signal is constant between sampled points in time is shown in Figure 2.5b.

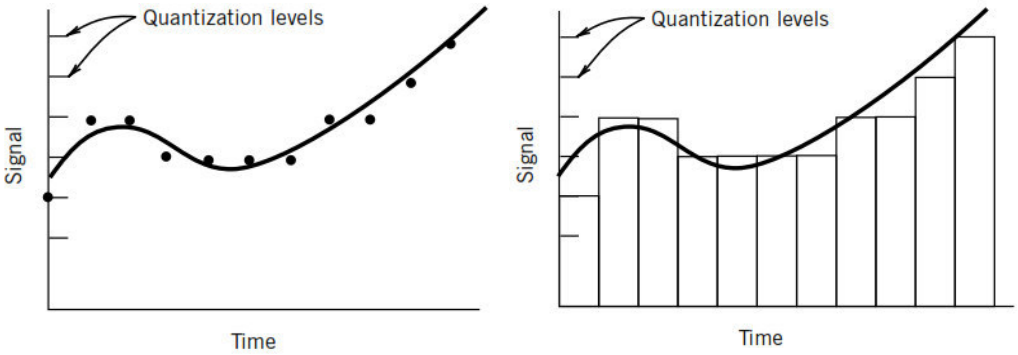

(a) (b)

Figure 2.5 Concept of digital signal: (a) digital signal representation, (b) digital waveform

Source: Figliola & Beasley 2011

Associated with the description of waveforms, signals can be divided into deterministic and non-deterministic. Deterministic signals do not vary over time and can be described by a mathematical relationship between function and time. They can be further characterised as being periodic or non-periodic. A signal is periodic if the variation in magnitude repeats at regular intervals in time. Periodic waveform may be divided into simple and complex periodics. Simple periodic waveforms contain only one frequency, while complex periodic waveforms contain multiple frequencies and are represented as a superposition of multiple simple periodic waveforms. Non-periodic is the term used to describe deterministic signals that do not repeat at regular intervals. A non-periodic signal can be further categorised into almost-periodic and transient.

In contrast, a non-deterministic signal is defined as a time-dependent signal. A signal representing random physical phenomenons cannot be described in a point by point manner by means of a mathematical equation. It cannot be prescribed before it occurs, although certain characteristics of the signal may be known in advance. Non-deterministic signals can be characterised as either stationary or non-stationary. Stationary is characterised by signal statistics which are unchanged across the signal length. If the random process is stationary and the mean value does not differ when computed over different sample segments measured for the process, the random process is defined as ergodic (Reytier et al. 2012); otherwise, it is defined as non-ergodic. In the case of non-stationary processes, the statistics are dependent on the time of a measurement. They can be divided into mildly and heavily non-stationary. Mildly non-stationary is defined as a random process with stable statistics for most records, but with short periods of changed statistics due to the presence of transient behaviour. Heavily non-stationary is defined as being similar to a mildly non-stationary signal, but with the presence of transient events over a large interval of the time history. Types of signals are summarised in Figure 2.6.

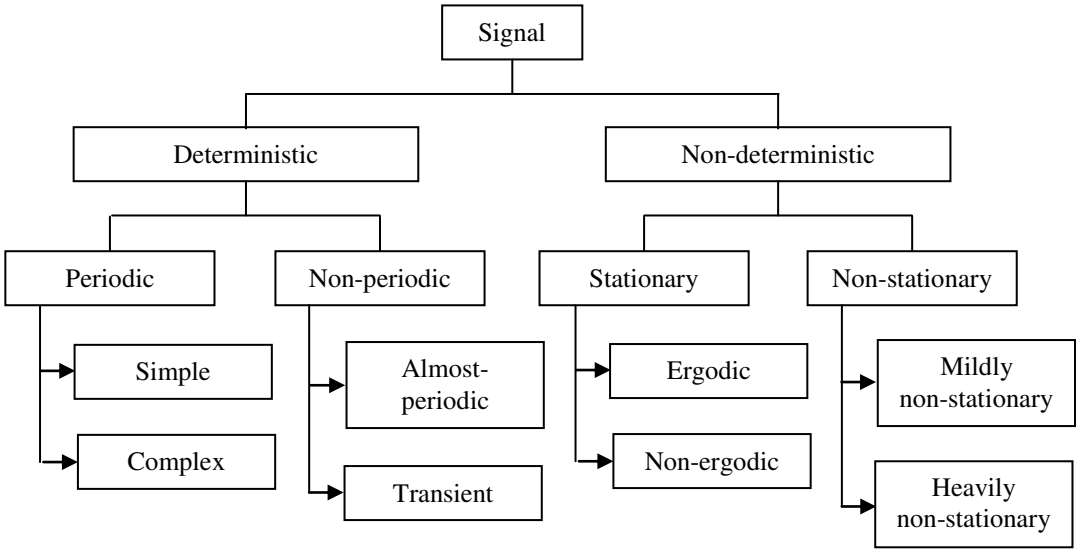

Figure 2.6 Classifications of signals

Source: Norton & Karczub 2007

A signal can be connected to a probability distribution, and an example of the signal distribution is normal or Gaussian distribution, also known as a “bell-shaped distribution”. It is most commonly credited to its founder, C.F. Gauss in 1809, but was

also discovered independently by two other eighteenth-century mathematicians, P.-S. Laplace and A. de Moivre. For most cases, the Gaussian distribution is used because it can produce an optimum resolution for the time and frequency axes simultaneously (Shimmel & Gallart 2005). The Gaussian distribution is symmetric about the mean value; it gains its maximum value at the mean and the minimum value is at plus and minus infinity, such as shown in Figure 2.7. The Gaussian distribution G for a signal F_j is given by:

$$G_{(F_j)} = \frac{1}{SD\sqrt{2\pi}} e^{-\left(F_i-\bar{x}\right)^2/2SD^2} \tag{2.14}$$

where SD is the standard deviation and $\bar{x}$ is the mean value.

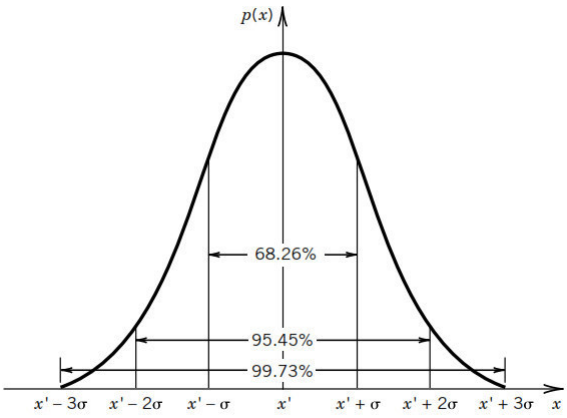

Figure 2.7 Example of the Gaussian distribution

Source: Figliola & Beasley 2011

One important problem, which was discovered at an early stage of the fatigue research, is the scatter in fatigue strength or fatigue life. One of the first attempts in this direction was made by Weibull (1951). In order to obtain a quantitative estimate of failures, the nature of a distribution is considered. The Weibull distribution is a probability distribution combining stochastic with statistic theory modelled through the extreme distribution condition of minimum or maximum using two- or three-parametric conditions, namely the location α, the shape β and the scale λ parameters. The cumulative distribution function (CDF) and the probability density function

(PDF) of a Weibull random variable W are respectively described by the following equations:

$$W = 1 - e^{-\frac{(F_j - \alpha)^\beta}{\lambda}} \tag{2.15}$$

$$W = \frac{\beta}{\lambda}\left(\frac{F_j - \alpha}{\lambda}\right)^{\beta-1} e^{-\frac{(F_j - \alpha)^\beta}{\lambda}} \tag{2.16}$$

In the equations, the shape parameter describes the failure experienced by a component. A shape parameter below one indicates that the failure rate decreases over time; a shape parameter equal to zero indicates that the failure is constant over time; and a shape parameter greater than one indicates that the failure rate increases over time. Furthermore, the scale parameter determines the spread of the distribution, while the location parameter is to adjust the skewness of the distribution. The plots of the Weibull distribution are shown in Figure 2.8.

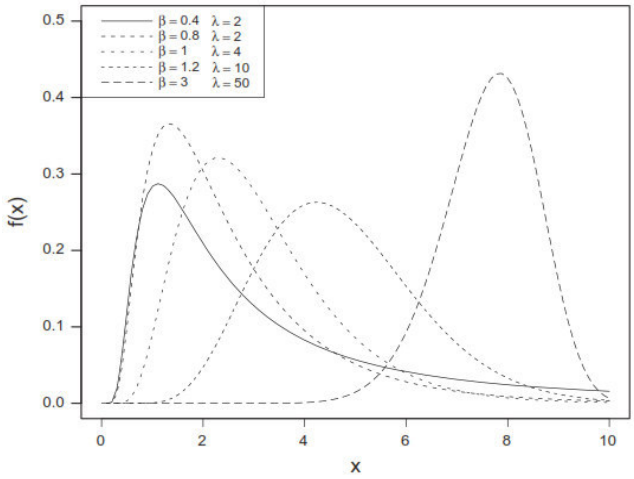

Figure 2.8 Plots of the Weibull distribution for different shape and scale parameters

Source: Peng & Yan 2014

The Weibull distribution has more reliable values than other distributions in fatigue evaluations (Sakin & Ay 2008). It was successfully employed to predict the probability of fatigue failure (Sivapragash et al. 2008) and scatter data of fatigue limit

could be satisfactorily described (Mohd et al. 2013). According to Chuliang & Kege (2011), when fatigue life follows two-parameter Weibull distribution, at least a 95 % confidence level is required. The Weibull parameters allow for estimating life using an appropriate reliability function (Souza et al. 2014).

A fatigue signal consists of a measurement of cyclic loads, such as strain and stress against time defined as CAL and VAL, as shown in Figure 2.9. A CAL oscillates between the fixed minimum and maximum amplitudes with a zero-mean amplitude. Figure 2.10 shows the peak-valley reversals used to determine the minimum and maximum stress levels. A peak is a change in the slope from positive to negative, while a valley is a change in the slope from negative to positive (ASTM E1049-85 1997). In general, the peak is a local maximum and the valley is a local minimum.

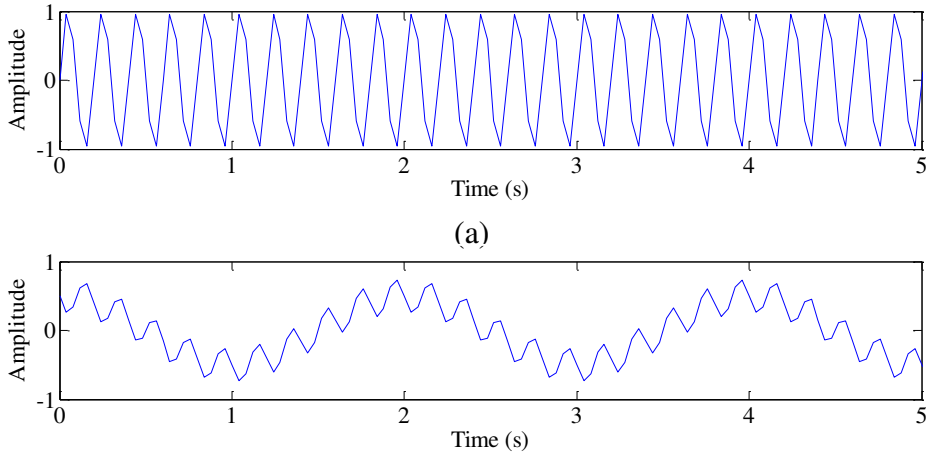

Figure 2.9 Types of repeated loads: (a) constant, (b) variable

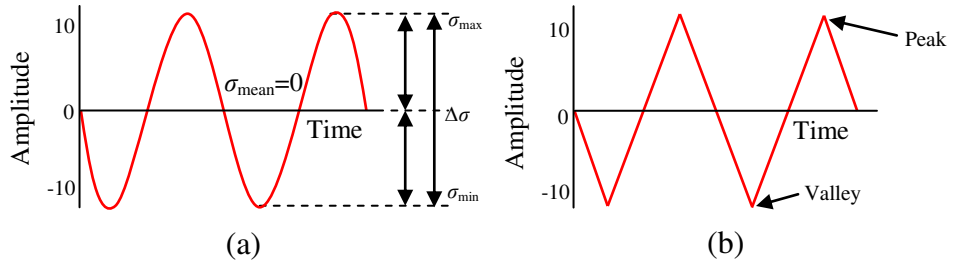

Figure 2.10 Representation of a constant loading: (a) time series, (b) peak-valley reversals

Source: de Jesus & da Silva 2010

The stress σ is expressed as (Callister & Rethwisch 2012; Juvinall & Marshek 2012):

$$\sigma = \frac{\Delta\sigma}{2} \tag{2.17}$$

and the stress range $\Delta\sigma$ is:

$$\Delta\sigma = \sigma_{max} - \sigma_{min} \tag{2.18}$$

where σ_{min} is the minimum stress and σ_{max} is the maximum stress. The mean stress σ_{mean} is generally defined as:

$$\sigma_{mean} = \frac{\sigma_{min} + \sigma_{max}}{2} \tag{2.19}$$

Actual structural components are usually subjected to alternating loads with a mean stress. The stress ratio is often used as representation of the mean stress. The stress ratio σ_r is defined as the ratio of the minimum stress σ_{min} to the maximum stress σ_{max}:

$$\sigma_r = \frac{\sigma_{min}}{\sigma_{max}} \tag{2.20}$$

The majority of fatigue lives of a machine part or mechanical system have conventionally been measured using a CAL for determining stress-life or strain-life curves, such as for a airplane structure (Nascimento et al. 2011; Lipski & Mroziński 2012), bridge deck (Aygül et al. 2012) and turbine (Wang et al. 2013a). Most fatigue signals found in real life, however, exhibit variable characteristics which provide challenges for analysis (Khan et al. 2014).

Thus, another type of loading is VAL defined as the cyclic load oscillating between the variable minimum and maximum amplitudes that also change in certain behaviour, as shown in Figure 2.11. The simplest type of VAL is the occurrence of a

small number of high peak loads. The experimental investigations have shown that the fatigue life of a component subjected to a VAL can be well below the fatigue life predicted using a CAL at the equivalent stress range level (Kim et al. 2006; Mottitschka et al. 2010). The reason for these differences is due to this type of loading containing a mixture of lower and higher amplitude cycles contributing to the cycle sequence effect. Higher amplitude cycles in a VAL influence the increase of effective stress for the subsequent lower amplitude cycles. Hence, crack growth rate for the lower amplitude cycles is increased, and even cycles below the fatigue limit can cause a significant amount of fatigue failure (Carvalho et al. 2010).

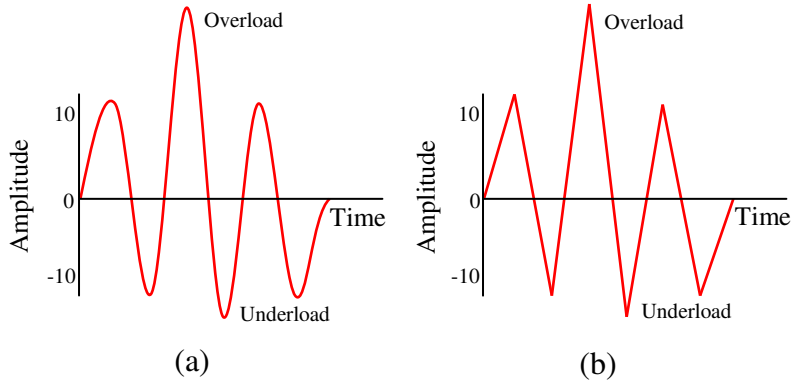

Figure 2.11 Representation of a variable loading: (a) time series, (b) peak-valley reversals

Source: de Jesus & da Silva 2010

Three types of loading sequences can occur in a VAL, namely overload, underload and overload followed by underload. Underload is defined as larger compressive stress, while overload refers to larger tensile stress. The combination between overload, underload and overload / underload makes a VAL more complex than a CAL because the stress or strain values are not constant, but vary on the data set. Therefore, fatigue life for a VAL is more difficult to predict (Cui 2002; Taheri et al. 2003). Extensive studies of the effect of overload and underload on the fatigue of metal components have been performed. Lee & Choi (2009) and White et al. (2009), respectively, conducted fatigue tests using steel and aluminum alloy. Both the studies found that the different load types gave different crack growth rates. Since it is very sensitive to peak and valley, fatigue life assessments are ideally based on the number of meaningful cycles.

2.2.3 Cycle Counting Methods

Fatigue life is likely to occur in finite or infinite period, so the number of cycles determines the fatigue life. Thus, the main point in analysing a component subjected to repeated loading is determining the number of cycles required for fatigue failure. Therefore, it is necessary to reduce the random service history into a simpler form of discrete events (Aid et al. 2011), pairing peaks and valleys. This process involves what is termed as cycle counting. In practice, several algorithms have been introduced to perform cycle counting, which require the entire loading history to be known before the counting process begins, as reported in ASTM E1049-85 (1997), Stephens et al. (2001), Lee et al. (2005) and Manson & Halford (2006).

The level crossing counting method, in Figure 2.12, is considered as the simplest approach. The magnitude of the loading time series is divided into several levels. It involves counting the number of positive slope crossings at specific levels above the mean and counting the negative slope crossings below the mean. Calculation at a certain level is estimated if a positive slope cycle across level is above a reference loading, or a negative slope cycle across level is under a reference loading. Reference loading level is usually determined by the overall mean value of the load. The calculated cycles are then arranged based on the highest range probability cycle, followed by the second highest range probability cycle, and so on. This process continues until all cycles are calculated. Despite its simplicity, it is not recommended for fatigue analysis as it does not maintain the original history sequence, which may be significant in fatigue life assessments.

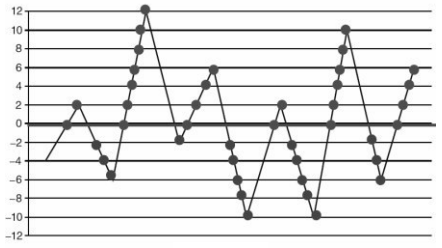

(a)

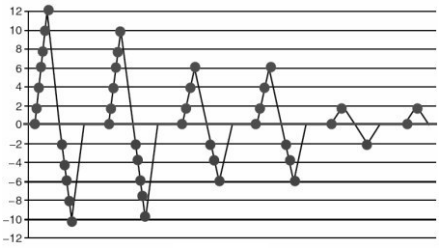

(b)

Range	Cycles
22	1
20	1
12	2
4	1

(c)

Figure 2.12 Method of level crossing counting: (a) the load of time series, (b) compilation of the cycle, (c) summary of results

Source: Lee et al. 2005

The peak counting method, in Figure 2.13, identifies peak-valley in a time series loading and arranges cycles from cycles with the probability of having the highest damage to those with the probability of having the lowest damage. The number of peaks above the reference loading level is calculated to determine the number of cycles, as are the number of valleys below the reference loading level. To eliminate small amplitude loadings, mean-crossing peak counting is often used. Instead of count all peak-valley, only the largest peak or valley between two successive mean crossings is counted. This method is not recommended as it does not relate peaks to their corresponding valleys.

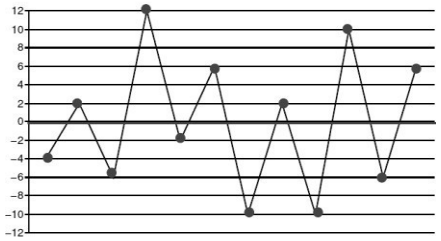

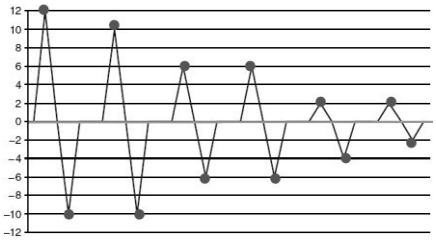

Range	Cycles
22	1
20	1
12	2
6	1
4	1

(a) (b) (c)

Figure 2.13 Method of peak counting: (a) the load of time series, (b) compilation of the cycle, (c) summary of results

Source: Lee et al. 2005

The simple-range method, in Figure 2.14, is defined as a difference between two successive reversals. Positive and negative ranges are determined by positive and negative reverse slopes. The range is positive when a valley is followed by a peak and negative when a valley follows a peak. If only positive and negative ranges are

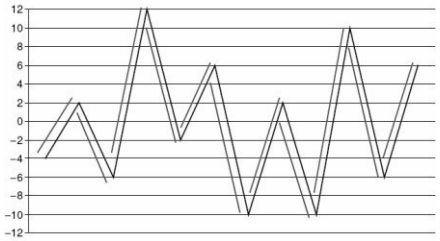

Range	Counts
+20	1
+18	1
+12	2
+8	1
+6	1
-8	1
-12	1
-14	1
-16	2

Range	Cycles
20	0.5
18	0.5
16	1
14	0.5
12	1.5
8	1
6	0.5

(a) (b) (c)

Figure 2.14 Method of simple-range: (a) the load of time series, (b) list of the calculated range, (c) summary of results

Source: Lee et al. 2005

counted, then each is counted as one cycle. If both positive and negative ranges are counted, then each is counted as one-half cycle. This method is not recommended as it may omit large overall cycles.

The most commonly utilised cycle counting method is the rain flow counting developed by M. Matsuishi and T. Endo in 1968. This method is regarded as the best representation to identify fatigue cycles (Baek et al. 2008; Xiong & Shenoi 2008). This method can determine cycles in a complex sequence loading. Figure 2.15 presents an example of the rain flow counting performed for a loading history. In order to apply this counting method for the whole time history, the load needs be rearranged from the maximum peak or the minimum valley, whichever is greater in absolute magnitude. In this example, the highest peak with a magnitude of twelve occurs first as opposite to the lowest valley and is therefore chosen as the beginning point for the rearranged load time history, as illustrated in Figure 2.15b. The main idea of this method is to treat small cycles as interruptions to larger cycles. Small cycles in Figures 2.15c to 2.15e are extracted in the beginning of the process, leaving larger cycles in Figures 2.15f to 2.15h to be extracted at the end of the process. The main task undertaken during the durability analysis is the fatigue life of components such as engine, suspension and car structure. Thus, aside from estimating the useful life, fatigue life assessment is an important stage in the design process of mechanical structures (Ottosen et al. 2008), because it ensures the components do not experience failure.

2.2.4 Fatigue Life Assessment

Fatigue life is defined as the number of cycles of stress or strain that sustains a component before failure (Ayoub et al. 2011). It is expressed as a repeat of blocks required to failure, indicating how long the component can last without failure under the given loading, in which one block represents a repetition of the loading. Fatigue life is the sum of both the crack initiation life and the crack propagation life (Upadhyaya & Sridhara 2012).

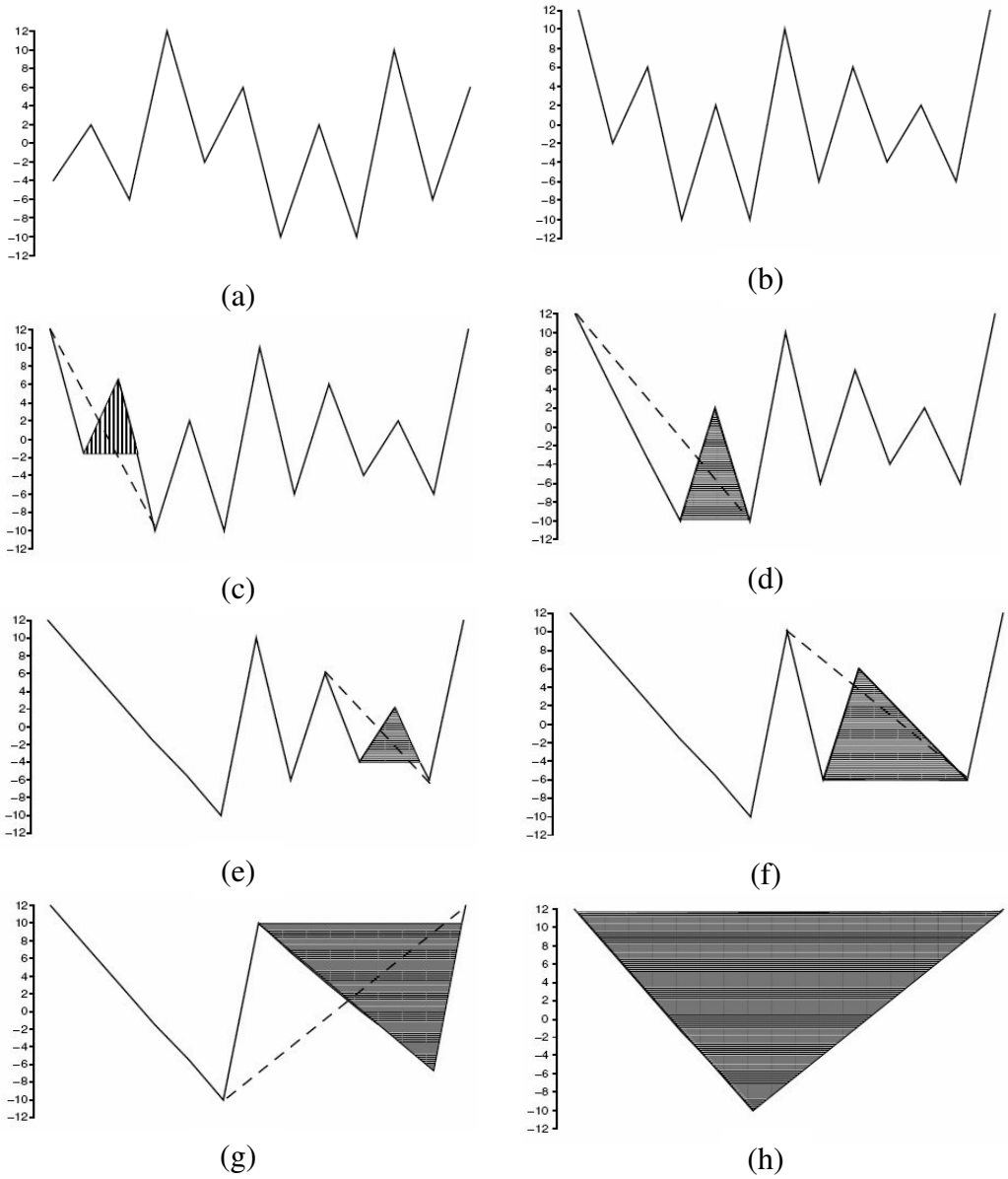

Number of cycles	From	To	Range	Mean
1	-2	6	8	2
1	-10	2	12	-4
1	-4	2	6	-1
1	-6	6	12	0
1	10	-6	16	2
1	12	-10	22	1

(i)

Figure 2.15 Method of rain flow counting: (a) - (h) the sequence of methods, (i) summary of results

Source: Lee et al. 2005

Fatigue failure is a phenomenon that involves increasing the crack with exposure to a loading. Fatigue failure occurs when the plastic deformation reaches an arbitrary limit, such as 0.2 % offset in a standard tensile test. Example of a coil spring experiencing fatigue failure is shown in Figure 2.16. As the crack progresses, the component at the crack root at any particular time is subjected to destructive localised reversed yielding. As the crack deepens, thereby reducing the section and causing increased stresses, the rate of crack propagation increases until the remaining section is no longer able to support a single load application and final fracture occurs, usually in accordance with the principles of fracture mechanics.

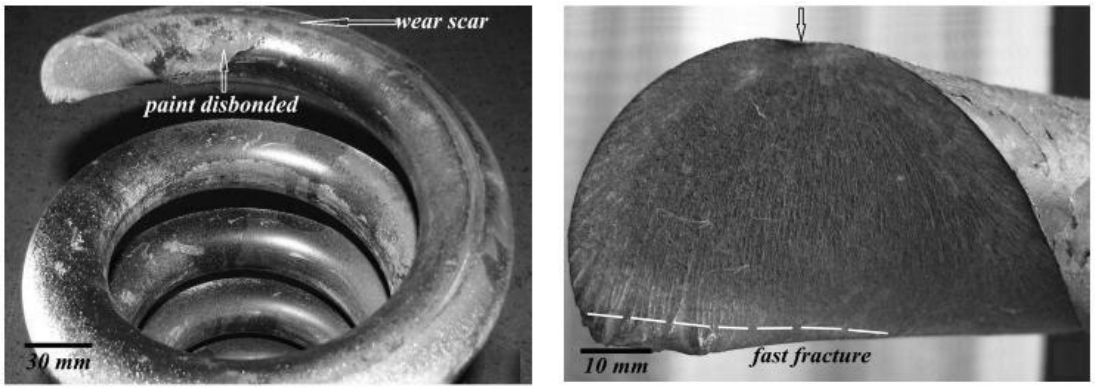

(a) (b)

Figure 2.16 Photograph of a failed coil spring: (a) fracture surface, (b) magnified image of the fracture surface

Source: Zhu et al. 2014

Fracture mechanics, proposed by Griffith (1921), are concerned with the propagation of cracks in materials. It uses analytical solid mechanics to calculate the driving force on a crack and those of experimental solid mechanics to characterise the material resistance to fracture. The ability to inspect for cracks and monitor their growth until a maximum allowable defect size is reached enables the life of its use to be extended beyond the original designed safe life. Damage propagation theory considers the fatigue life from the initial crack up to fracture. This propagation period is known as “the destroyer”.

Components with fatigue fracture experience surface damage that has fatigue and rupture zones, as shown in Figure 2.17. According to Ossa et al. (2011), Bhagi et al. (2013), Pantazopoulos et al. (2014) and Zambrano et al. (2014), fatigue zone is an

area of a crack growing and has a smooth and velvety texture, formed by the repeated pressing together and separating of the mating crack surfaces, identified based on the curvature of "beach marks". Fatigue fracture begins with a minute (usually microscopic) crack at a critical area of high local stress. An inspection of the surface after final fracture often reveals where the crack has gradually enlarged from one "beach mark" to the next, until the section is sufficiently weakened that the final fracture occurs on one final load application. However, final fracture is usually largely brittle. A distinguishing characteristic of fatigue fracture of a ductile material is that little if any macroscopic distortion occurs during the entire process, whereas failure caused by static overload produces gross distortion.

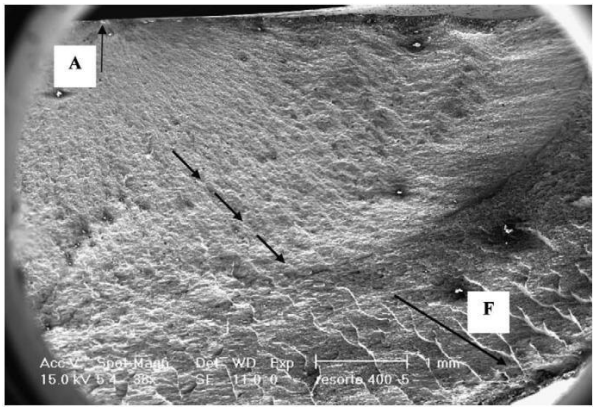

Figure 2.17 "Beach marks" (indicated by arrow), crack initiation (A) and fast fracture (F)

Source: Llano-Vizcaya et al. 2006

Theoretically, the crack growth rate relationships are based on the curves derived from of experiments. Through this curve decision, the process of fatigue failure of a component can be divided into three discrete periods based on three major regions (Rösler et al. 2007; Callister & Rethwisch 2012; Juvinall & Marshek 2012): stage I; the formation of cracks where damage begins in the sub-microscopic scale; stage II; visible damage, cracks start and medium crack propagation, where cracks are caused by surface scratches and steadily grow due to increased stress; and stage III; acceleration of crack growth and peak failure, where the final fracture occurs. However, only the processes (II) and (III) are involved in fracture mechanics. Figure 2.18 shows the regions of fracture and Figure 2.19 shows a plot of crack propagation rate (crack growth) versus stress intensity factor.

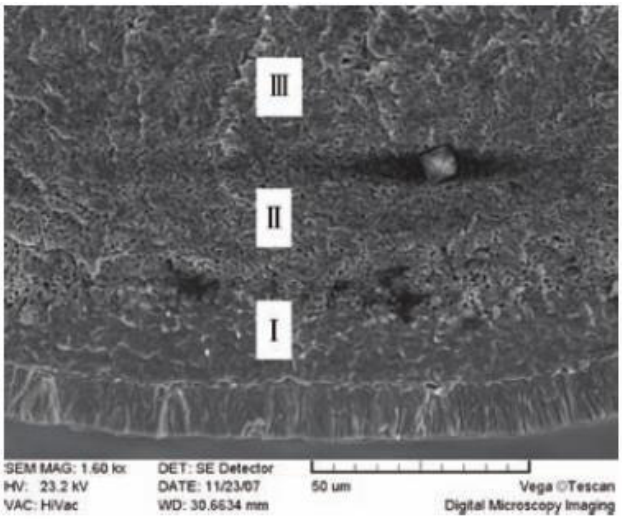

Figure 2.18 Regions of fracture occurring in a spring assembly

Source: Weiguo et al. 2011

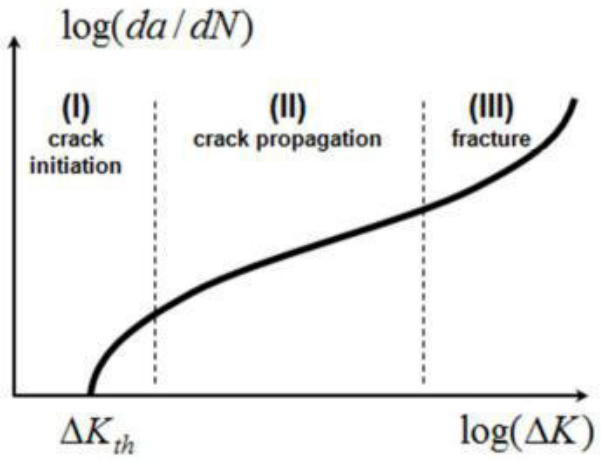

Figure 2.19 Regions of crack propagation rate

Source: Krasovskyy & Virta 2014

Based on the growth mechanism of very small cracks, crack propagation behaviour in stage I is then mathematically described in a manner similar to stage II. The crack growth rate can be described by an equation developed by Paris et al. (1961), known as the Paris equation:

$$\frac{\partial a}{\partial N_f} = B\Delta\breve{K}^e \tag{2.21}$$

where a is the crack length and N_f is the number of cycles to failure. B and e, respectively, are the coefficient and the exponential factors of the material properties, which are dependent upon factors such as frequency, temperature and stress ratio. $\Delta\breve{K}$ is the range of the stress intensity factor, described as (Juvinall & Marshek 2012):

$$\Delta\breve{K} = \breve{K}_{\max} - \breve{K}_{\min} \tag{2.22}$$

where $\breve{K}_{\max}$ and $\breve{K}_{\min}$ are the maximum and the minimum stress intensity factors, respectively.

Figure 2.20 illustrates the propagation of fatigue cracks for repeated loadings. The crack growth rate increases with cycles of alternating load. Specimens experiencing high stress range reach the critical point earlier than specimens experiencing low stress range, as well as result in smaller cracks. When the peak load is tensile, the crack growth is slowed down in comparison to the normal growth rate. This continues for a number of cycles until the original growth rate is resumed (Taheri et al. 2003). A limitation of fracture mechanics is that the allowable stress should not exceed approximately 80 % of the yield strength since the actual stress-strain distribution within the plastic zone is difficult to obtain (Cui 2002).

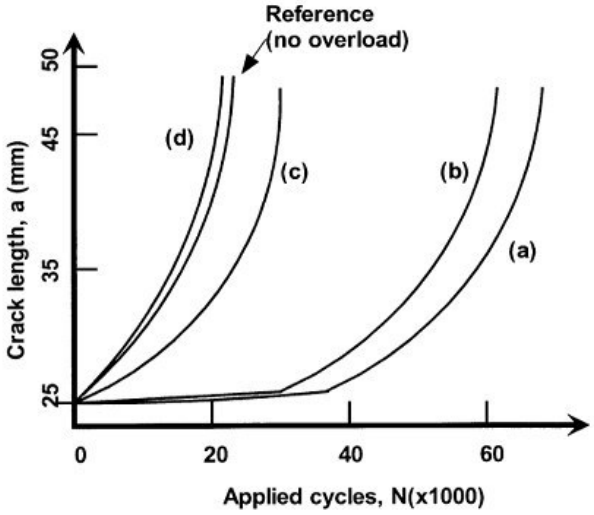

Figure 2.20 Behaviour of crack growth: (a) tension, (b) compression - tension, (c) tension - compression, (d) compression

Source: Taheri et al. 2003

According to Beaurepaire & Schuëller (2011), a long initial crack must be initially present. In such a case, fatigue life cannot be estimated from a curve and only simulation will allow model fatigue crack initiation and propagation.

Pantazopoulos et al. (2014) recommended periodic maintenance and inspection to prevent and minimise risk for future failures. This action is only suitable for high value components, such as aircraft structures (Chuliang & Kege 2011). It is not generally feasible to apply the crack inspection process for inexpensive components that are made in large numbers. Components which fall into this category are automobile engines, steering and suspension parts. Performing periodic inspections on these components generally increase the cost of the items (Cui 2002). For these components, it is important to predict crack initiation in order to avoid fatigue failure by replacing the cracked parts from service at the appropriate time (Jiang & Murthy 2011). These components are considered failed if there is a small crack. For the large percentage of mechanical parts subjected to randomly varying stress cycle intensity, the prediction of fatigue life is further complicated (Juvinall & Marshek 2012). To predict whether the stress at a critical point at a component causes a failure, a fatigue feature determined by means of the stress-life approach is usually used in this case.

Stephens et al. (2001), Schijve (2004), Lee et al. (2005) and Manson & Halford (2006) reported that an early empirical model by W. Gerber in 1874 was proposed to compensate the mean stress effect on high cycle fatigue strength, formulated as:

$$\frac{\sigma}{\sigma_{\text{limit}}} + \left(\frac{\sigma_{\text{mean}}}{\sigma_{\text{uts}}} \right)^2 = 1 \tag{2.23}$$

where σ_{limit} is the fatigue limit and σ_{uts} is the ultimate tensile strength. The main drawback of the model is that it does not distinguish between compression and tension. Thus, the relationship had been modified by Goodman (1914), and takes the following form:

$$\frac{\sigma}{\sigma_{\text{limit}}} + \frac{\sigma_{\text{mean}}}{\sigma_{\text{uts}}} = 1 \tag{2.24}$$

Similar concept was also used by C.R. Soderberg in 1930, as reported by Lee et al. (2005), who proposed the use of the yield strength σ_{yield} instead of the ultimate tensile strength σ_{uts}:

$$\frac{\sigma}{\sigma_{\text{limit}}} + \frac{\sigma_{\text{mean}}}{\sigma_{\text{yield}}} = 1 \tag{2.25}$$

These discoveries had been introduced to a new character known as the fatigue limit or the endurance limit (Sadananda et al. 2007), in addition to previous metal analyses namely the yield point and the UTS. By definition, the fatigue limit is the maximum amount of stress that can be repeated in infinite time at a zero-mean stress without any failures as fatigue life becomes very large. The fatigue limit σ_{limit} for a smooth specimen is defined as (Lee et al. 2005):

$$\sigma_{\text{limit}} = 0.5\sigma_{\text{uts}} \tag{2.26}$$

Figure 2.21 shows the stress-life curve exhibiting a plateau level after 10^6 cycles. Above the endurance limit, fatigue life decreases abruptly because of higher stress amplitudes, and is often referred to as one of infinite fatigue life occurring when the applied stress is below the endurance limit. Under certain stress amplitudes, testing specimens do not break (Benedetti et al. 2010; Lei et al. 2010). Predicting the life of a component above the endurance limit is at best a rough procedure.

The stress-life approach, however, has disadvantages too. First is the very complicated calculation of the stress concentration factor. Also, in fatigue analysis with a complex stress, it gives results which are often not confirmed in experiments (Prokopowicz et al. 2009). According to dos Santos et al. (2012), the Soderberg model leaded to conservative fatigue predictions. However, Karthik et al. (2012a; 2012b) stated that the Goodman model was more conservative when used for loading sequences which were predominantly tensile in nature, while when the time histories

were predominantly zero-mean, the Gerber model was more conservative. Based on a study by Ghafoori et al. (2015), the Gerber model suggested a parabola for ductile metals, but this model was not conservative for fatigue design. A better result was provided by the Goodman model proposing a straight line. It presented a safe regime of cyclic loading for infinite fatigue life in ductile metals. However, the Goodman model required a lot of computation and was non-conservative for brittle metals.

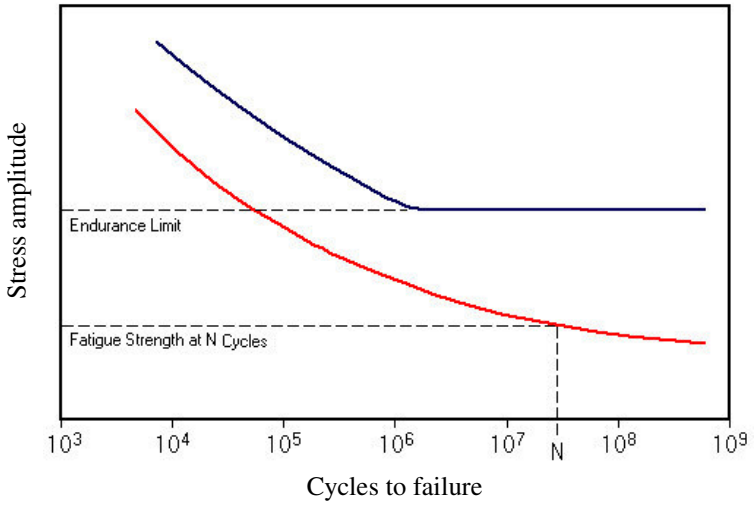

Figure 2.21 Common engineering curve of the stress-life

Source: Chapetti & Jaureguizahar 2012; Niesłony & Böhm 2013

Although the stress-life approach describes the relationship between the stress amplitude and the mean stress, it has the drawback of requiring a new set of fitting parameters for every level of the stress amplitude and the mean stress (Bruchhausen et al. 2015). Niesłony & Böhm (2013) added that all the presented models do not take directly into account the relationship between the number of cycles to failure and the mean stress sensitivity of the materials. This is a significant deficiency of the common models because the mean stress sensitivity depends considerably on the cycle range in which fatigue failure is expected or observed. It does not depend only on the mean stress value, but also on the number of cycles to failure, and thus, this effect is often considerable and cannot be neglected during fatigue life assessments for most constructional materials.

In addition, the stress-life-based approach is valid when it is used to analyse components that have long fatigue life (Ince & Glinka 2011; dos Santos et al. 2012; Niesłony & Böhm 2013; Ghafoori et al. 2015), at approximately 10^5 cycles (Nascimento et al. 2011; Schaumann & Steppeler 2013; Ye et al. 2014; Bruchhausen et al. 2015). The approach is widely used in design applications where the stresses are mainly in the elastic range. The approach was developed for the high cycle fatigue or so called fatigue limit assessment using material constants determined based on a tensile test. However, it is not possible to describe the fatigue behaviour of materials in the right way, since these parameters do not involve information on how the materials behave under time-variable loading, especially when cyclic hardening or softening of the materials occurs in the middle cycle fatigue (Niesłony & Böhm 2013). Under the transition point, the stress-life approach is not valid because the nominal stress becomes the elastic-plastic. For these cases, the strain-life-based approach is the appropriate method.

The strain-life approach is accurate enough for fatigue life assessments, since it considers plastic forming events that exist in a local area. The approach is usually applied to ductile materials since the low cycle fatigue of small components (dos Santos et al. 2012; Nagode 2014; Ghafoori et al. 2015), which is only within 10^3 cycles (Nascimento et al. 2011; Schaumann & Steppeler 2013; Ye et al. 2014), do not require high operating costs and do not require extensive crack observation in which the failure occurs. Moreover, the strain-life approach can also be used for situations where the long fatigue life has some plasticity considering plastic strain (Ince & Glinka 2011), and thus, it is a comprehensive approach that can be used as a substitute for the stress-life-based approach (Fajdiga & Sraml 2009).

The strain-life approach can be performed based on the curve shown in Figure 2.22, obtained through experiments at a CAL. Loads applied are a fully reversed strain cycle producing elastic and plastic strain ranges. For high fatigue life, the elastic strain is dominant and the plastic strain is relatively small. This condition is called high cycle fatigue. For low fatigue life, the plastic strain is greater than the elastic strain, and it is called low cycle fatigue. In the middle of its life, there is a point where the elastic and plastic strains have the same strain. The strain-life curve provides the

mechanical properties of a material, such as the fatigue strength coefficient σ'_f, the fatigue strength exponent b, the fatigue ductile coefficient ε'_f and the fatigue ductile exponent c. A detailed explanation to construct a strain-life curve can be found in Williams et al. (2003) and ASTM E739-91 (2004).

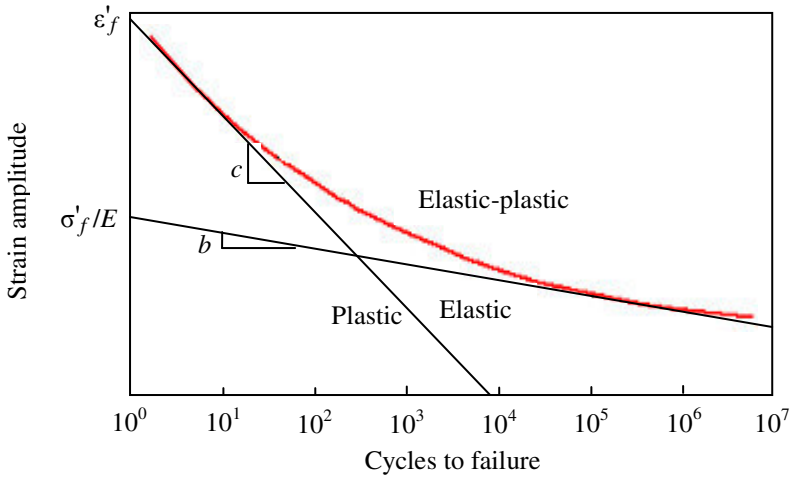

Figure 2.22 Common engineering curve of the strain-life
Source: Chapetti & Jaureguizahar 2012; Niesłony & Böhm 2013

The strain-life approach is actually based on the linear relation between a stress amplitude and a number of cycles, which was introduced by O.H. Basquin in 1910, as reported by Stephens et al. (2001), Lee et al. (2005) and Manson & Halford (2006). Referring to Equation (2.17) and Figure 2.22, the stress σ is presented by:

$$\frac{\Delta\sigma}{2} = \sigma'_f \left(2N_f\right)^b \tag{2.27}$$

The elastic strain ε_e is obtained by dividing Equation (2.27) by the material modulus of elasticity E:

$$\varepsilon_e = \frac{\sigma'_f}{E}\left(2N_f\right)^b \tag{2.28}$$

Since the stress-life-based approach is mostly applicable in high cycle regimes, Manson (1954) expressed linear damage rule for low cycle regimes in terms of the plastic strain range ε_p as:

$$\varepsilon_p = \varepsilon_f^{'} \left(2N_f\right)^c \tag{2.29}$$

Thus, the total strain ε is produced using the elastic ε_e and the plastic ε_p strains, as follows:

$$\varepsilon = \varepsilon_e + \varepsilon_p \tag{2.30}$$

The elastic and the plastic strains were combined to obtain a correlation between the fatigue life and the strain, known as the Coffin-Manson model, which is the basis of the strain-life approach. It is defined as follows:

$$\varepsilon = \frac{\sigma'_f}{E}\left(2N_f\right)^b + \varepsilon'_f \left(2N_f\right)^c \tag{2.31}$$

Petrenec et al. (2010) found that the strain-life curves of cast iron at different temperatures could be well approximated by the Coffin-Manson model. However, Praveen & Singh (2008) found exhibiting dual slopes in various heat treatment conditions for superalloys. The Coffin-Manson model sets the fatigue life assessment for strain loads with a zero-mean stress to show the drawbacks of the relationship between the fatigue life and the strain. Thus, the model was modified by several researchers. Niesłony et al. (2008) proposed a three-dimensional method, with the plastic part of strain, stress and fatigue life as the coordinates, to determine the cyclic parameters by describing the stress-strain curve adequately. Runciman et al. (2011) also proposed a modified Coffin-Manson model serving as a satisfactory model for various testing modes for fatigue life prediction. Furthermore, Karunananda et al. (2011) modified the model considering the effect of high amplitude loadings. Finally, Pathak (2012) modified the model for an iterative analysis of contact fatigue crack initiation.

Fatigue behaviour of engineering materials is very sensitive to certain types of specific variables, such as mean stress, geometric design, surface effect, metallic variables and environment (Callister & Rethwisch 2012). The mean stress, however, is a major factor in fatigue analysis (Klimkeit et al. 2011; Ghafoori et al. 2015), where the influence of the mean stress is more significant in low strain or high cycle fatigue regimes (Tao & Xia 2007; Kovacs et al. 2013). Figure 2.23 shows the types of different loadings on the mean values developed by the Society of Automotive Engineers (SAE). The tensile or positive mean stress reduces the fatigue life, whereas the compressive or negative mean stress may increases it (Ince & Glinka 2011; Chiou & Yang 2012; Taheri et al. 2013; Khan et al. 2014; Bruchhausen et al. 2015), as shown in Figure 2.24.

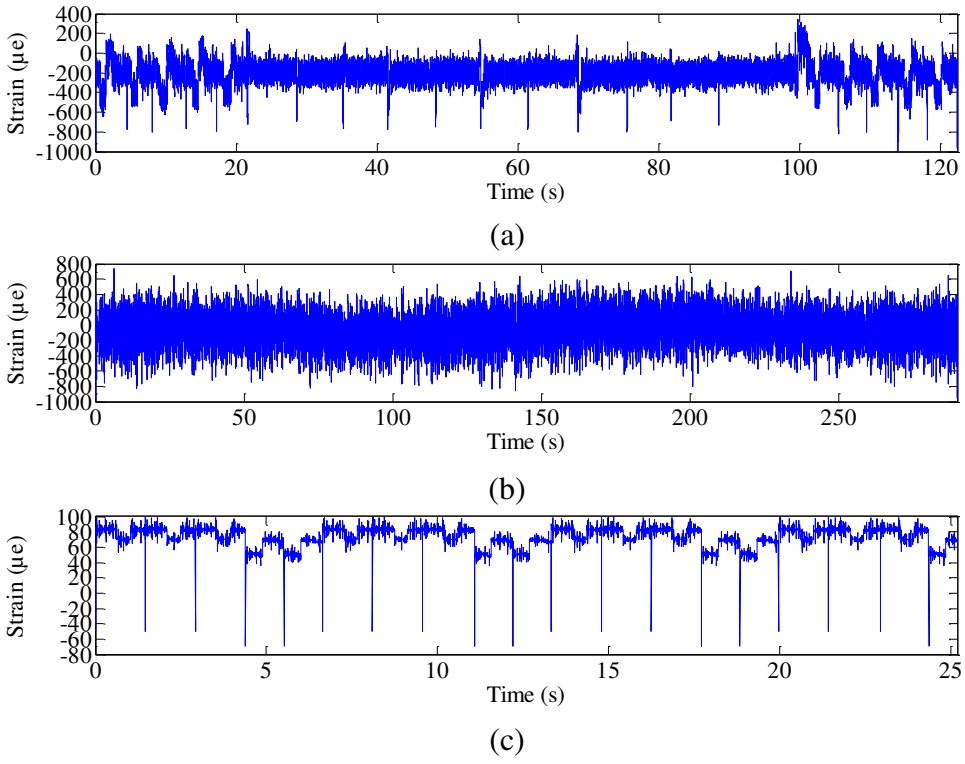

Figure 2.23 Strain signals at different mean values: (a) SAESUS, mean value is less than zero, (b) SAEBKT, zero-mean value, (c) SAETRN, mean value is greater than zero

Source: Oh 2001

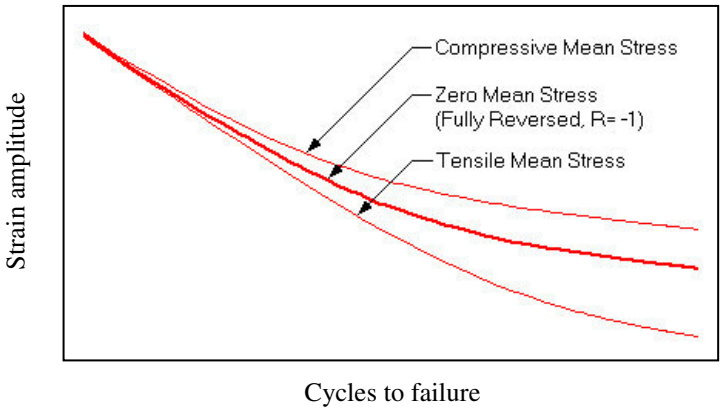

Figure 2.24 Effect of mean stress on the strain-life curve
Source: Bruchhausen et al. 2015

Therefore, the parameters of fatigue failure are mostly developed considering the mean stress effects on the fatigue properties. As reported by Stephens et al. (2001), Lee et al. (2005) and Manson & Halford (2006), the Morrow model, developed by J. Morrow in 1968, is one of the strain-life models that can be used for applications involving the effects of the mean stress. The Morrow model states that normal mean stress is accounted for by adjusting the elastic strain-life curve by mean stress. It replaced the fatigue strength coefficient σ'_f with the fatigue strength coefficient minus the mean stress σ'_f-σ_{mean}, such that:

$$\varepsilon = \frac{\sigma'_f - \sigma_{mean}}{E}\left(2N_f\right)^b + \varepsilon'_f\left(2N_f\right)^c \tag{2.32}$$

In the equation, the mean stress is taken to be positive for tension and negative for compression.

Stephens et al. (2001) and Lee et al. (2005) also reported another mean stress correction model suggested by K.N. Smith, P. Watson and T.H. Topper in 1970, often called the SWT parameter. The parameters taken into account for fatigue damage were considered based on the maximum stress and strain amplitudes per cycle. The SWT parameter was based on strain-life testing data obtained at various mean stresses assuming that for different combinations of strain amplitude and mean stress, the

products of maximum stress and strain amplitude remain constant for a given life. This model was derived from Equation (2.31) multiplied by (2.27):

$$\sigma_{\max}\varepsilon = \left(\frac{\sigma'_f}{E}\left(2N_f\right)^b + \varepsilon'_f\left(2N_f\right)^c\right)\left(\sigma'_f\left(2N_f\right)^b\right) \tag{2.33}$$

Thus, the SWT model is mathematically defined as:

$$\sigma_{\max}\varepsilon = \frac{\left(\sigma'_f\right)^2}{E}\left(2N_f\right)^{2b} + \sigma'_f\varepsilon'_f\left(2N_f\right)^{b+c} \tag{2.34}$$

Various mean stress effects have been specified for various types of materials and experimental techniques producing a variety of mean stress theories. However, the Morrow and SWT mean stress correction models are the most popular models. The Morrow model gave better results for steel materials, while the SWT model was the better choice for general use (Cui 2002). According to Liao et al. (2009), the SWT model is dominated by the principal strain amplitude and thus was appropriate for predicting the fatigue life of structures subjected to axial loading. In a study by de Jesus & da Silva (2010), the Morrow model gave conservative predictions for low and long fatigue lives. In another study by Taheri et al. (2013), the SWT model was acceptable for a CAL, but was non-conservative for a VAL. Finally, Nagode (2014) proposed a SWT-based model for continuous damage parameter calculation considering the mean stress effect.

According to Abdullah (2005), for tensile sequence loadings, the SWT model was more conservative. In cases where the load was compressive cycles, the Morrow model produced more realistic results. This was supported by Ince & Glinka (2011) who found that the SWT model provided close predictions for tensile mean stresses, while the Morrow model was suitable for compressive mean stress values. They also found that the Morrow model predicted more effects on the mean stress which can be derived at long life, where the elastic strains dominate. The model also predicted that the mean stress has little effect on shorter life, where the plastic strain is large. The prediction trend of the Morrow model was consistent with observations that the mean stress has a greater impact at a longer life.

A different statement was given by Karthik et al. (2012a; 2012b). For a tensile sequence loading, the Morrow model was more sensitive and therefore recommended. The model was detrimental in predicting compressive mean stresses but was beneficial for tensile mean stresses. They also found that the Morrow and SWT models gave lower fatigue life compared to the Coffin-Manson model. Both the Morrow and SWT models were also applicable for a zero-mean stress. Although the models give different results in fatigue life assessments, they are still widely used and are associated with the Palmgren-Miner linear cumulative fatigue damage rule to obtain material properties in order to develop a strain-life curve.

2.2.5 Theory of Linear Cumulative Damage

Cumulative fatigue damage is calculated by the addition of normal and shear energy for each peak-valley in each block loading. Therefore, the cumulative fatigue damage is influenced by variable amplitude and frequency cycles. In 1945, M.A. Miner of the United States developed a linear cumulative fatigue damage criteria proposed by A. Palmgren of Sweden in 1924, now known as the Palmgren-Miner linear cumulative fatigue damage rule, as reported by Manson & Halford (2006), Rösler et al. (2007) and Juvinall & Marshek (2012).

The fatigue damage for each loading cycle D_i can be calculated as follows:

$$D_i = \frac{1}{N_f} \tag{2.35}$$

The Palmgren-Miner rule is then used to calculate the cumulative fatigue damage D of a loading block, and it is defined as follows:

$$D = \sum \left(\frac{n_i}{N_f} \right) \tag{2.36}$$

where n_i is the number of applied cycles.

Fatigue damage has a range of zero to one, where zero indicates no damage (infinite cycles to failure) and one is assumed as failure (one cycle to failure) (Upadhyaya & Sridhara 2012). It very logically proposed the simple concept that if a part is cyclically loaded at a stress level causing failure in 10^5 cycles, each cycle of this loading consumes one part in 10^5 of the life. If other stress cycles are interposed corresponding to a life of 10^4 cycles, each of these consumes one part in 10^4 of the life, and so on. When, on this basis, 100 % of the life has been consumed, fatigue failure is predicted (Juvinall & Marshek 2012). If a component experiences 100 % of the fatigue damage and cause fracture, the Palmgren-Miner equation can be rewritten as follows:

$$\sum \frac{n_i}{N_f} = 1 \tag{2.37}$$

Through this concept, the number of cycles before failure at a particular stress can be predicted.

The rule, however, is not for an accurate fatigue life assessment. Some limitations have been found during the use of the Palmgren-Miner rule (Lee et al. 2007; Carvalho et al. 2010; Xu et al. 2012; Taheri et al. 2013): (1) loading level properties which are independent, (2) the lack of contribution to fatigue failure for stress under the fatigue limit, and (3) the lack of interaction between cycles. Many researchers tried to modify the rule, such as performed by Karunananda et al. (2011) considering the effect of high amplitude loading and Aid et al. (2011) taking into account the damage evolution at different load levels, but due to its intrinsic deficiencies, no matter which version is used fatigue life assessments based on this rule are still not performed correctly and are often unsatisfactory. Despite the Palmgren-Miner rule being weak for a VAL, it is still widely used and is still regarded as an important method in determining the fatigue life of a structural design (Chen et al. 2011; Ghafoori et al. 2015). Fatigue life assessments using the rule are acceptable to the present. This is because the range of errors that exist is not very large or significant (Garcia et al. 2005; Kang et al. 2007; Taheri et al. 2013).

A few fundamental concepts in understanding the patterns of observed fatigue behaviour are (Juvinall & Marshek 2012): (1) fatigue failure results from repeated plastic deformation after thousands or even millions of cycles and can occur at stress levels far below the conventionally determined yield point or elastic limit, (2) because highly localised plastic yielding can be the beginning of fatigue failure, strengthening potentially vulnerable locations, such as holes, sharp corners, surface scratches and corrosion, is often as effective as making the entire part from a stronger material, (3) the repeated load cycling will cause a loss of local ductility until the cyclic strain imposed at the vulnerable spot can no longer be withstood without fracture, and (4) the initial fatigue crack usually results in an increase in local stress concentration.

A metallic structure is able to withstand failure at higher stress but fails if the load fluctuates. This proves that a safe limit for a design with repeated loads are below the allowable static loads. It shows that fatigue failure not only occurs as a result of the load cycle, but also because of the medium stress. Thus, some guidelines usually considered during the design of a component are: (1) eliminating or reducing stress concentration producing a smooth surface, (2) avoiding sharp surfaces caused by punches, shears or other manufacturing processes, (3) preventing the formation of irregular surfaces during processing, and (4) eliminating or reducing tensile residual stresses caused by manufacturing process. Due to the long period required for the crack growth, which is from the beginning to the end of the failure, there is much time to detect the fatigue failure and accomplish the appropriate repairs. In the past few years, several techniques for signal analysis were proposed with the aim to evaluate the dynamic characteristics of structures (Ditommaso et al. 2012).

2.3 SIGNAL ANALYSIS

Signal analysis is a non-destructive process converting a signal into information providing the signal source and predicts the pattern. It aims to know the information contained in the signal that cannot be seen by direct observation. Signal analysis can be performed in the time, frequency and time-frequency domains.

2.3.1 Time Domain Analysis

Statistical parameters are used for random signal classification and pattern monitoring (Kreyszig 2011; Montgomery 2013; Brandt 2014). For a signal F_j with the number of data n, the mean value $\bar{x}$ is given by:

$$\bar{x} = \frac{1}{n}\sum_{j=1}^{n} F_j \tag{2.38}$$

Standard deviation (SD) measures the distribution of a data set based on the mean value. SD for a number of sampling data F_j that exceed thirty can be expressed as follows:

$$SD = \sqrt{\frac{1}{n}\sum_{j=1}^{n}\left(F_j - \bar{x}\right)^2} \tag{2.39}$$

If the number of sampling data F_j is less than thirty, SD can be expressed as follows:

$$SD = \sqrt{\frac{1}{n-1}\sum_{j=1}^{n}\left(F_j - \bar{x}\right)^2} \tag{2.40}$$

Root-mean square (r.m.s.) is the second statistical moment used for determining the total energy contained in a signal. r.m.s. of signals with a zero-mean value is equal to SD. r.m.s. of discrete data F_j can be calculated as follows:

$$r.m.s. = \sqrt{\frac{1}{n}\sum_{j=1}^{n} F_j^{\,2}} \tag{2.41}$$

Skewness is the third statistical moment used for measuring the symmetry of a data distribution based on the mean value. Skewness of a symmetric distribution, such as a sinusoidal or Gaussian distribution, is zero. Negative skewness indicates that the

probability distribution is skewed to the left, whereas positive skewness indicates that the probability distribution is skewed to the right, referring to the mean value. The skewness of a signal F_j can be expressed as follows:

$$Skew = \frac{1}{n(SD)^3} \sum_{j=1}^{n} \left(F_j - \bar{x}\right)^3 \tag{2.42}$$

Kurtosis is the fourth statistical moment that is very sensitive to spikes and it represents the continuity of peaks in a time series loading. Kurtosis K for a set of discrete data F_j is formulated as:

$$K = \frac{1}{n(SD)^4} \sum_{j=1}^{n} \left(F_j - \bar{x}\right)^4 \tag{2.43}$$

Crest factor CF is defined as the ratio between the maximum amplitude of a time series F_{jmax} and r.m.s., given by:

$$CF = \left| \frac{F_{j\max}}{r.m.s.} \right| \tag{2.44}$$

Crest factor for a sinusoidal time series is equal to 1.41, and it is close to 4.00 in the cases of a Gaussian distribution with infinite length.

Fatigue signals are generally described by statistics that represent their characteristics. Thus, statistical analysis was required and was considered in this stage. Statistical parameters are commonly found in engineering applications and have emerged as good indicators of fatigue failure for years. From those parameters, SD, r.m.s. and kurtosis give significant effects to evaluate the randomness of fatigue signals. Fatigue studies utilising statistical parameters can be found in literature, such as in Aygül et al. (2013) using SD for determining the fatigue strength characteristics of welded bridge joints. Furthermore, Kihm & Delaux (2013) and Chen (2014), respectively, applied statistical parameters for observing the influence of clipping a random drive signal and for calculating the cross-wind fatigue of wind-excited

structures. Finally, Kinloch et al. (2014) utilised SD for determining the error of the fracture toughness and the fatigue resistance of polymer blends. The success of statistical parameters in previous fatigue studies, motivated the author to prove their abilities in estimating fatigue life.

The selection of mean value aimed to identify the types of loads experienced by the coil spring, which were either tensile or compressive forces. SD and r.m.s were involved since in actual applications, most fatigue signals have a non-zero-mean value. SD was used to determine the distribution of the strain signals. Lower SD indicates each point in one data set is near the mean value; otherwise, it shows that the point is far from the mean value. Furthermore, r.m.s. represents the internal vibration energy of discrete data. Lower r.m.s. indicates the energy contained in a signal is low; otherwise, the energy is higher (Wang et al. 2012a). The last one, the kurtosis value of a Gaussian distribution is close to 3.0 (Kihm & Delaux 2013; Chen 2014). Kurtosis lower than 3.0 indicates stationary data, and a value above 3.0 indicates non-stationary data (Braccesi et al. 2009). However, the frequency information in a time domain analysis is unavailable. Therefore, the frequency domain analysis is needed.

2.3.2 Frequency Domain Analysis

The frequency domain analysis is performed in order to convert a time domain signal into the frequency domain. This analysis determines noisy content based on a certain frequency range. Its results are usually represented with a graph with frequency on the *x*-axis and amplitude on the *y*-axis. For a periodic time function, the frequency domain can be performed using the classical Fourier transform *FT* (Fourier 1878), defined as:

$$FT_{(\omega)} = \int_{-\infty}^{\infty} F_{\mathrm{j}(t)} e^{-i\omega t}\, dt \tag{2.45}$$

where t is the time and ω is the angular frequency, defined by:

$$\omega = 2\pi f \tag{2.46}$$

where f is the frequency.

According to Figliola & Beasley (2011) and Kreyszig (2011), the main equipment in the frequency domain analysis is the discrete Fourier transform (DFT). It operates by converting a signal in the time domain to a set of points in the frequency domain. The frequency information obtained can be reverted back into the time domain using the inverse discrete Fourier transform (IDFT). The DFT, however, is quite difficult to implement because it involves repeated addition and multiplication operations. To overcome the shortcomings of the DFT, a fast algorithm had been introduced by Cooley & Tukey (1965), known as the fast Fourier transform (FFT). It effectively breaks a signal down into discrete sinusoidal waves. This method can reduce the repetition required in digital signal conversion processes (Figliola & Beasley 2011). The frequency information obtained from the FFT can also be reverted back into the time domain using the inverse fast Fourier transform (IFFT).

In addition to the DFT and the FFT, for most fatigue studies, the frequency domain analysis is performed using the power spectral density (PSD). It is a spectrum analysis taking into account the energy of a signal in the frequency domain. According to MATLAB (2008a) and Wijker (2009), the PSD can be expressed as:

$$PSD = \frac{1}{2\pi} \sum_{n=-\infty}^{\infty} F_{\mathrm{j}(n)} e^{-i\omega t} \tag{2.47}$$

The PSD resolution can be determined by varying the FFT multiplication parameter which is directly proportional to the resolution. A PSD plot is shown in Figure 2.25, where the maximum frequency is equal to half of the sampling frequency. The PSD plot shows the strength of the energy variations as a function of frequency. In other words, it indicates at what frequency the variation is strong and at what frequency the variation is weak. The PSD can be used as the input for generating a time varying signal as performed in the IDFT or the IFFT. The generated time series, however, is not as accurate as the original signal since the PSD does not contain the original signal phase information. Assumptions of the signal phase content can be made in order to regenerate a statistically equivalent time history (Wolfsteiner & Breuer 2013).

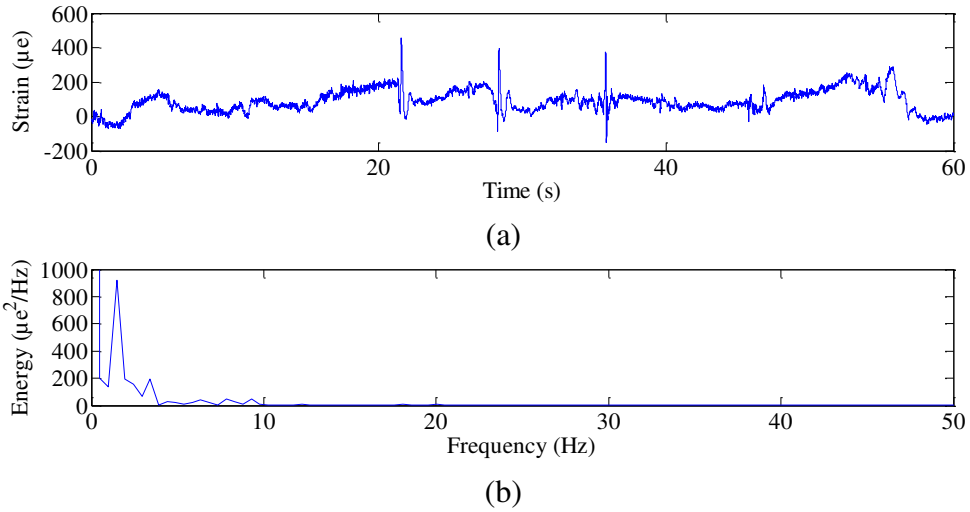

Figure 2.25 Analysis of the PSD: (a) time series signal, (b) energy distributions in the range of 0 Hz to 50 Hz

Source: Putra 2010

The usual way to describe the severity of damage for random vibration is in terms of its PSD, a measure of a vibration signal power intensity in the frequency domain (Kumar 2008). According to Reytier et al. (2012), Julien et al. (2013) and Böhm & Niesłony (2015), the PSD function of stress or strain could be used for predicting fatigue life and mechanical system behaviour. The evaluation of an expected value of any random parameter derived from the PSD was equivalent to estimating the same parameter in an unlimited time history of the stress random process. Therefore, it was clear that a fatigue evaluation performed in the frequency domain significantly reduced the time dedicated to design calculations of computational times, compared to a traditional approach based on the time domain (Braccesi et al. 2009). The PSD analysis is an adequate tool for random vibrations and huge structures with many degrees of freedom (Wolfsteiner & Breuer 2013).

Using the frequency domain analysis, the overall frequency components of a signal can be known. The analysis, however, also has an obvious weakness, where it only produces frequency information and does not provide time information (Ditommaso et al. 2012). Because time information is lost, it is not reasonable to detect when and how long a particular event occurs. For stationary signals, in which frequency information is not changed by time, this drawback is not very important. Most signals, however, contain non-stationary patterns with variable amplitudes. This

means that the frequency domain analysis is unsuitable for non-stationary signals (Misiti et al. 2008). To overcome this problem, the time-frequency domain analysis becomes an important tool that provides a more accurate local description of the characteristics of non-stationary signals.

2.3.3 Time-Frequency Domain Analysis

One method of the time-frequency domain analysis that have been extensively used for engineering problems would be the short-time Fourier transform (STFT) (Gabor 1945), or also known as the windowed Fourier transform. The STFT can be defined as follows:

$$STFT_{(t',\omega)} = \int_{-\infty}^{\infty} F_{j(t)} w_{(t-t')} e^{-i\omega t} dt \tag{2.48}$$

where t' is the time at the center of the window and w is the window function.

According to Pinnegar & Mansinha (2003), local spectrum for all points on the time axis produces the STFT. It maps to a time and frequency function providing information of events occurred (Misiti et al. 2008). In order to accomplish this, the STFT divides the signal being analysed into small segments, where the FFT is applied to each segment aiming to produce frequency information. The STFT approach assumes that if a signal with variable time is divided into several segments, each segment can be considered as stationary for analytical purposes. Spectrogram functions produce a matrix consisting of the STFT for each segment, where the columns of the matrix represent the time and the lines of the matrix represent the frequency. The matrix is then plotted in the form of a two-dimensional graphic display for obtaining the power distribution at the time and frequency axis, shown in Figure 2.26.

The STFT resolution depends on the selection of the window length (Tang et al. 2010). The width of a segment is given by multiplying the frequency and the length of the window. Therefore, the frequency and the window length are closely

interlinked. The STFT, however, has a resolution problem. The information is only obtained with limited accuracy to analyse signals having relatively wide bandwidths that change rapidly with time (Zhang et al. 2003; Ditommaso et al. 2012). The STFT uses a single window for all frequencies, so width and shape of the window used is fixed at each time and frequency axis (Kim et al. 2007). It was recommended by Antoni (2006) and Ditommaso et al. (2012) to use a window length as short as enabled by the frequency resolution. Shorter windows present good time resolution but poor frequency resolution. On the other hand, longer windows present good frequency resolution, but poor time resolution (Combet & Gelman 2009). Many signals require a more flexible approach for determining the time or frequency accurately to overcome the shortcomings of the STFT, such as a wavelet transform (Tang et al. 2010).

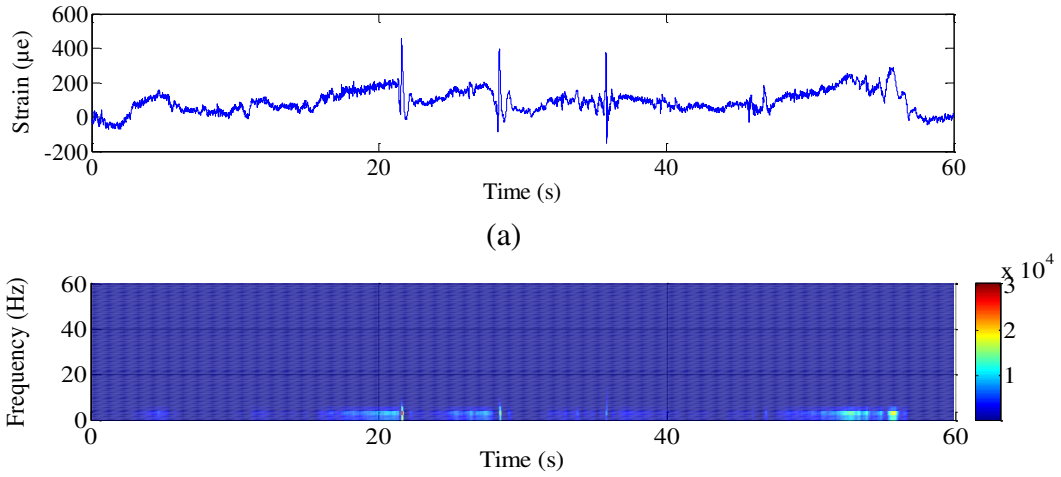

Figure 2.26 Analysis of the STFT: (a) time series signal, (b) energy distribution
Source: Putra 2010

The wavelet transform is a significant tool for representing local features of a signal. It cuts a time domain signal into various frequency components by applying multi-resolution analysis, namely through the usage of a variety of window sizes determining the resolution. Applying a windowed technique, it changes the window along the signal and calculates the spectrum for each position. Different window sizes are used because lower frequency signals can be analysed using a wider window size since the oscillations are slower compared to a high frequency signal requiring smaller sized windows. This process is repeated several times with the window slightly

shorter or longer for each new cycle. In the end, the result is a set of time-frequency representations of the signal with different resolutions. The wavelet transform presents information in both time and frequency domains simultaneously. It provides information on when and at what frequency the signal changes occur. The main profit of the wavelet transform is the ability to analyse the local area also known by the local analysis (Misiti et al. 2008).

The wavelet transform can be classified as either continuous wavelet transform (CWT) or discrete wavelet transform (DWT). The CWT is defined as the sum over all time of a signal multiplied by the scale (Kim et al. 2007). It is conducted on each reasonable scale, producing abundant data, and is used to determine the values of a continuous decomposition so as to accurately reconstruct the signal (Misiti et al. 2008). In contrast, the DWT, firstly invented by Hungarian mathematician Haar (1910), is used when the energy of a signal is finite. Not all the decomposition values are needed to reconstruct the original signal accurately and analysis is more efficient (Misiti et al. 2008).

The wavelet transform begins with a basic function, called the mother wavelet, scaled to display the signal being analysed. Using the mother wavelet, the signal is moved from a space to a scale domain in order to provide the localised features of the signal. The Morlet wavelet is one of the advanced mother wavelets that involve the CWT (Chen et al. 2010). Morlet et al. (1982a; 1982b) introduced the Gabor works (Gabor 1945) to the seismology community and modified it to keep the same wavelet shape over equal octave intervals. The Morlet wavelet can be described by the following equation:

$$\psi_{(t)} = \frac{1}{\pi^{1/4}} e^{i 2\pi f_0 t} e^{-t^2/2} \tag{2.49}$$

where f_0 is the frequency at the central of the mother wavelet Ψ. The Morlet wavelet is symmetrical and exhibits a linear phase response (Smith et al. 2007), as shown in Figure 2.27.

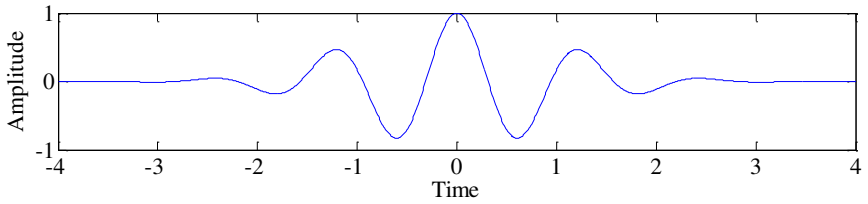

Figure 2.27 Shape of the Morlet wavelet

Source: Jiang et al. 2011

Wavelet decomposition calculates the resemblance index, also called as the coefficient (Tang et al. 2010). The coefficient is the result of a signal regression generated at different scales in a wavelet, establishing the correlation between the wavelet and a section of the signal being analysed. Higher coefficient indicates strong resemblance, whereas a lower coefficient indicates weak resemblance (Misiti et al. 2008). The wavelet coefficient *WC* of the CWT is expressed with the following integral (Daubechies 1992):

$$WC_{(p,q)} = \frac{1}{\sqrt{p}} \int_{-\infty}^{+\infty} F_{j(t)} \psi\left(\frac{t-q}{p}\right) dt \tag{2.50}$$

where q is the time shifting and p is the scale index. The scaling factor allows controlling the shape of the basic wavelet and balances the time and frequency resolutions. Decreasing the scale index increases the frequency resolution but decreases the time resolution. When the scale index tends to zero, the wavelet becomes a cosine function which has the finest frequency resolution, and when it tends to infinity, the wavelet has the finest time resolution. So, there always exists an optimum scale index that has the best time-frequency resolution for a certain signal localised in the time-frequency plane.

The wavelet coefficient *WC* of the DWT is derived from the discretisation of the CWT, given by:

$$WC_{(p,q)} = \frac{1}{\sqrt{2^p}} \int_{-\infty}^{\infty} F_{j(t)} \psi\left(\frac{t-2^p q}{2^p}\right) dt \tag{2.51}$$

where p and q are replaced by 2^p and $2^p q$. The basic steps of the DWT are illustrated in Figure 2.28. In the decomposition steps, the discrete signal is convolved with low and high pass filters, resulting in two vectors, which are the approximate cA and the detailed cD coefficients. The symbol $\downarrow 2$ denotes down sampling, i.e. omitting the odd indexed elements of the filtered signal, so that the number of coefficients produced by the basic steps is approximately the same as the number of elements of the discrete signal. An important property of these steps is (Purushotham et al. 2005):

$$F_{\mathrm{j}} = cA + cD \tag{2.52}$$

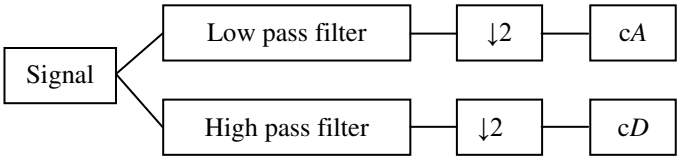

Figure 2.28 Basic steps of decomposition of the DWT

Source: Purushotham et al. 2005

The wavelet coefficients are presented in Figure 2.29. Through the two-dimensional display in the time-frequency domain, the level of coefficient is estimated based on the contours of different colours, whereby, white indicates the highest magnitude level, followed by yellow, brown and black, respectively. The colour intensity at each x-y point is proportional to the absolute value of the wavelet coefficient as a function of the dilation and translation parameters (Darpe 2007). The wavelet transform, however, involves a complex analysis. The biggest challenge in a wavelet analysis is the selection of the mother wavelet as well as the decomposition level of a signal. Another main difficulty is the order of the mother wavelet (Tang et al. 2010; Jiang et al. 2011).

Therefore, the S-transform was introduced by Stockwell et al. (1996), where its derivation originates from the STFT idea. The S-transform, however, is related to the wavelet transform as well (Leonowicz et al. 2007). It is defined as a CWT with a specific mother wavelet. The general formula of the S-transform ST takes the form:

$$ST_{(t',j)} = \int_{-\infty}^{\infty} F_{\mathrm{j}(t)} w_{(t-t',j)} e^{-i\omega t}\, dt \tag{2.53}$$

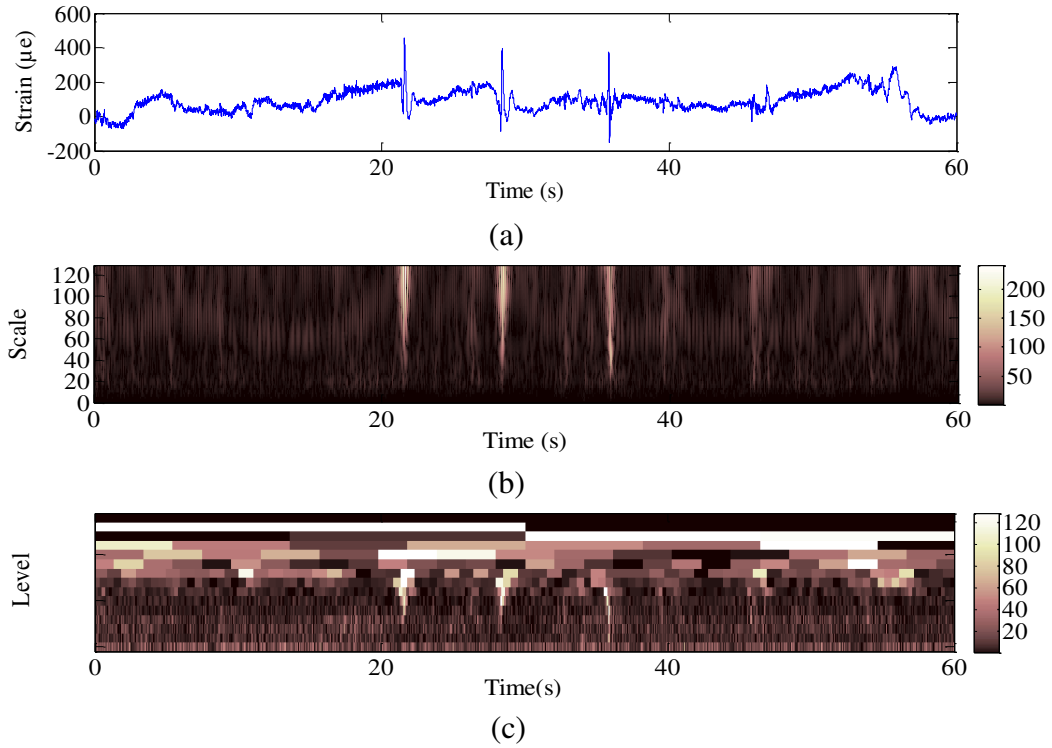

Figure 2.29 Analysis of the wavelet transform: (a) time series signal, (b) continuous coefficient, (c) discrete coefficient

Source: Putra 2010

where *j* is the dilation factor and its window function *w* is:

$$w_{(t'-t,j)} = \frac{|f|}{\sqrt{2\pi}} e^{-\left(t^2/2u^2\right)} \tag{2.54}$$

where *u* is the coefficient, defined as:

$$u = \frac{1}{|f|} \tag{2.55}$$

Finally, taking into account the above considerations, the S-transform *ST* can be derived as:

$$ST_{(t',j)} = \int_{-\infty}^{\infty} F_{j(t)} \frac{|f|}{\sqrt{2\pi}} e^{-\left((t'-t)^2 f^2/2\right)} e^{-i\omega t} dt \tag{2.56}$$

Like the wavelet transform, the S-transform also applies various window sizes in its analysis. This mathematical function is the multiplication product of the Fourier transform and the window function, depending on the frequency. It applies the Fourier transform only at the small part of a signal in certain times maintaining the absolute phase for each frequency component. Besides the type of window, the window size should be determined to control the time-frequency resolution, where the window width decreases at higher frequencies, as shown in Figure 2.30. This situation provides a better frequency resolution at lower frequencies and gives a better time resolution at higher frequencies (Pinnegar & Mansinha 2003). One difficulty and drawback of this method is its large time-frequency graph size and consumption of computing resources (Stockwell 2007). It is better if the size of the graph is restricted as needed.

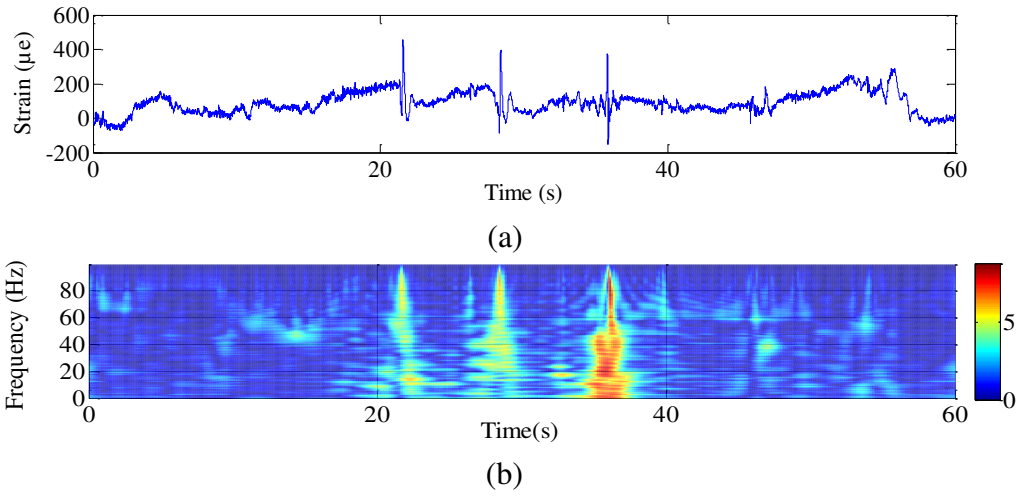

Figure 2.30 Analysis of the S-transform: (a) time series signal, (b) energy distribution

Source: Putra 2010

Fatigue signal analysis is shown in Figure 2.31. In the last decades, signal processing approaches have been used for fatigue studies. As mentioned earlier, fatigue signal analysis can be performed in the time, frequency and time-frequency domains, and the wavelet transform is one method that can be performed in the time-frequency domain. Since fatigue signals usually exhibit non-stationary behaviour, they give time difference providing a challenge in the analysis. Thus, the wavelet transform is extensively applied. Compared to other time-frequency domain techniques, the transformation is probably the most advanced solution presently available to

overcome non-stationary signals (Jiang et al. 2011). It appears that the wavelet transform applying the multi-resolution window can give a better resolution in time-frequency representation (Liu et al. 2014). The STFT has a fixed window making it inaccurate. Wider windows give a good frequency resolution but can affect the time resolution, while the reverse occurs for the use of smaller window sizes. On the other hand, the S-transform does not give a restricted graph size.

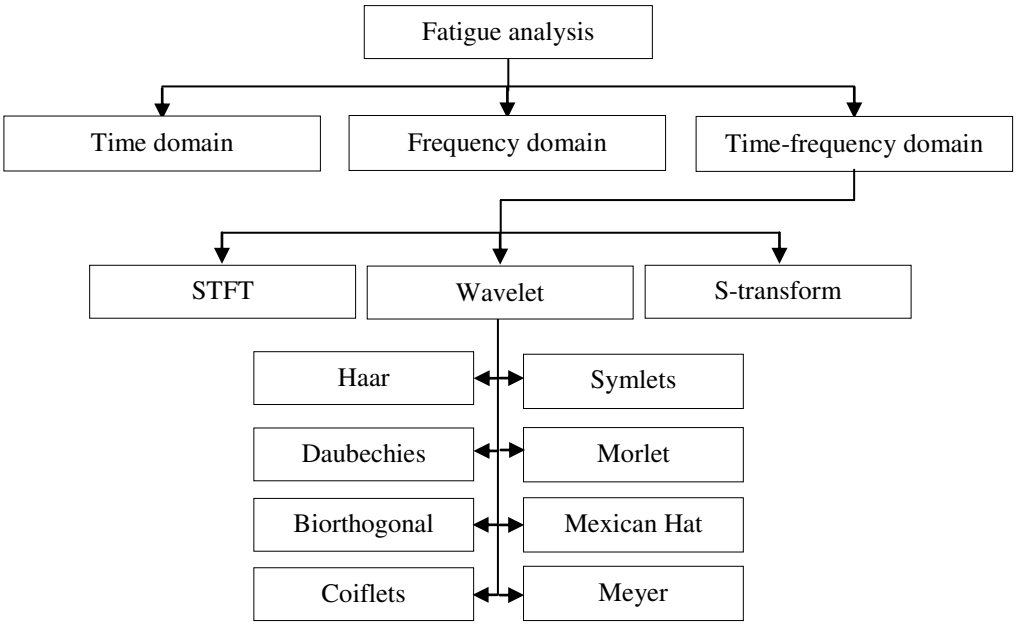

Figure 2.31 Mainstream of the signal processing techniques

Source: Norton & Karczub 2007; Misiti et al. 2008

The wavelet transform can be performed either continuously or in discrete time. In the CWT, there are several mother wavelets that can be used as the basic functions for different purposes, such as Haar, Daubechies, Biorthogonal, Coiflets, Symlets, Morlet, Mexican Hat and Meyer (Su et al. 2010). Except for Morlet and Mexican Hat, other basic functions can also be applied in the DWT (Misiti et al. 2008). One of the earliest practical applications of the wavelet transform came from the analysis of earthquake voice record by Goupillaud et al. (1984), utilising the Morlet wavelet. Since then, it has been extensively used in many engineering applications. The Morlet wavelet was not only used in engineering fields, but was also successfully applied in the field of health for detecting heart sound (Mgdob et al. 2003) and for measuring blood flow velocity (Zhang et al. 2003) as well as in the field of science for identifying dominant orientations in a porous medium (Neupauer & Powell 2005).

According to the reading and the knowledge of the author, however, the Morlet wavelet is still rarely used in the scope of fatigue studies. A fatigue study associated with the Morlet wavelet by Kim & Melhem (2003) suggested that the wavelet-based approach offered great promise for damage detection and health monitoring of concrete beams. Another fatigue study related to the Morlet wavelet was by Lin & Zuo (2003); it developed an adaptive wavelet filter to detect periodic impulses automatically for recognition of gear tooth fatigue cracks. Although the wavelet transform has not been able to reliably give fatigue life yet, it can give better results than other methods. It gives a new dimension in the field of fatigue research, although its use is still in the preliminary stages. In real applications, fatigue random time histories are mostly long and often contain a mixture of lower and higher amplitude cycles. In relation to this issue, the fatigue damage associated with the lower amplitude cycles may be minimum. Consequently, engineers want to eliminate the non-damaging cycles from the original histories collected at a component and accelerate fatigue tests for the reasons of time and cost (Ko et al. 2005; Xiong & Shenoi 2008).

2.4 FATIGUE DATA EDITING

Much durability testing involve a lengthy complex VAL, considered as one of the vital inputs. Automotive manufacturers increasingly seek to reduce testing times (Upadhyaya & Sridhara 2012) while simultaneously achieving higher quality levels for their cars. Among the alternative solutions for achieving an accelerated durability test are (Oh 2001): increasing frequency, increasing amplitude and eliminating lower amplitude cycles in a time series signal. For a simple method, increasing frequency of cyclic loading can be made on the basis that the frequency has minimal effect on component fatigue strength. In the second approach, automotive manufacturers tend to increase loading levels by scaling up service loads by a constant value. Therefore, the test of a component can be accelerated using a modified load. However, there are some disadvantages in using the frequency and amplitude increasing techniques, such as cause resonance and the fatigue limit of a modified load can be found at shorter fatigue life compared to the original fatigue limit. In addition, accelerated tests at high frequency are limited by high frequency test set up (Upadhyaya & Sridhara 2012).

Thus, the durability testing can often be accelerated by the use of the lower amplitude cycle removal technique, known as FDE, to produce a new shortened fatigue signal as required which contains high amplitude cycles. The idea behind this technique is that lower amplitude events do not cause much fatigue damage. The FDE is defined as a method to identify and extract higher amplitude segments that lead to fatigue damage in a signal. On the other hand, lower amplitude segments are removed because they theoretically contribute to a minimum amount of fatigue damage. The shortest modified fatigue signal without compromising the original features is the main criterion in the FDE. The concept of accelerating a test by removing non-damaging events is distinctly different from the two previous approaches. Using both the previous approaches, original fatigue signals are not compressed, so that modified signals have the same time length as the original fatigue signals. The last approach achieves the accelerated fatigue test considering less than the complete set of an original fatigue signal since only a sub-set of the signal is required to produce the same amount of damage. Therefore, the FDE is widely utilised; especially in automotive fields.

Since first developed in 1979, several FDE algorithms using various approaches have been found in literature to accelerate fatigue tests. The preliminary FDE by eliminating lower amplitude cycles in the SAE-owned strain histories was performed by Conle & Topper (1979) in the time domain. The lower amplitude cycles were removed based on the strain range level used to determine the retained fatigue damage. Evaluation of the criteria was carried out by estimating the amount of fatigue damage generated by each amplitude level of the original strain histories, selecting several strain range levels for history editing and then comparing the amount of damage reduction predicted by each criterion with actual fatigue test results. However, it was apparent that when high overall strain levels were encountered in the total record of the strain histories, great care should be taken to eliminate lower cycles. A similar technique was performed by Conle & Topper (1980) to edit the strain histories, but using lower overall strain levels in order to omit lower cycles. The fatigue damage results obtained from this study indicated the presence of an overstrain effect much larger than in the previous work.

Phillips (1979) studied the effects of truncation on a compression-loaded spectrum. The results indicated that the method significantly affected the fatigue life, producing life greater than those obtained in the baseline. It concluded that high loads should be retained and that large reduction in the low load could be applied. Buch (1980) did an extensive study on the effect of some aircraft loading modifications on the fatigue life of open holed specimens. It was found that in particular loading cases, rare load peaks may have not only a beneficial effect, but also a detrimental effect on the number of simulated flights.

Heuler & Seeger (1986) edited a load based on notch or local stress and compared the crack initiation life and the crack propagation life using the original and edited loads. An omission level of 50 % of the fatigue limit was chosen as a fraction of the maximum load range for simplicity and convenience. This omission level was applicable in the fatigue tests increasing total life. However, the specimens with different geometry were used in the fatigue tests of different materials. Lanciotti & Lazzeri (1992) studied the effects of truncating high loads and of omitting small cycles on the crack propagation of an aircraft. The omission of stress ranges reduced about 33 % of the number of load cycles, as shown in Figure 2.32.

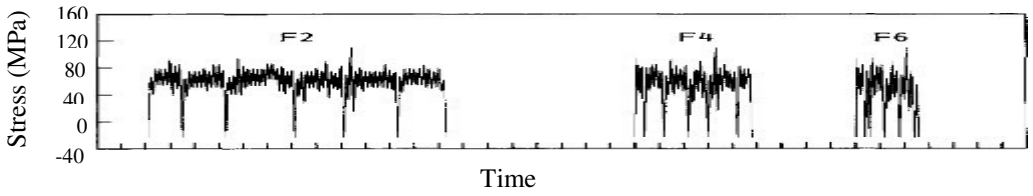

Figure 2.32 FDE performed by Lanciotti & Lazzeri (1992)
Source: Lanciotti & Lazzeri 1992

One of the FDE algorithms involving peak-valley reversals was performed by Stephens et al. (1997). A fatigue signal developed by the SAE fatigue design and evaluation was selected for editing purposes due to a large number of lower cycles in the total record length. The combination of strain amplitude and mean obtained from the SWT model was used in order to produce an omission level to edit the peak-valley service history, where all the cycles which were less than the omission level were removed. This method showed that 90 % and 50 % of the fatigue damage for two

kinds of specimens were retained in the edited signals removing 89 % and 99.6 % of the history length, respectively, shown in Figure 2.33. This implied that both the conventional strain range and new SWT parameter editing methods were successful. The SWT parameter editing method, however, removed more cycles and thus was more efficient.

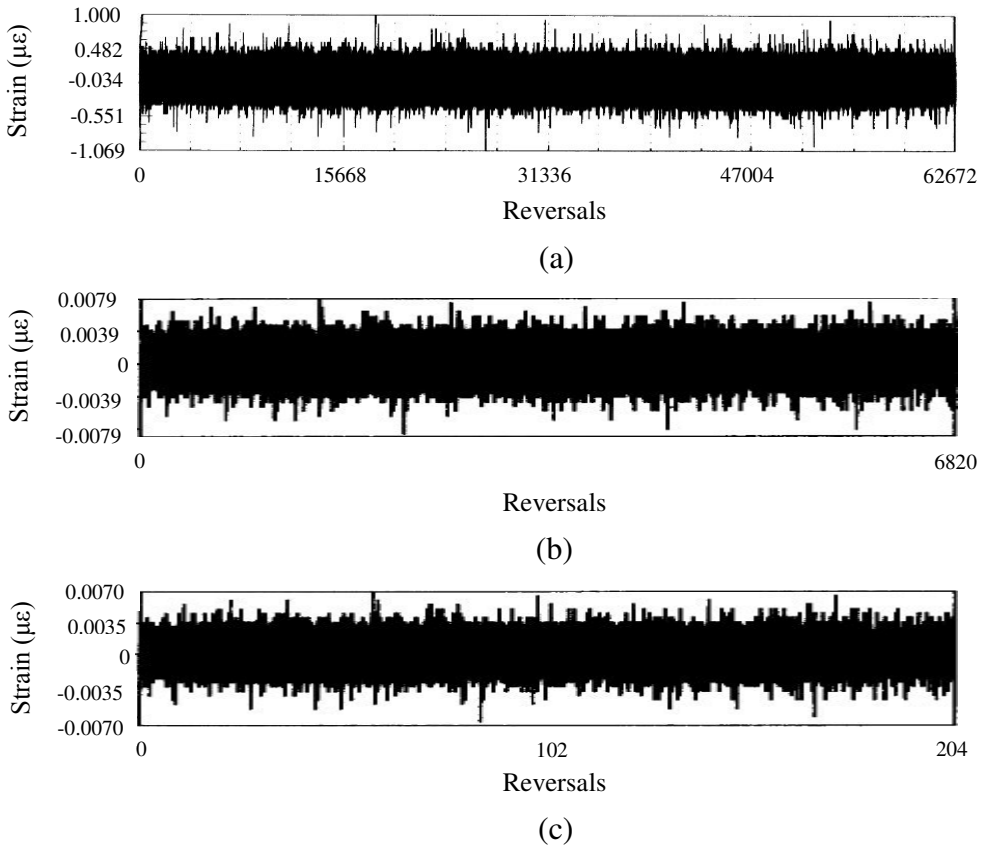

Figure 2.33 FDE performed by Stephens et al. (1997): (a) full strain history, (b) SWT parameter edited to 90 % fatigue damage, (c) SWT parameter edited to 50 % fatigue damage

Source: Stephens et al. 1997

Furthermore, Nyman et al. (2000) carried out a study regarding load sequence effects on the fatigue life of composite structures. Using an aircraft service load, it showed that the lower cycles were omitted from the original load according to the fatigue limit criteria. It was found that the elimination level can be set to approximately 50 % of the maximum range for in-plane loaded structures. At chosen elimination levels, approximately 80 % to 90 % of loading states were eliminated.

A work by Ko et al. (2005) investigated the effect of original and edited loads on the fatigue crack growth behaviour of aluminum alloy specimens. CAL fatigue tests were performed to monitor the variations of the opening loads with crack advances. The crack aspect ratio under a CAL was somewhat different from that under a VAL, but was not noticeable. There were 80 % and 92 % reductions in length with only about 6 % and 16 % reductions in fatigue damage, respectively. The more omissions of small amplitude cycles, the higher the opening loads and the longer the fatigue life. The load history editing effect was closely related to the crack closure phenomena. The technique could be applied to compress the original signal without changing the main history. Furthermore, Xiong & Shenoi (2008) established a load history generation for accelerated fatigue tests. Primary focus was placed on the load cycle identification in order to minimise experimental time while having no significant effects on the new generated load history. A large percentage of small amplitude cycles were deleted, while a certain number of high cycles were maintained, as shown in Figure 2.34. Good agreement between the original and generated load histories was obtained, demonstrating the practical and effective use of the proposed approach.

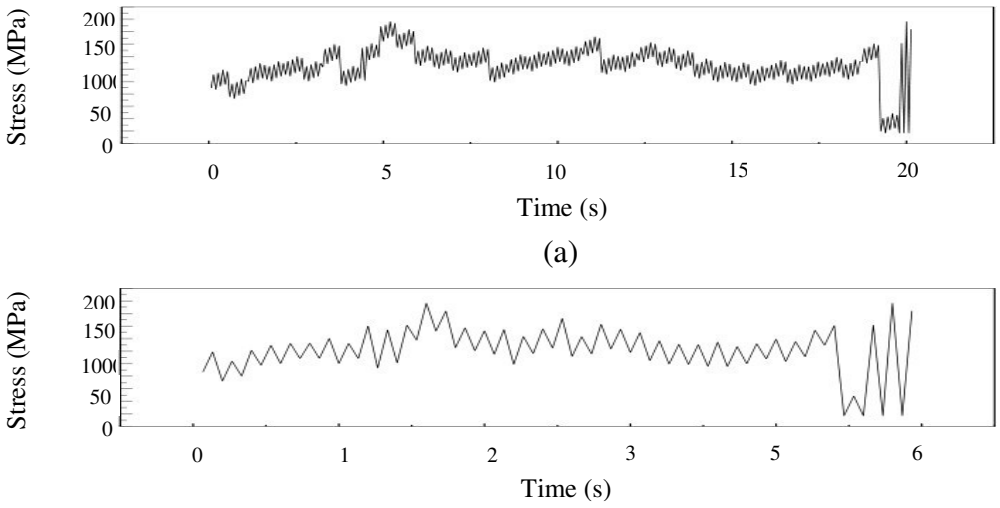

Figure 2.34 FDE performed by Xiong & Shenoi (2008): (a) original strain signal, (b) edited strain signal

Source: Xiong & Shenoi 2008

For producing an accurate fatigue damage result, however, the time domain-based FDE is not appropriate. It is because frequency information is unavailable in the time domain, whereas low-frequency content is most important for most fatigue signals. The distribution of frequency in a fatigue signal should be determined because it provides the identity of the signal. Meanwhile in the frequency domain, fatigue loading time histories are often low-pass filtered (Sheen 2009; MATLAB 2008a) in order to reduce lower amplitudes located in the higher frequency region. Unfortunately, the low-pass filter does not reduce the signal lengths but almost certainly reduces fatigue damage. This is because the low-pass filter smoothes high amplitude signals and thus causes the loading ranges to be lowered. Thus, the frequency domain-based FDE technique is not recommended, as the time series regenerated from a frequency spectrum does not produce the same fatigue life.

With the development of the use of signal analysis in fatigue studies, the FDE is not only limited to the conventional methods in the time domain, but also in the time-frequency domain. Compared to time domain, the time-frequency domain is the best choice. Normally, the sudden change in a fatigue signal occurs at higher frequencies where it requires a smaller window. This situation appears more favorable to the wavelet transform because it provides a smaller window at a higher frequency. It is able to detect amplitude changes in a fatigue signal better than fixed window analysis.

The trend of the FDE emerged when Oh (2001) used the wavelet transform to de-noise and remove spikes of strain signals. Comparisons of fatigue damage between the original and edited signals for four strain histories were made for the purpose of evaluating the editing technique. Strain histories developed by SAE and a VAL measured from a light railway train component traveling over a rail at the maximum speed were used for the analysis. Using the 30^{th} order of the Daubechies wavelet, the noise and spikes of the original signals were removed. As a result, the original signals were compressed by 71 % and approximately 80 % of the original fatigue damage was retained.

Another wavelet-based FDE had also been developed by Abdullah et al. (2006). The idea for this study came after realising that the algorithm developed by Giacomin et al. (2001) was not suitable for fatigue signals. Thus, a fatigue mission synthesis algorithm, called wavelet bumps extraction, was developed using the 12th order of the Daubechies wavelet to summmarise long records of fatigue loading. It extracted fatigue damaging events in the records that cause the majority of fatigue damage whilst preserving the loading cycle sequences. The algorithm was found to highly compress the signals, where the fatigue damage and statistical parameters of 100 % and more than 10 %, respectively, were retained in 31 % and 41 % of the edited strain signals. One of the strain signals edited in the study is presented in Figure 2.35.

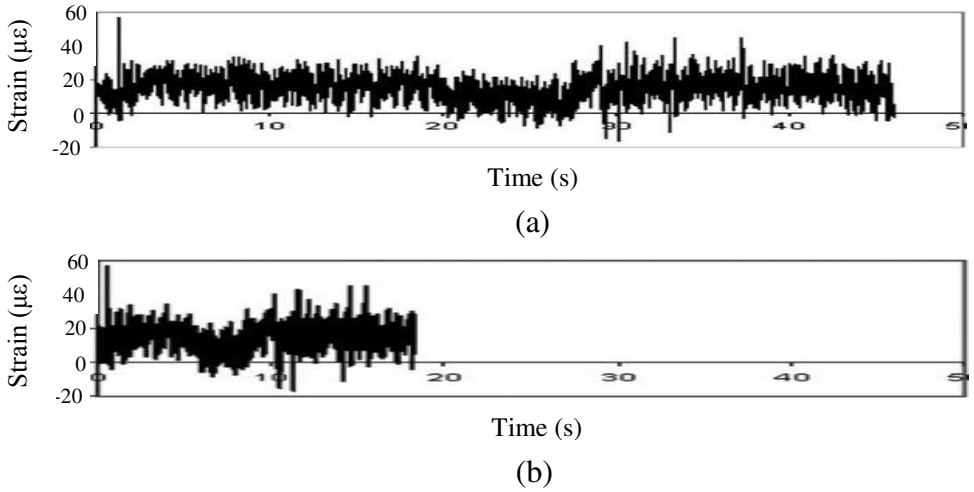

Figure 2.35 FDE performed by Abdullah et al. (2006): (a) original strain signal, (b) edited strain signal

Source: Abdullah et al. 2006

All FDE techniques discussed in this section used different fatigue signals and produced different results. A major weakness of the techniques was that the lengths of edited signals resulted in were not consistent, depending on the original behaviour of the signals. The time reductions in edited signals were not significant compared to the eliminated fatigue damage. Occasionally, an FDE algorithm was only able to shorten a signal less than 30 %. Considering that 20 % of the original fatigue damage could be removed, it was not comparable to the edited signal obtained, which was only shorter by 30 % (Oh 2001). There seems to be no generally agreed upon rules that clarify

which method is best, or what amplitude should be chosen for load omission (Yan et al. 2001). Practically, any FDE must reduce the testing period and costs to be technically valid.

In automotive applications, a modified signal should have less than 10 % deviation compared to the original signal (Stephens et al. 1997; Giacomin et al. 2001). A difference of 10 % is used considering that at least 10 % of an original signal contains a lower amplitude cycle leading to the minimum fatigue damage to obtain a final signal corresponding to the original signal. This range is important to ensure that the resulted modified signal is as close as possible to the original signal; so as to keep the majority of fatigue damage, the vibration energy and the amplitude range. In an FDE technique, the fatigue signal clustering is required to ensure that higher amplitude segments can be detected and removed from original signals and at the same time maintain fatigue damage.

2.5 FATIGUE DATA CLUSTERING

Clustering is the classification of data into different groups. In other words, clustering maps a data set into smaller clusters, such that the data in all clusters share several common characteristics according to the defined distance measure (Abu-Mahfouz & Banerjee 2014). One of the keys in clustering is the function used to measure the similarity between two data being compared. These data could be in various forms, including raw values of equal or unequal length (Liao 2005).

There are broadly two grouping schemes: hierarchical and partitional schemes. A hierarchical clustering works by grouping data into a tree of clusters. There are generally two types of hierarchical clustering methods: agglomerative and divisive, depending upon whether a bottom-up or top-down strategy is followed. An agglomerative starts by placing each data in its own cluster and then merge clusters into larger and larger clusters, until all data are in a single cluster or until certain termination conditions such as the desired number of clusters are satisfied. A divisive does just the opposite. A purely hierarchical clustering method suffers from its inability to perform adjustments once a merge or split decision has been executed. For improving the clustering quality of hierarchical methods, there is a trend to integrate hierarchical clustering with other clustering techniques (Liao 2005).

Traditional clustering approaches generate partitions. In a partition, each pattern belongs to one and only one cluster. Hence, the clusters in a hard clustering are disjointed. A partitional clustering determines all groups immediately. This kind of algorithm is divided into three types: Fuzzy (Zadeh 1965), *k*-means (MacQueen 1967) and quality threshold. Fuzzy extends this notion to associate each pattern with every cluster using a membership function. The key to the Zadeh idea is to represent the similarity a point shares with each cluster with a function. The output of such algorithm is a clustering, but not a partition. Fuzzy was initially applied to clustering by Ruspini (1969). Dunn (1974) first extended the *C*-means algorithm to allow for Fuzzy partitions.

The most popular Fuzzy clustering algorithm is the Fuzzy *C*-means (FCM), developed by Bezdek (1981). The objective function *J* of the FCM is described by:

$$J_{(U,v)} = \sum_{k=1}^{n}\sum_{i=1}^{C} U_{ik}^{\dot{g}} \left\| F_{j_k} - v \right\|_{wm}^{2} \tag{2.57}$$

where *U* is the Fuzzy *c*-partition, *v* is the vector of centers, *C* is the number of clusters, $\dot{g}$ is the weighted exponent and *wm* is the positive-definite weight matrix. The FCM method can place the members of a group with the shortest distance to the centroid in a clustering. The centroid is the average of all points in a cluster, where the coordinate is the average arithmetic for each separate dimension for all points in a group. The other benefits of this method are its simplicity and speed to analyse large data sets. However, the FCM algorithm does not give consistent results in each analysis because a generated group depends on the initial random assignment.

Some clustering methods had been applied to fatigue analysis. To the best of the author's knowledge, however, no studies used the FCM method in the field of fatigue research. The idea to utilise the FCM in the study came from the view of current research trends, where the clustering method has been applied extensively in vibration random signal attempts, such as for tool wear status recognition (Fu et al. 2011) and twist drill wear and damage detection (Abu-Mahfouz & Banerjee 2014). Figure 2.36 shows the three-dimensional FCM clustering performed by Fu et al.

(2011). Strain signal type was hypothesised to be similar to vibration random signal pattern. Based on a clustering plot, a correlation among strain signals could be identified.

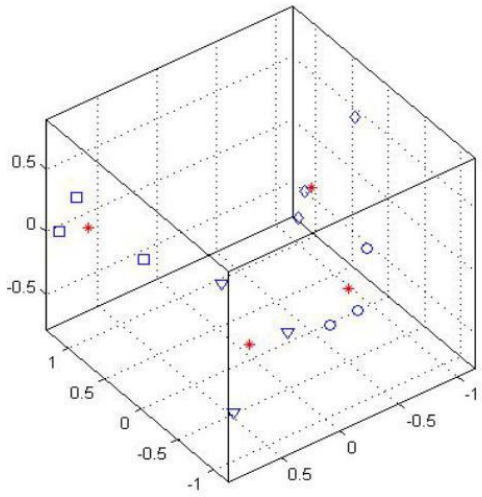

Figure 2.36 FCM performed by Fu et al. (2011)
Source: Fu et al. 2011

2.6 CORRELATION OF DISCRETE DATA

Regarding the quality of a clustering result, uncertainty analysis estimates the quality from anticipated or completed tests. Uncertainty analysis is the process of identifying, quantifying and combining errors. In a measurement assigning a value to a physical variable based on a sampling from the population of that variable, errors are a property. They cause a difference between the measurement and the true value of the population. Measuring errors are introduced from various elements, for example, the instrument calibration, data set finite statistics and the approach used. But because the true value is not known and only measured value is known, exact value of errors is not known. Instead, estimation of the range of probable errors is drawn. In some uncertainty analyses, predicted values should fall within a stated probability, although some variables are unknown.

Whenever mathematical approximation formulas are used, one should try to find out how much the approximate value can at most deviate from the unknown true value. The maximum possible error, that is the difference between the true and

approximation values, should be computed. The probability of an event in an experiment is supposed to measure how frequently the event is about to occur if many trials are performed. The corresponding problem would be determining two numerical quantities that depend on the sample values and include the unknown value of the parameter with certainty (Kreyszig 2011).

The standard "goodness of fit" measure for a regression-type model has been a statistic called the coefficient of determination. The coefficient of determination is a measure of how well the regression line represents a data set. The most general definition of the coefficient of determination R^2 is (Hardy & Bryman 2009; Ross 2009; Montgomery 2013):

$$R^2 = 1 - \frac{\sum (F_1 - F_2)^2}{\sum (F_1 - \bar{x})^2} \tag{2.58}$$

where F_1 is the vector of true value and F_2 is the vector of n prediction. The value of the coefficient of determination is always between zero and one. A value of 0.9 or above is very good, a value above 0.8 is good and a value of 0.6 or above may be satisfactory in some applications, although in such cases, errors in prediction may be relatively high. When the value is 0.5 or below, the regression explains only 50 % or less of the variation in the data; therefore, prediction may be poor (Sivák & Ostertagová 2012).

In statistics, the mean squared error (MSE) measures the average of the squares of the error, that is, the difference between the estimator and what is estimated. According to Martínez-Morales et al. (2012), it is described as:

$$MSE = \frac{1}{n} \sum_{i=1}^{n} (F_1 - F_2)^2 \tag{2.59}$$

The root-mean square error (RMSE) is the average of the squared errors between actual and estimated readings in a data sample. Squaring the difference removes the possibility of dealing with negative numbers. It also gives bigger differences more

weight than smaller differences in the result. The RMSE of the predictor is (Sivák & Ostertagová 2012):

$$RMSE = \sqrt{MSE} \tag{2.60}$$

According to Ross (2009) and Brandt (2014), one way to report the results of a hypothesis test is to state that the null hypothesis is or is not rejected at a specified significance level. A test result, calculated from the null hypothesis and the sample, is called statistically significant if it is deemed unlikely to have occurred by chance, assuming the truth of the null hypothesis. A statistically significant result, when a probability (*p*-value) is less than a threshold (significance level), justifies the rejection of the null hypothesis. Formally, *p*-value, first investigated by Pearson (1900), is defined as the smallest level of significance that would lead to acceptance of the null hypothesis. A *p*-value conveys much information about the weight of evidence against null hypothesis, and so a decision maker can draw a conclusion at any specified level of significance.

Before determining a *p*-value, degree of freedom and chi square should be first determined. The degree of freedom is a measure of the amount of variability involved in a test. The degree of freedom *DF* is equated as one less than the number of variability *N*:

$$DF = N - 1 \tag{2.61}$$

The chi square X^2 is a numerical value that measures the difference between the expected E_i and the observed *O* values, described by:

$$X^2 = \sum_{j=1}^{n} \frac{(O - E_i)^2}{E_i} \tag{2.62}$$

The significance level is a measure of how certain the null hypothesis is. Low significance values correspond to a low probability that results happened by chance, and vice versa. Significance levels are written as a decimal, which corresponds to the percentage chance, as presented in Table 2.1.

Table 2.1 Significant level for each percentage change
Source: Hardy & Bryman 2009

Percentage change (%)	**Significant level**
90.0	0.100
95.0	0.050
99.0	0.010
99.9	0.001

Analysis of variance (ANOVA), proposed by Fisher (1918), is a statistical method which is used to discuss the relative importance of the entire control factor. An ANOVA test is also used to find the contribution of each parameter. In its simplest form, ANOVA provides a statistical test of whether or not the means of several groups are equal (Montgomery 2013). It includes one-way, two-way or multiple ANOVA, depending upon the type and arrangement of data. The model of one-way ANOVA is:

$$y_{ij} = \mu + \breve{T}_{\mathrm{i}} + \in_{\mathrm{ij}} \tag{2.63}$$

where y is the observation, μ is the overall mean, ϵ is the random error component and $\breve{T}$ is the treatment effect, described by:

$$\breve{T}_{\mathrm{i}} = \bar{x} - \mu \tag{2.64}$$

The ANOVA coefficient F_{ANOVA} has the following test statistics (Ross 2009; Montgomery 2013; Brandt 2014):

$$F_{\mathrm{ANOVA}} = \frac{MS_{\mathrm{T}}}{MS_{\mathrm{E}}} \tag{2.65}$$

where MS_T and MS_E are the mean sum of squares due to treatment and error, described by the following equations, respectively:

$$MS_T = \frac{\sum_{i=1}^{n} n_i \breve{T}_i^2}{N_T - 1} \tag{2.66}$$

$$MS_E = \frac{\sum \left(F_j - \bar{x}\right)^2}{N_E - 1} \tag{2.67}$$

where N_T and N_E are the number of variability for treatment and error, respectively. The higher the F_{ANOVA}-value, the more dominant the parameters are (Elanchezhian et al. 2014).

The interval with endpoints of the quantities is called a confidence interval or interval estimate for the unknown parameter, introduced by Neyman (1937). The confidence interval *CI* can be computed by:

$$CI = \frac{\hat{c} SD}{\sqrt{n}} \tag{2.68}$$

where $\hat{c}$ is the confidence coefficient, that depends on the confidence level. The confidence coefficient for each confidence level is presented in Table 2.2.

Table 2.2 Confidence coefficient for each confidence level

Source: Kreyszig 2011

Confidence level (%)	**Confidence coefficient**
90.0	1.645
95.0	1.960
99.0	2.576
99.9	3.291

The selection of the confidence level considers the affordable risk of making a wrong decision. The 100 (1 - significance level) % confidence interval is a measure of the precision of estimation of the difference in the two means. Once the confidence interval is obtained, the two-sided confidence limit θ is determined by:

$$\theta = \bar{x} \pm CI \tag{2.69}$$

and it is denoted by:

$$\{\theta_1 \leq \theta \leq \theta_2\} \tag{2.70}$$

where θ_1 and θ_2 are called the lower and the upper confidence limits, respectively.

The methods discussed above are widely employed in fatigue studies. ANOVA and *p*-value had been used for determining the fatigue strength of dental composites (Papadogiannis et al. 2007; Staninec et al. 2008), as well as for analysing the fatigue testing time (Pessoa et al. 2013). Gocmez et al. (2010) applied the coefficient of determination for quantifying the quality of the fit of the energy-based model. The confidence interval was used by Chuliang & Kege (2011) for predicting economic life of aircraft structures. The coefficient of determination, the RMSE and the confidence interval were utilised for qualifying the measurements of the regression model by Sivák & Ostertagová (2012). Finally, the coefficient of determination was also used for analysing statistical parameters of the measured strain signals (Ye et al. 2012b), determining the degree of fit of the scatter behaviour of fatigue limit (Mohd et al. 2013) and observing the hydrogen influence on the mechanical behaviour (Bruchhausen et al. 2015).

2.7 SUMMARY

This chapter discusses the basic concepts and the previous works that had been performed many researchers. A suspension system is not necessary if roads are perfectly flat. Roads, however, are far from flat and therefore exert vibration excitation to tyres. The vibration, then, contributes to the fatigue life of suspension

components, such as coil spring, before propagating to other vehicle components. Thus, fatigue life assessment is one of the key stages in the engineering design for which the durability analysis is extensively performed in most related industries. Therefore, during the durability testing of machines, such as automobiles, load histories under particular driving conditions are often collected. Some strain signal histories are generated using components operated under varying service conditions.

High cost, time consumption and presence of errors have inhibited a strain signal acquisition. Thus, an MBD simulation was developed based on the equation of motion to generate simulated strain signals. Car driving on public road surfaces was conducted to get actual strain signals at the coil spring of a sedan. Thus, three types of strain signals measured at the component were used for the simulation. The work was continued by generating the vibration responses of the coil spring in forms of acceleration subjected to the actual strain signals. The acceleration signals affected by the road surfaces were the main input for the simulation. Applying the acceleration signals into the MBD simulation, simulated strain signals were gained. The simulation was predicted to be able to provide a strain signal having behaviour similar to the actual strain signal. For validation purposes, several analyses were performed, including fatigue tests. In general, the methodology performed in the current study is explained in Chapter 3.

CHAPTER III

METHODOLOGY

This study aims to propose a model for generating simulated strain signals. For solving the subject matters, the work focuses on the following main stages: acceleration trend investigation, simulated strain signal generation and strain signal validation. Figure 3.1 shows the general process of the current study, dividing the work into simulation and experiment. An FEA was performed on the coil spring of a sedan car, modelled using a CAD software, to determine the stress distribution. Thus, the critical areas at the component could be identified. A strain signal acquisition was performed, by placing a strain gauge at the critical area of the component and driving the car on public road surfaces.

Actual strain signals were the input into a developed mathematical expression to generate acceleration signals. The acceleration signals were the input into an MBD simulation, and then, simulated strain signals were yielded as well. Fatigue life assessments were performed to validate the simulated strain signals. Furthermore, both the actual and simulated strain signals were extracted using the wavelet transform to generate shorter modified strain signals. Finally, laboratory experiments were performed as well involving static and cyclic tests using the strain signals. The static test aimed to define particular mechanical properties, while the cyclic test was to ensure that the simulated strain signals were able to give an accurate fatigue life. The results of the cyclic tests determined the ability of the developed MBD simulation. The simulation should be able to produce strain signals that are as realistic as possible.

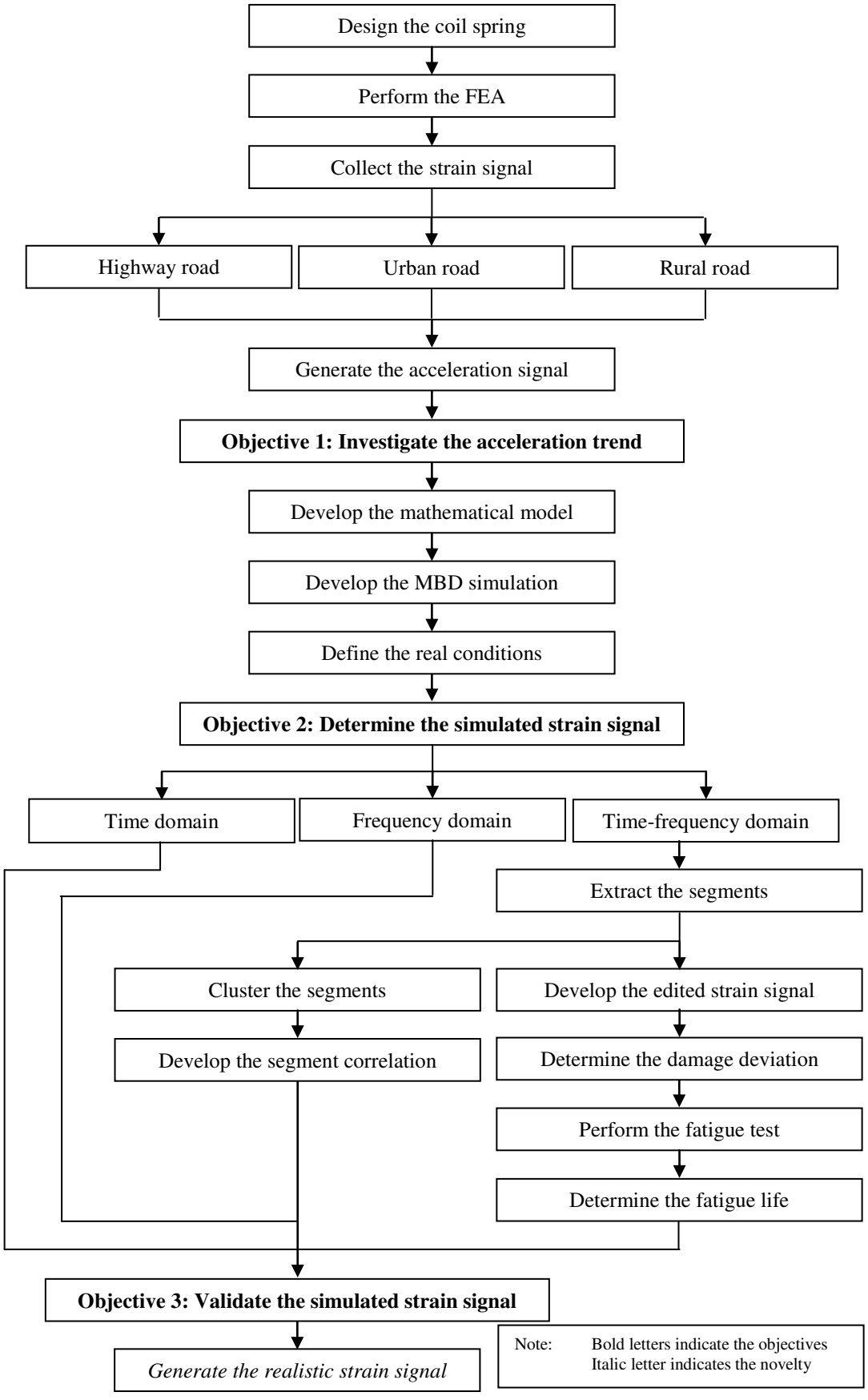

Figure 3.1 Process flow of the developed simulation

3.1 ACCELERATION TREND INVESTIGATION

3.1.1 Finite Element Analysis

The frontal coil spring of a 1,300 cc Proton SAGA sedan was used as a case study. Its design is simple so it is easily modelled in the simulation. Proton SAGA is the first car produced by the Malaysian automobile manufacturer since 1980's, and is well-known as the national symbol of Malaysia. The car is still in production and remains one of Proton best selling cars. It uses a passive McPherson strut suspension system with the spring stiffness and the damping ratio of 18,639 N/m and 0.95, respectively, that can be categorised as an under damped system. The specifications were from Proton Sdn. Bhd. Figure 3.2 shows the design of the coil spring and its dimensions are listed in Table 3.1.

Figure 3.2 Design of the frontal coil spring of a Proton SAGA sedan

Table 3.1 Dimensions of the frontal coil spring of a Proton SAGA sedan

Parameters	Values
Unstretched spring length (mm)	385
Mean coil diameter (mm)	130
Diameter of round wire (mm)	12
Number of active coils	6

The selected material for the simulation was the SAE5160 carbon steel since it is commonly employed in automotive industries for fabricating a coil spring (Prawoto et al. 2008). The material is also used for fabricating vehicle leaf springs (Gonzales et

al. 2010; Karthik et al. 2012a; Karthik et al. 2012b; Scuracchio et al. 2013). Its chemical compositions and material properties are tabulated in Tables 3.2 to 3.3, respectively. The chemical compositions of the SAE5160 carbon steel are provided in Gonzales et al. (2010), however, the mechanical properties for the material are not complete in the literature. Therefore, the mechanical properties were obtained from nCode (2007).

Table 3.2 Chemical compositions of the SAE5160 carbon steel
Source: Gonzales et al. 2010

Carbon	Silicon	Manganese	Chrome	Molybdenum	Vanadium
0.56-0.64 %	0.15-0.3 %	0.75-1 %	0.7-0.9 %	0.15-0.25 %	0.15 %

Table 3.3 Mechanical properties of the SAE5160 carbon steel
Source: nCode 2007

Properties	Values
Ultimate tensile strength (MPa)	1,584
Material modulus of elasticity (GPa)	207
Yield strength (MPa)	1,487
Fatigue strength coefficient (MPa)	2,063
Fatigue strength exponent	-0.08
Fatigue ductility exponent	-1.05
Fatigue ductility coefficient	9.56
Cyclic strain hardening exponent	0.05
Cyclic strength coefficient (MPa)	1,940
Poisson ratio	0.27

The SAE-owned SAESUS, SAEBKT and SAETRN strain random signals, as shown in Figure 2.23, were also applied. This was due to the fact that the strain signals were certified with respect to their accuracies and had been used by other researchers in the analysis of the fatigue signals (Oh 2001; Karthik et al. 2012a; Karthik et al. 2012b). The frequency of the strain signals was assumed to be sampled at 204.8 Hz. The SAESUS, SAEBKT and SAETRN strain signal recorded lengths were 122.4 seconds, 289.8 seconds and 25.2 seconds, respectively, measured from a lower suspension arm, bracket and transmission. The SAE1045 carbon steel was the material type chosen for the simulation. It is a common material used for fabricating a vehicle lower suspension arm structure (Khalil & Topper 2003). The material was also

utilised in fatigue life assessments for the SAEBKT and SAETRN strain signals (Karthik et al. 2012a; Karthik et al. 2012b). The material properties of the SAE1045 carbon steel are tabulated in Table 3.4.

Table 3.4 Mechanical properties of the SAE1045 carbon steel
Source: nCode 2007

Properties	Values
Ultimate tensile strength (MPa)	621
Material modulus of elasticity (GPa)	204
Fatigue strength coefficient (MPa)	948
Fatigue strength exponent	-0.092
Fatigue ductility exponent	-0.445
Fatigue ductility coefficient	0.26

In order to achieve a comfortable ride, a coil spring should have a good elasticity to improve its durability. Thus, coil springs are designed to be highly resistant in order to avoid failure during their use. Coil springs are formed at high temperatures, then cooled, and through heat treatment processes a coil spring is produced having elastic characteristics to fit the purposes. The chemical composition and the heat treatment given to coil springs are such that the damping capacity is high. Based on the carbon composition, the material used is medium carbon steel, balancing ductility and strength and with a good wear resistance. Silicon helps in stabilising the microstructure during the tempering operation. On the other hand, manganese increases the coil spring plasticity (Das et al. 2007). Other alloying elements improve the ease with which steel can be hardened. Coil springs made of steel often have high yield strength which enables them to return to their original form after a significant force is applied (Abidin et al. 2013).

The behaviour of a phenomenon in a system is dependant on the geometry, the property of the material and the boundary, initial and loading conditions. Hence, the analysis to obtain the complete three-dimensional stress distributions at a potential failure site is the primary objective. For an engineering system, the geometry, the boundary and the initial conditions can be very complex. It is therefore, in general, very difficult to solve the governing differential equation via analytical means. In

practice, most of the problems are solved using numerical methods (Aykan & Celik 2009). Among those, finite element method (FEM) is the most popular due to its practicality and versatility. The FEM is performed by dividing the problem domain into several elements. FEM essentially involves five steps (Georgiadis 2003), namely: (1) element discretisation, (2) displacement approximation, (3) formulation of element equations, (4) assemblage of global equations, and (5) solution of the global equations. With the introduction of the FEM, the distribution of displacement in stress analysis can be determined as difficult to obtain analytically.

Modelling and simulation are essential and indispensable when dealing with a complex engineering system. Thus, an CAD software is needed to generate a model automatically and to animate the results. CATIA® software package (Kogent Learning Solutions 2011) was used to draw the three-dimensional model of the coil spring with dimensions and geometry similar to the original product. The model was adopted for the FEA simulation by applying a static force and constraints. A dynamic analysis was performed because of its simplicity using Abaqus® software package (Abaqus 2008) for determining the stress distributions at the coil spring.

The accuracy of inputs in the pre-processing stage makes certain the validity of the analysis. The value and the direction of the force, the boundary condition and the material properties, such as the material modulus of elasticity and the Poisson ratio provided in Table 3.3, were inputs for the stress analysis. A force of 3,600 N was applied on the bottom of the component model and the upper was fixed (Ismail 2010), considering the car weight of 10,600 N as well as the passenger(s) and the load carried of 3,800 N. The total force was divided by four because the car weight and the passenger(s) were assumed to uniformly distribute to four springs (He et al. 2010). Static and cyclic analyses were performed with load amplitude was from 0 to 3,600 N. The boundary condition of the component is shown in Figure 3.3.

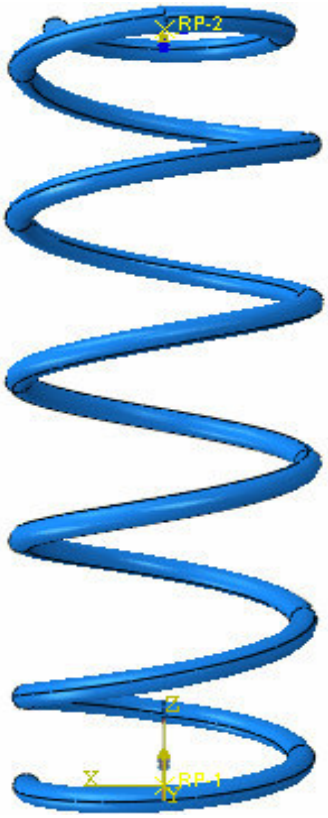

Figure 3.3 The boundary condition of the coil spring

In problems where the stresses are concentrated in some areas, smaller elements are recommended in these regions. Thus, mesh quality should be high, which implies a preference for element meshes with good shape characteristics. Unfortunately, the more the elements, the longer the computational time that is required. Hence, it is always necessary to limit the number of elements (Liu & Quek 2003). Thus, a tetrahedral mesh type is generally regarded as satisfactory (Bishop et al. 2000) and probably becomes preferable for a high quality meshing for boundary representation of the solid model (Baek et al. 2008; Mulia et al. 2012) and to give an accurate solution (Prawoto et al. 2008). Meshing was performed to discretise the geometry of the component model created into small pieces called elements using a set of nodes (Liu & Quek 2003). The von Mises yield criterion, described in Equation (2.13), was then applied to each small element. The stress distributions facilitated to classify the critical area at the coil spring. Once the location had been identified, a strain signal acquisition during automobile operation could be performed.

3.1.2 Strain Signal Acquisition

The strain signal acquisition had been carried out to find time series strain loadings at the coil spring affected by road surfaces. The required strain signals have traditionally been obtained by driving a prototype automobile, or at least a similar automobile, over the referenced road surface. The strain signal acquisition procedure was divided into two stages, namely the equipment installation stage and the strain signal measuring stage. Equipments used to conduct the acquisition were as follows: (1) a 2-mm strain gauge, (2) SoMat eDAQ data acquisition, and (3) a computer with TCE software package (SoMat 2002). The position of the strain gauge installation was selected based on the possibility of higher stress area based on the FEA. The strain gauge installed on a higher stress area should provide higher strain amplitudes, and they were more easily detected by the strain gauge, and thus, made the simulation go smoothly. Figure 3.4 shows the strain gauge installation, including the strain signal acquisition set up.

(a) (b)

Figure 3.4 Acquisition of the strain signals: (a) strain gauge installation, (b) SoMat e-DAQ data acquisition set up

The strain gauge condition during the acquisition was a key factor for ensuring the accuracy of the strain signals. To ensure that the strain signals were accurate, the strain gauge installation process was performed carefully and cautiously (ASTM E1237-93 2009). During the installation, several factors were addressed to not disturb the obtained readings. First, the coil spring surface where the strain gauge was to be placed should be flat and dirt-free. Thus, the area was scrubbed with 400-grade sand paper to create a flat surface (ASTM E112-96 2004). Ensuring that the strain gauge

adhered to the surface was important to provide accurate readings. Second, due care was taken to ensure that the copper wires for both strain gauge poles were not in contact with each other or touching the coil spring to avoid short circuits that can cause inaccuracies in the readings. Third, the adhesive used was appropriate. If the adhesive was less than required, it could cause the strain gauge to wear off, whereas too much adhesive could affect the sensitivity of the strain gauge.

The strain gauge was connected to the data logging instrument through a connector. The SoMat eDAQ fatigue data logger was used to record the strain signals measured by the strain gauge. Measuring parameters were set up using TCE software package (SoMat 2002) to align the strain gauge reader, set the type of collected strain signals, set the strain signal storage area and upload the strain signals from the fatigue data logger into the computer. According to Ilic (2006), the sampling frequency for a strain signal acquisition should be greater than 400 Hz, so that the essential components of the signal are not lost. Using a collection rate higher than 500 Hz can increase the upper limit of the frequency range as small amplitude and high frequency load cycles will be captured. Collecting load histories at a frequency of 500 Hz is sufficient to detect and capture all damaging load cycles (Haiba et al. 2003), and the selection of 500 Hz was seemingly suitable for the on-site strain signal collection.

After installing the equipments, the car was then driven on highway, urban and rural road surfaces at velocities of 70 km/h to 80 km/h, 30 km/h to 40 km/h and 20 km/h to 40 km/h, respectively, as summarised in Table 3.5. Figure 3.5 shows the road surfaces travelled during the measurement, while the measuring track areas are shown in Appendix A. The road surfaces were chosen because they are the most commonly used in Malaysia. The velocities above were matched with an average car

Table 3.5 Car velocities for each road surface

Road surfaces	**Velocites (km/h)**
Highway	70 – 80
Urban	30 – 40
Rural	20 – 40

(a) (b) (c)

Figure 3.5 Types of road surfaces used for the strain signal acquisition purpose: (a) highway, (b) urban, (c) rural

speed when driven on specified road conditions (Ilic 2006; Lajqi & Pehan 2012; Tong & Guo 2012). Furthermore, the measured strain signals were the input into a mathematical expression for generating acceleration signals.

3.1.3 Acceleration Signal Generation

Motivated by the success of the researches related to automotive suspension system simulations as discussed in Section 2.1.3, the study used the equation of motion as the basic formula to develop a mathematical expression for generating acceleration signals. The equation of motion for a damped forced vibration is represented by Equation (2.6). Typically, it is separated into internal and external forces. Internal forces are found on the left side of the equation, and external forces are specified on the right side. External forces induced from engine operations, tyres and the like have an influence on the simulation results, however, they were not considered due to limitations observed in the equipments and the MBD software package. A tyre force, for example, is measured during the prototype phase and is mostly estimated using tyre models and auxiliary sensors. The measurement of a tyre force involves many sensors to be placed in many locations since the force does not always flow in the same way for different manoeuvres.

Thus, the equation of motion became a damped free vibration, generated as follows (Kelly 2012; Magrab 2012):

$$m\ddot{x} + d\dot{x} + kx = 0 \tag{3.1}$$

Then, the acceleration $\ddot{x}$ is derived as:

$$\ddot{x} = \frac{-d\dot{x} - kx}{m} \tag{3.2}$$

Since the displacement x was known, the velocity $\dot{x}$ might be determined through differentiation of the time-dependent displacement (Figliola & Beasley 2011). Expanding Equation (3.2), it is obtained:

$$\ddot{x} = \frac{-d\left(\frac{\partial x}{\partial t}\right) - kx}{m} \tag{3.3}$$

Figure 3.6 shows the response of a damped free vibration.

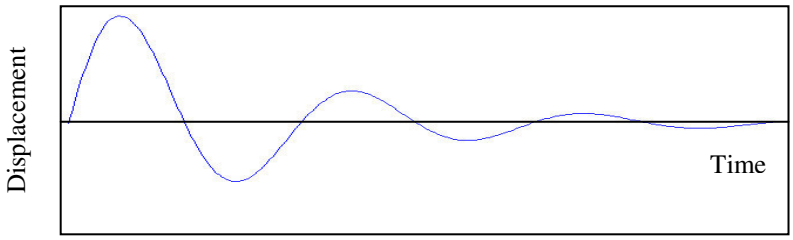

Figure 3.6 Response of a damped free vibration

Source: Chikhale & Deshmukh 2013

Shearing forces cause shearing deformation. An element subjected to shear does not change in length but undergoes a change in shape. The change in angle at some point of an element is called the shear strain γ, where this kind of strain is associated to torsion in a spring. It is expressed as:

$$\gamma = \frac{x}{D_0} \tag{3.4}$$

where D_0 is the original unloaded diameter, and then:

$$x = \gamma D_0 \tag{3.5}$$

Substituting Equation (3.5) into (3.3), the acceleration $\ddot{x}$ results:

$$\ddot{x} = \frac{-d\left(\frac{\partial(\gamma D_0)}{\partial t}\right) - k\gamma D_0}{m} \tag{3.6}$$

Based on Equation (3.6), a MATLAB (matrix laboratory) Simulink®-based model (Simulink 2013) was developed. The model was constructed from graphical blocks with input and output ports that were connected by drawing lines. The measured strain signals were used to obtain velocities, and the velocities were utilised to obtain acceleration signals. In the schematic diagram in Figure 3.7, block A was used to input the strains. The strains were presented in block B as a graph, and were provided as values in block C. The strains were then transformed into the displacements using block D, containing the coil spring original unloaded diameter. Block E functioned to transform the displacements into the velocities and the velocities were then transformed into the accelerations using block F. The values of the damping coefficient and the spring stiffness were inputs in block G. Submitting the damping ratio, the spring stiffness and the mass into Equation (2.3), the damping coefficient of 15,564 Ns/m was obtained. The spring stiffness was also the input in block H together with the mass. Finally, the accelerations were viewed in block I and were provided as values in block J. The function of the blocks is summarised in Table 3.6. The fatigue-based acceleration signals were the input for the MBD simulation for simulated strain signal generation.

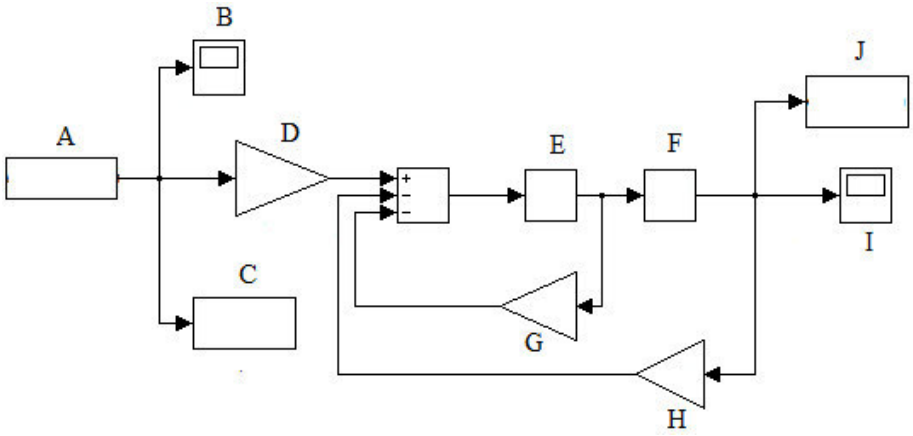

Figure 3.7 Schematic diagram of MATLAB Simulink®-based model for generating acceleration signals

Table 3.6 Function of each block in the strain model

Blocks	Functions
A	Input the strains
B	Present the strain graph
C	Present the strain values
D	Transform the strains into the displacements
E	Transform the displacements into the velocities
F	Transform the velocities into the accelerations
G	Input the damping coefficient and the spring stiffness
H	Input the spring stiffness and the mass
I	Present the acceleration graph
J	Present the acceleration values

3.2 SIMULATED STRAIN SIGNAL GENERATION

The dynamic analysis differs from the static analysis in two aspects, where dynamic loading is applied as a function of time or frequency and this time or frequency varying load application. This time or frequency varying characteristics makes dynamic analysis more complicated and more realistic than static analysis. Thus, in the study, a dynamic analysis was developed as evident on the flowchart in Figure 3.8, where the error reflected to the fatigue damage deviation determined using the strain-life approach. The 10 % error is to ensure that the resulted modified signal is as close as possible to the original signal; so as to keep the majority of fatigue damage, the vibration energy and the amplitude range (Stephens et al. 1997; Giacomin et al. 2001).

3.2.1 Multi-body Dynamic Simulation

Computer-based modelling and virtual experimentation has proven to be a powerful mechanism for solving problems in many areas (Claeys 2008). In classical analyses, mechanical systems are investigated which consist either of a single rigid body or of several rigid bodies in some particularly simple geometric configuration. The important role they play in classical mechanics is due to the fact that their equations of motion can be integrated in closed form. This is not possible, in general, if a system is constructed of many rigid bodies in some arbitrary configuration. The engineer is confronted with an endless variety of such systems. The assumption that the individual bodies of such systems are rigid is an idealisation. Thus, the human body

composed of obviously non-rigid members may well be treated as a system of interconnected rigid bodies when only its gross motion is of interest. This does not exclude springs and dampers interconnecting bodies.

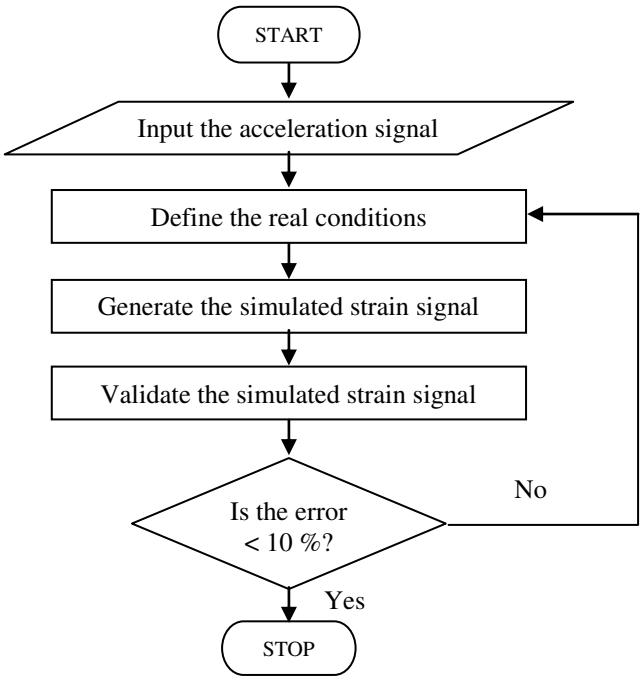

Figure 3.8 Flowchart of the MBD simulation procedure

An MBD simulation was involved because it composes of various rigid or elastic bodies where the connections between the bodies can be modelled with kinematic constraints or force elements. Joints and force elements have in common that they connect bodies and that they exert forces of equal magnitude and opposite direction on the two connected bodies. The difference between joints and force elements is the nature of these forces. In a force element, the force vector (direction and magnitude) is a known function of the positions and / or the velocities of the two bodies connected by the force element. The essential feature of force elements is that they do not create kinematical constraints. In contrast, the force exerted on two bodies by a joint connecting these bodies is a pure kinematical constraint force. It is caused by frictionless rigid body contacts. It cannot be expressed as function of position and velocity variables. Constraint forces do not enter the equations of motion because they have zero virtual work and zero virtual power (Wittenburg 2008). In a MBD simulation, system is assumed as homogeneous parts (Dymola 2011a).

The simplest force elements are springs and dampers, as shown in vibration model in Figure 2.3, which are passive elements. An active force element was admitted in which the force was determined by a given control law from observed position and velocity variables (Wittenburg 2008). In the current study, the force was resulted from Equation (3.6) and the schematic diagram in Figure 3.7. A modelling methodology based on object orientation and equations for dynamic systems had been used for generating a strain signal having behaviour similar to the actual strain signal. Dymola® (dynamic modeling language) software package (Dymola 2011a; Dymola 2011b) was used to model the three-dimensional mechanical multi-body system of the coil spring. The software, developed by Elmqvist (1978), was an early effort to support physical modelling. The shear strain γ is generated by inverting Equation (3.1) and submitting Equation (3.5) into it. Re-arranging Equation (3.1), it is obtained:

$$k\gamma D_0 = -m\ddot{x} - d\dot{x} \tag{3.7}$$

then:

$$\gamma = \frac{-m\ddot{x} - d\dot{x}}{kD_0} \tag{3.8}$$

Finally, the equation solves for the shear strain γ, by integrating the acceleration $\ddot{x}$ to obtain the velocity $\dot{x}$:

$$\gamma = \frac{-m\ddot{x} - d\int \ddot{x}}{kD_0} \tag{3.9}$$

In the schematic diagram developed based on Equation (3.9) as shown in Figure 3.9, the coil spring responses in terms of strain were observed in order to reach the main objective of the study. In the simulation, block A aimed to input a variable data set, then it was connected to the translational mechanics in block B determining the movement of the coil spring system. Block C defined the coordinate system, including the gravity of 9.81 g, and block D defined the degree of freedom. Block E

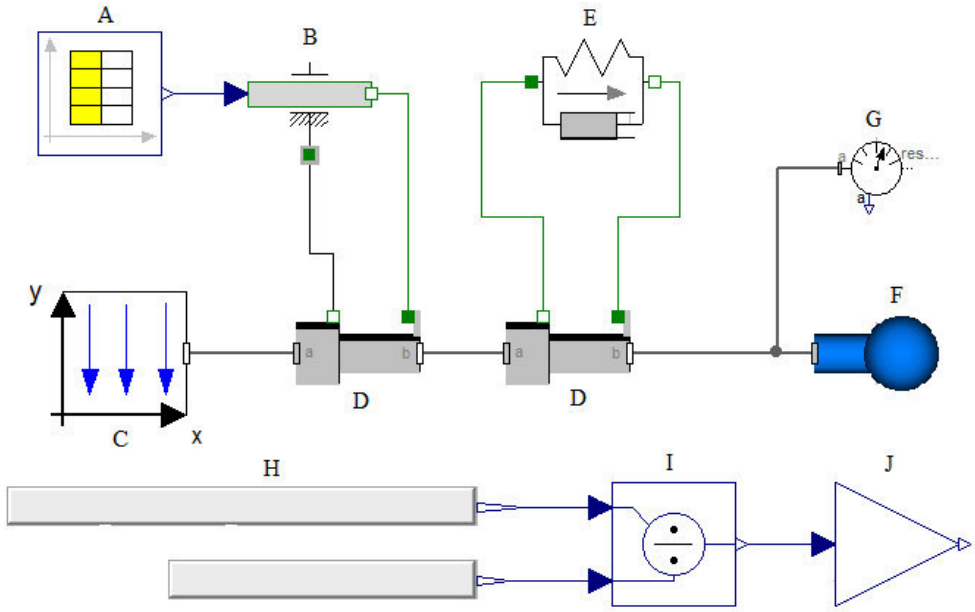

Figure 3.9 Schematic diagram of Dymola®-based model for generating strain signals

was the coil spring system to input the damping coefficient and the spring stiffness, while the mass was the input for block F. Block G was the sensor transforming the variable data set into accelerations. In block I, the strains were determined based on the input in block H, which was the original unloaded diameter of the coil spring. Finally, the simulated strain signals caused by the accelerations were provided in block J. The function of the blocks is summarised in Table 3.7. Furthermore, the characteristics of the simulated strain signals were analysed.

Table 3.7 Function of each block in the acceleration model

Blocks	Functions
A	Input the variable data set
B	Define the translational mechanics
C	Define the coordinate system
D	Define the degree of freedom
E	Input the damping coefficient and the spring stiffness
F	Input the mass
G	Transform the variable data set into the accelerations
H	Input the original unloaded diameter of the coil spring
I	Determine the strains
J	Present the strains

3.2.2 Strain Signal Analysis

Since non-stationary signals are common in the cases of fatigue field, signal analysis has often been used due to its simplicity and efficiency for the purpose of a simulation. Time series analysis aims to determine the characteristics of the original function by manipulating a series of discrete numbers. One of probabilistic analyses considered in validating the simulated strain signals was the Weibull distribution. Its purpose was to find out whether the actual and simulated strain signals show common behaviour.

The Weibull distribution described in Equations (2.15) to (2.16) was applied in MATLAB® software package (MATLAB 2008b). The shape parameter of two was selected since the failure rate of a coil spring increases over time, the scale parameter was from the time of the strain signals and the location parameter was assumed as zero (Jiang & Murthy 2011). The advantages of two-parameter Weibull distribution are (Sakin & Ay 2008): (1) it can be explained with a simple function and easily applied, (2) it is used frequently in the evaluation of fatigue life, (3) its usage is easy with present graphics and simple calculation methods, and (4) it gives some physical rules concerning failure when the slope of the Weibull probability plots is taken into account.

Common statistical parameters that are directly related to the observation of strain signal behaviour were used for the analysis, namely mean value, SD, r.m.s. and kurtosis. These parameters are clarified in Equations (2.38), (2.39), (2.41) and (2.43), respectively. The statistical analysis utilised GlyphWorks® software package (nCode 2007), as the display is shown in Figure 3.10. In the figure, block A functioned to input the strains. Statistical parameters needed were determined in block B, such as mean value, SD, r.m.s., kurtosis and others. Then, the results of statistics were presented in block C.

Furthermore, MATLAB® software package (MATLAB 2008a) was also used to determine the frequency spectrum of the strain signals based on Equation (2.45). The PSD formulated in Equation (2.47), was also used to characterise the strain

signals in frequency representation, using the programming language software as well. The PSD comparisons were carried out to observe differences between the actual and simulated strain signals in the energy contents. The energy was determined by calculating the width of areas provided in the PSD view. Ideally, the simulated strain signals provided the PSD view which was similar to the actual PSD pattern.

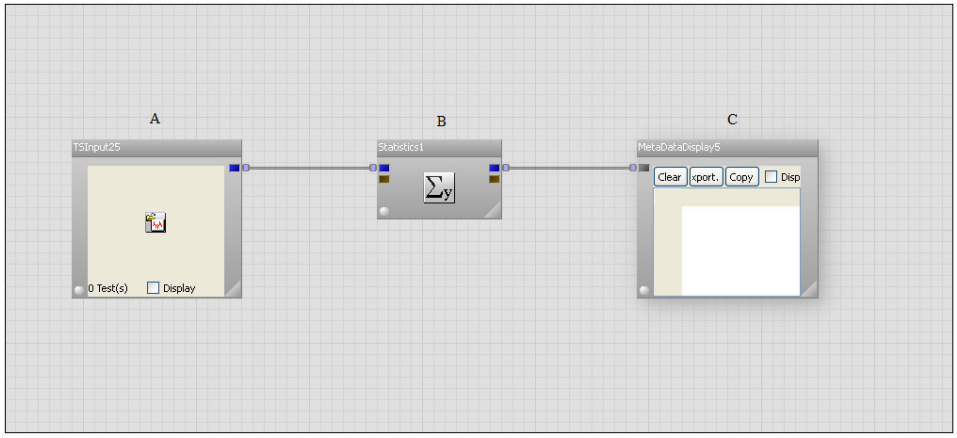

Figure 3.10 Glyphwork®-based process for statistical analysis

In this study, fatigue life assessment aimed to predict the life of the coil spring when subjected to a load of varying amplitudes. Based on the findings of previous research (Williams et al. 2003), it is common that the service loads due to machines or vehicles are evaluated using the strain-life approach due to its widely acceptance in automotive industries. The strain-life approach is the most suitable method for automobile applications because it is commonly applied to predict the fatigue life for small components that have low cycle fatigue. Because it is difficult to categorically select one procedure in preference to the others, all the strain-life models were involved in the study. The strain amplitudes were determined using the Coffin-Manson, Morrow and SWT models, mathematically defined in Equations (2.31), (2.32) and (2.34), respectively. Fatigue damage was determined using the Palmgren-Miner linear cumulative fatigue damage rule based on a number of repeated simple or complex loads. The number of cycles was determined using the rain flow cycle counting method. Fatigue damage for each cycle was calculated using Equation (2.35) and was then accumulated in order to get the total fatigue damage for the load using Equation (2.36). Ideally, both the actual and simulated strain signals should have an equivalent fatigue damage.

All the above procedures were performed using GlyphWorks® software package (nCode 2007). Aside from statistical analysis, the software provides fatigue cycle counting, stress-life and strain-life-based fatigue life assessments, among others, where the workspace is shown in Figure 3.11. Block A functioned to input the strains. Fatigue damage models, such as Coffin-Manson, Morrow or SWT, could be selected in block B. Fatigue damage, fatigue cycle and fatigue life were provided as value in block C. Fatigue damage distribution was presented in block D and F as value and graph, respectively. Fatigue damage distribution for each cycle was presented in block E as a three-dimensional histogram. In order to validate the simulation-based strain signals, they were compared to the actual strain signals through simulated and experimental works.

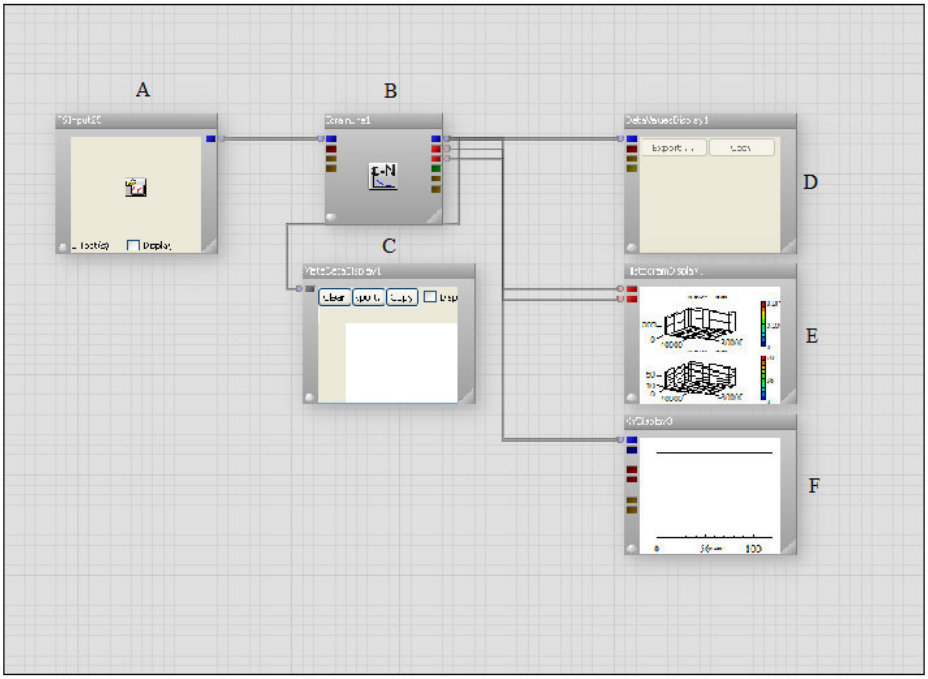

Figure 3.11 Glyphwork®-based process for fatigue life assessment

3.3 VALIDATION PROCESS

3.3.1 Fatigue Feature Extraction

For the first validation procedure, both the actual and simulated strain signals were extracted using the wavelet transform to generate damaging segments and then form edited strain signals. For the development of the FDE algorithm, the required input

was the distribution of the wavelet-based energy for the achievement of fatigue resistance characteristics. The wavelet-based FDE applied a method removing lower amplitude energy. Wavelet-based FDE algorithms found in literature were based on discrete time. Because it aimed to investigate if the CWT could be used to precisely extract the strain signals, it had been selected as the method used in the current study. Continuous analysis involves a simpler analysis than discrete method requiring some levels of analyses. In addition, it is easier to interpret, has made all information more visible and is sufficient for exact reconstruction. It possesses suitable properties for signal analysis and has only required to be admissible, leading to the freedom in the selection of a mother wavelet (Su et al. 2010). A mother wavelet must be carefully chosen so that the content of the son wavelet is largely similar to that of the analysed signal to ensure good results.

Although many new and complicated basic functions have been proposed to improve the effectiveness of wavelet-based methods, to date, no general guideline has been proposed for the correct selection of a mother wavelet. At the same time, little attention has been paid to the inherent deficiencies of the wavelet transform (Guo et al. 2012). Thus, the chosen mother wavelet was Morlet, described in Equation (2.49), since it results in an internal energy plot that is similar to the fatigue damage distribution, because it is more sensitive to amplitude changes in a strain signal. The wavelet transform, particularly Morlet, possess its own priority than other transformations in the time-frequency domain. The Morlet wavelet has a great potential for predicting fatigue failure (Kim & Melhem 2003; Lin & Zuo 2003).

Figure 3.12 shows the FDE computational algorithm flowchart developed using MATLAB® software package (Misiti et al. 2008). The wavelet transform was employed to convert a time domain signal into the time-frequency domain displaying the wavelet coefficient in time and frequency axes simultaneously in two dimensions, as observed in the time-frequency surface. According to Jiang et al. (2011), how to select an appropriate scale is not given. Thus, in this function, a higher scaling factor was used to obtain a better time resolution. This was because the time resolution is more important to detect the position of a high magnitude.

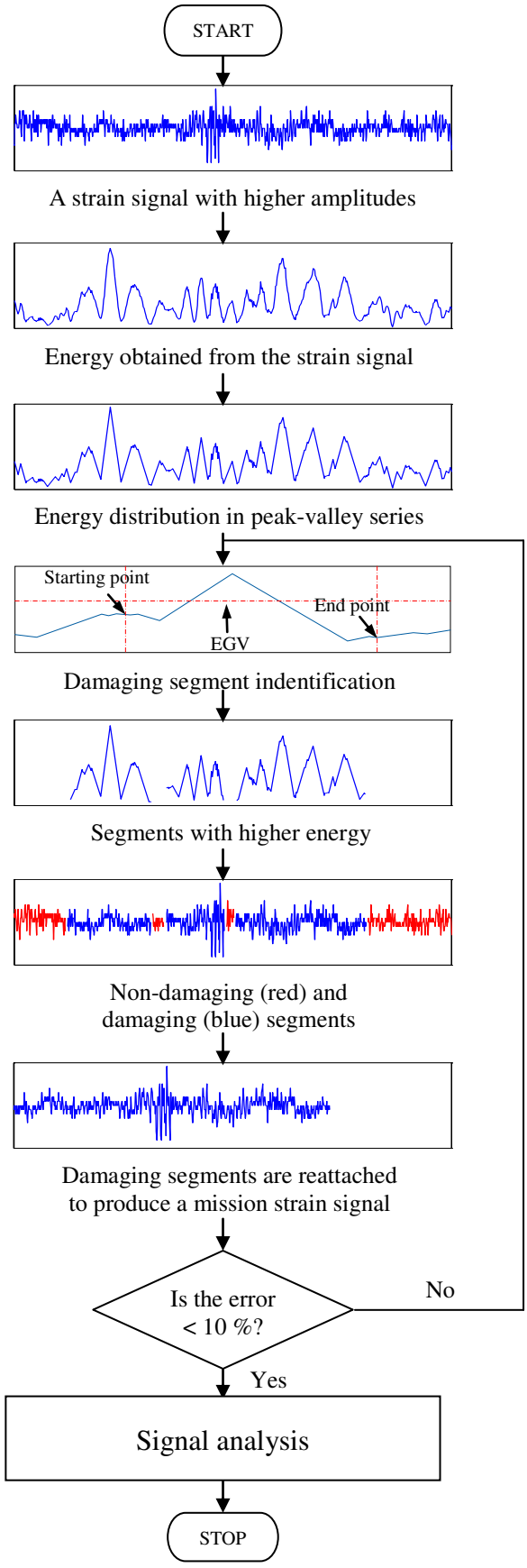

Figure 3.12 Flowchart of the developed FDE algorithm

The mother wavelet is square integrable or, equivalently, has finite energy. Thus, the wavelet coefficient, obtained using Equation (2.50), provided a display of the energy distribution of a particular time and frequency by squaring the coefficient at each time interval. The wavelet-based signal internal energy $\bar{e}$ can be expressed as follows (Mallat 2009):

$$\bar{e}_{(p,q)} = \int_{-\infty}^{+\infty} \left| WC_{(t)} \right|^2 dt \tag{3.10}$$

Based on Equation (3.10), the distribution of energy was decomposed into the time domain spectrum by taking the magnitude cumulative value for an interval of time. The energy was then utilised to detect the amplitude changing in the strain signals. A lower scale in the wavelet coefficient shows a higher frequency and has a smaller strain amplitude, which means this cycle has a lower energy, indicating a minimum or no potential for fatigue damage. A larger scale in the wavelet coefficient shows a lower frequency and higher strain amplitude, indicating this cycle has a higher energy causing fatigue damage (Darpe 2007). Clearly, lower frequency shows a higher magnitude and lower magnitude distribution is shown in higher frequency events.

Identification of the peak-valley could be used to cut the strain signals so that each segment contains a number of certain peaks and valleys, according to the need of the study. This is especially useful for fatigue signals, because characteristics of the peak-valley are dominant in the rain flow method used for the calculation of the number of cycles (Xiong & Shenoi 2008). The peak-valley-based technique associated with the wavelet transform successfully extracted the typhoon image (Zhang et al. 2007). Thus, an algorithm was developed to produce a new magnitude taking the points of peak and valley only by comparing the magnitude values.

Furthermore, highly fatigue damaging segments in the strain signals were extracted, based on high energy distribution, in order to result in segments contributing to fatigue damage. Energy gate value (EGV), which is the energy spectrum variable, was then applied as a parameter to determine the minimum magnitude level to be retained in the wavelet domain. Let the maximum wavelet-based energy be $\bar{e}_{\max}$, then, the EGV is represented as:

$$EGV = \bar{e}_{\max}^{h} \tag{3.11}$$

where h is the multiplicative factor that can be any positive number. Energies that were higher than the EGV should be maintained based on their positions on the time axis in order to produce segments contributing to cumulative fatigue damage for further analysis. Instead, all energies that were less than the EGV were removed. Because segments consisting of a low magnitude represent segments with low fatigue damage, the fatigue characteristic extraction was expected to be able to maintain the majority of fatigue damage in the strain signals.

Figure 3.13 shows the concept of segment identification. The selection of a retained segment was based on energy loss, which occurs when the selected segment was at the beginning of the swing so that it ends. The starting point of the segment was the valley point if the previous peak was higher than the peak after the valley point. Meanwhile, the endpoint of the segment was the valley point if the peak after the point was higher than the peak before the point. Thus, the identification of the extracted segment was performed by finding the inverse of two points (on each peak). Once all the extracted segments were identified, the energy time history was then scrapped to remove lower energy (less than the EGV) contained in the range of the original time history. The positions of the extracted segments were then transferred to the original strain signal in the time domain for the removal of segments that were not required. The segments to be removed were then cut from the original strain signal based on the position of the segments. The extraction concept above refers to the concept of the cut-off level used in the extraction in the time domain by Stephens et al. (1997).

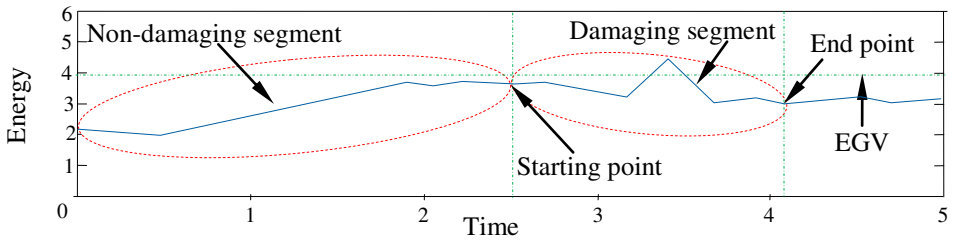

Figure 3.13 Concept of the segment identification

To obtain the optimum EGV, the maintained segments were then merged with each other to form a shorter modified strain signal, in comparison to the original strain signal, but had equivalent behaviour to the original strain signal. A different EGV resulted in a differently modified strain signal. After increasing the EGV, a shorter modified strain signal was produced because more magnitude cycles were under the higher EGV. Therefore, resulting strain signal was shorter when more segments were removed. However, the edited strain signal at a higher EGV provided real decline in maintaining the original characteristics of the strain signal. If the obtained modified strain signal did not meet the criteria, the EGV was reduced to obtain the required modified strain signal. After decreasing the EGV, the characteristics of the modified strain signal increased and were even equal to the original characteristics. The question then arose as to how accurate the wavelet transform was in shortening the strain signals. Thus, the resulted lower and higher amplitude segments from the extraction process were clustered to answer the question. Therefore, a fatigue feature clustering algorithm had to be developed.

3.3.2 Fatigue Feature Clustering

In the cases of large data, it is difficult to keep track of the importance of each feature in clustering. In addition, it is not possible to use large data directly in clustering because of computational costs. Thus, a solution is to develop as much data as possible. Therefore, the most challenging step in clustering is feature extraction. Several feature extraction approaches had been designed to obtain combinations of data which could be used to represent a pattern.

The clustering method used in the study was the FCM because it provides a good result based on the distance to the centroid of each segment that is closer. The FCM, formulated in Equation (2.57), is one of widely used clustering methods. Each retained and removed segments derived from the FDE algorithm were clustered using MATLAB® software package (MATLAB 2008c). The FCM was employed to cluster fatigue features in order to observe the FDE ability in identifying damaging segments. The clustering method scattered the segments based on the differences in SD, r.m.s., kurtosis, wavelet-based energy and fatigue damage. It was hypothesised that there are correlations among these parameters that contributes to the result of shorter fatigue signals.

This method began by determining the number of groups. Furthermore, each segment was classified into the nearest cluster center, also known as the centroid (Das 2013). So segments in each group were as close as possible and as far as possible to other segments in other groups (Liao 2005). This search was accomplished by repeatedly moving the centroid to various places. The process stopped when the nearest distance was obtained (Das 2013), which meant that the process was obtaining the desired segment distribution. It provided centralised scattering for certain segments. This method considered a segment as something that had a position and distance of each other. Since the clustering method is new in fatigue field, the results of the current study are expected to provide a new knowledge on the applicability of the FCM in fatigue researches.

In many engineering and industrial experiments, it is already known that the estimator and what is estimated to differ, yet the amount of difference is usually the significant finding. In order to understand what happened to the simulated strain signals, tests need to be conducted to demonstrate that the developed simulation was correct. Observations can lead to theories or hypotheses about what makes a simulation work to really understand cause-and-effect relationships in the simulation (Montgomery 2013). Thus, for quality measurements of the regression model, the coefficient of determination and the RMSE were applied. Both the methods are represented in Equations (2.58) and (2.60), respectively.

A hypothesis test was also performed to examine whether or not the observations follow a specified probability distribution. In order to observe the significance of the simulated strain signals toward the actual strain signals, one-way ANOVA model described in Equation (2.63) was applied. One-way ANOVA was used because only one factor was investigated, which was strain. With the use of an ANOVA statistical tool, each strain column was treated as a separate group, and evaluated as to whether the population means of the strain strains were equal. The goal was to test if the null hypothesis was plausible. In the study, the null hypothesis was that the simulated strain signals conform to the actual strain signals. The alternative hypothesis was that the simulated strain signals have a different distribution.

The differences between the actual and simulated strain signals could be judged by calculating a *p*-value. The *p*-value was used as an auxiliary tool to determine equal or unequal variances between the strain signals. To get the *p*-value, the degree of freedom and the chi square value were calculated first using Equations (2.61) and (2.62), respectively. Since Equation (2.62) includes Σ (sigma) operator, individual chi square values were calculated for each possible outcome, then added to the results to get one general chi square value. A chi square distribution table, shown in Appendix B, was used to determine the *p*-value. This table is generally set up with the vertical axis on the left corresponding to degree of freedom and the horizontal axis on the top corresponding to *p*-value. To use the chi square distribution table, then read the row across from the left to the right until the first value bigger than the chi square value was found. Looking at the corresponding *p*-value at the top of the column, the *p*-value was between this value and the next-largest value (the one immediately to the left of it).

Once the *p*-value was known, the decision maker could determine how significant the strain signals were (Montgomery 2013). In the study, a 90 % confidence level was applied (Sivák & Ostertagová 2012; Motra et al. 2014). The confidence level meant being 90 % certain about the correlation between the actual and simulated strain signals and was seen as "successful". A 90 % confidence level reflects a significance level of 0.1 (Hardy & Bryman 2009). If the *p*-value was higher than the significance level, it is highly likely that there was a correlation between the actual and simulated strain signals. Thus, the null hypothesis would be rejected at any *p*-value below 0.1. Rejecting the null hypothesis would imply that different treatments result in altered effects.

In addition, it is often preferable to provide an interval within which the values of the parameter(s) in question are expected to lie. An interval on the difference in means was used in answering this question. This interval statement is called confidence interval, described in Equation (2.68). Since a 90 % confidence level was applied (Sivák & Ostertagová 2012; Motra et al. 2014), then, it could be expected that about 90 % of the strains would yield confidence intervals that include the confidence limits, whereas the remaining 10 % would not. Hence it would be correct in about

nine out of ten strains, while the remaining strains would be false. All these statistics methods used MATLAB® software package (MATLAB 2008b) as well. Although hypothesis testing is a useful procedure, it sometimes does not tell the entire story (Montgomery 2013). Thus, for strengthening the reliability of the simulated strain signals, experimental validations were performed. Aside from fatigue life assessments using the strain-life approach, cyclic tests were conducted as well.

3.3.3 Fatigue Test

Before performing a fatigue test, the selected material was examined through a tensile test in order to determine the cyclic mechanical properties of the material. It was performed to make sure that the material was SAE5160 carbon steel. The material was from APM Automotive Holdings Bhd., as the supplier of coil springs to Proton cars. For the tensile test, the specimen was designed according to ASTM E8/E8M-11 (2012), as shown in Figure 3.14. and its dimensions are tabulated in Table 3.8. The specimen was fabricated using computer numerical controls and grinding machines and was mechanically polished (ASTM E112-96 2004) in order to ensure complete removal of machining marks in the testing section. A sand paper with a grit size of 240 was used to give the rounded shape and the finer 1,500 grades gave a suitable surface finish.

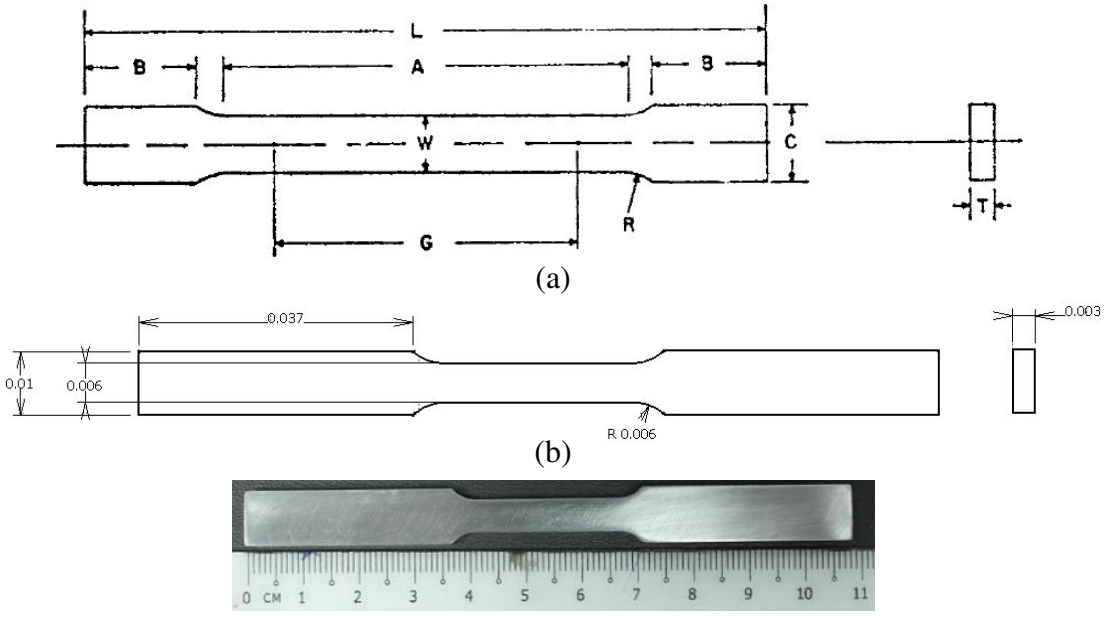

Figure 3.14 A specimen for the tensile test: (a) geometry based on ASTM E8/E8M-11 (2012), (b) specimen modelling, (c) photograph of the specimen

Table 3.8 Dimensions of the tensile specimen

Dimensions (mm)	
G	25
W	6
T	3
R	6
L	112
A	32
B	34
C	10

Zwick Roell tensile machine with the load range of ±100 kN was the main apparatus used to perform the tensile test. The test started by clipping the specimen into the top clamp of the extensometer, as shown in Figure 3.15. It was important that the specimen be aligned vertically. Otherwise, there was some torque applied, skewing the results. The tensile grips were separated at a constant strain rate of speed, depending on the preparation of the specimen shape and the temperature of the testing

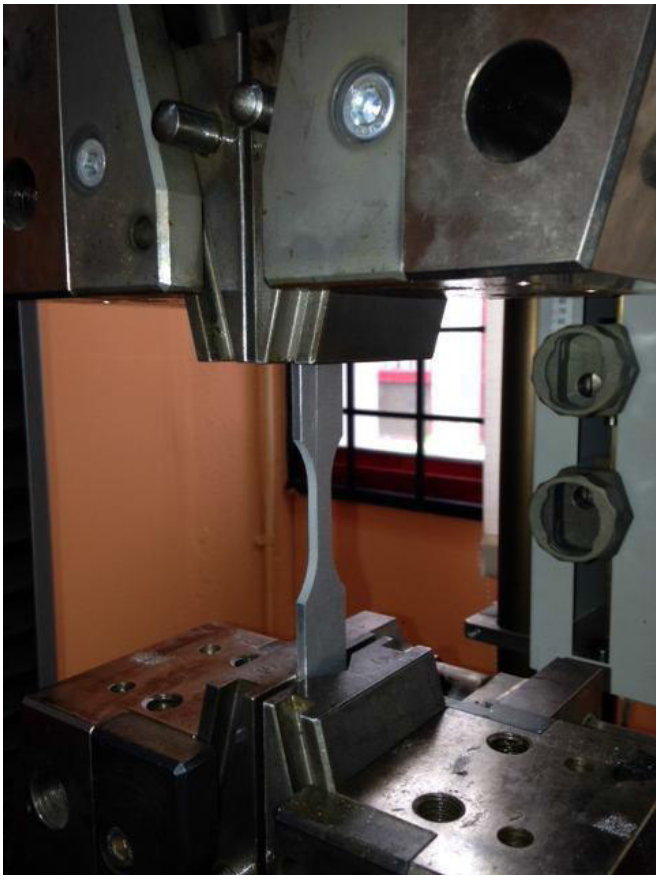

Figure 3.15 A specimen at the Zwick Roell tensile grips

environment, until the specimen broke or the force applied reached a maximum. The strain rate of speed was 1.5 mm/min obtained by multiplying the gauge length of the specimen with 1 x 10^{-3} sec^{-1}. The test was performed at the room temperature, which was 20 ^{o}C (ASTM E8/E8M-11 2012). As the specimen was pulled during the test, it was determined how much it elongates under given pressure, how it reacts to force being applied in tension and exactly how brittle or ductile the material acts under given stress, along with the amount of the force needed to break it.

There are several problems occurred in fatigue research. First, current industrial practices use the Palmgren-Miner linear cumulative fatigue damage rule normally applied to the established strain-life approach. Fatigue life for a CAL can be calculated accurately, but the accuracy for calculating a VAL is doubtful because the Palmgren-Miner rule does not account for loading sequence effects. Second, fatigue signals are difficult to be measured directly and their measurements have a high cost and are time consumption. In addition, because of inaccuracies in the measuring apparatuses, errors may be present. A wide variety of techniques exists for measuring strain signals, and each technique has its own advantages and disadvantages.

Third, fatigue signals are long and consist of much lower amplitudes. If those signals are used in non-modified forms for laboratory fatigue tests, lengthy testing times are required that can take days or even weeks to arrive at a result. It is very time consumption to test with an original loading history because there are numerous lower amplitude cycles that contribute to a minimum fatigue damage. Thus, the main reasons to perform VAL fatigue tests in the study were: (1) to investigate the cycle sequence effect, (2) to validate the fatigue life of the actual, simulated and edited strain signals, and (3) to show the time reduced from using the edited strain signals.

The major reason for carrying out a VAL fatigue test (Aykan & Celik 2009; Niesłony & Böhm 2013) was the fact that a prediction of fatigue life under this complex loading is impossible by any hypothesis (Sonsino 2007; Carvalho et al. 2010). A VAL fatigue test is principally carried out like a CAL fatigue test on different loading levels, with a given load being continuously repeated until a failure is obtained. The only difference is that in cases of CAL, the amplitude (or range)

remains unchanged. Thus, VAL fatigue tests are more complicated and often more time consumption and expensive than CAL fatigue tests (Rognin et al. 2009). There are no exact methodologies that have been addressed, but there are several factors that should be considered when a VAL fatigue test is performed (Sonsino 2007), namely the material, specimen geometry, loading range, frequency and characteristics of a fatigue testing machine. The procedures of performing the fatigue life assessment for uni-axial and multi-axial VALs had been discussed by Banvillet et al. (2004).

The fatigue testing specimens were designed according to ASTM E606-92 (1998), as shown in Figure 3.16 and their dimensions are listed in Table 3.9. The specimens were assumed to have real conditions as a whole spring. The geometry and the dimensions of the specimens were specified along with appropriate grips for the fatigue testing machine used. An Instron 8801 closed-loop servo-hydraulic machine was used to conduct the tests, under uni-axial loadings for a particular number of cycles to failure. The machine is able to apply a uni-axial cyclic loading at various mean values, load ranges and cycle frequencies. The machine permits a fatigue test to be performed under loading mode, providing a load in the range of ±100 kN. Figure 3.17 shows the specimen at the grips of the machine. The tests were performed at

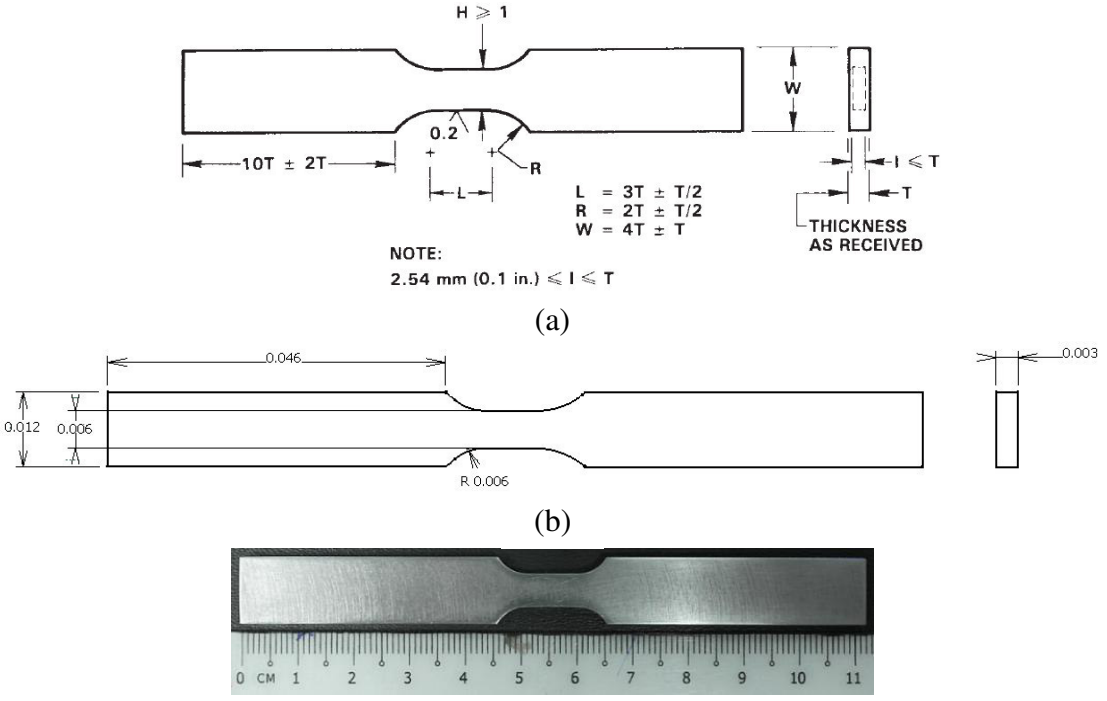

Figure 3.16 A specimen for the fatigue test: (a) geometry based on ASTM E606-92 (1998), (b) specimen modelling, (c) photograph of the specimen

Table 3.9 Dimensions of the fatigue specimen

Dimensions (mm)	
H	6
T	3
W	12
R	6
L	9

Figure 3.17 A specimen at the Instron fatigue grips

the room temperature, which was 20 ^{o}C (ASTM E606-92 1998), and involved smooth specimens as well (ASTM E112-96 2004), as performed in the tensile test. Since fatigue cracks begin to occur at irregular surfaces, the condition of a specimen surface is important in fatigue tests. It reduced stress concentration to prevent crack initiation at those sites.

With an aim to identify the cycle sequence effect to fatigue life, two-step loading fatigue tests were carried out to compare low-high and high-low cycle sequences. The cycle sequence is a rule where the load applied on a specimen exists in

both levels of fatigue, at micro and macro cracks. Randomly fluctuating loads arranged in blocks (called block method) are often used in experimental studies to characterise a VAL (Ayoub et al. 2011; Khan et al. 2014). This procedure has been developed based on the failure of various stages of loadings. Figures 3.18 to 3.20 show the five levels of strain amplitudes for the application of the Palmgren-Miner rule. For a valid VAL test, the sequence must be repeated at least five times in order to achieve a service-like load mixing (Sonsino 2007). A stress ratio of -1 is the common reference testing condition used for obtaining fatigue properties (Klimkeit et al. 2011; Upadhyaya & Sridhara 2012; Bruchhausen et al. 2015), called fully reserved

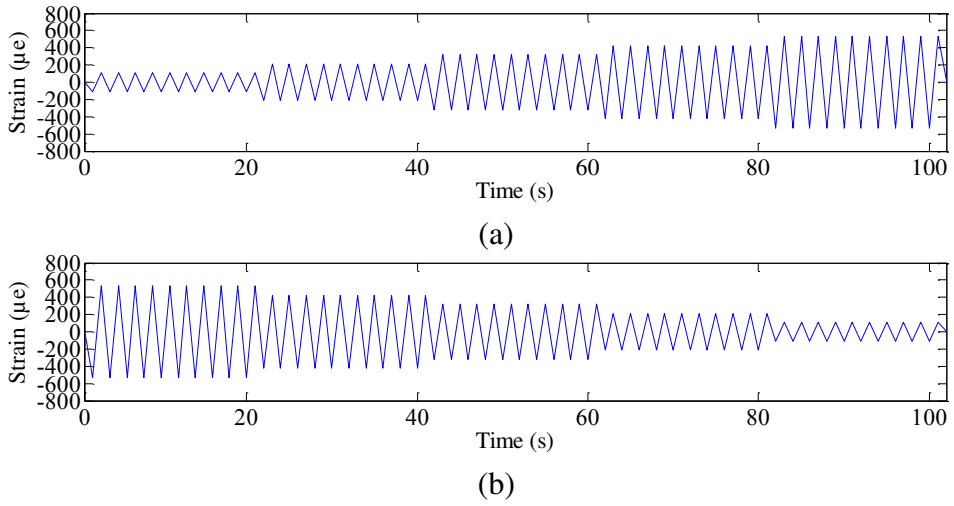

Figure 3.18 Loading arrangements for the highway strain signal: (a) low-high cycle, (b) high-low cycle

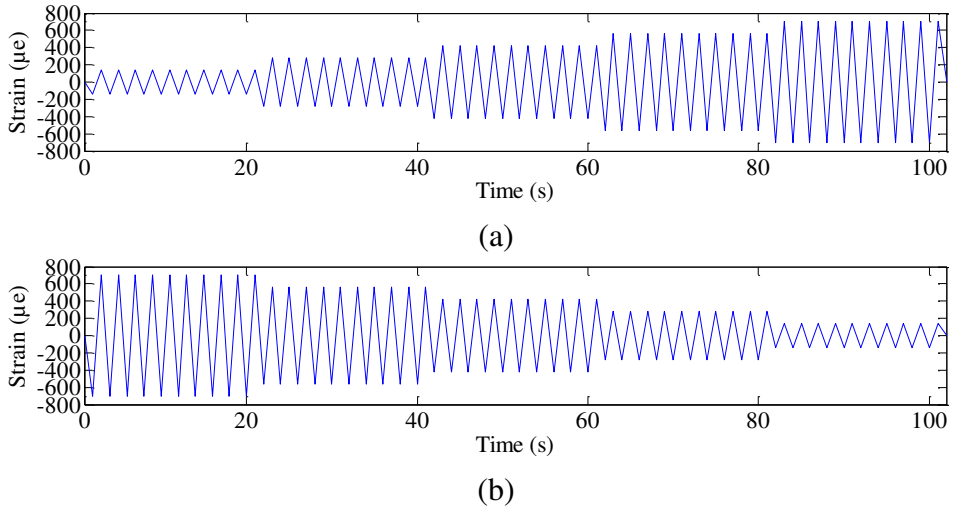

Figure 3.19 Loading arrangements for the urban strain signal: (a) low-high cycle, (b) high-low cycle

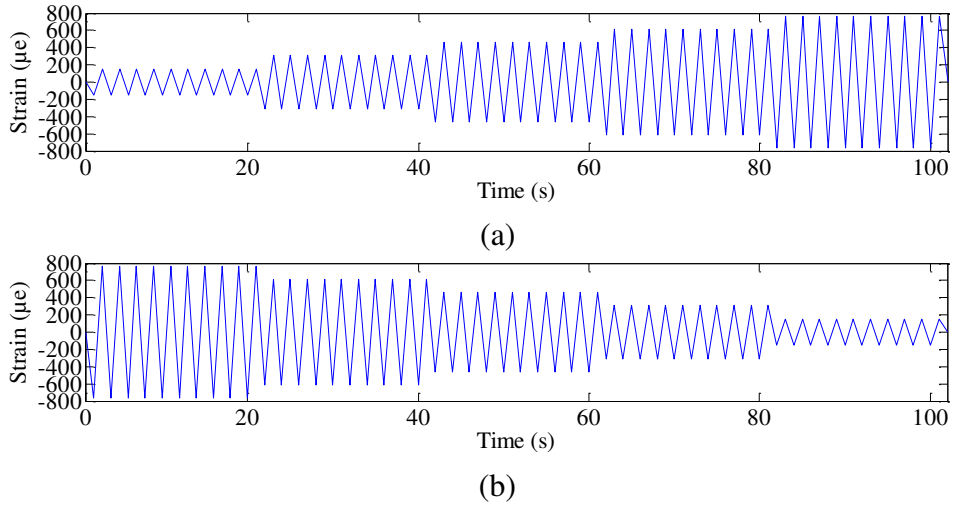

Figure 3.20 Loading arrangements for the rural strain signal: (a) low-high cycle, (b) high-low cycle

condition, since the minimum stress amplitude σ_{min} is equal to the minus of the maximum stress amplitude $-\sigma_{max}$ (Manson & Halford 2006; Rösler et al. 2007; Callister & Rethwisch 2012).

Fatigue damage for all the strain load arrangements was determined to ensure they had similar fatigue damage to the original strain signals. The strains in the block loading were converted into the stresses using the Ramberg-Osgood equation (Ramberg & Osgood 1943), as described in Equation (2.9). The material modulus of elasticity, the cyclic strain hardening exponent and the cyclic strength coefficient are provided in Table 3.3. Using Equation (2.7), the stresses could then be converted into the loads as the input for the fatigue testing machine. The cross-sectional area for the equation was 18 mm coming from the area of gauge length of the specimen. Using block loading, six uni-axial fatigue tests were performed at different strain amplitudes, where compression - tension tests (ASTM E606-92 1998) and frequency at 2 Hz (Williams et al. 2003) were selected. Frequencies less than 5 Hz are recommended since stable load amplitudes cannot be maintained at higher frequencies.

For validating the fatigue life of the actual, simulated and edited strain signals and for showing the time reduced from using the edited strain signals, the strain signals were converted into the loads as well, as performed in the block method. Twelve complexity reversed VAL fatigue tests were performed, where frequency at

100 Hz (Hosoi et al. 2011; Schaumann & Steppeler 2013) were selected. Increasing the frequency was to accelerate the tests. There is no effect of higher frequency on crack initiation (Hosoi et al. 2011; Kovacs et al. 2013). The influence of frequency on a fatigue testing result is often considered minimal for frequencies reaching 1,000 Hz (Schaumann & Steppeler 2013). In addition, it did not give any effect to the objective of the study since all the strain signals were tested at the same frequency. Based on the developed methods in the study, the simulated strain signals could be generated. Some validation procedures, either simulations or experiments, were performed to ensure that the simulated strain signals are as realistic as possible compared to the actual strain signals. Since much strain signals utilised in the study, the strain signals were labeled for simplicity.

3.4 SIGNAL LABELING

The actual strain signals collected on the highway, urban and rural road surfaces were called S1, S2 and S3, respectively. S1, S2 and S3 were then transformed into acceleration signals, called A1, A2 and A3, respectively. The simulated strain signals resulted from the MBD simulation based on A1, A2 and A3 were called S4, S5 and S6, respectively. Using the developed FDE algorithm, S1, S2, S3, S4, S5 and S6 were extracted and then formed edited strain signals, called S7, S8, S9, S10, S11 and S12, respectively. Finally, all the strain signals were the input in the fatigue testing machine in order to determine their fatigue life.

3.5 SUMMARY

An MBD simulation for generating strain signals was developed. Several strain signals were applied to attempt the suitability of the MBD simulation. The work began by designing a passenger car coil spring and performing the FEA to determine the area experiencing maximum stress caused by a static loading, namely the weight of the car and the passenger(s). Then, a strain signal acquisition was undertaken on three types of road surfaces, that provided the strains received by the coil spring in accordance with the road surface profiles. Based on the strain signals, acceleration signals were obtained usually used to describe the bumpiness of a road surface. The acceleration signals were then used as an input for the MBD simulation in order to generate simulated strain signals.

In order to validate the simulated strain signals, several procedures were performed. First, their fatigue damage was calculated and compared to the fatigue damage of the actual strain signals. Second, the actual and simulated strain signals were extracted based on the energy distribution. Lower energy amplitudes were categorised as non-damaging segments, while higher energy amplitudes were categorised as damaging segments. At the end of the process, the segments containing higher energy that contributed to more fatigue damaging events were retained and were then joined to produce an optimum mission signal length. Furthermore, statistical parameters, energy and fatigue damage for each extracted single segment were determined and scattered in order to identify the segment scattering patterns and observe the correlation. Statistical parameters and energy should be in-line with fatigue damage. Finally, the cyclic tests were performed to ensure that the simulated and edited strain signals could maintain the original characteristics. Four types of the strain signals, namely the original actual, original simulated, edited actual and edited simulated strain signals for each road surface were applied. If the difference of the validation was below 10 %, the resulted modified signal was close to the original signal; so as to keep the majority of fatigue damage, the vibration energy and the amplitude range. It means the MBD simulation performed was correct and could improve the reliability of the simulated strain signals. The results of methodology developed in this chapter will be discussed in the next chapter.

CHAPTER IV

RESULTS AND DISCUSSION

4.1 ACCELERATION TREND

4.1.1 Static Stress Distribution

The FEA was important because the focus of the study was on the maximum stress area since this area experiences the earliest failure. FEA results can be used to understand the behaviour of a component and also to improve its design. This is based on the assumption that there is no error or the component is correctly modelled, the environmental conditions are properly defined and FEA software itself performs correctly (Aykan & Celik 2009). Meshing of the coil spring is shown in Figure 4.1. A thousand well-shaped 4-noded tetrahedrons should provide good results (Sum et al. 2005). The differences between the results when using hexahedral and tetrahedral elements were very small (Aygül et al. 2012). The number of nodes was also considered because the calculation of the analysis is faster than more nodes to provide the same accurate result. Thus, based on the global seeds, a total of 3,710 elements using 10,999 nodes was generated.

The stress concentration experienced by the coil spring based on the static analysis is provided in colour contours in Figure 4.2. Areas with the highest stress concentration are represented by red, followed by orange, yellow, green and blue, respectively. Red areas had a maximum von Mises stress of 1.199 MPa occurred at node 3,463. Referring to Table 3.3, the maximum stress was very low compared to the yield strength, which was 1.487 GPa, indicating the force did not cause a failure to the component. Applying same force, a cyclic analysis was performed as well.

4.1.2 Cyclic Stress Distribution

The stress concentration experienced by the coil spring based on the cyclic analysis is provided in colour contours in Figure 4.3. Compared to the static analysis, there is no difference in terms of the stress distributions since both analyses applied same force, with a maximum von Mises stress of 1.199 MPa occurred at node 3,463. The stress in the spring could be determined by modelling the spring as a force screw. The central axis of this force screw was not parallel to the spring geometrical central axis, and changed position as the spring was compressed. The central axis of the force screw was coincident with the line of action of the spring force. The spring force resulted in torsional and shear force, added together on the inner side of the spring. If the radial sections rotate through an angle with respect to each other about spring axis, the inner side will be subjected to much higher stress than the outer side. The reason for this was the short length at the inner side of the component. Thus, the inner surface of the coil spring was the critical area. The result was similar to the analyses reported by Weiguo et al. (2011), Mulia et al. (2012), Abidin et al. (2013) and Zhu et al. (2014). Through the stress distributions, the parts receiving high loading were known. Thus, a strain sensor could be installed in the correct position.

Figure 4.1 Meshing of the coil spring

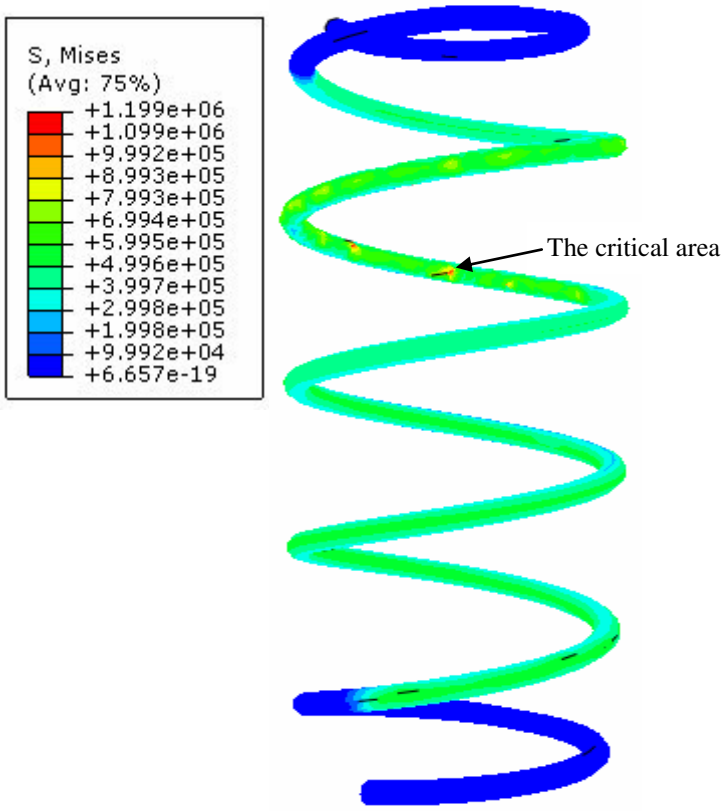

Figure 4.2 Stress distributions based on static analysis

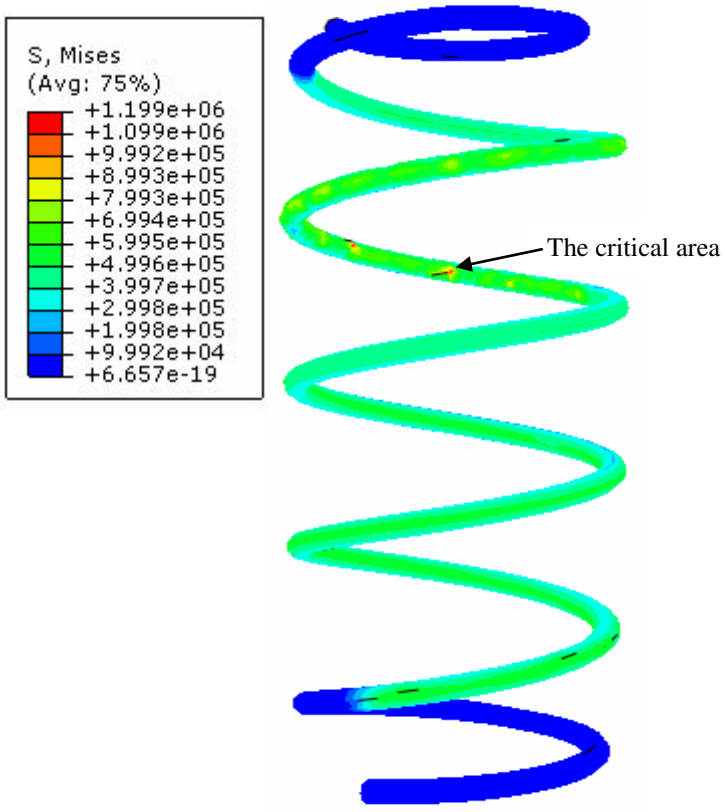

Figure 4.3 Stress distributions based on cyclic analysis

Referring to Figure 3.4a, however, the strain gauge was placed on the outer surface of the coil spring. The strain gauge could not be physically fixed at the most critical area because the inner surface was narrow, causing a higher damage probability for the sensor. It gave an additional reason about the importance to develop a simulated strain signal due to component design problems. The outer surface had a von Mises stress of 0.699 MPa, which was 42 % less than the maximum stress in the inner surface. Although the strain gauge was placed at a non-critical area, the measured strain signals could still be used for general representation. No matter where the strain gauge was placed, the pattern of the strain signals was similar because every point of the coil spring gives a similar response, with differences only at the amplitudes (Ismail 2010).

4.1.3 Actual Strain Signal

The strain signal acquistion was performed by placing a strain gauge at the coil spring and driving the car on various road surfaces. The strain signals produced by the strain gauge were a VAL because the component actually experienced various amplitudes. The total recorded length was each 120 seconds for 60,000 data points, as shown in Figure 4.4, which were sufficient for observing fatigue-based strain signal behaviour and evaluating fatigue life. The highway strain signal, called S1, provided the lowest amplitude range, which was between -188.9 με and 506.3 με. Higher amplitude range could be seen in the urban strain signal, called S2, distributed between -805.3 με and 729.6 με. However, the rural strain signal, called S3, had the highest amplitude range, which was between -1,365 με and 871.2 με. The rural road gave higher amplitudes than the highway and urban roads because its surface was uneven. Differences of the strain amplitude range could be correlated to the road surface profiles.

Based on the statistics listed in Table 4.1, all the strain signals had a non-zero-mean value. S1 and S3 were tensile since they had a positive mean value, which was 77 με and 35.6 με, respectively, while S2 was compressive since it had a negative mean value of -48 με. Due to the rural road having a rough surface containing higher amplitudes, S3 has the highest SD, which was 190.3 με, showing that the strains were distributed far from the mean value. S3 also gave the highest r.m.s., which was

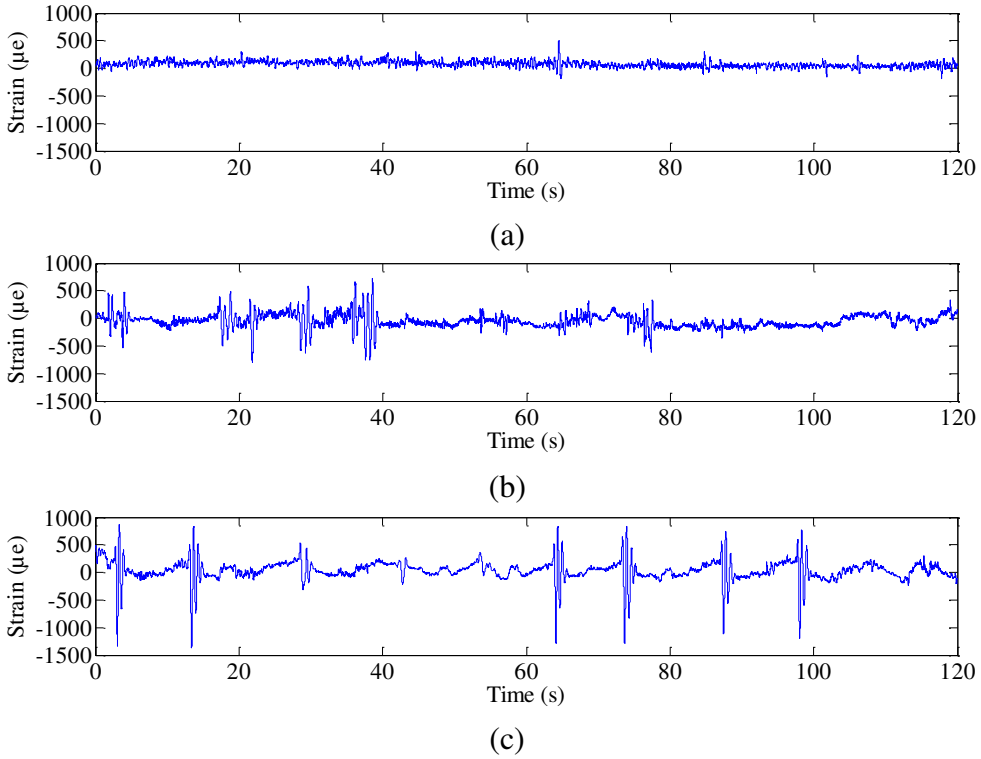

Figure 4.4 Time history plots of the actual strain signals: (a) S1-highway, (b) S2-urban, (c) S3-rural

Table 4.1 Statistics for the actual strain signals collected during the measurement

Properties	S1	S2	S3
Mean (με)	77.0	-48.0	35.6
SD (με)	54.1	132.8	190.3
r.m.s. (με)	94.1	141.2	193.6
Kurtosis	6.0	8.3	16.5

193.6 με, indicating that the strain signal measured on the rural road gave higher vibration energy compared to other roads because it had an uneven road surface. A higher r.m.s. indicated a higher energy content (Wang et al. 2012a), which in turn indicated higher fatigue damage (Kihm & Delaux 2013) in the strain signal. Differences of SD and r.m.s. for each strain signal were influenced by the amplitude ranges.

Peaks reveal higher fatigue damage, suggesting that a higher kurtosis indicates the random pattern of a signal contributing to higher fatigue damage (John & Phillip 2012). Kurtosis for S1, S2 and S3 was 6, 8.3 and 16.5, respectively. Thus, all the strain signals could be categorised as non-stationary behaviour because of their

kurtosis were greater than 3.0 (Kihm & Delaux 2013; Chen 2014). Signals classified as a non-stationary mostly reflect changes in the mean value and contain segments with sharp increases in peak values, as shown in Figure 4.4. During driving at a constant speed, excited vibration is stationary, while if the car is driven at a non-constant speed, excited vibration is non-stationary (Zhang et al. 2002).

The parameters listed in Table 3.3 were taken to be the product of strain amplitudes in order to determine fatigue damage. Since a structure has fewer loads at a single stress or strain level, fatigue damage is derived from the number of cycles to failure. Based on the results listed in Table 4.2, the number of cycles for S1, S2 and S3 was 10,921, 10,070 and 10,019, respectively. Since S3 gave the highest strain amplitude contributing to the highest stress at the coil spring, which can be seen in Figure 4.4, and had the highest statistical parameters, as listed in Table 4.1, the strain signal was found to have the highest fatigue damage, which was 1.10×10^{-2}, 1.08×10^{-2} and 1.05×10^{-2} damage per block for the Coffin-Manson, Morrow and SWT models, respectively.

Table 4.2 Number of cycles, fatigue damage and fatigue lives for one block for the actual strain signals collected during the measurement

Properties		**S1**	**S2**	**S3**
Number of cycles		10,921	10,070	10,019
Fatigue damage	Coffin-Manson	3.74×10^{-6}	2.52×10^{-3}	1.10×10^{-2}
(damage per block)	Morrow	1.39×10^{-5}	2.40×10^{-3}	1.08×10^{-2}
	SWT	2.09×10^{-5}	2.32×10^{-3}	1.05×10^{-2}
Fatigue lives	Coffin-Manson	267,100	397	91
(reversals of blocks)	Morrow	72,040	417	92
	SWT	47,800	430	95

Findings indicated that the rural road surface contributed to stronger vibration to the coil spring since the road was uneven; meanwhile the highway road gave the lowest vibration since it had a smooth surface. Fatigue damage increases with the acceleration subjected to the component that may lead to fracture. Comparing the fatigue damage, the differences between each model were small. This was because the strain signals had mean values that were almost zero, and thus they were less influenced by the effect of the mean stress in the cycles. These results also show that the strain signals with higher statistical values generally denoted higher fatigue

damage. It meant fatigue damage had a correlation with statistical parameters. Thus, the statistical parameter calculations in a fatigue signal are important for reviewing signal characteristics.

Since S3 gave the highest fatigue damage, the strain signal also provided the shortest fatigue life, which was only 91, 92 and 95 reversals of blocks for the Coffin-Manson, Morrow and SWT models, respectively. It indicated that the rural road surface also provided the shortest useful life compared to the urban and highway roads, since the road had a rough surface. Holes, bumps, turns, brakes, accelerations, speed changes and the effects of an uneven patch of tars on a road surface are examples of a non-stationary vibration and are factors that cause higher strains. These features support the potential for higher fatigue damage. After analysing more than 3,000 repaired cars, Roman et al. (2014) concluded that automotive suspension components must be replaced quite early, after about five years or with a travelling distance of 73,500 km. According to data of the Ministry of Transport of United Kingdom, suspension components recorded a high fault, which was 13.18 % of 24.2 million vehicle tests (Hamed et al. 2014).

The SAESUS strain signal, measured from a lower suspension arm, provided an amplitude range between -999 με and 345 με, while the SAEBKT strain signal, collected at a bracket, was distributed between -999 με and 738 με, and the SAETRN strain signal, measured from a transmission, had an amplitude range between -69 με and 100 με. From the statistics listed in Table 4.3, the SAESUS and SAEBKT strain signals were compressive with a mean value of -206.6 με and -52 με, respectively, while the SAETRN strain signal was tensile with a mean value of 73.4 με. Since it had the highest amplitude range, the SAEBKT strain signal was the farthest distributed strain from the mean value, with an SD of 223.1 με.

Table 4.3 Statistics for the SAE strain signals

Properties	**SAESUS**	**SAEBKT**	**SAETRN**
Mean (με)	-206.6	-52.0	73.4
SD (με)	134.6	223.1	14.5
r.m.s. (με)	246.6	229.1	74.8
Kurtosis	4.3	2.7	26.2

The SAESUS strain signal gave the highest vibration energy since it contained bumps with an r.m.s. of 246.6 με. However, since the SAETRN strain signal contains sharp segments, it gave the highest kurtosis value, which was 26.2, followed by the SAESUS and SAEBKT strain signals with of 4.3 and 2.7, respectively. Thus, the SAEBKT, SAESUS and SAETRN strain signals could be categorised as stationary, mildly non-stationary and heavily non-stationary, respectively. The SAEBKT strain signal had a kurtosis below 3.0 categorised as stationary strain signal, the SAESUS strain signal had short periods of changed statistics due to the presence of transient behaviour, while the SAETRN strain signal had transient events over a large interval of the time history.

In Table 4.4, the number of cycles for the SAESUS, SAEBKT and SAETRN strain signals was 1,253, 2,968 and 2,200, respectively. Since the SAEBKT strain signal had the highest amplitude range, it gave the highest fatigue damage, which was 5.28×10^{-2}, 5.03×10^{-2} and 4.89×10^{-2} damage per block for the Coffin-Manson, Morrow and SWT models, respectively. Since the SAEBKT strain signal had the highest fatigue damage, it gave the fatigue life of 19 reversals of blocks for the Coffin-Manson model and 20 reversals of blocks for the Morrow and SWT models. The value of the SAEBKT strain signal was measured at a bumpy surface containing higher amplitudes accelerating fatigue failure compared to the values given by the SAESUS and SAETRN strain signals. Furthermore, together with the measured strain signals called S1, S2 and S3, the SAE strain signals were the input for observing vibration responses.

Table 4.4 Number of cycles, fatigue damage and fatigue lives for one block for the SAE strain signals

Properties		**SAESUS**	**SAEBKT**	**SAETRN**
Number of cycles		1,253	2,968	2,200
Fatigue damage	Coffin-Manson	2.03×10^{-3}	5.28×10^{-2}	4.57×10^{-7}
(damage per block)	Morrow	1.40×10^{-3}	5.03×10^{-2}	8.68×10^{-7}
	SWT	1.08×10^{-3}	4.89×10^{-2}	1.56×10^{-6}
Fatigue lives	Coffin-Manson	492	19	2,188,000
(reversals of blocks)	Morrow	713	20	1,152,000
	SWT	929	20	640,900

4.1.4 Vibration Response

The measurement of an acceleration signal is required for a variety of purposes. In this part, acceleration trends were investigated in order to observe the effect of the road surfaces to the coil spring. Vibration responses in the form of accelerations at the coil spring were determined based on the actual strain signals. It is an interesting fact that a lot of random vibrations that occur should have a Gaussian distribution. Accelerations occur around a fixed point and have a zero-mean over time (Wijker 2009), such as measured at a bearing (Guo et al. 2012; Wang et al. 2013b; Maraini & Nataraj 2014), wind turbine (Jiang et al. 2011), vehicle suspension system (Goga & Kľúčik 2012; Wang et al. 2012b), jacket-type platform (Li et al. 2012), shaker system (Kihm & Delaux 2013), rotor (Asnaashari & Sinha 2014), vehicle transmission gearbox (Liu et al. 2014) and ground motion (Sireteanu et al. 2014). Figure 4.5 shows an acceleration signal having a zero-mean value.

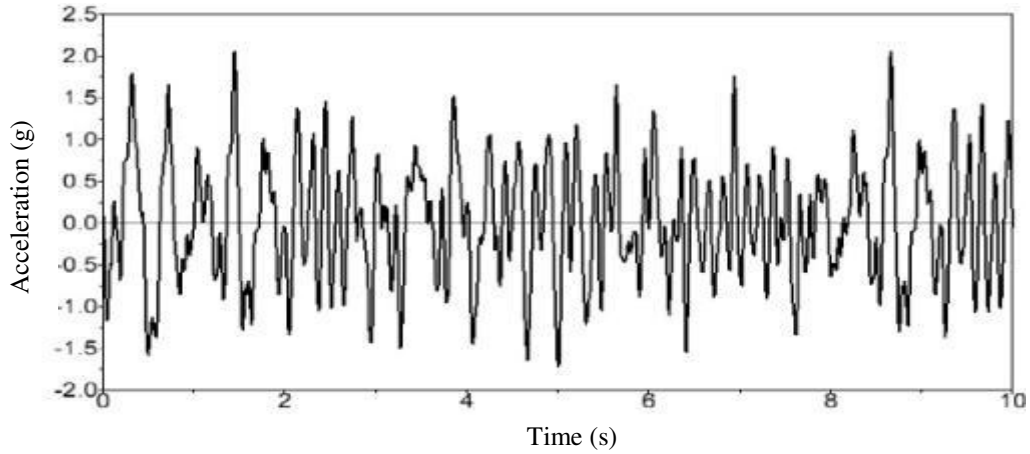

Figure 4.5 An acceleration signal measured at a coil spring
Source: Wang et al. 2012b

Thus, the strain signals were normalised by subtracting the strain ε with their own mean values $\bar{x}$, where:

$$\varepsilon_{\text{normalised}} = \varepsilon - \bar{x} \tag{4.1}$$

Using Equation (4.1), the strain signals with a zero-mean value were produced, as shown in Figures 4.6 to 4.7, for the measured and SAE strain signals, respectively. The strain signals with a zero-mean value were the input for the strain model developed in Section 3.1.3 in order to yield acceleration signals. Referring to Equation (3.6), the main inputs for the model were the strains, the damping coefficient, the spring stiffness, the mass, as well as the original diameter, and the acceleration responses could be observed. Since all the parameters were known, the model yielded the corresponding acceleration.

Trends of the acceleration for the highway, urban and rural strain signals are shown in Figure 4.8, and are called A1, A2 and A3, respectively, while for the SAESUS, SAEBKT and SAETRN strain signals shown in Figure 4.9 are called SAESUS, SAEBKT and SAETRN acceleration signals, respectively. Referring to Equation (3.6), the acceleration is parallel to the strain. The strain with higher amplitudes produced the acceleration with higher amplitudes as well. These were in line with the strain signals provided in Figures 4.4 and 2.23. For the measured strain-

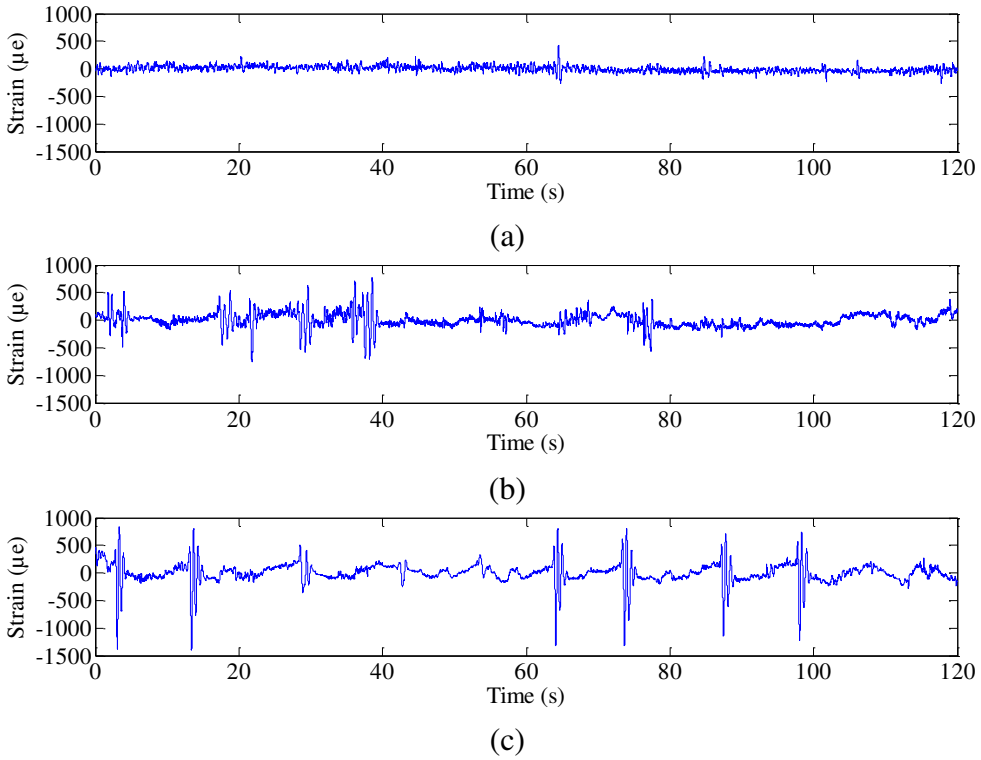

Figure 4.6 Normalisation of the measured strain signals: (a) S1-highway, (b) S2-urban, (c) S3-rural

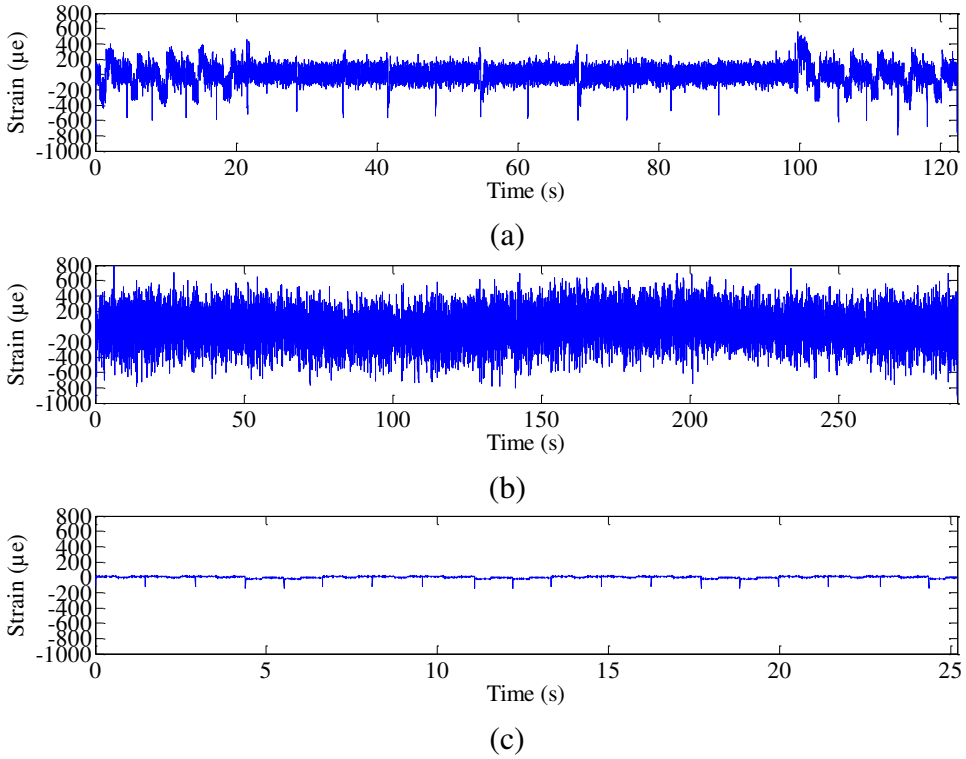

Figure 4.7 Normalisation of the SAE strain signals: (a) SAESUS, (b) SAEBKT, (c) SAETRN

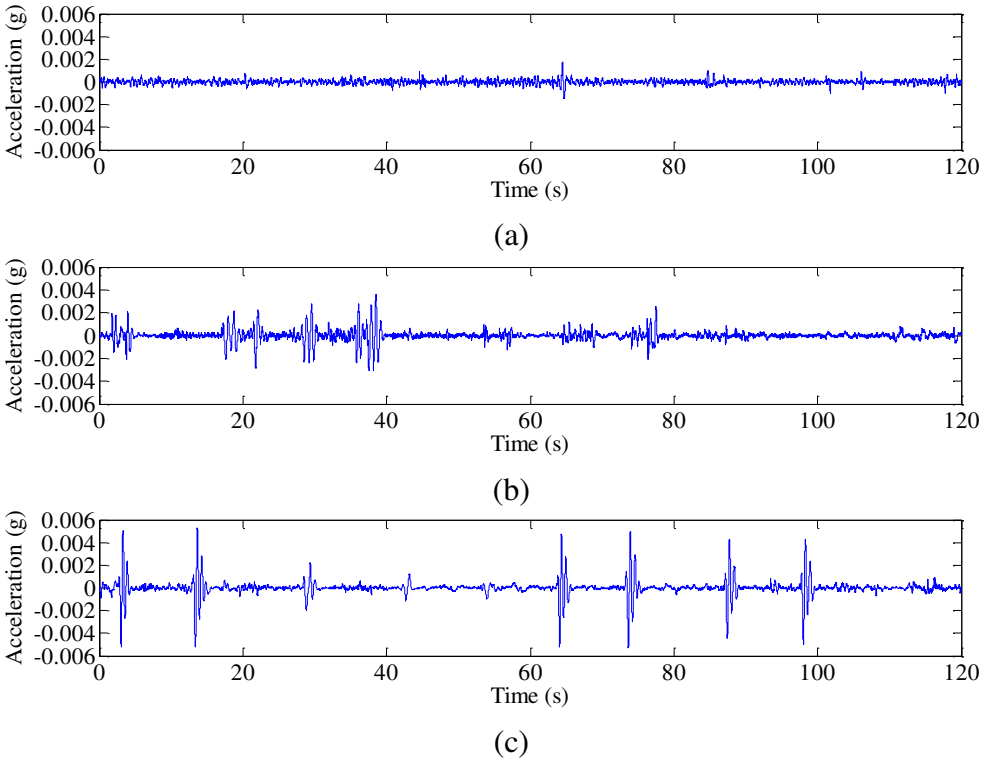

Figure 4.8 Time history plots of the measured strain-based acceleration signals: (a) A1-highway, (b) A2-urban, (c) A3-rural

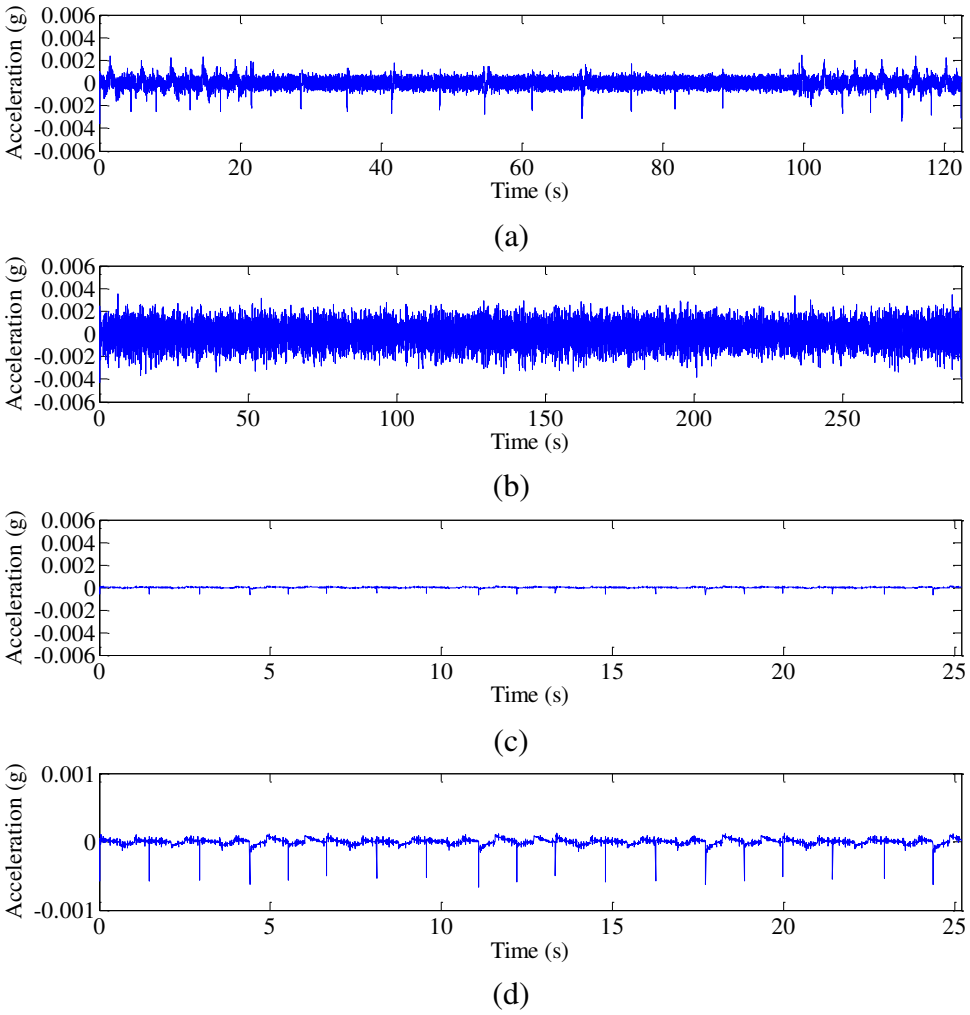

Figure 4.9 Time history plots of the SAE strain-based acceleration signals: (a) SAESUS, (b) SAEBKT, (c) SAETRN, (d) zoom in for SAETRN

based acceleration signals, A3 gave the highest amplitude, followed by A2 and A1. The accelerations for the rural road were distributed between -0.00529 g and 0.00525 g compared to the highway road, which were distributed between -0.00148 g and 0.00174 g, and the urban road, which were distributed between -0.00311 g and 0.00364 g. A3 provided high amplitudes that sometimes contained spikes when the tyre touched a pothole, bump or curb. The road surface conditions caused a higher loading rate to the car coil spring. For the SAE strain-based acceleration signals, the highest amplitude was the SAEBKT acceleration signal distributed between -0.00427 g and 0.00351 g, followed by the SAESUS acceleration signal distributed between -0.00357 g and 0.00242 g and the SAETRN acceleration signal distributed between -0.00066 g and 0.000128 g.

The rural and SAEBKT acceleration signals gave higher amplitudes than others did because they were produced from the strain signals measured on uneven surfaces. These indicated that the road surfaces gave higher vibration energy since they also had higher strain amplitude. It could be observed in the rural and SAEBKT strain signals having the highest fatigue damage. The validity of the acceleration signals will be discussed in Section 4.3.1. Furthermore, the acceleration signals were the input into the MBD simulation in order to yield subsequent strain signals.

4.2 SIMULATED STRAIN SIGNAL

4.2.1 Fatigue-Based Strain Signal

The fatigue-based strain signals were generated by utilising the acceleration model developed in Section 3.2.1 based on Equation (3.9). To run the MBD simulation, the accelerations that resulted from the previous strain model, the damping coefficient, the spring stiffness and the original diameter as well as the mass were the inputs. However, the simulated strain signals had a zero-mean value as well, as shown in Figure 4.10 for the highway, urban and rural strain signals called S4, S5 and S6, respectively, and Figure 4.11 for the SAESUS, SAEBKT and SAETRN strain signals called the simulated SAESUS, SAEBKT and SAETRN strain signals, respectively. Thus, the mean values were re-added to the strain signals in order to result in the strain signals with a non-zero-mean value. The time series of the simulated strain signals are shown in Figures 4.12 to 4.13. For the purpose of identifying their characteristics, the simulated strain signals were validated via comparisons to the actual strain signals.

4.2.2 Strain Signal Characteristics

Figures 4.14 to 4.15 plot the actual and simulated strain signals in one graph for the measured and SAE strain signals, respectively. Its purpose was to determine whether the simulated strain signals were actually similar in their actual characteristics. The plots reflected the high uniformity, especially for the measured strain signals, indicating that the probability of similarity between both the strain signals was big.

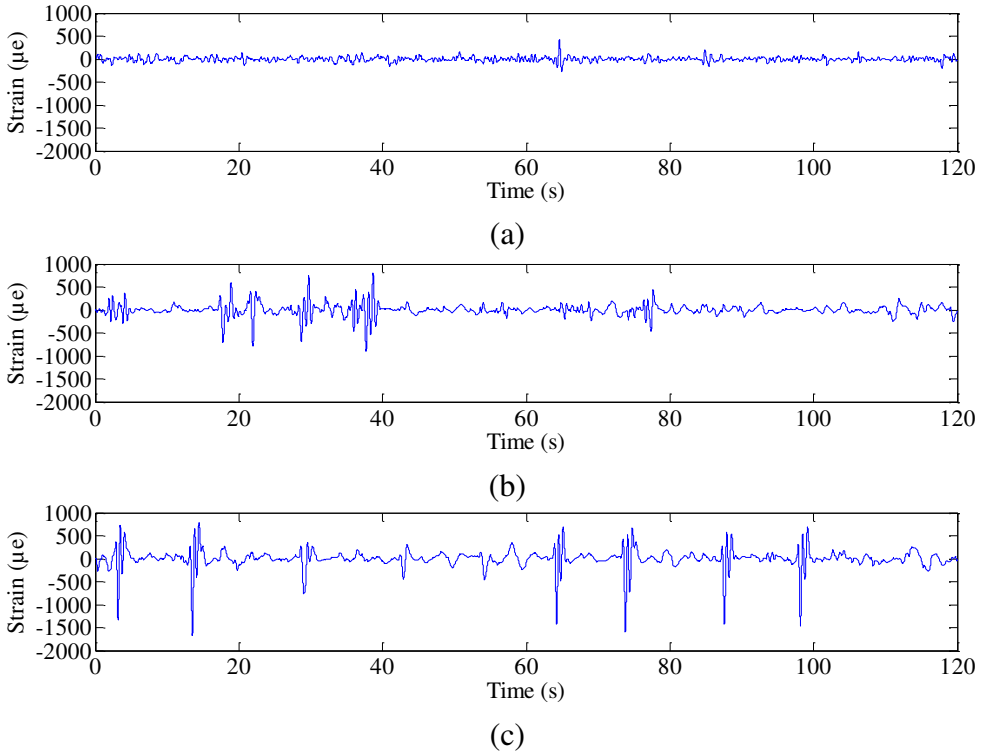

Figure 4.10 Normalisation of the measurement-based simulated strain signals: (a) S4-highway, (b) S5-urban, (c) S6-rural

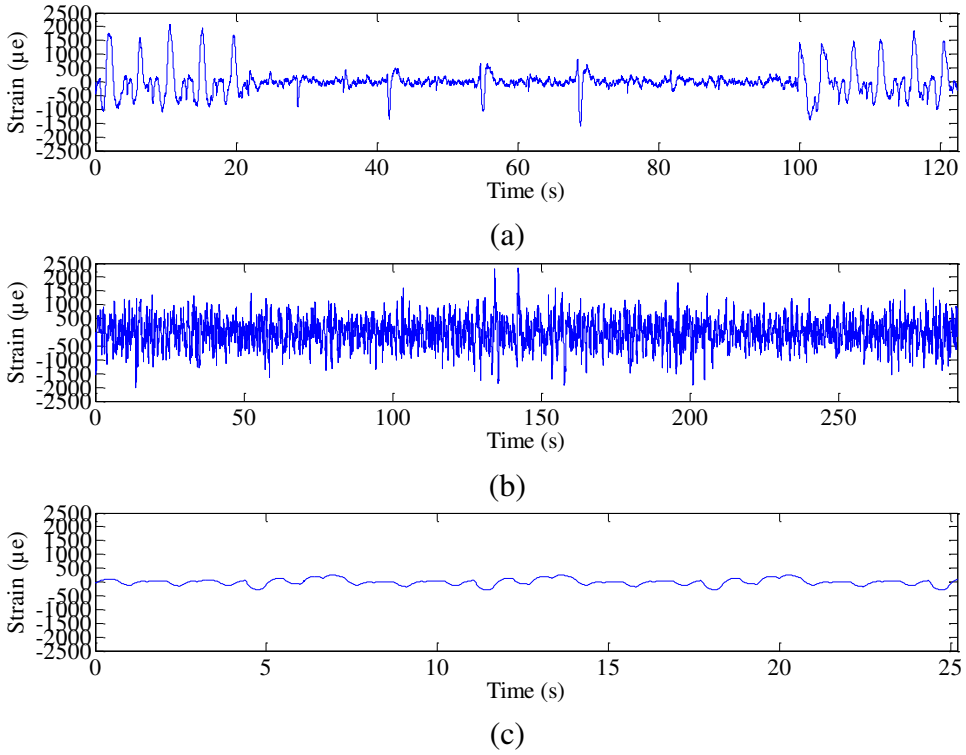

Figure 4.11 Normalisation of the SAE-based simulated strain signals: (a) SAESUS, (b) SAEBKT, (c) SAETRN

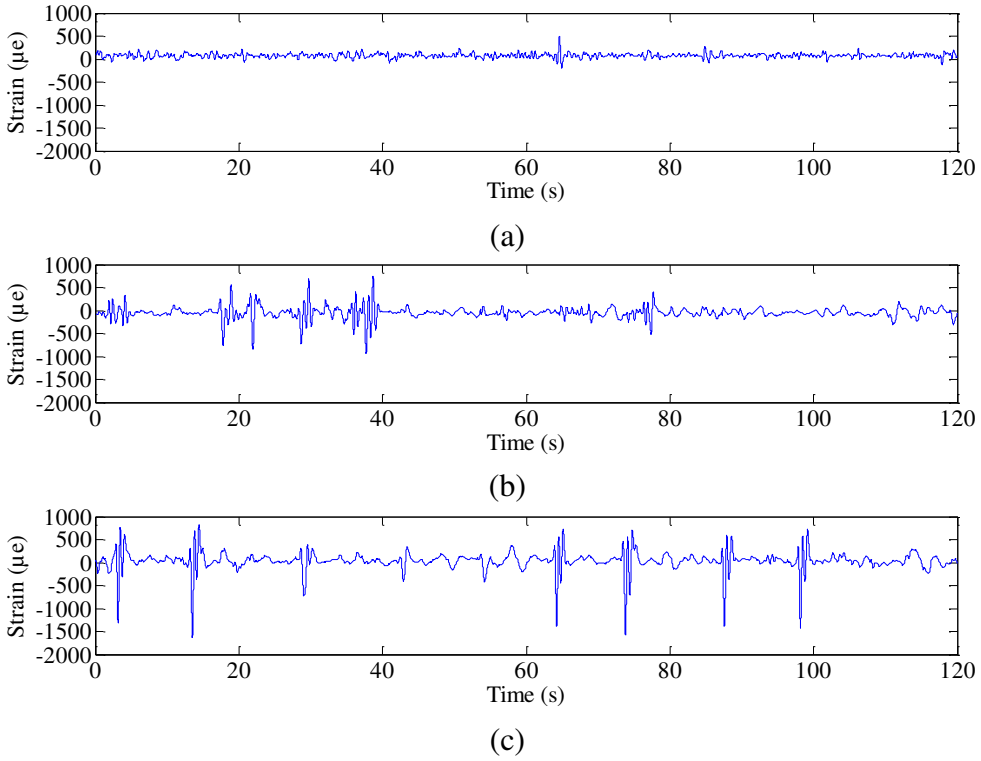

Figure 4.12 Measurement-based simulated strain signals: (a) S4-highway, (b) S5-urban, (c) S6-rural

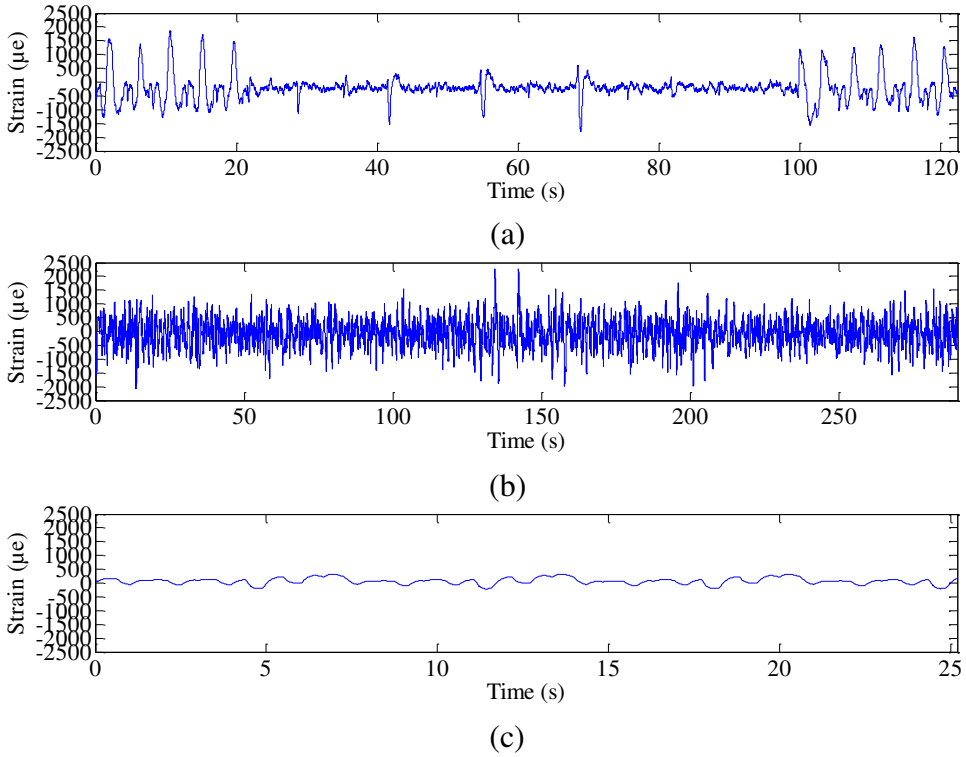

Figure 4.13 SAE-based simulated strain signals: (a) SAESUS, (b) SAEBKT, (c) SAETRN

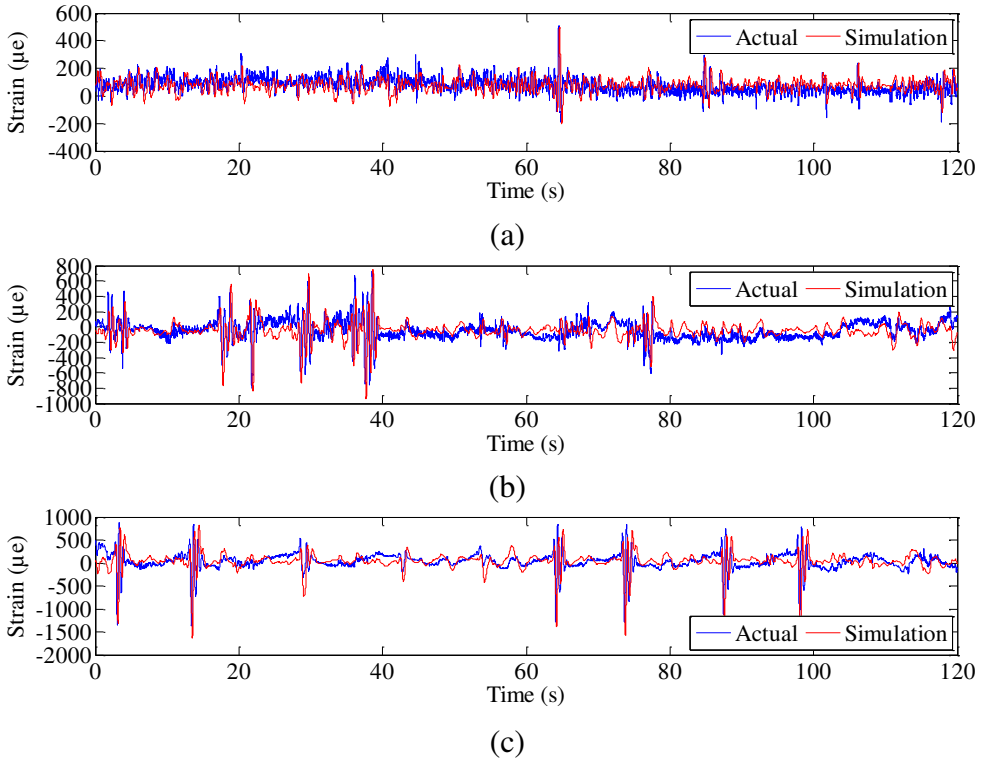

Figure 4.14 Comparisons of the measured strain signals: (a) highway, (b) urban, (c) rural

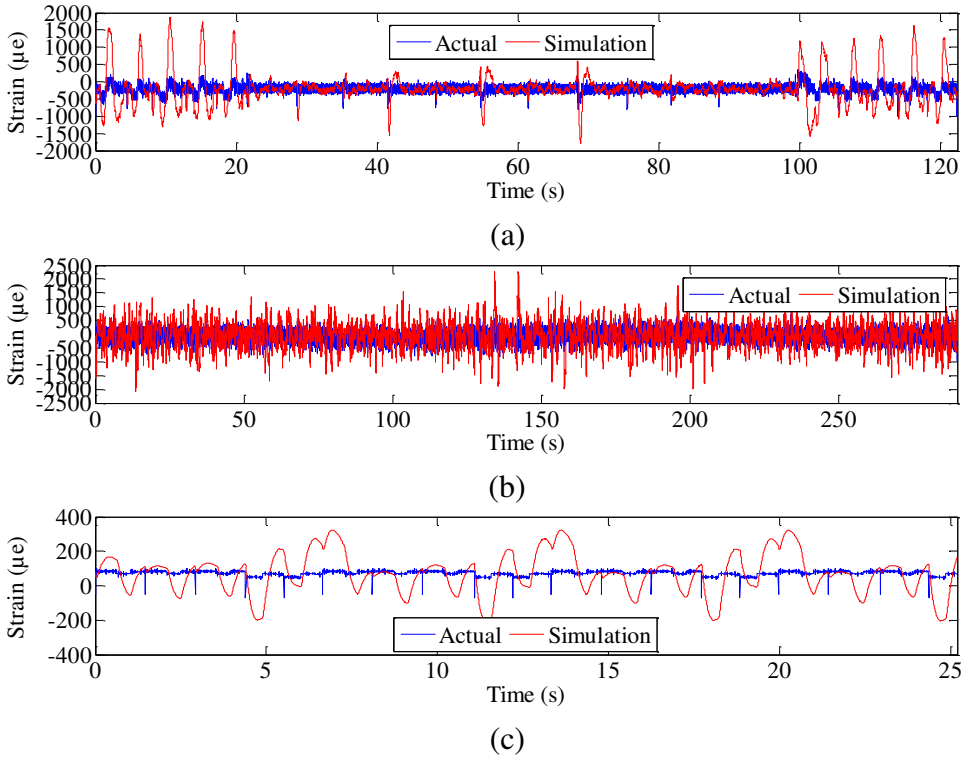

Figure 4.15 Comparisons of the SAE strain signals: (a) SAESUS, (b) SAEBKT, (c) SAETRN

The simulated strain signals, however, changed the actual amplitude ranges. This was because the equation of motion used to develop the simulated model being simplified, without considering external forces. The highway strain signal with the actual amplitude range between -188.9 με and 506.3 με changed to -200 με and 495.3 με in the simulated strain signal. The actual urban strain signal distributed between -805.3 με and 729.6 με became -938.4 με and 746.5 με after the simulation. For the rural strain signal, the actual amplitude range between -1,365 με and 871.2 με became -1,627 με and 815.4 με in the simulated strain signal.

A more significant change could be seen in the SAE strain signals. The actual SAESUS strain signal with the amplitude range between -999 με and 345 με changed to -1,797.1 με and 1,864 με in the simulated strain signal. The actual SAEBKT strain signal distributed between -999 με and 738 με became -2,079.4 με and 2,264.5 με in the simulated strain signal. For the actual SAETRN strain signal, the amplitude range between -69 με and 100 με became -208.4 με and 322.6 με in the simulated strain signal. Besides effect of the simplified simulated model, the simulation gave highly different responses to the SAE strain signals because the SAESUS, SAEBKT and SAETRN strain signals were collected from a lower suspension arm, bracket and transmission, respectively, whereas the simulation was developed for observing the coil spring behaviour.

Figures 4.16 to 4.17 present the box plots for the actual and simulated strain distributions, respectively. The box plots illustrate the average size and the spread of the strains, measured by the median. For the measured strain signals, the box plots show fairly symmetric distributions with a fairly equal spread. Since the bars appear to be fairly equal in length, it was likely that the equal variance assumption was satisfied. The box plots indicate that none of the strains includes outliers. This display indicated no significant differences in mean strength between the two strain signals. It also indicated that the simulation produced reasonably symmetric distributions of strength with similar variability or spread. For the SAE strain signals, the lines above and below the simulated box plots were suspiciously long, since the SAE strain signals were not collected at a coil spring.

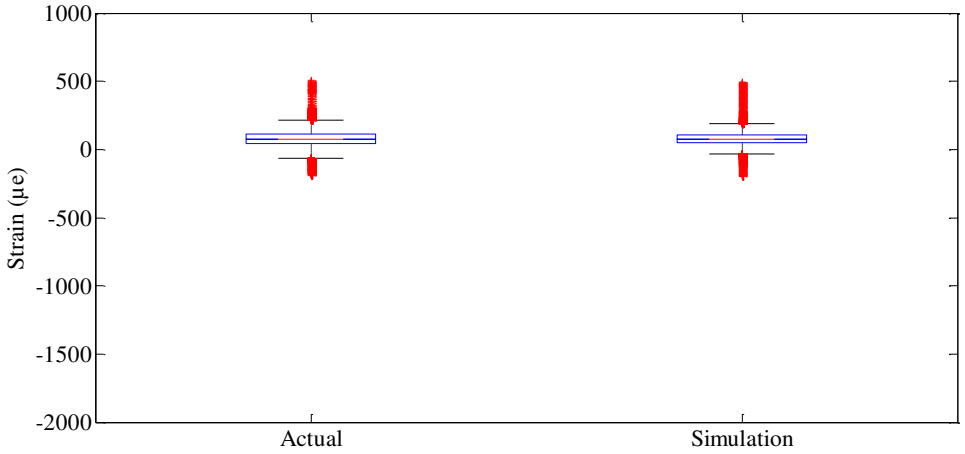

(a)

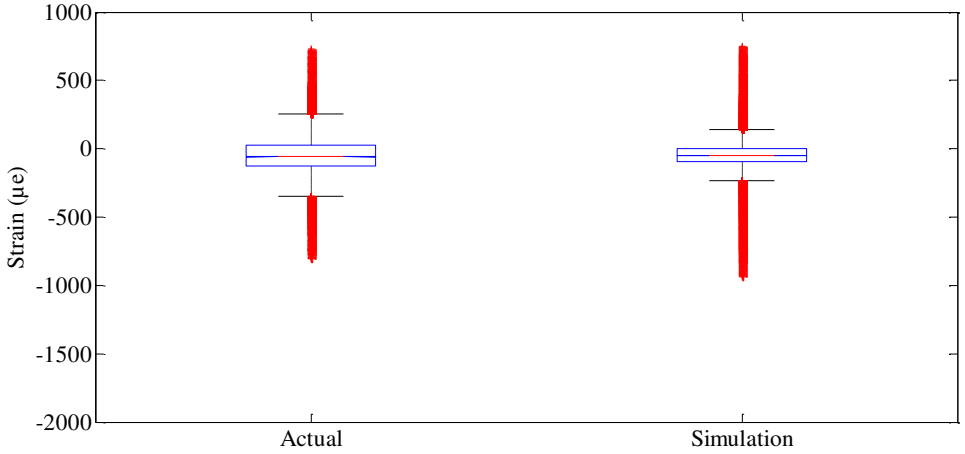

(b)

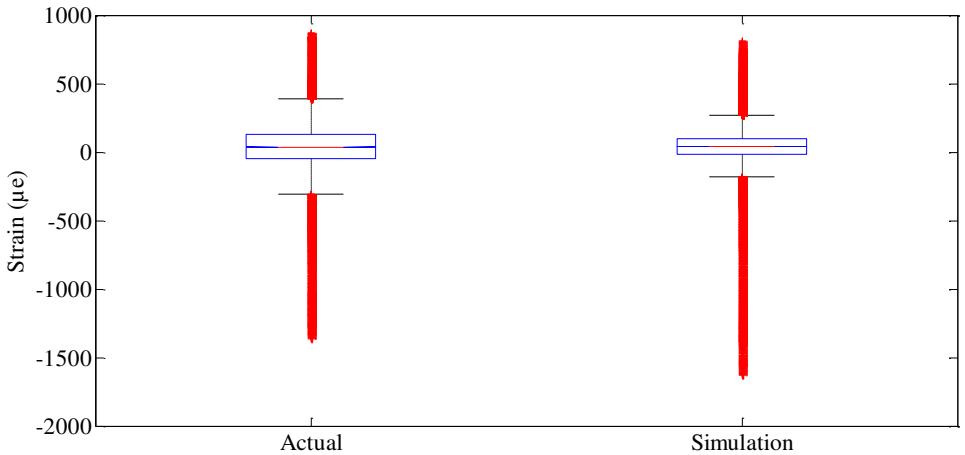

(c)

Figure 4.16 ANOVA for the measured strain signals: (a) highway, (b) urban, (c) rural

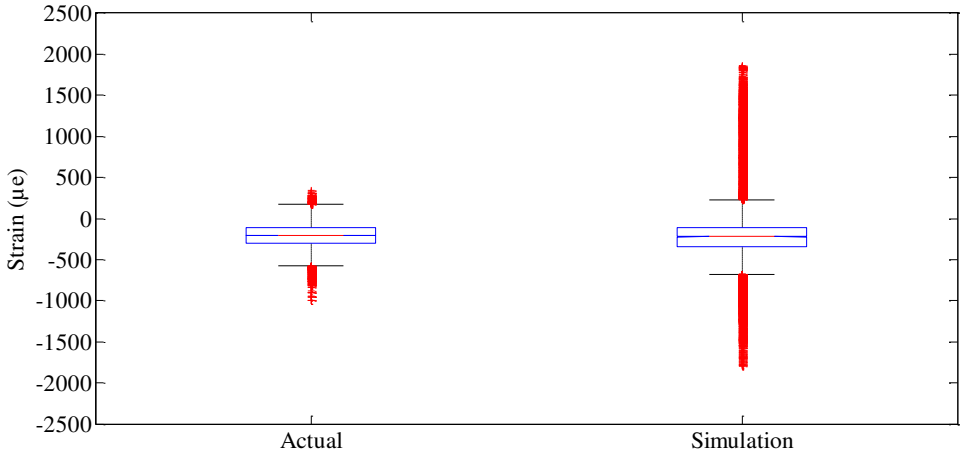

(a)

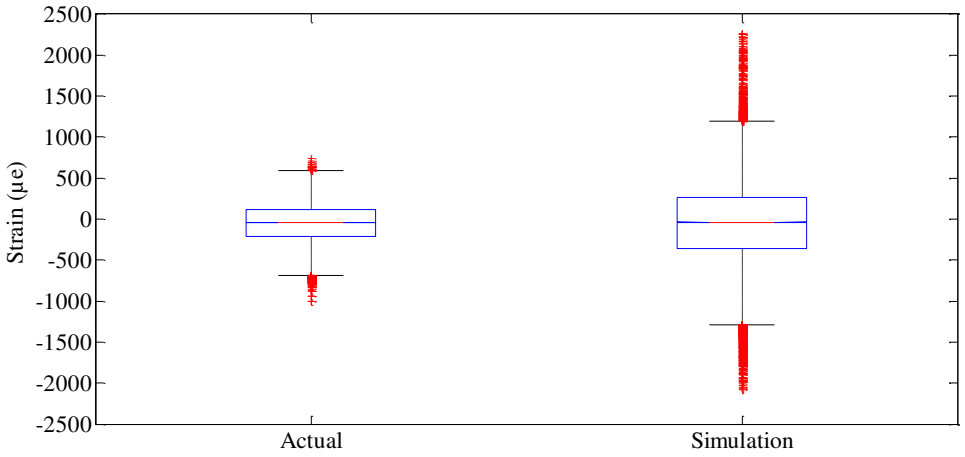

(b)

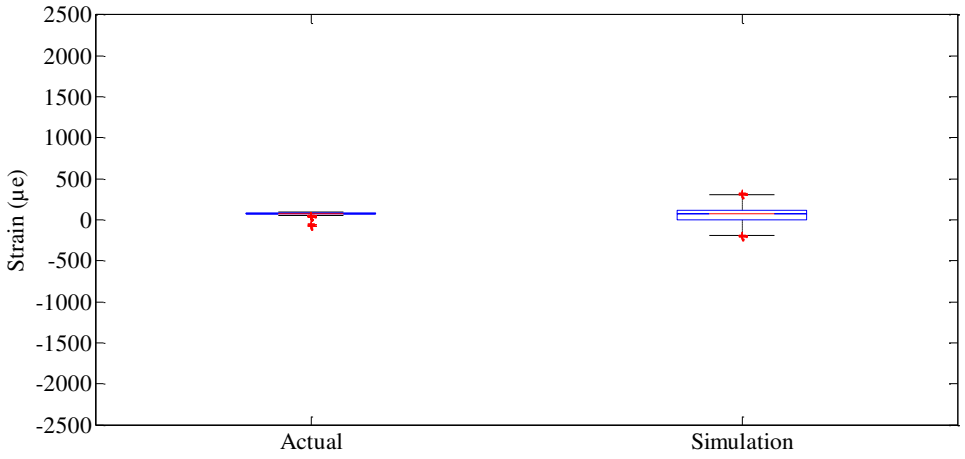

(c)

Figure 4.17 ANOVA for the SAE strain signals: (a) SAESUS, (b) SAEBKT, (c) SAETRN

The box plots suggested the size of the *p*-value and the F_{ANOVA}-statistic. For a significance level of 0.1, most of the strain signals gave a *p*-value more than the critical value, as shown in Table 4.5; except for the SAETRN strain signal, since transmission mechanism has a significant difference compared to the coil spring mechanism. A *p*-value more than 0.1 was considered to be not statistically significant. The large *p*-value indicated that the differences between the strain signal means were not significant and were highly consistent with the null hypothesis. It is therefore concluded that the null hypothesis was accepted, and the simulated strain signals conformed statistically to the actual strain signals since they had higher similarity.

Table 4.5 *p*-values for each strain signal

Strain signals	***p*-values**
Highway	0.6189
Urban	0.8458
Rural	0.4751
SAESUS	0.7010
SAEBKT	0.9188
SAETRN	0.0008

The F_{ANOVA}-value stated how far away the simulated strain signals were from the null hypothesis. Bars that overlap with one another suggested that the means for these strain signals were not significantly different, and the overall *F*-test would not be significant. Small differences in the centre lines of the boxes corresponded to large *p*-values and correspondingly small F_{ANOVA}-values, as listed in Table 4.6. A small F_{ANOVA}-value implied that the actual and simulated strain signals were relevant.

Table 4.6 F_{ANOVA}-values for each strain signal

Strain signals	$\boldsymbol{F_{ANOVA}}$**-value**
Highway	0.25
Urban	0.04
Rural	0.51
SAESUS	0.15
SAEBKT	0.01
SAETRN	11.35

In addition, it is known that from a sample strain signal, it cannot draw conclusions about the corresponding strain signal that are 100 % certain. This is depicted in Figures 4.18 to 4.19, providing analysis of fit with 90 % confidence interval for each strain signal. It was estimated that 90 % of the means in the strain distribution lie between 76.999 με and 77.001 με for the highway strain signal, -48.002 με and -47.998 με for the urban strain signal, 35.597 με and 35.603 με for the rural strain signal, -206.604 με and -206.596 με for the SAESUS strain signal, -52.003 με and -51.997 με for the SAEBKT strain signal, and 73.398 με and 73.402 με for the SAETRN strain signal - a very narrow range. Most the strains were concentrated in the range of lower and upper confidence limits, identifying a strong correlation between the actual and simulated strain signals. The area outside those bounds contained 10 % of the total area and was divided symmetrically in each tail. The area is often called the “critical region” (Hardy & Bryman 2009).

It is a fact that not all data follows the normal distribution. Referring to Tables 4.1 and 4.3, most of the strain signals had higher kurtosis. Higher kurtosis shows that the value is too high compared to the appropriate value in the Gaussian distribution, indicating that only a small proportion of data is closer to the mean value (Braccesi et al. 2009). Thus, the difference between the actual and simulated strain signals could be judged by observing the Weibull distribution. Therefore, the strain signals were scattered in order to observe their probability with the shape and scale parameters.

Generally, similar behaviour is shown amongst the strain signals, as presented in Figures 4.20 to 4.25. Similarity of the plots, especially for the measured strain signals, strengthened the previous findings that the simulation produced similar strain distribution patterns to the actual strain patterns. In the plots, however, it can be seen that the strain signals were high scattering or extremely distributed, especially for the SAETRN strain signal since transmission mechanism has a significant difference compared to the coil spring mechanism. The extreme distribution referred to the distribution of a large number of unbounded random observations (Souza et al. 2014). The CDF function found the area under a probability curve between two set endpoints, thus finding the probability of the event occurring in that range. Meanwhile, the PDF

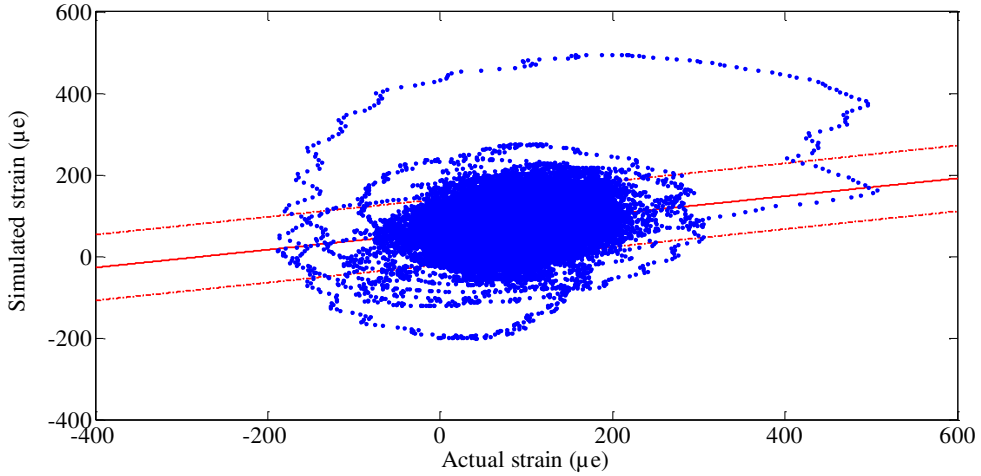

(a)

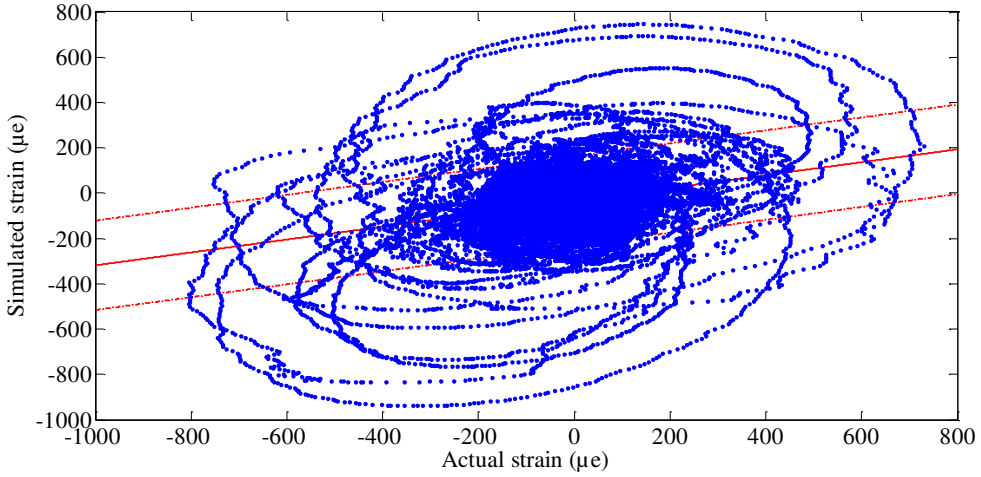

(b)

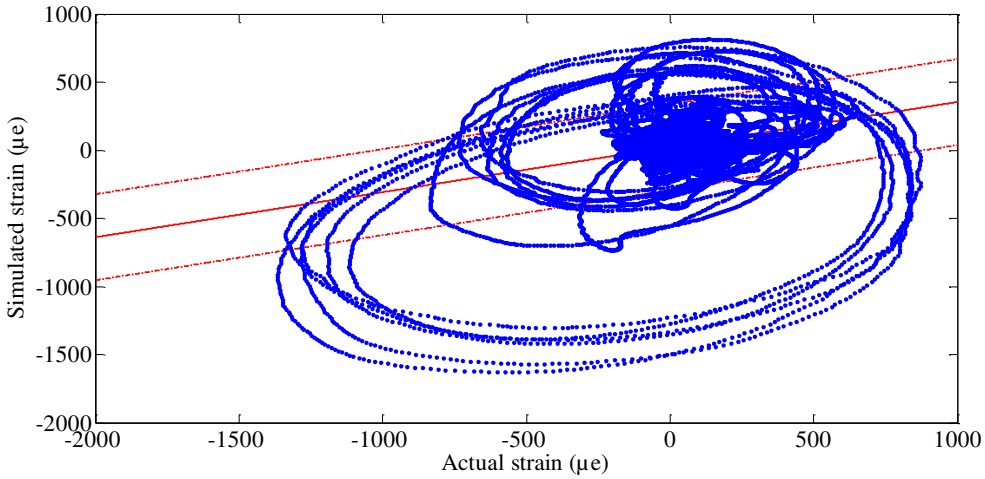

(c)

Figure 4.18 Strain distributions for the measured strain signals in the 90 % confidence interval: (a) highway, (b) urban, (c) rural

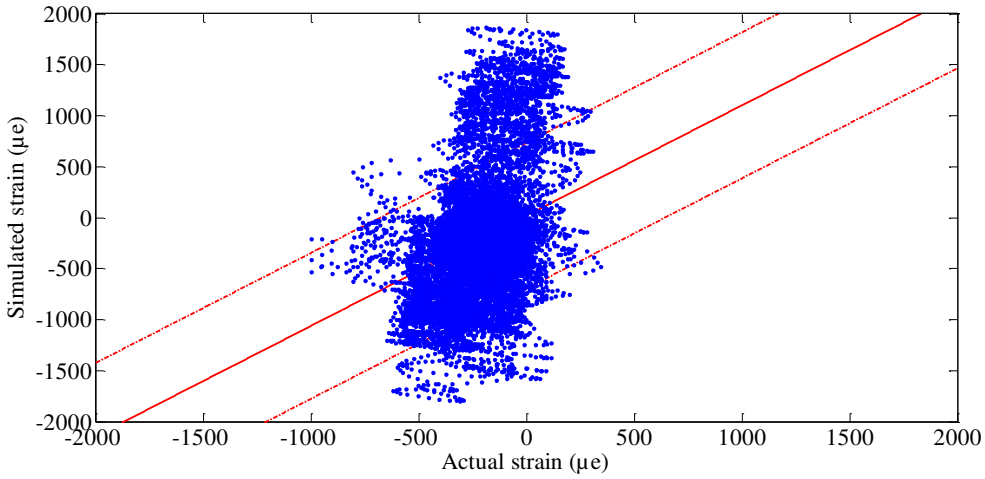

(a)

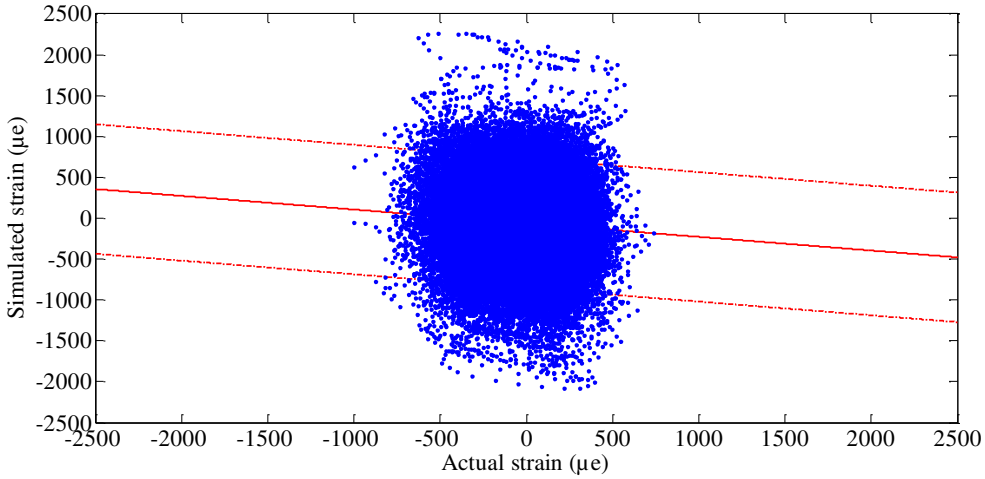

(b)

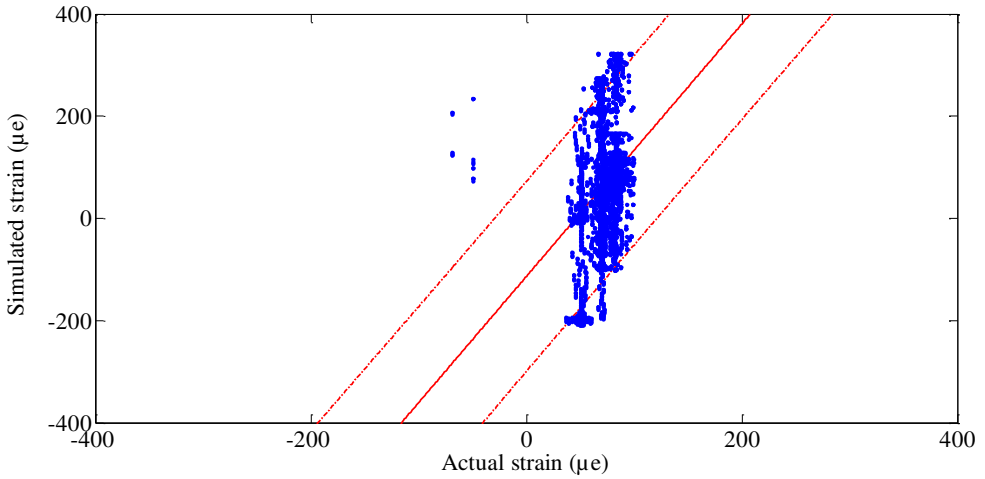

(c)

Figure 4.19 Strain distributions for the SAE strain signals in the 90 % confidence interval: (a) SAESUS, (b) SAEBKT, (c) SAETRN

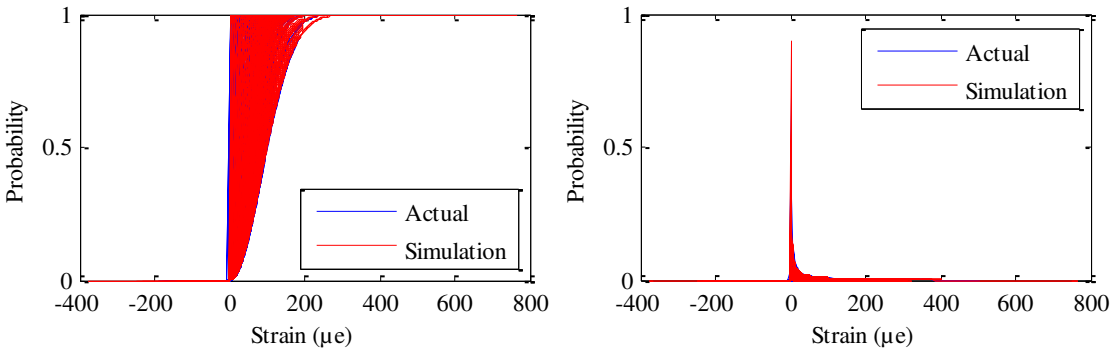

Figure 4.20 Probability plots of the Weibull distribution for the highway strain signal: (a) CDF, (b) PDF

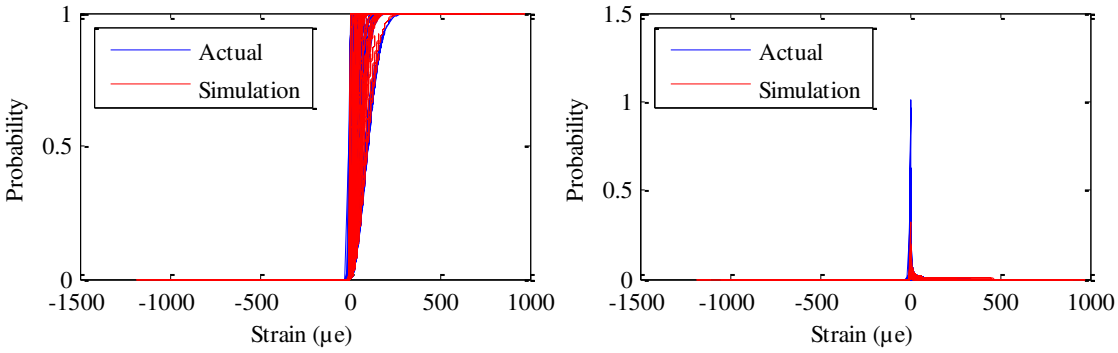

Figure 4.21 Probability plots of the Weibull distribution for the urban strain signal: (a) CDF, (b) PDF

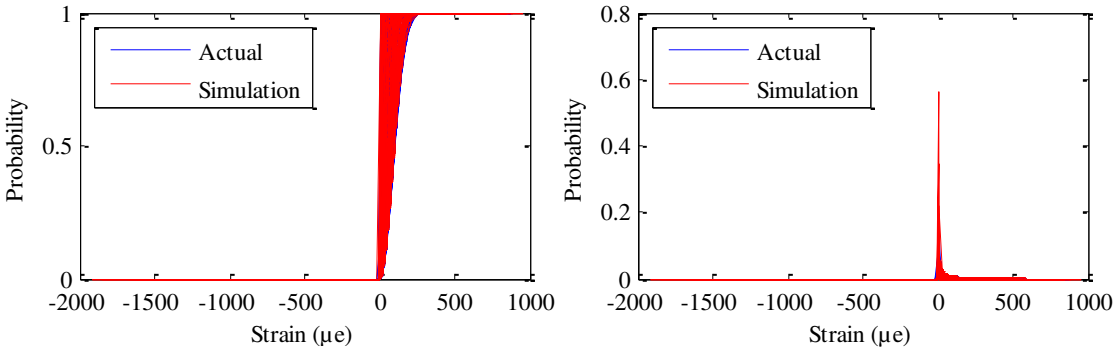

Figure 4.22 Probability plots of the Weibull distribution for the rural strain signal: (a) CDF, (b) PDF

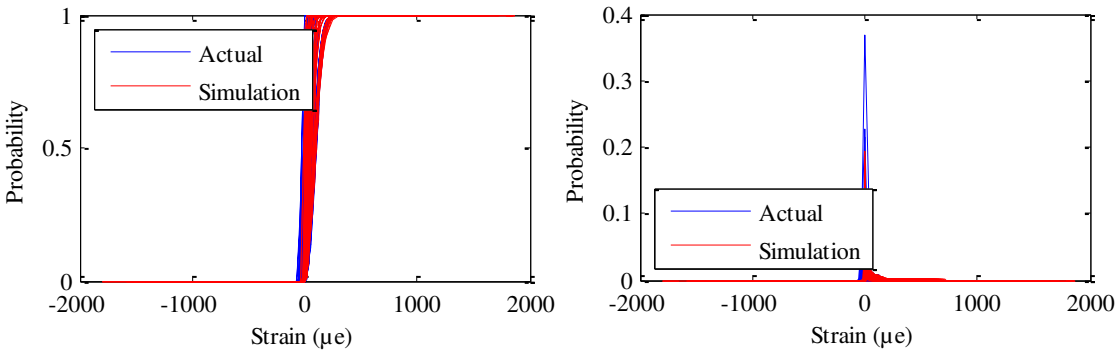

Figure 4.23 Probability plots of the Weibull distribution for the SAESUS strain signal: (a) CDF, (b) PDF

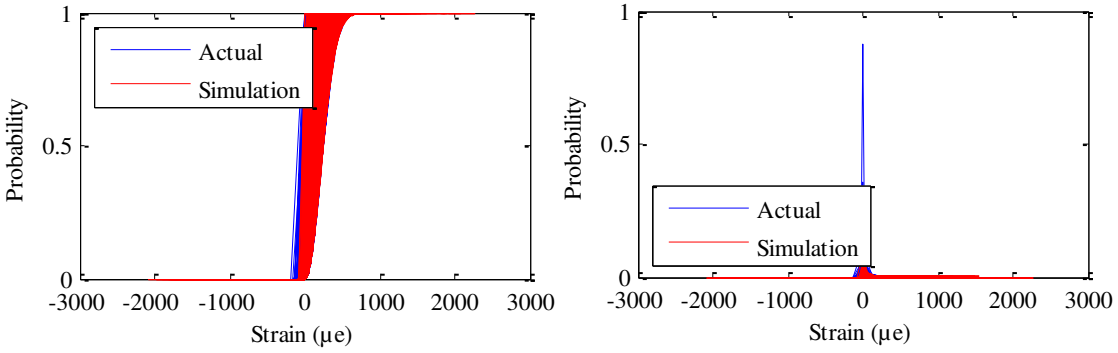

Figure 4.24 Probability plots of the Weibull distribution for the SAEBKT strain signal: (a) CDF, (b) PDF

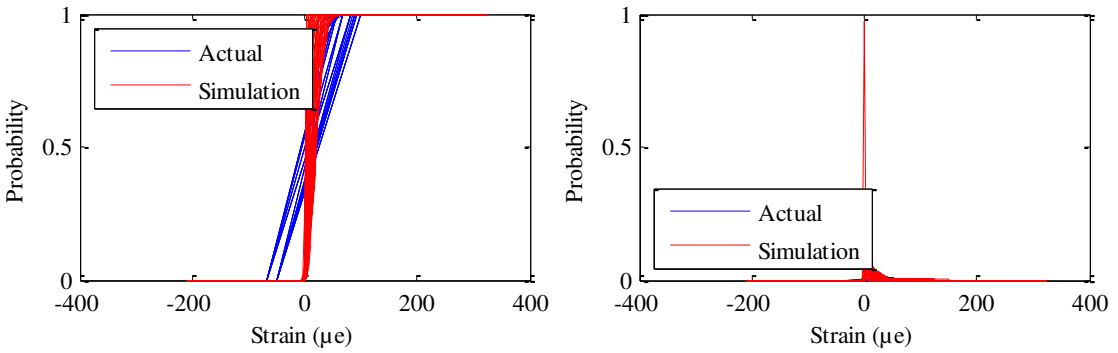

Figure 4.25 Probability plots of the Weibull distribution for the SAETRN strain signal: (a) CDF, (b) PDF

function only found the probability for a single specific outcome, and thus can only be used for distributions that are not continuous. In the PDF plots for the highway, SAESUS and SAETRN strain signals, the distributions were skewed to the right, giving a mean value higher than SD. Meanwhile, for the urban, rural and SAEBKT strain signals, the PDF plots gave a distribution skewed to the left, indicating that mean values were lower than SD; which is a basic feature of large shape parameters (Jiang & Murthy 2011).

Table 4.7 lists the percentages of the statistical parameter differences between the actual and simulated strain signals. In the table, positive values denote an increase of statistics, while negative values denote a decrease of statistics. Except for kurtosis showing obvious changed of up to 66.4 %, indicating that the simulated strain signals were more random compared to the actual strain signals, other values for the measured strain signals were below 7 %. SD for the highway and urban strain signals decreased by 6.9 % and 5.3 %, respectively, indicating that the simulated highway and urban strain signals had lower amplitude ranges, while for the rural strain signal, SD increased to 6.1 % since it had higher amplitude range. Furthermore, r.m.s. also decreased for the highway and urban strain signals by 2.1 % and 4.7 %, respectively, influenced by the decreases of SD, indicates that the energy in the simulated strain signals decreased as well. An increase of 5.9 % in r.m.s. for the rural strain signal, as SD increases, indicates an increase of energy. The differences were because the equation of motion used to develop the simulated model being simplified. The differences of statistical parameters for the measured strain signals are summarised in Figure 4.26.

Meanwhile for the SAE strain signals shown in Figure 4.27, except for kurtosis that decreased by 88.7 % for the SAETRN strain signal, all other values increased. The kurtosis increases indicated that the simulated strain signals were more random compared to the actual strain signals. The SD increases reached 716.7 % indicating that the simulated strain signals had higher amplitude ranges. The increases in r.m.s., influenced by the increases of SD, indicated that the energy in the simulated strain signals increased as well. Besides effect of the simplified simulated model, higher statistical parameter differences for the SAE strain signals were because they were not collected at a coil spring. The accuracy of the simulated strain signals in terms of statistical parameters will be discussed in Section 4.3.2.

Table 4.7 Statistical differences between the actual and simulated strain signals

Strain signals	Actual			Simulation			Differences		
	SD (με)	r.m.s. (με)	Kurtosis	SD (με)	r.m.s. (με)	Kurtosis	SD (%)	r.m.s. (%)	Kurtosis (%)
Highway	54.1	94.1	6.0	50.4	92.1	8.5	-6.9	-2.1	42.4
Urban	132.8	141.2	8.3	125.8	134.6	13.8	-5.3	-4.7	66.4
Rural	190.3	193.6	16.5	202.0	204.9	22.9	6.1	5.9	39.4
SAESUS	134.6	246.6	4.3	458.4	502.3	7.2	240.5	103.7	66.1
SAEBKT	223.1	229.1	2.7	482.9	485.6	3.6	116.4	112.0	34.1
SAETRN	14.5	74.8	26.2	118.3	136.3	3.0	716.7	82.2	-88.7

Note: difference = (simulation - actual) / actual x 100 %

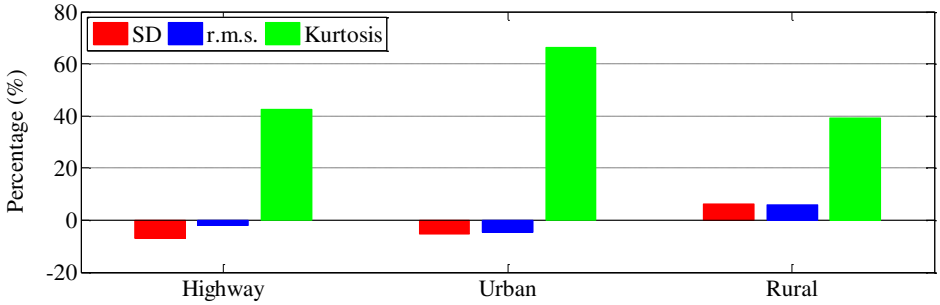

Figure 4.26 Percentage of the statistical parameter differences for the measured strain signals

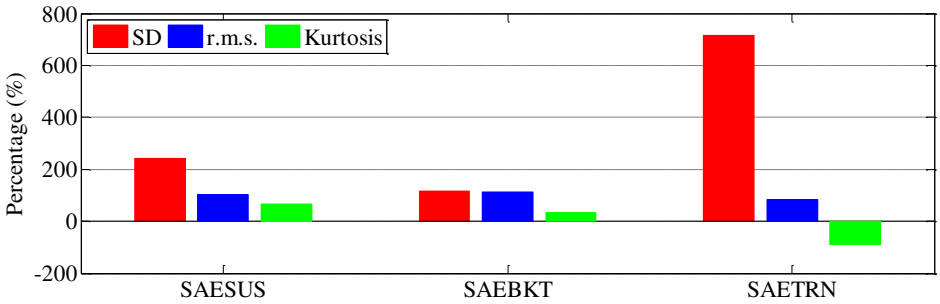

Figure 4.27 Percentage of the statistical parameter differences for the SAE strain signals

The frequency spectrum for the measured and SAE strain signals are shown in Figures 4.28 to 4.29, respectively. The variations of the fixed frequency appeared as distinctive peaks. For the measured strain signals in Figure 4.28, these peaks occurred between 0 Hz to 50 Hz, while for the SAE strain signals, they occurred between 0 Hz to 15 Hz, as shown in Figure 4.29. These peaks were caused by higher energy that occurred at lower frequency. At this lower frequency, the energy was transferred by non-linear processes, and then exponentially decreased towards a higher frequency

and was eventually lost as heat. Other than these peaks, the strain signals generally showed broad peaks (or what one might call a hill) at higher frequency range. This illustrated that high fatigue loadings occurred at lower frequency oscillations due to the peaks; while the existing high frequency loadings was in the form of vibrations, having lower amplitudes.

The PSD analysis was then performed as well to observe the energy content in the strain signals. The overlapping patterns of the PSD between the actual strain signals with blue and their simulated strain signals in red may be observed in Figures 4.30 to 4.31, displaying the preservation of the energy. From the obtained PSD displays, it was found that the high amplitudes occurred at low frequencies of about 5 Hz and below. The areas below the PSD graphs were calculated and the results are shown in Table 4.8 and Figures 4.32 to 4.33. The simulation decreased the energy by 6.4 %. It meant the simulated strain signals were able to maintain at least 93.6 % of their original energy. Decrease and increase of the energy were because the equation of motion used to develop the simulated model being simplified, without considering external forces. Meanwhile, the simulation increased the energy by 30 % for the SAEBKT strain signal. Higher increase of the energy could be caused by a significant difference between coil spring and bracket mechanisms, besides effect of the simplified simulated model.

Fatigue damage was the most important parameter to be analysed. The percentage of the fatigue damage differences are shown in Table 4.9 and Figure 4.34, where the Coffin-Manson model gave the lowest differences. Based on the model, the fatigue damage decreased up to 2.8 %. A maximum decrease of 6.9 % was obtained based on the Morrow model, and the SWT model gave the highest decrease, which was 7.5 %. The differences existing between the actual and simulated strain signals were because the equation of motion used to develop the simulated model being simplified. However, the differences were small. The simulated strain signals were able to retain the fatigue damage of more than 92.5 %. These findings show expected results where the differences were below 10 %. In Figure 4.35a, the fatigue damage of the measured strain signals was distributed in the range of 1:2 or 2:1 correlation.

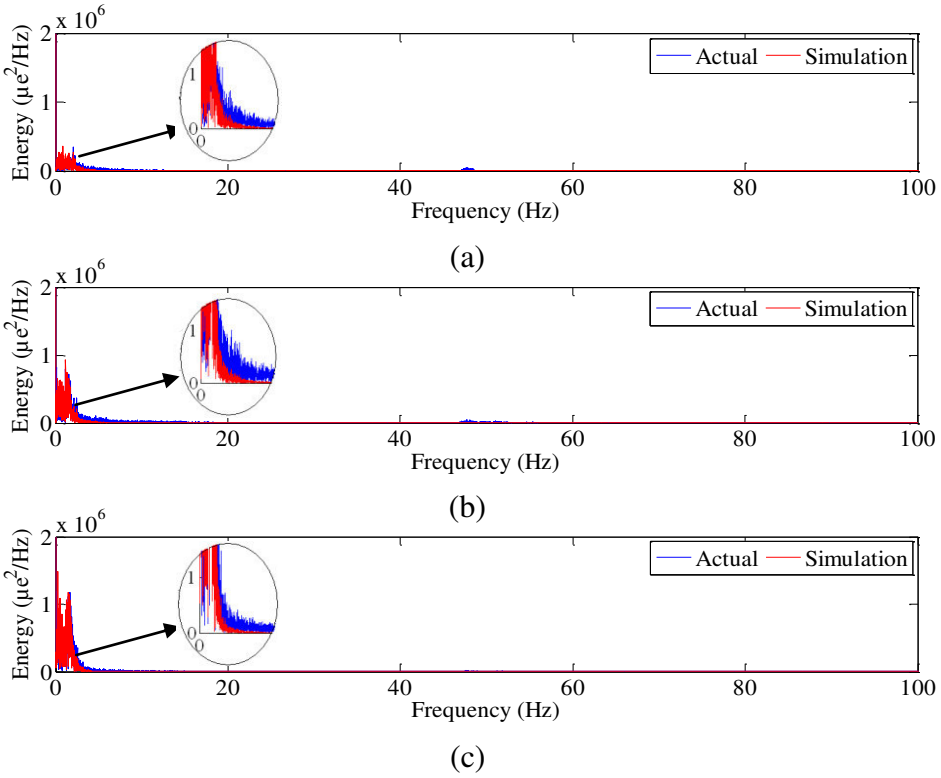

Figure 4.28 Frequency spectrum comparisons in the range of 0 Hz to 100 Hz for the measured strain signals: (a) highway, (b) urban, (c) rural

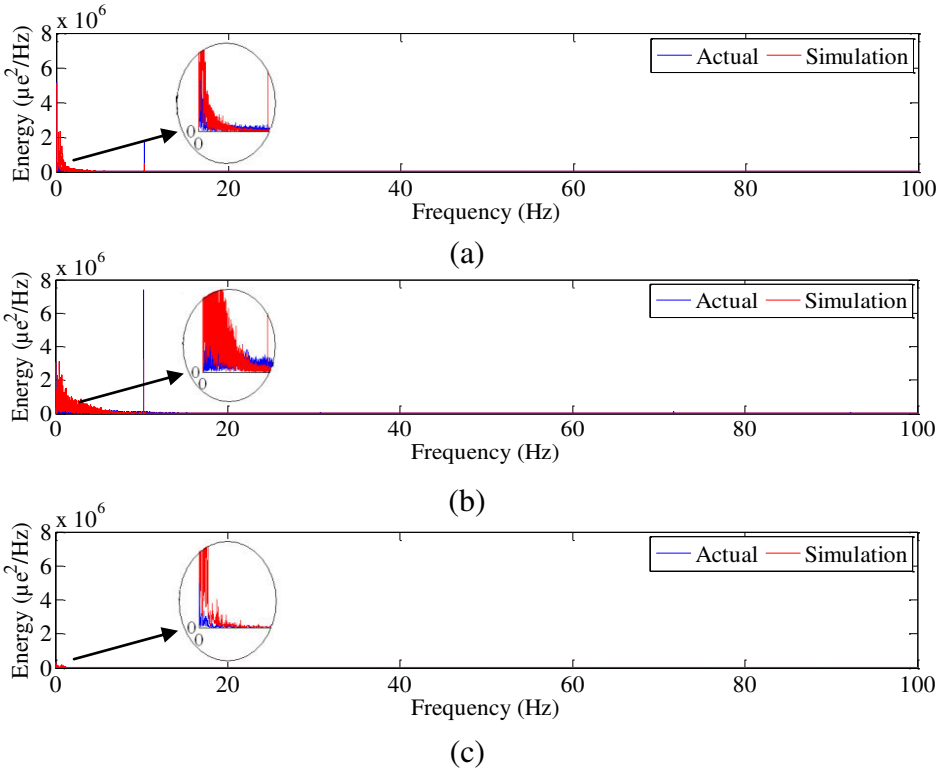

Figure 4.29 Frequency spectrum comparisons in the range of 0 Hz to 100 Hz for the SAE strain signals: (a) SAESUS, (b) SAEBKT, (c) SAETRN

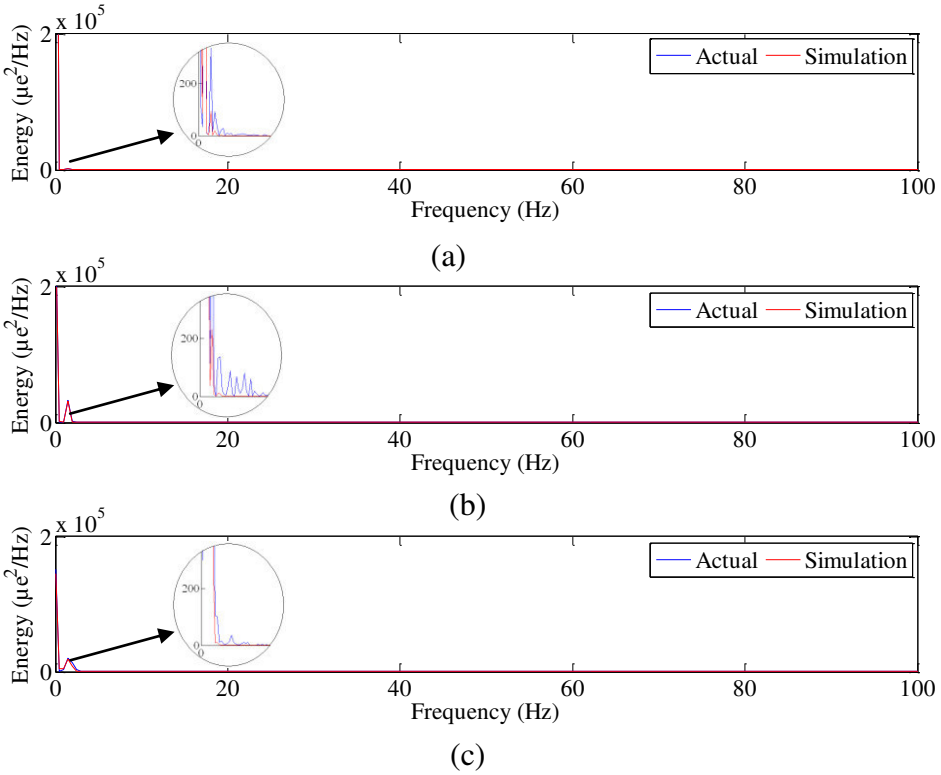

Figure 4.30 PSD comparisons in the range of 0 Hz to 100 Hz for the measured strain signals: (a) highway, (b) urban, (c) rural

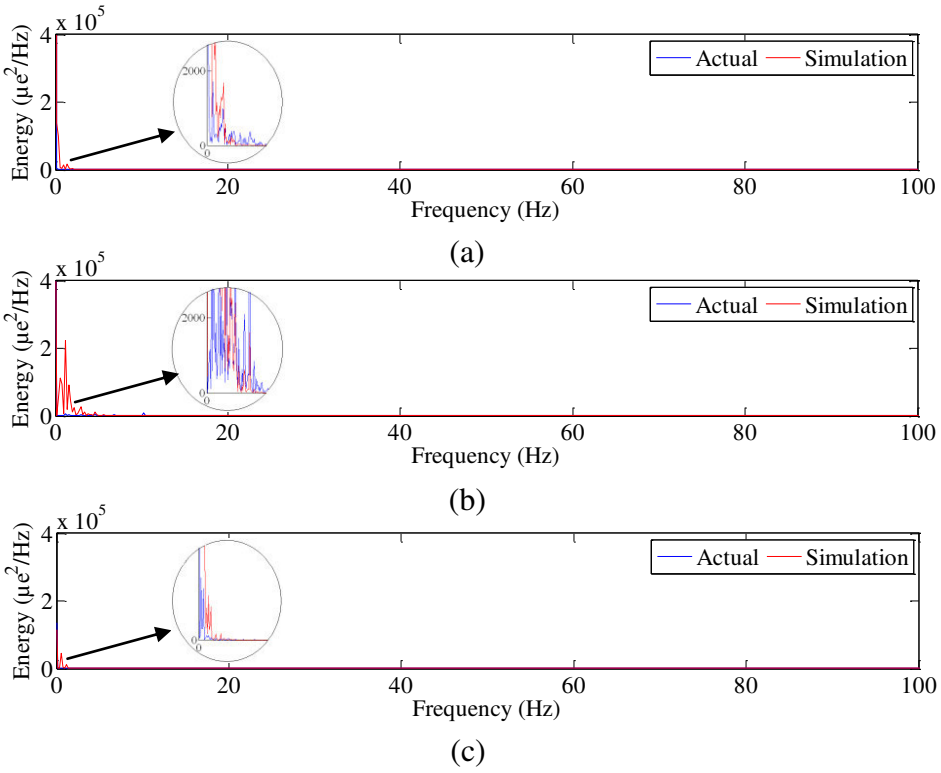

Figure 4.31 PSD comparisons in the range of 0 Hz to 100 Hz for the SAE strain signals: (a) SAESUS, (b) SAEBKT, (c) SAETRN

It gave an RMSE-based error of 0.008 % for the Coffin-Manson model and 0.002 % for the Morrow and SWT models. As presented in Figure 4.35b, it gave a coefficient of determination of 0.9995 and an error of 0.011 %. With lower errors and a higher correlation, it indicated that the simulated strain signals had similar characteristics to the actual strain signals.

For the SAE strain signals, the fatigue damage was distributed out as a 1:2 or 2:1 correlation, as shown in Figure 4.36a. It was acceptable because the simulated model developed was for observing coil spring behaviour, whereas the SAE strain signals were not collected at a coil spring, and thus, the simulation gave highly different responses to the SAE strain signals. In addition, the equation of motion used to develop the simulated model being simplified. However, the SAE strain signals gave only an error of 1.5 %. Figure 4.36b gave a coefficient of determination of 0.9915 with an error of 1.05 %. It indicated that the simulated SAE strain signals also had similar characteristics to the actual SAE strain signals, although they were not measured at a coil spring. From the analyses, it indicated that the MBD simulation was able to produce the strain signals showing similar pattern to the actual strain signals, especially for the measured strain signals. Comparing the results reflected the accurate boundary conditions and the acceleration signals in the dynamic analysis. Thus, the next significant portion of the research was validation. For that purpose, however, only the measured strain signals and their simulated strain signals were involved.

Table 4.8 PSD area differences between the actual and simulated strain signals

Strain signals	**Actual ($\mu\varepsilon^2$/Hz)**	**Simulation ($\mu\varepsilon^2$/Hz)**	**Differences (%)**
Highway	7.14×10^5	7.16×10^5	0.3
Urban	2.81×10^5	2.77×10^5	-1.2
Rural	1.65×10^5	1.54×10^5	-6.4
SAESUS	5.25×10^6	5.23×10^6	-0.4
SAEBKT	8.10×10^5	1.05×10^6	30.0
SAETRN	1.37×10^5	1.18×10^5	-13.5

Note: difference = (simulation - actual) / actual x 100 %

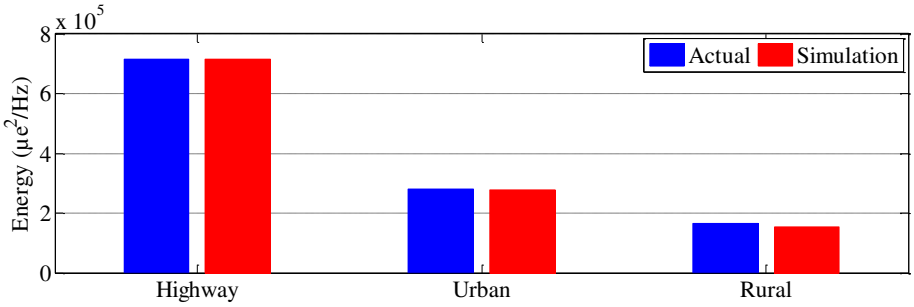

Figure 4.32 PSD differences for the measured strain signals

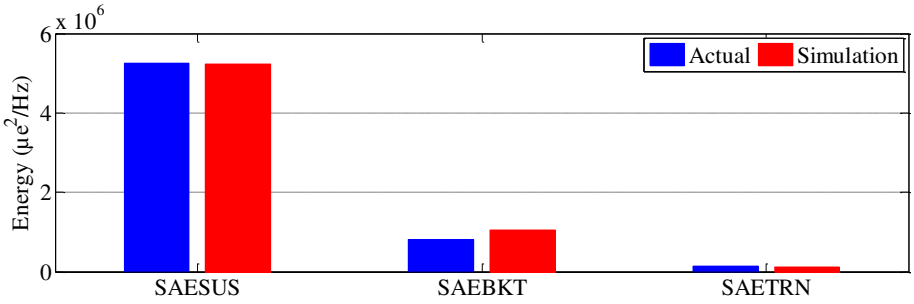

Figure 4.33 PSD differences for the SAE strain signals

Table 4.9 Fatigue damage differences between the actual and simulated strain signals

Strain signals		**Coffin-Manson (damage per block)**	**Morrow (damage per block)**	**SWT (damage per block)**
Actual	Highway	3.74×10^{-6}	1.39×10^{-5}	2.09×10^{-5}
	Urban	2.52×10^{-3}	2.40×10^{-3}	2.32×10^{-3}
	Rural	1.10×10^{-2}	1.08×10^{-2}	1.05×10^{-2}
Simulation	Highway	3.71×10^{-6}	1.29×10^{-5}	1.93×10^{-5}
	Urban	2.56×10^{-3}	2.42×10^{-3}	2.31×10^{-3}
	Rural	1.07×10^{-2}	1.08×10^{-2}	1.06×10^{-2}
Diff. (%)	Highway	-0.8	-6.9	-7.5
	Urban	1.5	0.6	-0.7
	Rural	-2.8	-0.2	0.4

Note: diff. = difference = (simulation - actual) / actual x 100 %

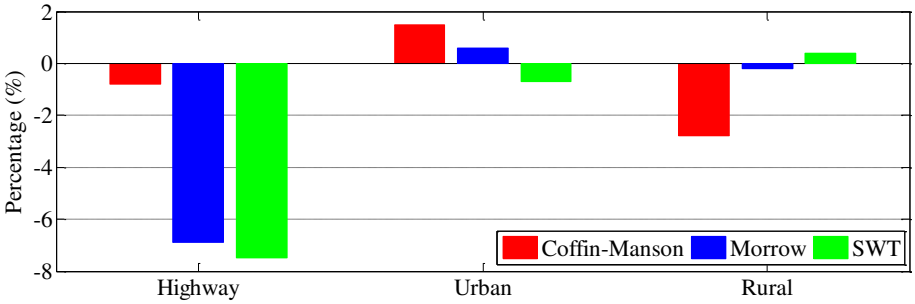

Figure 4.34 Fatigue damage differences for the measured strain signals

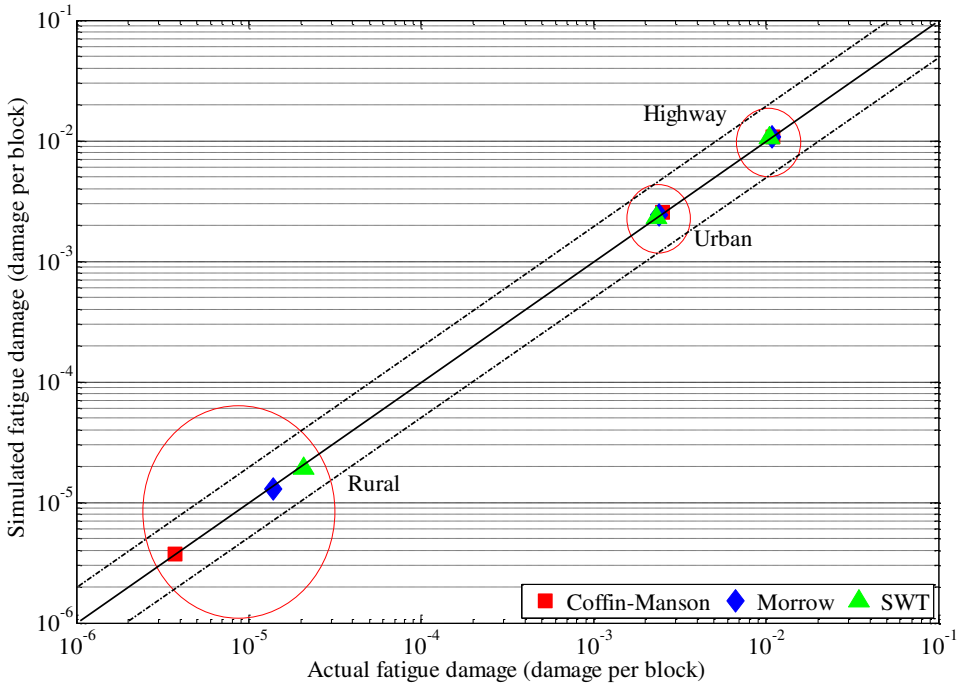

(a)

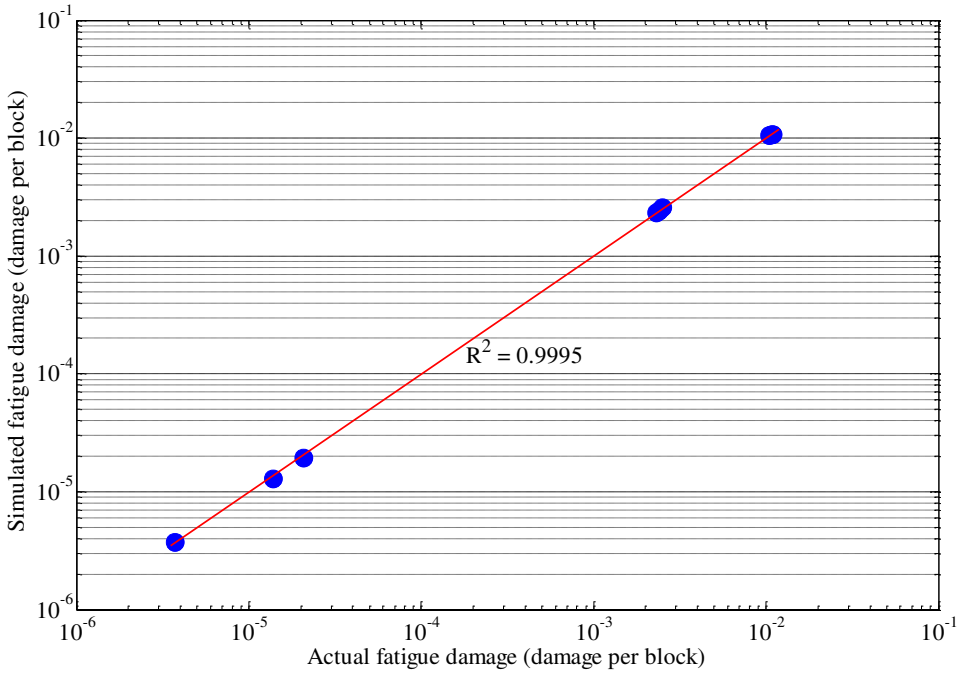

(b)

Figure 4.35 Fatigue damage distributions for the measured strain signals: (a) 1:2 or 2:1 correlation, (b) coefficient of determination

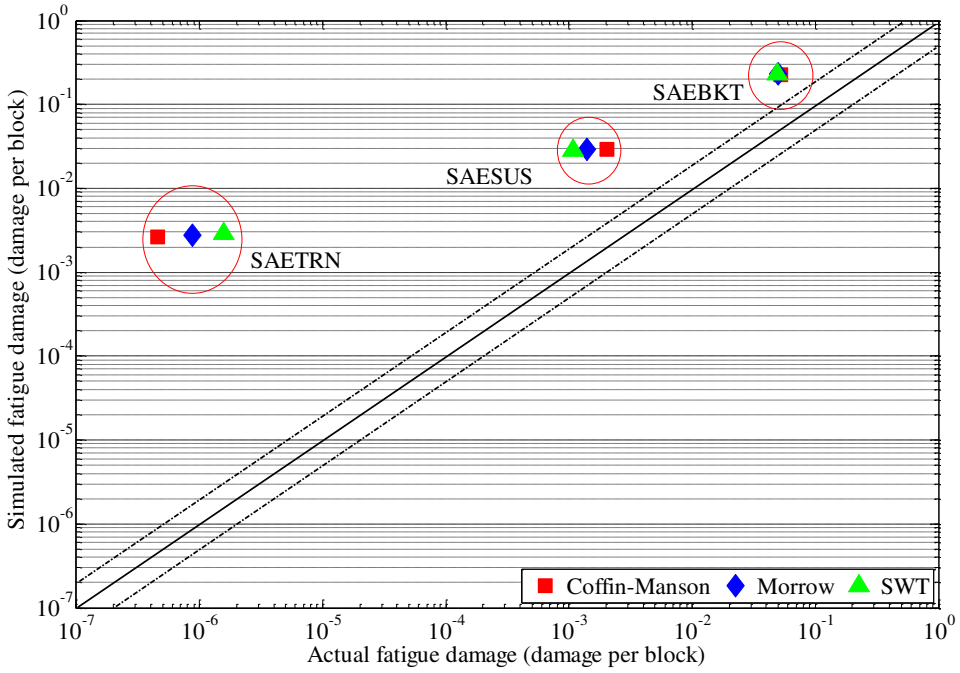

(a)

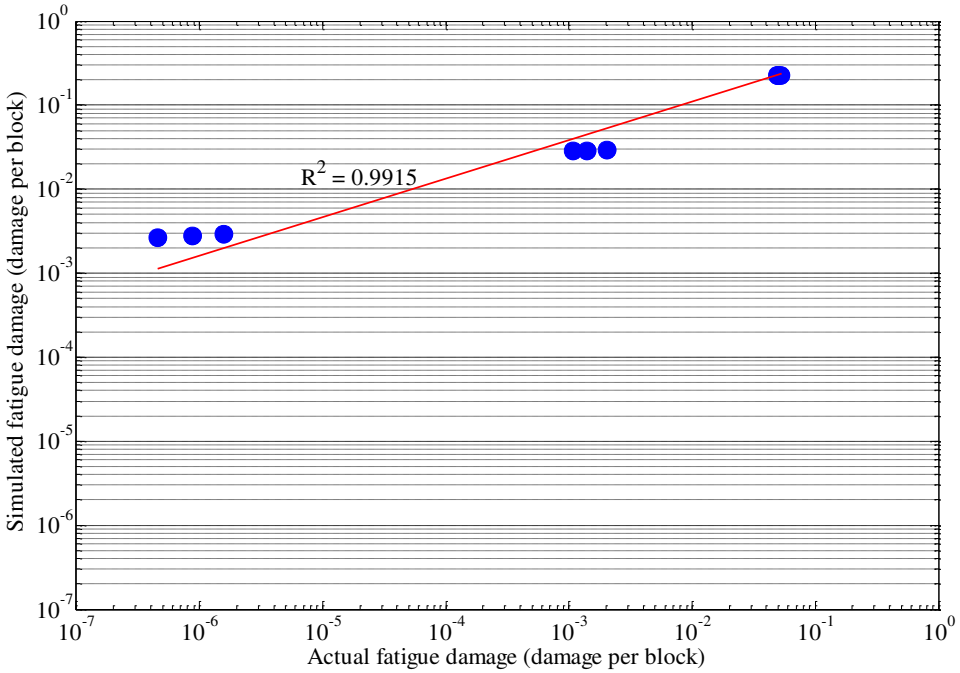

(b)

Figure 4.36 Fatigue damage distributions for the SAE strain signals: (a) 1:2 or 2:1 correlation, (b) coefficient of determination

4.3 STRAIN SIGNAL VALIDITY

4.3.1 Strain Signal Segmentation

For the segment by segment validation, the actual and simulated strain signals were extracted to obtain non-damaging and damaging segments using the wavelet-based FDE technique developed in Section 3.3.1. In the wavelet coefficients presented in Figures 4.37b, 4.38b and 4.39b for the highway, urban and rural strain signals, respectively, the matrix row (*x*-axis) denotes the time parameter and the matrix column (*y*-axis) denotes the scale parameter that is inversely related to the frequency. Comparing the wavelet coefficients, S1 provided the brightest colour, followed by S2 and S3, respectively. A bright colour indicates a higher coefficient, while a less bright colour indicates a lower coefficient.

The wavelet coefficients indicated how the energy of the strain signals was divided in the time-frequency domain (Darpe 2007). The energy contained in a particular scale and position was presented as a wavelet energy density function. The energy spectrum was plotted and the content provided important information about the pattern of the random strain signals. In Figures 4.37c, 4.38c and 4.39c for the highway, urban and rural strain signals, respectively, the scalogram surface shows the position of a dominant energy. The obtained magnitude provided high amplitude because it was generated in the form of the energy distribution in units of $\mu\varepsilon^2$/Hz. Comparing Figures 4.37c, 4.38c and 4.39c, S3 gave the highest amplitude, followed by S2 and S1. This was in line with the strain amplitudes in Figure 4.4, because energy fed to a strain signal usually originates from strain amplitude variations. Although S3 gave the darkest wavelet coefficient plot as shown in Figure 4.39b, peaks in the strain signal provided higher energy than other strain signals, contributing to higher cumulative energy.

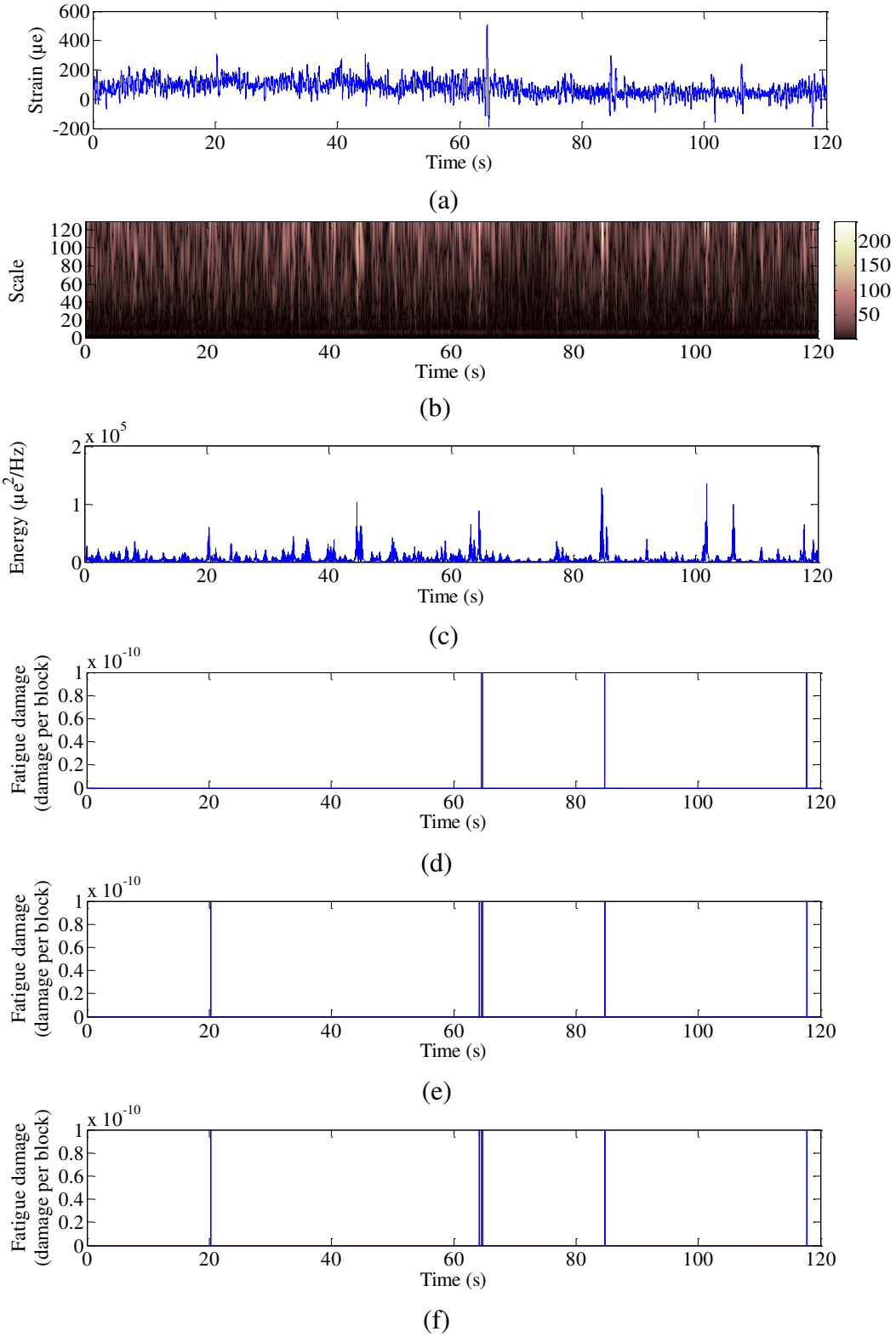

Figure 4.37 Fatigue feature extraction of the actual highway strain signal: (a) time history strain signal, (b) wavelet coefficient, (c) energy distribution, (d) Coffin-Manson-based damage, (e) Morrow-based damage, (f) SWT-based damage

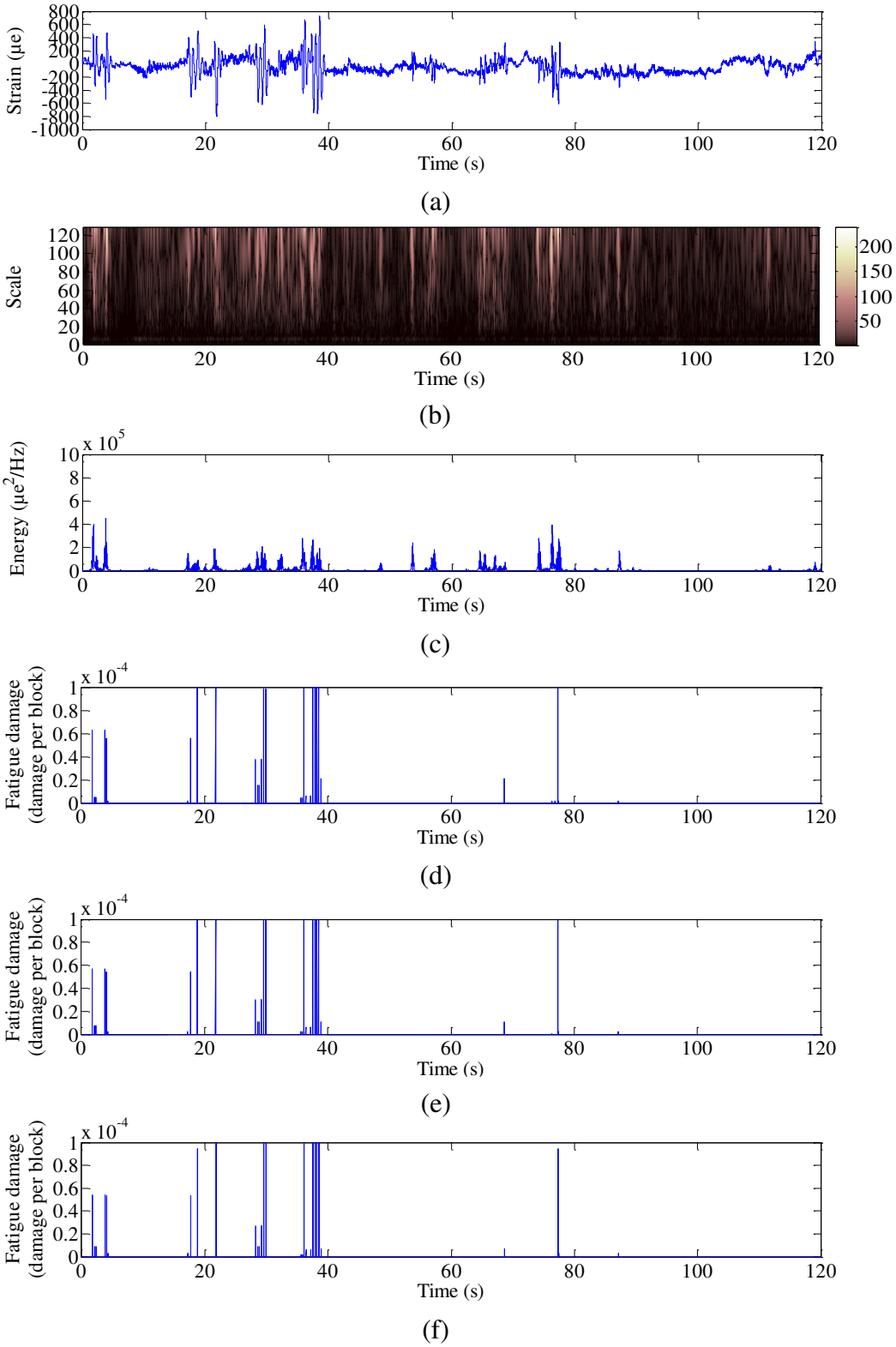

Figure 4.38 Fatigue feature extraction of the actual urban strain signal: (a) time history strain signal, (b) wavelet coefficient, (c) energy distribution, (d) Coffin-Manson-based damage, (e) Morrow-based damage, (f) SWT-based damage

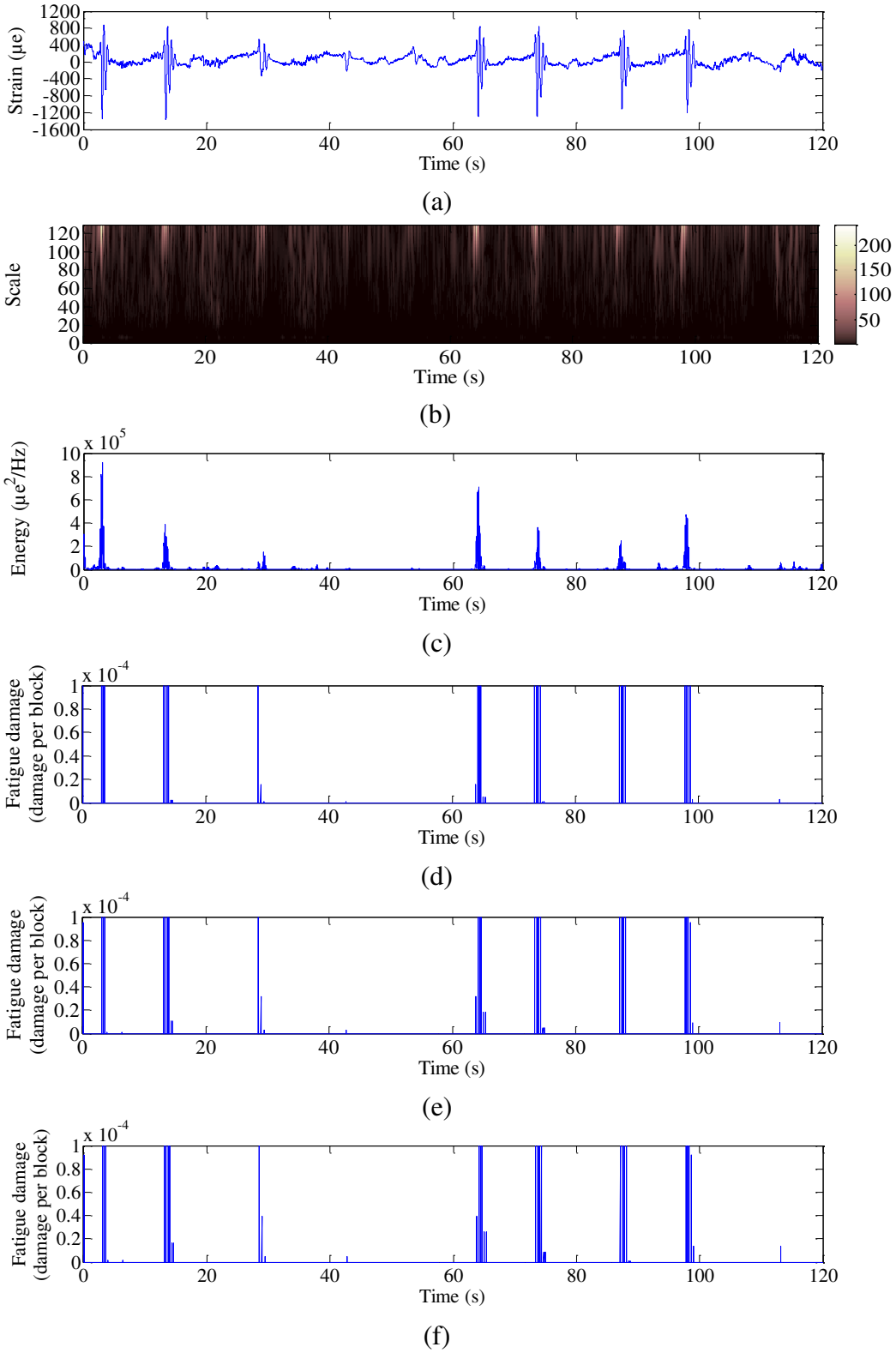

Figure 4.39 Fatigue feature extraction of the actual rural strain signal: (a) time history strain signal, (b) wavelet coefficient, (c) energy distribution, (d) Coffin-Manson-based damage, (e) Morrow-based damage, (f) SWT-based damage

Comparing the energy distributions in Figures 4.37c, 4.38c and 4.39c to the fatigue damage graphs in Figures 4.37d, 4.38d and 4.39d for the Coffin-Manson model, Figures 4.37e, 4.38e and 4.39e for the Morrow model and Figures 4.37f, 4.38f and 4.39f for the SWT model, it was found that high amplitudes for all the strain signals were located at the same positions. According to the findings, the higher wavelet coefficient was indicative of higher energy, which contributed to more fatigue damaging events; contrarily, lower fatigue damage was represented by lower energy. In other words, this relationship between the wavelet coefficient and the fatigue damage was strong and parallel. This meant that the wavelet-based energy was suitable for use as a parameter to accurately detect the changing amplitudes in the strain signals.

Time series energy magnitudes need to be converted into the form of peak-valley series. Equation (3.11), developed in Section 3.3.1, was then utilised to detect the locations of a higher amplitude in the strain signals based on the magnitude spectrum. Thus, highly fatigue damaging events in the strain signals were identified and extracted to produce non-damaging and damaging segments. A cutting level parameter, called EGV was used for the extraction of fatigue features. Various multiplicative factors were applied giving various EGVs, listed in Table 4.10.

Table 4.10 EGVs applied for each strain signal

Strain signals	**Maximum energies ($\mu\varepsilon^2$/Hz)**	**Multiplicative factors**			**EGVs ($\mu\varepsilon^2$/Hz)**		
		Extractions					
		1st	**2nd**	**3rd**	**1st**	**2nd**	**3rd**
S1	1.35×10^5	0.94440	0.95571	0.96568	7×10^4	8×10^4	9×10^4
S2	4.51×10^5	0.91015	0.91545	0.92040	1.4×10^5	1.5×10^5	1.6×10^5
S3	9.21×10^5	0.89898	0.90208	0.90505	2.3×10^5	2.4×10^5	2.5×10^5

For S1, the EGVs used were 70,000 $\mu\varepsilon^2$/Hz, 80,000 $\mu\varepsilon^2$/Hz and 90,000 $\mu\varepsilon^2$/Hz. Furthermore, S2 was extracted at 140,000 $\mu\varepsilon^2$/Hz, 150,000 $\mu\varepsilon^2$/Hz and 160,000 $\mu\varepsilon^2$/Hz. The last one, 230,000 $\mu\varepsilon^2$/Hz, 240,000 $\mu\varepsilon^2$/Hz and 250,000 $\mu\varepsilon^2$/Hz of EGVs were applied to S3. The EGVs were chosen because most the energies were below the EGVs. The energies with a magnitude exceeding the EGVs were maintained, whereas the energies with a magnitude less than the EGVs were removed from the strain signals. Lower energy segments were assumed as a non-damaging

segment, whereas if lower energy sections were removed, it did not affect the damage relevance and the original properties of the strain signals. After all the strain signals were extracted, retained higher energies were obtained, as shown in Figures 4.40 to 4.42.

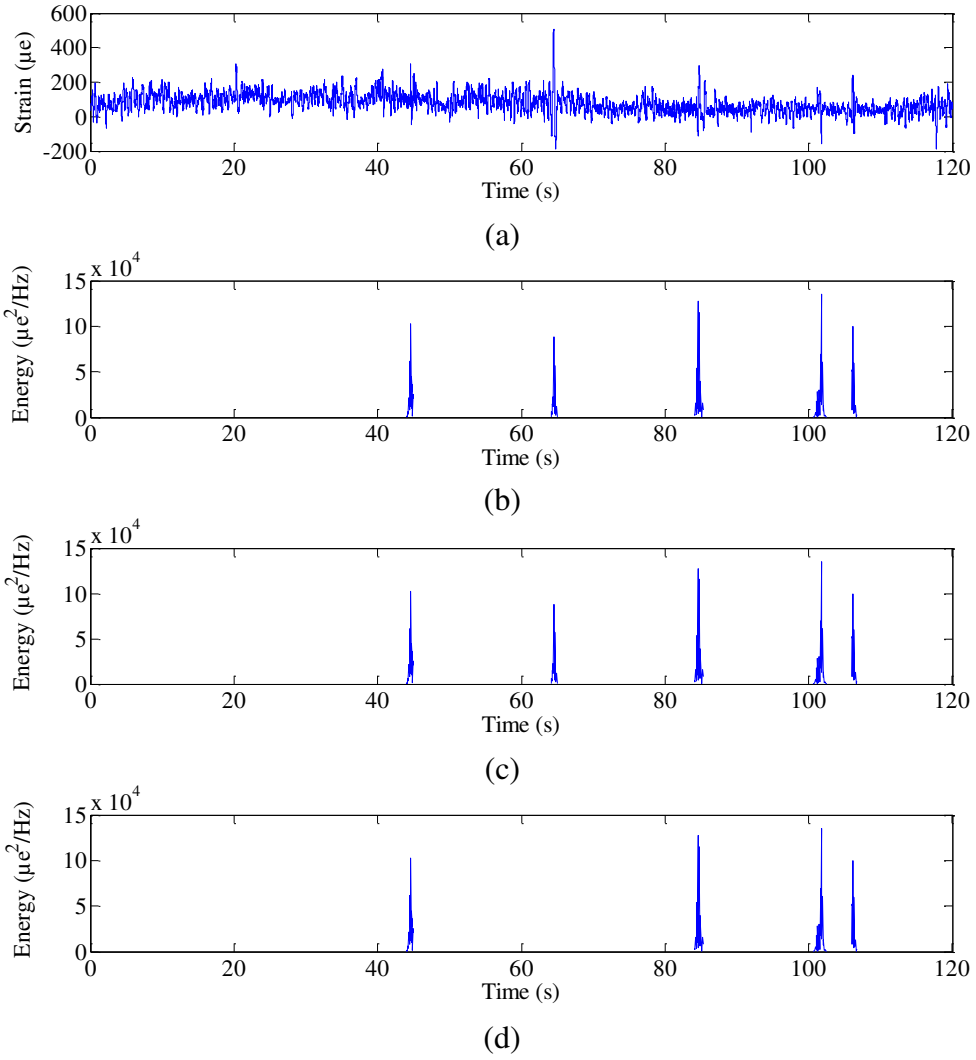

Figure 4.40 Energy for the highway strain signal at various EGVs: (a) time series strain signal, (b) 70,000 $\mu\varepsilon^2$/Hz, (c) 80,000 $\mu\varepsilon^2$/Hz, (d) 90,000 $\mu\varepsilon^2$/Hz

Furthermore, based on the time positions of the retained higher energies and referring to the actual strain signals in Figures 4.40 to 4.42, maintained segments were obtained. The maintained segments were damaging segments since they had slightly more energies than the EGV. Meanwhile, the removed segments were non-damaging

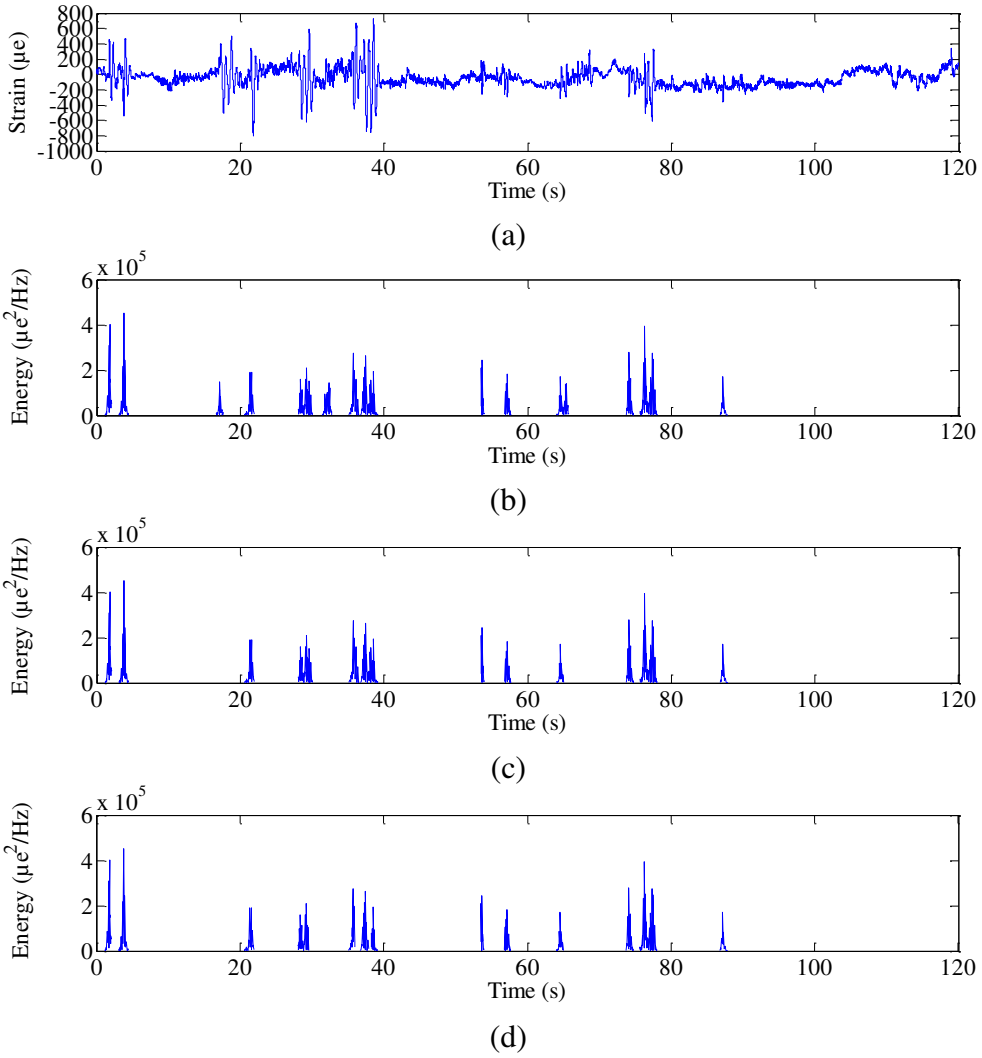

Figure 4.41 Energy for the urban strain signal at various EGVs: (a) time series strain signal, (b) 140,000 με^2/Hz, (c) 150,000 με^2/Hz, (d) 160,000 με^2/Hz

segments because the energy of the segments was lower than the EGV. The extraction produced segments that were not uniform in lengths because the FDE technique extracted the time series based on the energy contents, as shown in Figures 4.43 to 4.45.

Maintenance of the original characteristics was important in the FDE to ensure that the resulted modified strain signals were similar to the actual strain signals. Thus, the effects of the removal at a single EGV should be considered so that the retained segments meet the criteria required in the FDE, i.e. maintaining 90 % of fatigue damage. Therefore, the retained segments were reattached into a single strain signal to

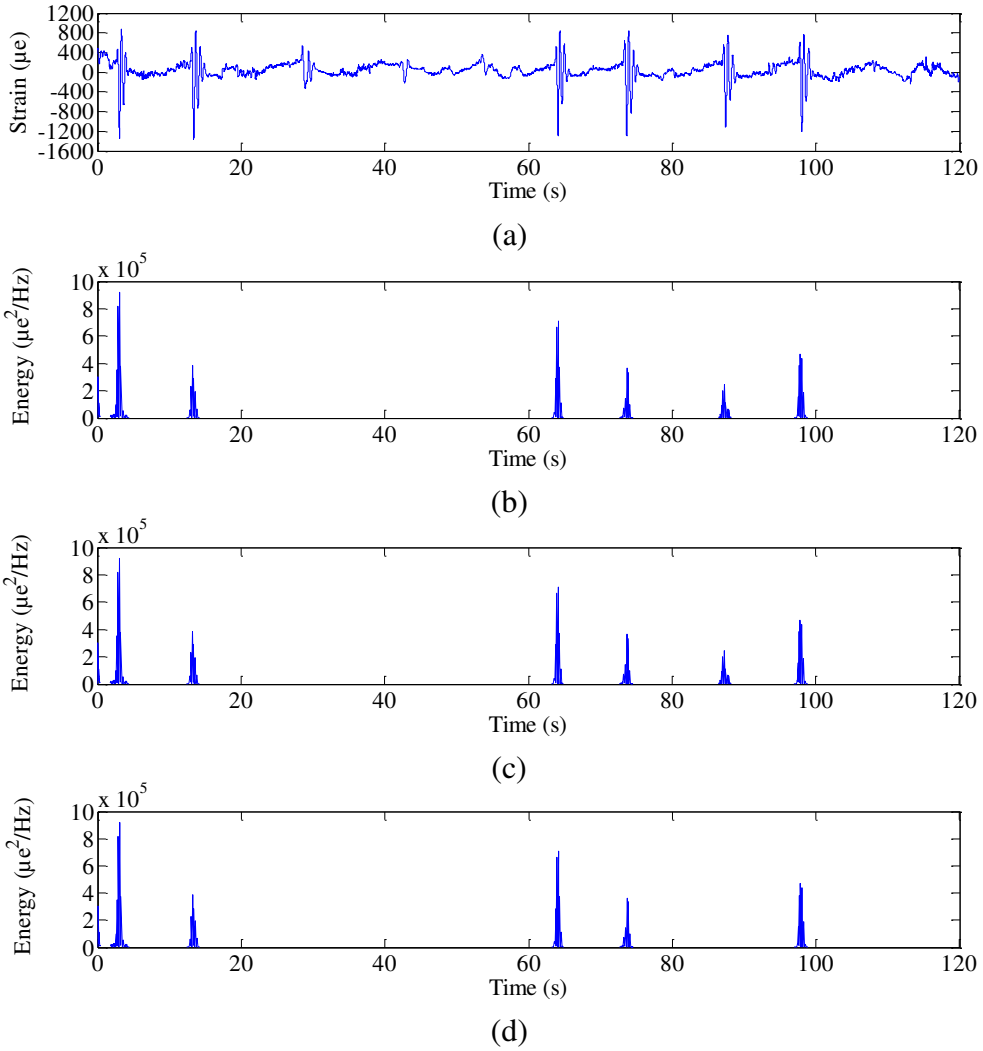

Figure 4.42 Energy for the rural strain signal at various EGVs: (a) time series strain signal, (b) 230,000 $\mu\varepsilon^2$/Hz, (c) 240,000 $\mu\varepsilon^2$/Hz, (d) 250,000 $\mu\varepsilon^2$/Hz

validate if the extraction performed satisfied the requirement. Figures 4.46 to 4.48 show the differences in the length of the modified strain signals at various EGVs. Verifications were performed by comparing the characteristics between the original and modified strain signals.

Tables 4.11 to 4.13 list the changes of statistical parameters. The third extraction should give a higher change since more energy amplitudes were removed at the extraction, followed by the second and first extractions, respectively. For S1 in Table 4.11, SD increased by 89.5 % for all EGVs, while r.m.s. increased by more than 28 %. Kurtosis also increased by more than 7 %. A similar condition also occurred for

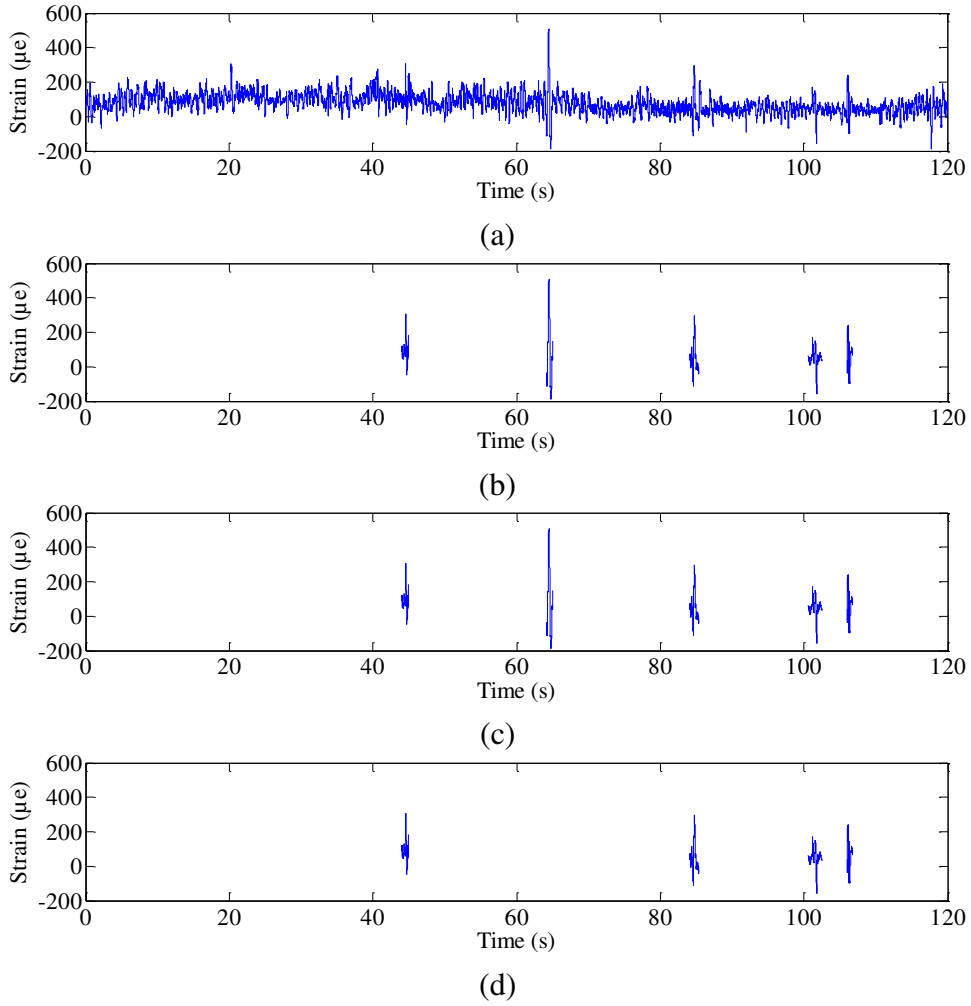

Figure 4.43 Retained segments of the highway strain signal at various EGVs: (a) time history strain signal (b) 70,000 $\mu\varepsilon^2$/Hz, (c) 80,000 $\mu\varepsilon^2$/Hz, (d) 90,000 $\mu\varepsilon^2$/Hz

S2 in Table 4.12, where SD increased by more than 83 %, and r.m.s. increased by more than 76 %. For kurtosis, however, the simulation decreased the value by more than 53 %. For S3 in Table 4.13, the simulation increased SD up to 162 % and increased r.m.s. by more than 155 %. However, kurtosis decreased by more than 80 %.

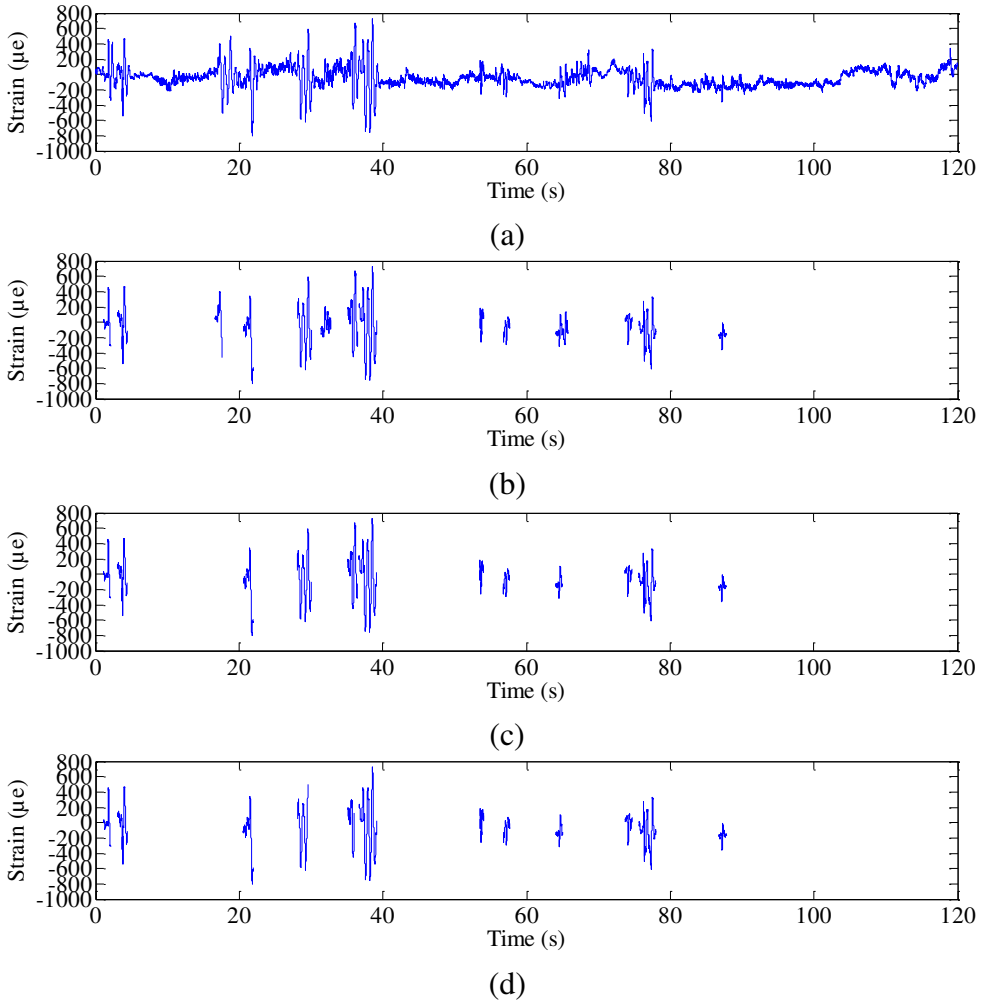

Figure 4.44 Retained segments of the urban strain signal at various EGVs: (a) time history strain signal, (b) 140,000 $\mu\varepsilon^2$/Hz, (c) 150,000 $\mu\varepsilon^2$/Hz, (d) 160,000 $\mu\varepsilon^2$/Hz

Trends of the use of different EGVs are illustrated in Figure 4.49, where the EGV equal to zero represents an original strain signal. The figure summarises the percentages of the statistical parameter changes at various EGVs. These percentages move up and down even when extracted at a set distance. It showed that statistical parameters did not provide a consistent change. Increased SD indicated that the edited strain signals were distributed farer than the original strain signals since lower strain amplitudes were removed. Increased r.m.s. indicated that the energy content in the edited strain signals also increased, showing a corresponding increase in SD. Different kurtosis showed that the FDE technique was capable of effectively removing lower strain amplitudes while maintaining higher strain amplitudes in the modified strain signals.

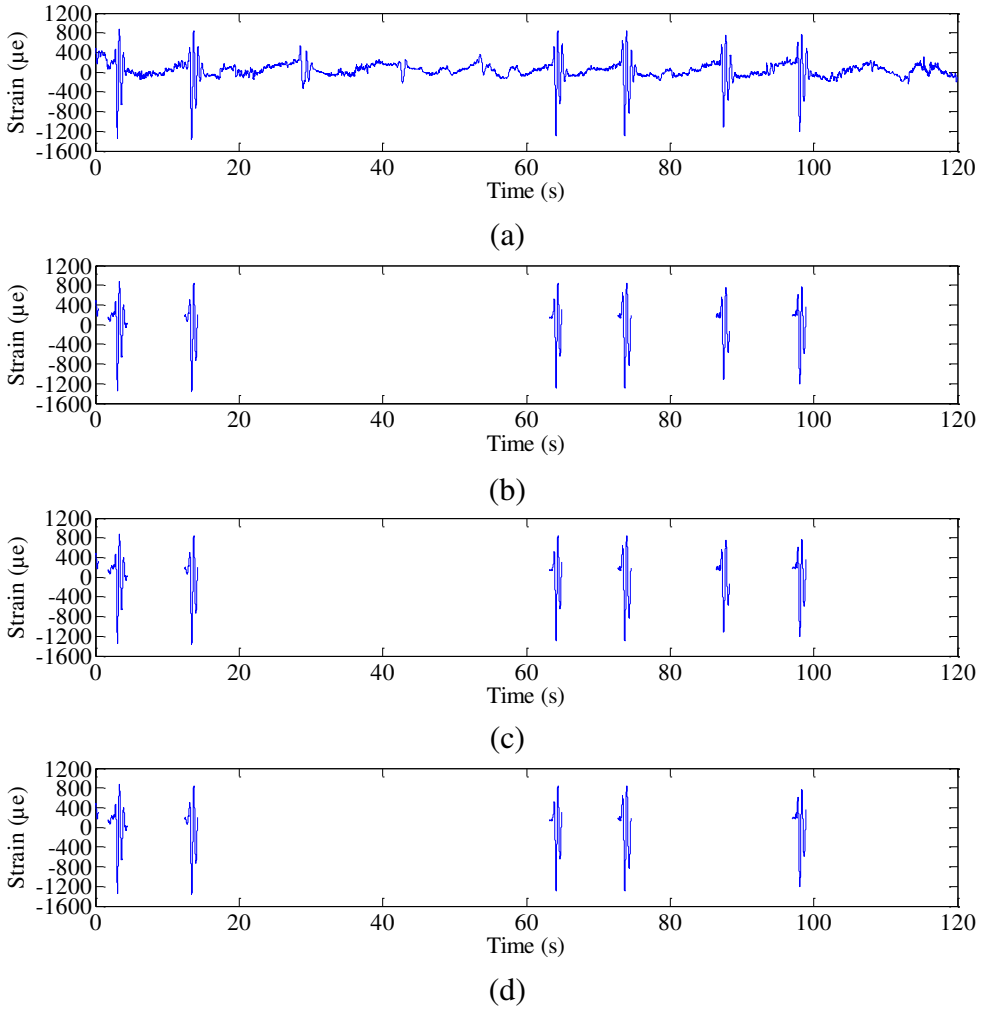

Figure 4.45 Retained segments of the rural strain signal at various EGVs: (a) time history strain signal, (b) 230,000 $\mu\varepsilon^2$/Hz, (c) 240,000 $\mu\varepsilon^2$/Hz, (d) 250,000 $\mu\varepsilon^2$/Hz

These obvious changes in statistical parameters certainly influence using the edited strain signals for further analyses, because most these parameters changed more than 10 %. Statistical parameters, however, were not considered in selecting an optimum edited strain signal because r.m.s. indicating signal energy was presented by the wavelet coefficient. Meanwhile, kurtosis describing peaks in the strain signals was presented by the peak-valley technique applied to extract damaging segments. Thus, without considering statistical parameters, the modified strain signals were expected to give a minimum deviation. The accuracy of statistical parameters for predicting fatigue damage will be discussed in Section 4.3.2.

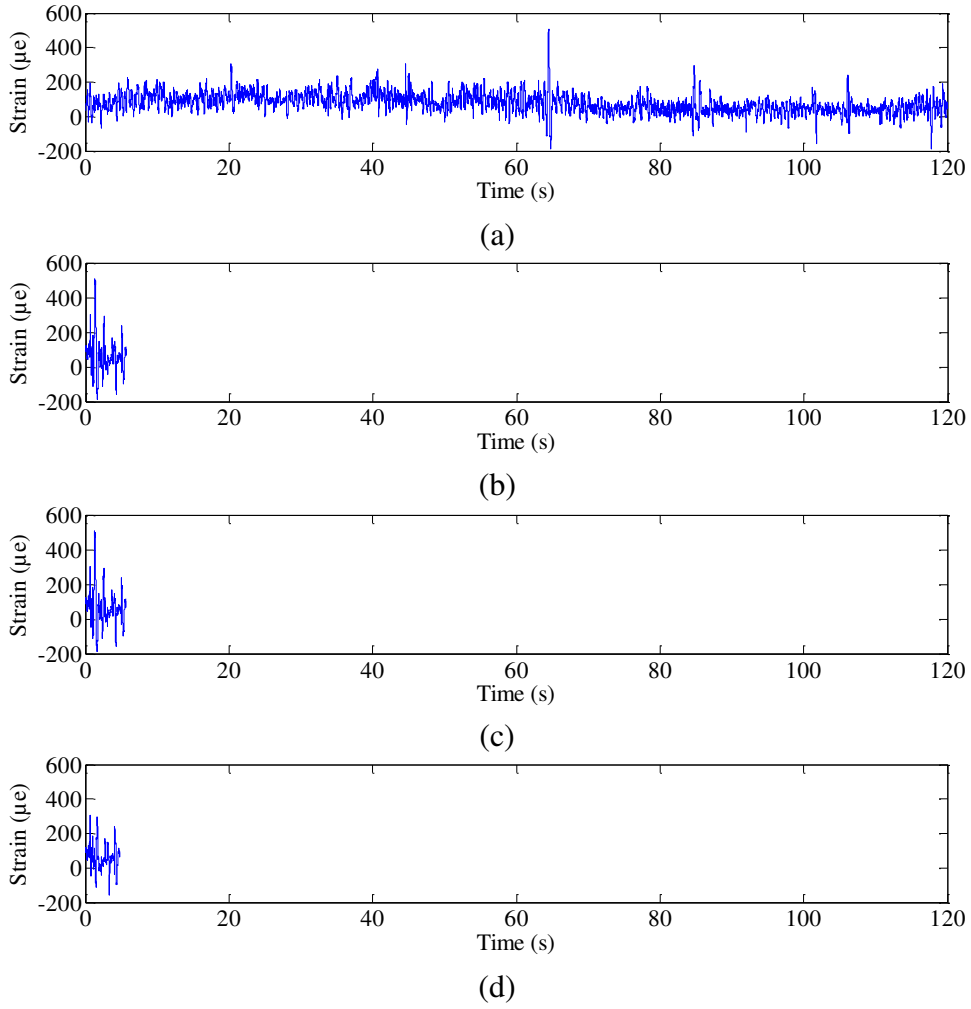

Figure 4.46 Modification of the highway strain signal at various EGVs: (a) time history strain signal, (b) 5.7-second modified strain signal extracted at 70,000 $\mu\varepsilon^2$/Hz, (c) 5.7-second modified strain signal extracted at 80,000 $\mu\varepsilon^2$/Hz, (d) 4.7-second modified strain signal extracted at 90,000 $\mu\varepsilon^2$/Hz

Tables 4.14 to 4.16 summarise the changes in signal length, number of cycles, fatigue damage and fatigue life. For S1, the number of cycles decreased by 96.1 % for the first and second extractions, and decreased by 96.6 % for the third extraction. For S2, a decrease of 88.3 %, 90.2 % and 90.7 % resulted for the first, second and third extractions, respectively. For S3, a decrease of 94.8 % resulted for the first and second extractions, and the third extraction gave a decrease of 95.7 %. These declines indicated that the FDE process was able to remove all the strain amplitude ranges under the EGVs in the time series signals. Thus, the signal length of S1 decreased by

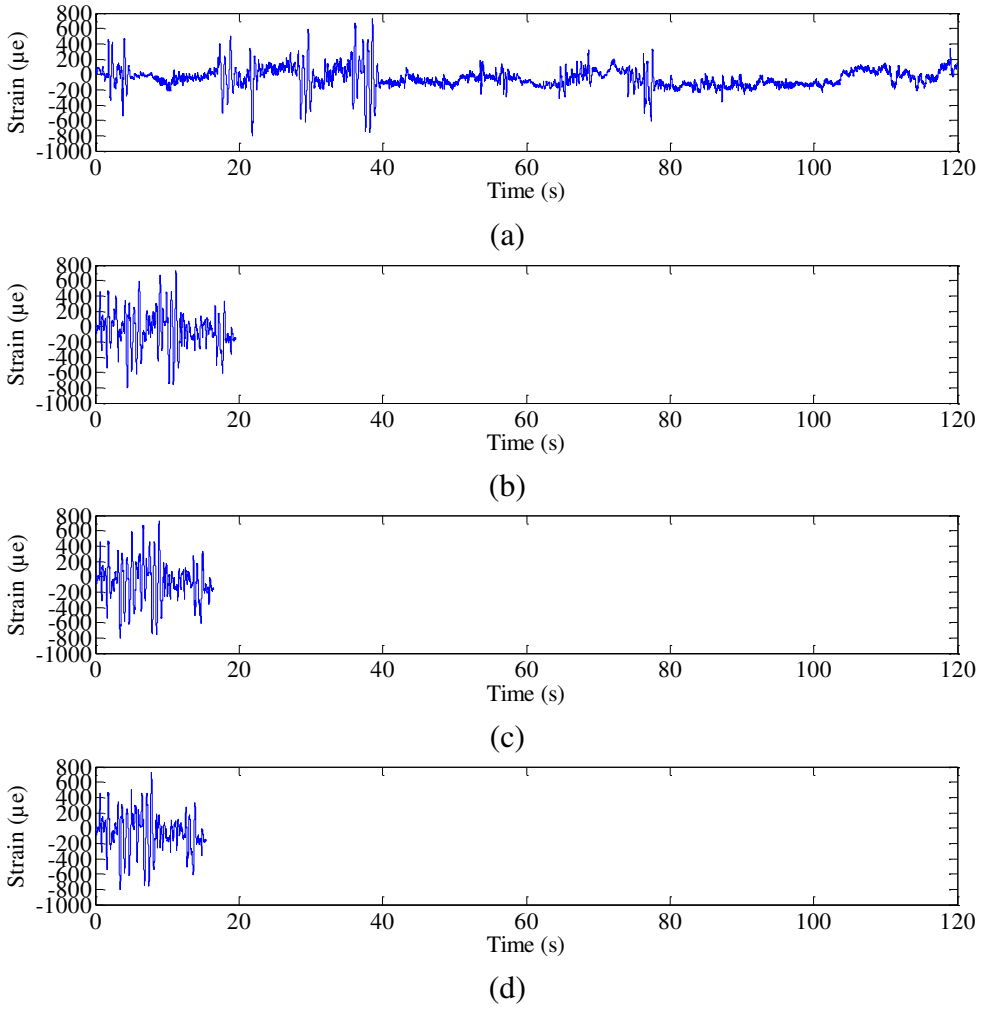

Figure 4.47 Modification of the urban strain signal at various EGVs: (a) time history strain signal, (b) 19.5-second modified strain signal extracted at 140,000 $\mu\varepsilon^2$/Hz, (c) 16.5-second modified strain signal extracted at 150,000 $\mu\varepsilon^2$/Hz, (d) 15.4-second modified strain signal extracted at 160,000 $\mu\varepsilon^2$/Hz

95.3 % for the first and second extractions and decreased by 96.1 % for the third extraction. For S2, decreases of 83.7 %, 86.3 % and 87.2 % were resulted for the first, second and third extractions, respectively. For S3, a decrease of 89.9 % was resulted for the first and second extractions, and the third extraction gave a decrease of 91.4 %. The decrease in the signal lengths was caused by the decrease of the number of cycles.

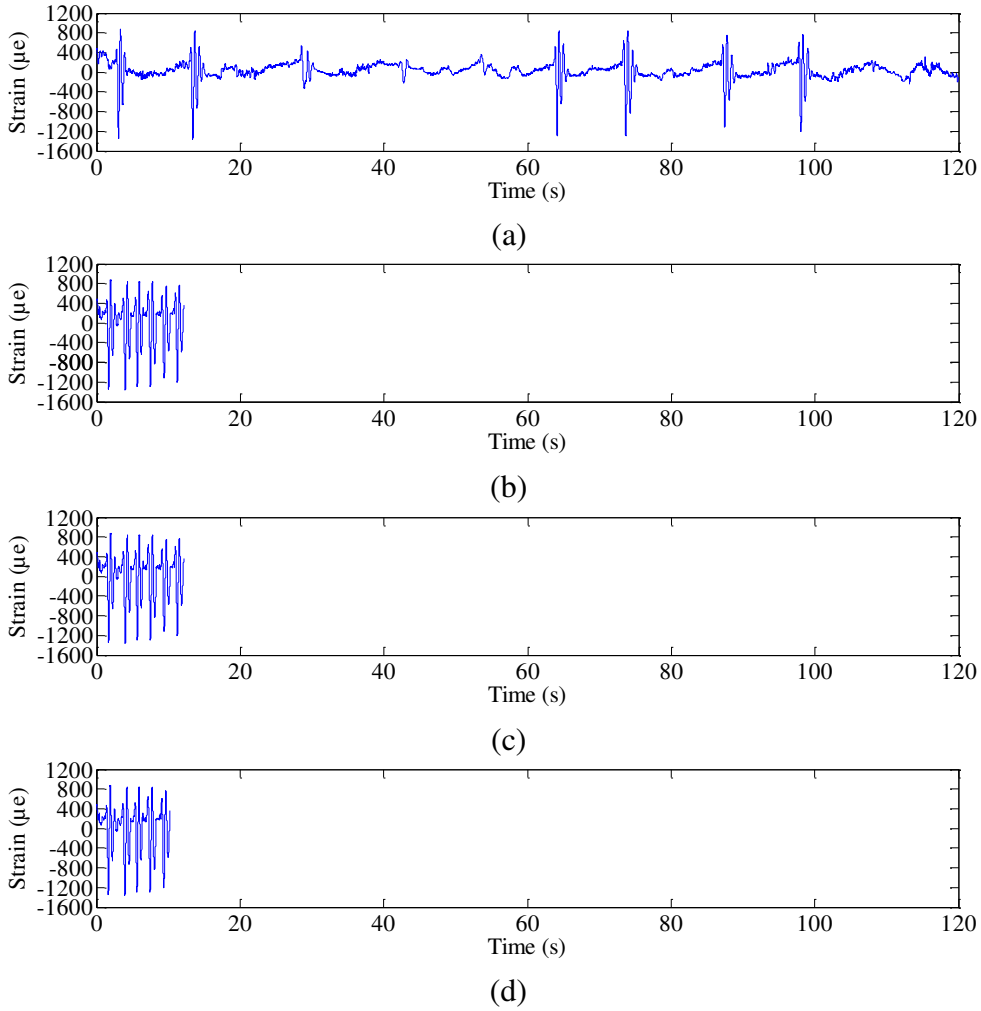

Figure 4.48 Modification of the rural strain signal at various EGVs: (a) time history strain signal, (b) 12.1-second modified strain signal extracted at 230,000 $\mu\varepsilon^2$/Hz, (c) 12.1-second modified strain signal extracted at 240,000 $\mu\varepsilon^2$/Hz, (d) 10.3-second modified strain signal extracted at 250,000 $\mu\varepsilon^2$/Hz

Table 4.11 Statistical differences between the original and edited highway strain signals

Statistical parameters	**Original strain signals**	**Edited strain signals**					
		70,000 $\mu\varepsilon^2$/Hz	**Diff. (%)**	**80,000 $\mu\varepsilon^2$/Hz**	**Diff. (%)**	**90,000 $\mu\varepsilon^2$/Hz**	**Diff. (%)**
SD (με)	54.1	102.6	89.5	102.6	89.5	102.6	89.5
r.m.s. (με)	94.1	120.6	28.1	120.6	28.2	120.6	28.2
Kurtosis	6.0	6.4	7.4	6.4	7.4	6.4	7.2

Note: diff. = difference = (edited - original) / original x 100 %

Table 4.12 Statistical differences between the original and edited urban strain signals

Statistical parameters	Original strain signals	Edited strain signals					
		140,000 $\mu\varepsilon^2$/Hz	Diff. (%)	150,000 $\mu\varepsilon^2$/Hz	Diff. (%)	160,000 $\mu\varepsilon^2$/Hz	Diff. (%)
SD (με)	132.8	244.2	83.9	256.7	93.3	244.5	84.1
r.m.s. (με)	141.2	248.8	76.2	262.7	86.0	252.2	78.6
Kurtosis	8.3	3.9	-53.5	3.6	-56.1	3.8	-54.2

Note: diff. = difference = (edited - original) / original x 100 %

Table 4.13 Statistical differences between the original and edited rural strain signals

Statistical parameters	Original strain signals	Edited strain signals					
		230,000 $\mu\varepsilon^2$/Hz	Diff. (%)	240,000 $\mu\varepsilon^2$/Hz	Diff. (%)	250,000 $\mu\varepsilon^2$/Hz	Diff. (%)
SD (με)	190.3	494.1	159.7	494.1	159.7	498.5	162.0
r.m.s. (με)	193.6	494.1	155.2	494.1	155.2	498.4	157.5
Kurtosis	16.5	3.2	-80.5	3.2	-80.5	3.3	-80.1

Note: diff. = difference = (edited - original) / original x 100 %

The strain signals were extracted with a deviation of fatigue damage by 10 % (Stephens et al. 1997; Giacomin et al. 2001). From the changes in fatigue damage, an optimum EGV for each strain signal was determined based on its ability (in reference to the modified strain signal) to produce the shortest strain signal with a minimum fatigue damage deviation. Controlling the difference in fatigue damage, most these edited strain signals had characteristics that were close to the original features. The decreasing number of cycles caused the fatigue damage in the modified strain signals to also decrease, since fatigue damage is derived from the number of cycles.

For S1, the fatigue damage decreases of 4.3 %, 2.5 % and 2 % resulted for the Coffin-Manson, Morrow and SWT models, respectively, for the first and second extractions. However, a decrease of almost 100 % was produced for the third extraction for all the models. For S2, decreases of 5.8 %, 6.3 % and 6.6 % were resulted for the Coffin-Manson, Morrow and SWT models for the first extraction. The decreases became 6.7 %, 7.1 % and 7.3 % for the Coffin-Manson, Morrow and SWT models for the second extraction. For the third extraction, the decreases became 21 %, 23.4 % and 25.2 % for the Coffin-Manson, Morrow and SWT models.

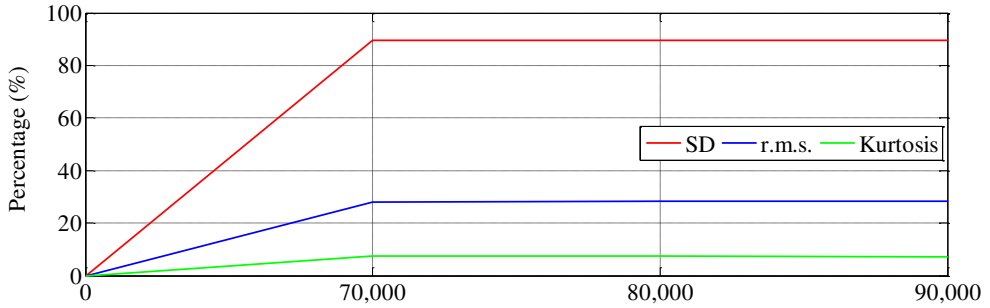

(a)

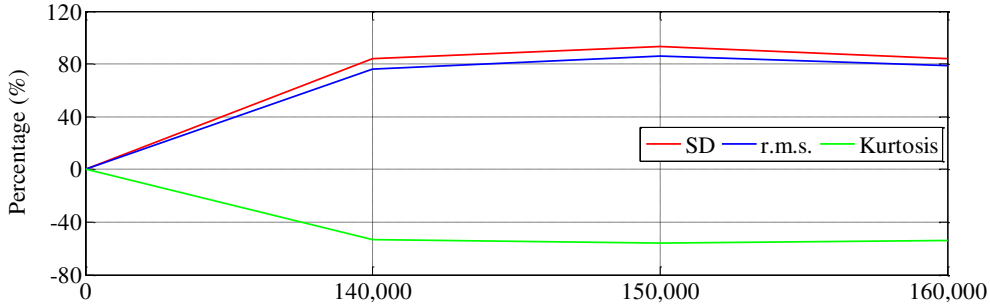

(b)

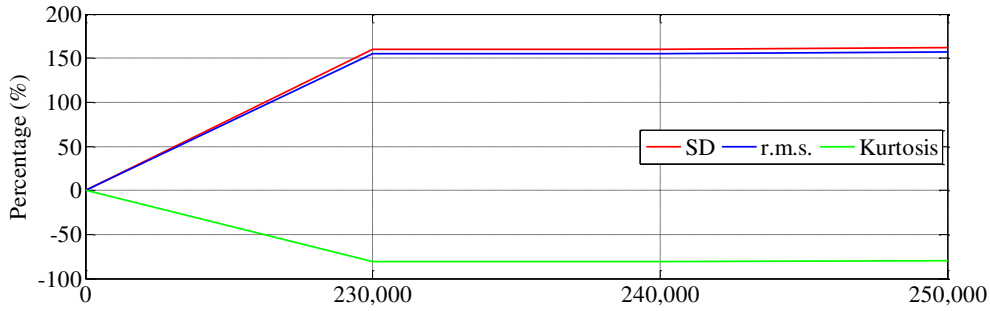

(c)

Figure 4.49 Percentage of the statistical parameter changes at various EGVs: (a) S1-highway, (b) S2-urban, (c) S3-rural

Table 4.14 Signal length, number of cycles, fatigue damage and fatigue life differences between the original and edited highway strain signals

Parameters	Original strain signals	Edited strain signals					
		70,000 με²/Hz	Diff. (%)	80,000 με²/Hz	Diff. (%)	90,000 με²/Hz	Diff. (%)
Lengths (s)	120	5.7	-95.3	5.7	-95.3	4.7	-96.1
Cycles	10,921	427	-96.1	427	-96.1	366	-96.6
Fatigue damage (damage per block)							
CM	3.74×10^{-6}	3.58×10^{-6}	-4.3	3.58×10^{-6}	-4.3	2.14×10^{-8}	-99.4
Morrow	1.39×10^{-5}	1.35×10^{-5}	-2.5	1.35×10^{-5}	-2.5	6.91×10^{-8}	-99.5
SWT	2.09×10^{-5}	2.05×10^{-5}	-2.0	2.05×10^{-5}	-2.0	1.63×10^{-7}	-99.2
Fatigue lives (reversals of blocks)							
CM	$2.67 \times 10^{+5}$	$2.79 \times 10^{+5}$	4.5	$2.79 \times 10^{+5}$	4.5	$4.67 \times 10^{+7}$	17,387.8
Morrow	$7.20 \times 10^{+4}$	$7.39 \times 10^{+4}$	2.5	$7.39 \times 10^{+4}$	2.5	$1.45 \times 10^{+7}$	19,986.1
SWT	$4.78 \times 10^{+4}$	$4.88 \times 10^{+4}$	2.0	$4.88 \times 10^{+4}$	2.0	$6.12 \times 10^{+6}$	12,707.5

Note: diff. = difference = (edited - original) / original x 100 %

Table 4.15 Signal length, number of cycles, fatigue damage and fatigue life differences between the original and edited urban strain signals

Parameters	Original strain signals	Edited strain signals					
		140,000 με²/Hz	Diff. (%)	150,000 με²/Hz	Diff. (%)	160,000 με²/Hz	Diff. (%)
Lengths (s)	120	19.5	-83.7	16.5	-86.3	15.4	-87.2
Cycles	10,070	1175	-88.3	985	-90.2	935	-90.7
Fatigue damage (damage per block)							
CM	2.52×10^{-3}	2.37×10^{-3}	-5.8	2.35×10^{-3}	-6.7	1.99×10^{-3}	-21.0
Morrow	2.40×10^{-3}	2.25×10^{-3}	-6.3	2.23×10^{-3}	-7.1	1.84×10^{-3}	-23.4
SWT	2.32×10^{-3}	2.17×10^{-3}	-6.6	2.15×10^{-3}	-7.3	1.74×10^{-3}	-25.2
Fatigue lives (reversals of blocks)							
CM	$3.97 \times 10^{+2}$	$4.22 \times 10^{+2}$	6.1	$4.26 \times 10^{+2}$	7.2	$5.03 \times 10^{+2}$	26.5
Morrow	$4.17 \times 10^{+2}$	$4.45 \times 10^{+2}$	6.7	$4.48 \times 10^{+2}$	7.6	$5.44 \times 10^{+2}$	30.5
SWT	$4.30 \times 10^{+2}$	$4.60 \times 10^{+2}$	7.0	$4.64 \times 10^{+2}$	7.9	$5.75 \times 10^{+2}$	33.6

Note: diff. = difference = (edited - original) / original x 100 %

Table 4.16 Signal length, number of cycles, fatigue damage and fatigue life differences between the original and edited rural strain signals

Parameters	Original strain signals	Edited strain signals					
		230,000 με²/Hz	Diff. (%)	240,000 με²/Hz	Diff. (%)	250,000 με²/Hz	Diff. (%)
Lengths (s)	120	12.1	-89.9	12.1	-89.9	10.3	-91.4
Cycles	10,019	516	-94.8	516	-94.8	433	-95.7
Fatigue damage (damage per block)							
CM	1.10×10^{-2}	1.09×10^{-2}	-0.7	1.09×10^{-2}	-0.7	9.50×10^{-3}	-13.5
Morrow	1.08×10^{-2}	1.07×10^{-2}	-1.6	1.07×10^{-2}	-1.6	9.25×10^{-3}	-14.5
SWT	1.05×10^{-2}	1.03×10^{-2}	-2.3	1.03×10^{-2}	-2.3	8.91×10^{-3}	-15.3
Fatigue lives (reversals of blocks)							
CM	$9.10 \times 10^{+1}$	$9.16 \times 10^{+1}$	0.7	$9.16 \times 10^{+1}$	0.7	$1.05 \times 10^{+2}$	15.6
Morrow	$9.23 \times 10^{+1}$	$9.39 \times 10^{+1}$	1.7	$9.39 \times 10^{+1}$	1.7	$1.08 \times 10^{+2}$	17.1
SWT	$9.51 \times 10^{+1}$	$9.73 \times 10^{+1}$	2.4	$9.73 \times 10^{+1}$	2.4	$1.12 \times 10^{+2}$	18.0

Note: diff. = difference = (edited - original) / original x 100 %

For S3, decreases were only 0.7 %, 1.6 % and 2.3 % for the Coffin-Manson, Morrow and SWT models for the first and second extractions. However, the decreases became 13.5 %, 14.5 % and 15.3 % for the Coffin-Manson, Morrow and SWT models for the third extraction. Figure 4.50 shows the percentage reductions in signal length, number of cycles and fatigue damage at various EGVs.

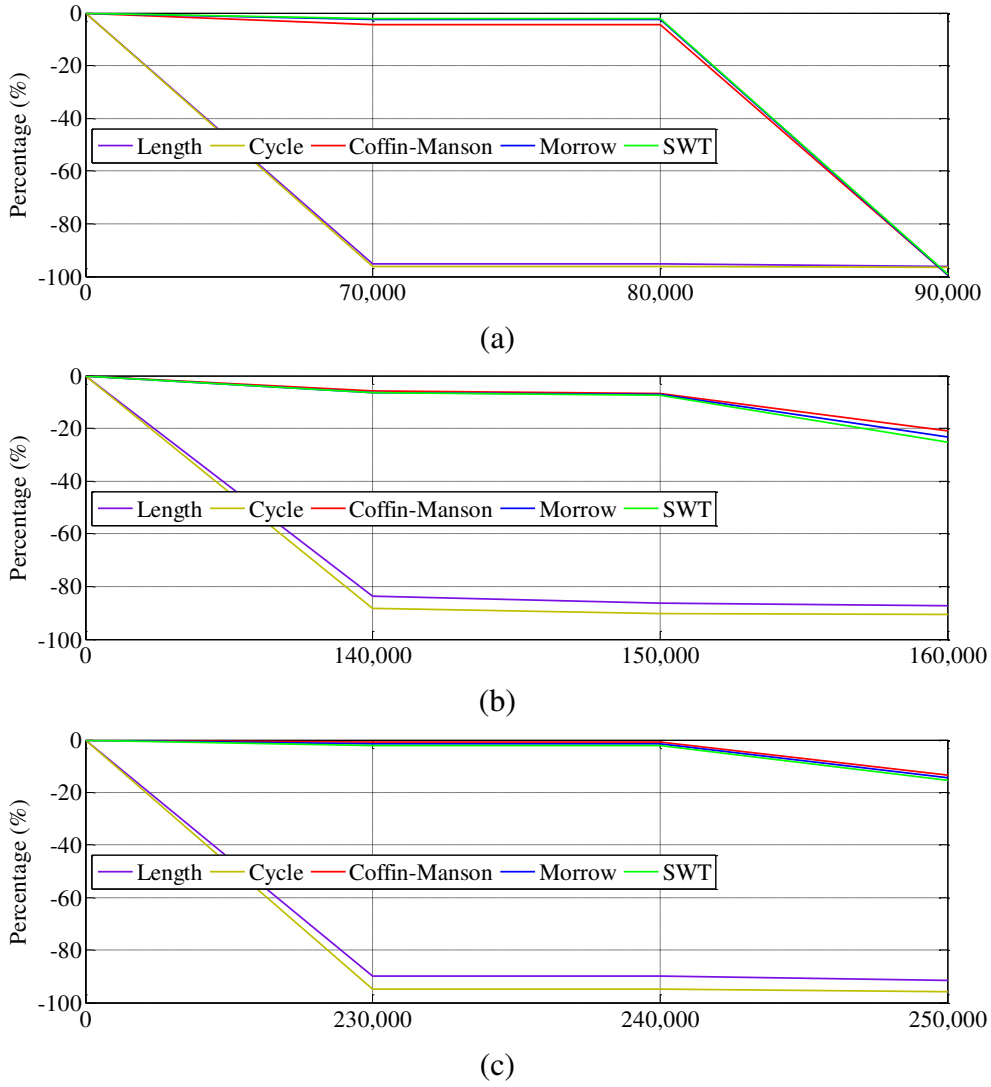

Figure 4.50 Percentage of the signal length, number of cycles and fatigue damage changes at various EGVs: (a) S1-highway, (b) S2-urban, (c) S3-rural

Decreasing the fatigue damage resulted in increasing the fatigue life. For S1, the fatigue life increases of 4.5 %, 2.5 % and 2 % were resulted for the Coffin-Manson, Morrow and SWT models, respectively, for the first and second extractions. An increase of more than 12,000 % was produced for the third extraction for all the models. For S2, increases of 6.1 %, 6.7 % and 7 % were resulted for the Coffin-Manson, Morrow and SWT models for the first extraction. The increases became 7.2 %, 7.6 % and 7.9 % for the Coffin-Manson, Morrow and SWT models for the second extraction. For the third extraction, the increases became 26.5 %, 30.5 % and 33.6 % for the Coffin-Manson, Morrow and SWT models. For S3, increases of 0.7 %, 1.7 % and 2.4 % were resulted for the Coffin-Manson, Morrow and SWT models the first and second extractions. The increases became 15.6 %, 17.1 % and 18 % for the

Coffin-Manson, Morrow and SWT models for the third extraction. Figure 4.51 shows an increase in fatigue life for each edited strain signal. As the EGV increased, the fatigue life increased as well.

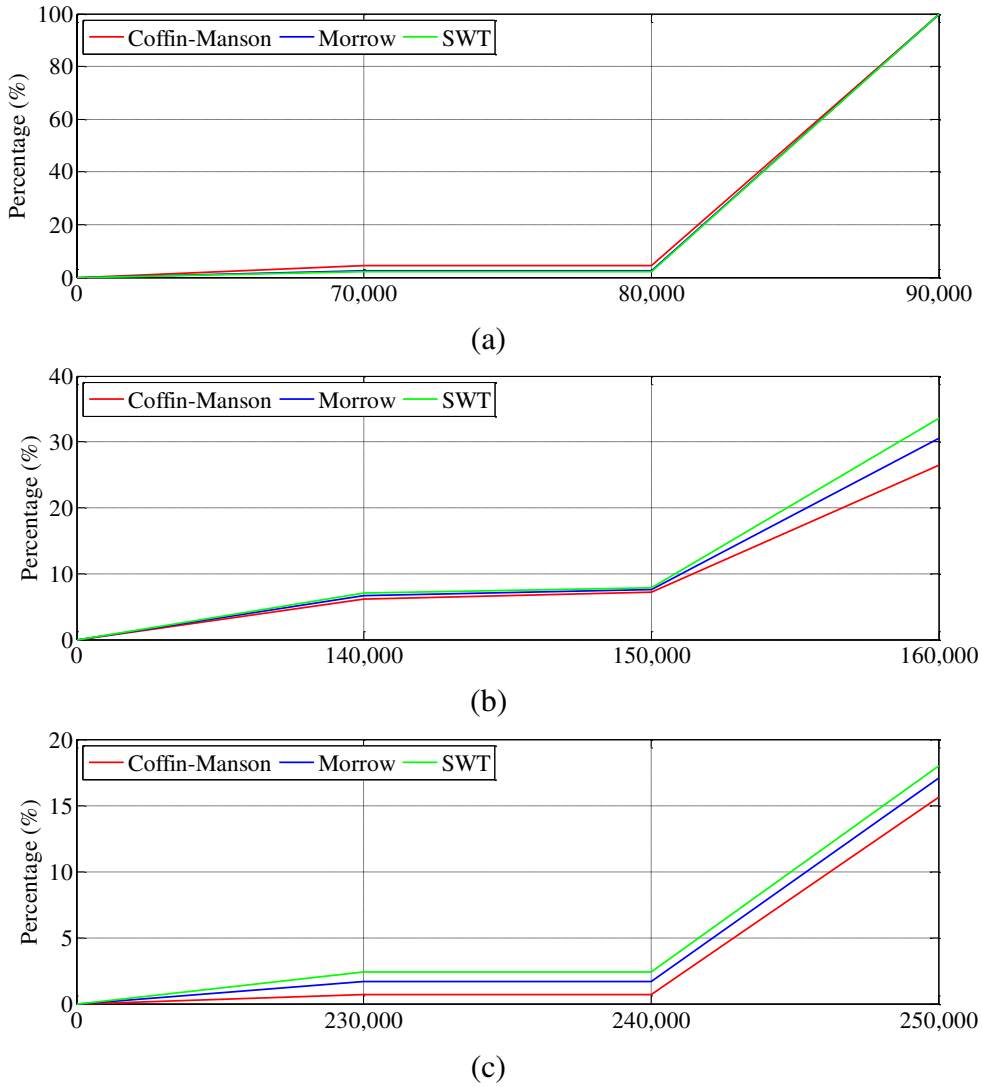

Figure 4.51 Percentage of the fatigue life changes at various EGVs: (a) S1-highway, (b) S2-urban, (c) S3-rural

Similar to the changes of statistical parameters shown in Tables 4.11 to 4.13, the changes of signal length, number of cycles, fatigue damage and fatigue life in Tables 4.14 to 4.16 show that the third extraction provided the highest changes as well, followed by the second and first extractions, respectively. It was due to the third extraction that the EGV applied was higher, and thus, more energy amplitudes were removed. As a result, the edited strain signals were shorter, and had a lower fatigue damage as well as a higher fatigue life.

Since 90,000 $\mu\varepsilon^2$/Hz of EGV for S1 could not give an eligible mission strain signal, out of necessity, the EGV was decreased. Thus, based on the results, 80,000 $\mu\varepsilon^2$/Hz was selected to be the optimum EGV, giving a 5.7-second mission strain signal. This short strain signal gave 95.3 % reduction in length, as the result of the lower energy amplitude removal. The number of cycles counted for the mission strain signal was 427 cycles, which was 96.1 % less than the original cycles. The decreasing number of cycles affected the cumulative fatigue damage. The fatigue damage for the Coffin-Manson, Morrow and SWT models was 3.58 x 10^{-6}, 1.35 x 10^{-5} and 2.05 x 10^{-5} damage per block, respectively, which was only 4.3 %, 2.5 % and 2 % rate of reduction compared to the original fatigue damage. The reduction of fatigue damage indicated that this EGV did not change the strain signal behaviour, since the reduction was in the required range, at ± 10 % of the difference (Stephens et al. 1997; Giacomin et al. 2001). Decreasing the fatigue damage resulted in the increasing fatigue life in the mission strain signal. The amounts of life gathered for the Coffin-Manson, Morrow and SWT models for the mission strain signals were 2.79 x 10^5, 7.39 x 10^4 and 4.88 x 10^4 reversals of blocks, respectively, which was an increase by 4.5 %, 2.5 % and 2 %.

S2 was modified by 83.7 % at EGV of 140,000 $\mu\varepsilon^2$/Hz and changed the fatigue damage for the Coffin-Manson, Morrow and SWT models to 5.8 %, 6.3 % and 6.6 %, respectively. However, according to the extraction results for S2, an EGV of 150,000 $\mu\varepsilon^2$/Hz was found to be an optimum EGV, containing at least 92.7 % of the original fatigue damage in the 16.5-second mission strain signal. An EGV of 150,000 $\mu\varepsilon^2$/Hz was considered optimum because at a higher EGV (160,000 $\mu\varepsilon^2$/Hz), the changes in fatigue damage reached more than 10 %, to the detriment of the original properties of the strain signal (Stephens et al. 1997; Giacomin et al. 2001). With respect to time retention, only 13.7 % of the original signal time length was retained in the optimum EGV. In addition, this extraction removed 90.2 % of the lower amplitude cycles. The number of life increased by at least 7.2 %.

At an EGV of 230,000 $\mu\varepsilon^2$/Hz, the 12.1-second edited strain signal of S3 experienced a decrease of fatigue damage by 0.7 %, 1.6 % and 2.3 % for the Coffin-Manson, Morrow and SWT models, respectively. However, the optimum EGV was

240,000 $\mu\varepsilon^2$/Hz. With the optimum EGV, a S3 of 120 seconds was also shortened by 89.9 % with the fatigue damage retained being at a similar EGV of 230,000 $\mu\varepsilon^2$/Hz. This indicated that the extraction process retained the fatigue damage of at least 97.7 %. Quantitatively, the difference of fatigue damage was in the required level: 10 % difference (Stephens et al. 1997; Giacomin et al. 2001). The counted number of cycles was reduced from 10,019 cycles until failure in the original strain signal to 516 cycles until failure in the mission strain signal. Its fatigue life increased by at least 0.7 %. For an EGV of 250,000 $\mu\varepsilon^2$/Hz, the wavelet-based extraction resulted in a 10.3-second edited strain signal, which was 91.4 % shorter than the original strain signal. Unfortunately, the fatigue damage for the Coffin-Manson, Morrow and SWT models of the mission strain signal changed by 13.5 %, 14.5 % and 15.3 %. Since the fatigue damage given by the mission strain signal was reduced by more than 10 %, the EGV could not be used as the parameter since it changed the original strain signal behaviour.

Figure 4.52a shows that the fatigue damage of the original and edited strain signals at the optimum EGVs was distributed in a 1:2 or 2:1 correlation. For the highway strain signal, the SWT model gave the highest fatigue damage, followed by the Morrow and Coffin-Manson models, respectively, while for the urban and rural strain signals, the highest fatigue damage was provided by the Coffin-Manson model, followed by the Morrow and SWT models, respectively. The RMSE for the Coffin-Manson, Morrow and SWT models was 0.007 %, 0.004 % and 0.001 %, respectively. In Figure 4.52b, the coefficient of determination was 0.9998 with an error of 0.0078 %. With such as a high correlation and a minimum error, there was no significant difference in terms of fatigue damage between the original and edited strain signals. It was indicated that the developed FDE algorithm successfully detected and removed lower amplitudes in the strain signals with a mininal effect to fatigue damage.

Overall, the FDE technique was able to identify segments having higher fatigue damage and remove non-damaging segments with magnitudes less than the EGV based on their positions on the time axis in the original strain signals to improve their fatigue life. According to the findings, the FDE technique effectively

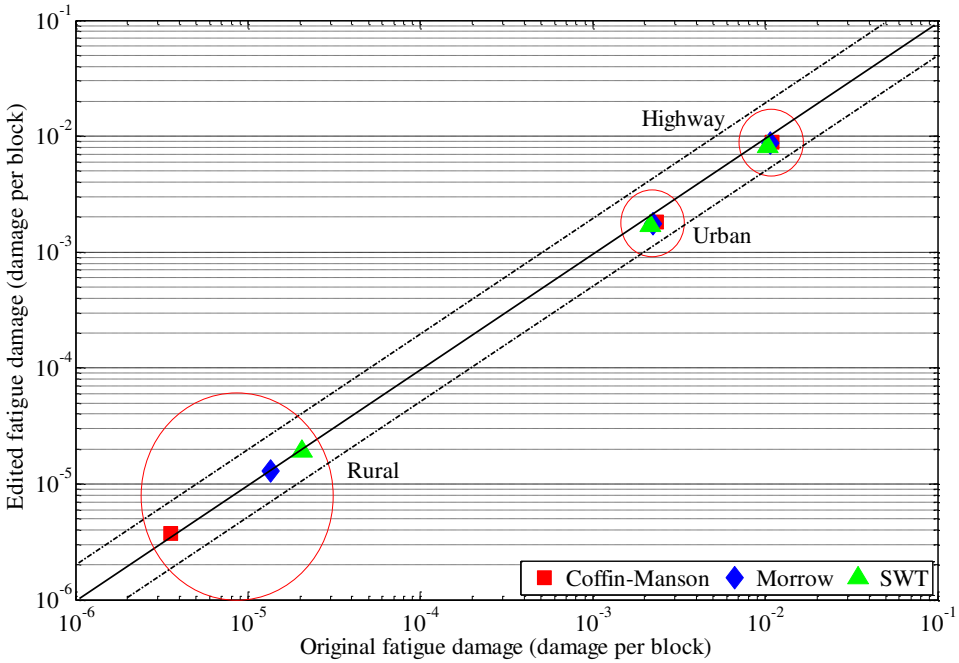

(a)

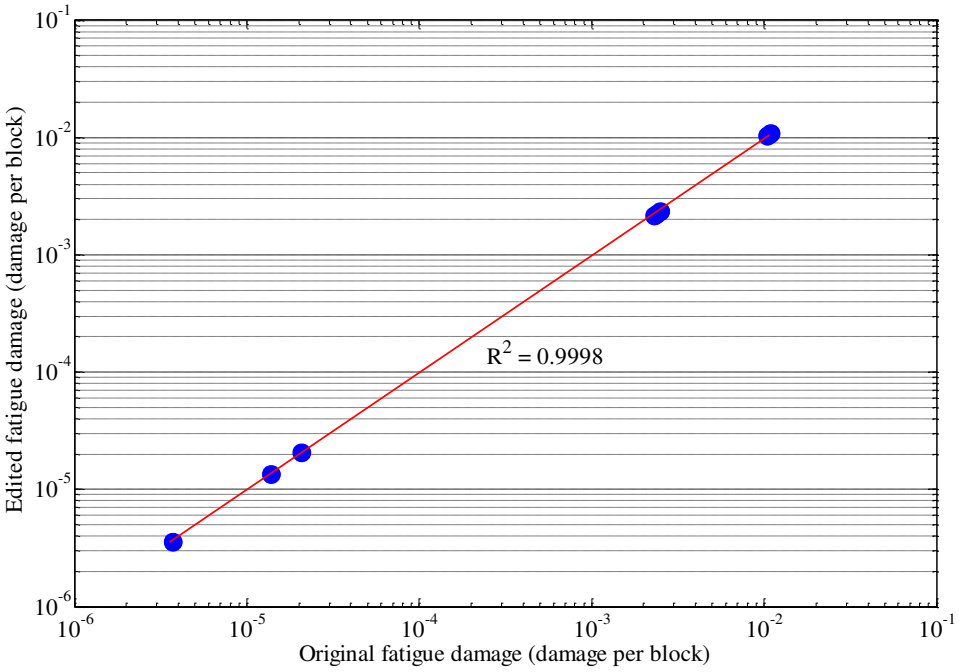

(b)

Figure 4.52 Fatigue damage distributions for the original and edited strain signals: (a) 1:2 or 2:1 correlation, (b) coefficient of determination

summarised the strain signals by more than 86 % with less than 10 % difference with respect to the fatigue damage (Stephens et al. 1997; Giacomin et al. 2001) to ascertain that the extractions did not significantly affect the original behaviour. For the differences of fatigue damage less than 5.7 %, the FDE technique was able to shorten S1 by up to 5.7 seconds, or 95.3 % shorter than the original strain signal. The modified strain signal of S2 gave 16.5 seconds, giving 86.3 % of the original time length reduction containing at least 92.7 % of the original fatigue damage. The optimum EGV for S3 provided 12.1 seconds of the edited strain signal with a reduction in length by 89.9 % and it was able to retain more than 97.7 % of the fatigue damage.

Any lower cycles were found at allowable levels to be omitted. These results show that all the edited strain signals qualify for the FDE requirement. It showed interesting results in the extraction of the strain signals measured at an automotive coil spring. Different strain signals gave different results, because each strain signal had a different behaviour. Lower amplitudes in the strain signals determined the length of the edited strain signals, since more amplitudes were removed. Thus, S1 with more low strain amplitudes had less time in its edited strain signal compared to S3 and S2. Furthermore, the edited strain signals of S1, S2 and S3 were called S7, S8 and S9, respectively.

The fatigue damage potential distributions for each cycle derived from the original and edited strain signals were displayed in the form of three-dimensional histograms in Figures 4.53 to 4.61. The *x*-axis represents the range of the strain, the *y*-axis represents the cycles and the fatigue damage to the number of fatigue cycles at the same range and mean, and the *z*-axis represents the mean strain. The counted number of cycles was reduced from 591, 931 and 1,413 cycles until failure in the original strain signals to 32, 65 and 113 cycles until failure in the mission strain signals for the highway, urban and rural strain signals, respectively.

Higher fatigue damage was located at higher cycle ranges, whereas the cycles at lower strain range showed lower fatigue damage despite having higher cycle numbers. The maximum fatigue damage was contributed by cycles that had the highest range, or the tallest column, in the histogram plots. The fatigue damage displayed on the histograms was products of the fatigue damage at one cycle with

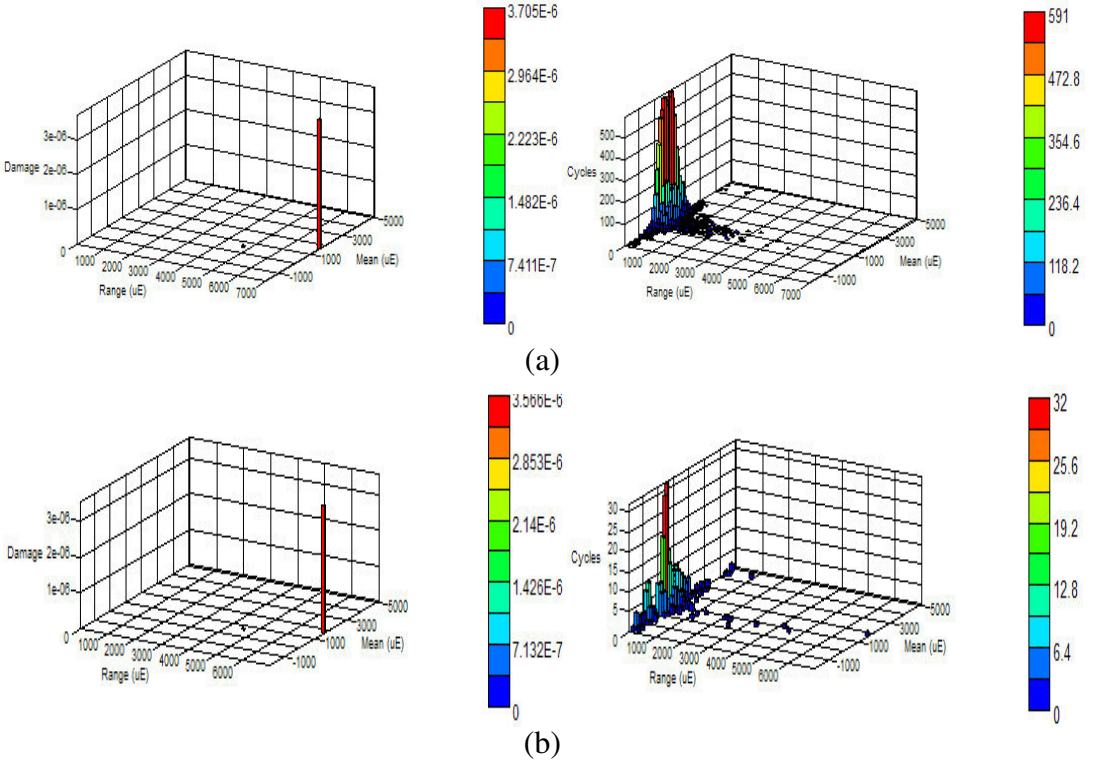

Figure 4.53 Distributions of fatigue damage and cycle range based on the Coffin-Manson model for the highway strain signal: (a) S1-original, (b) S7-edited

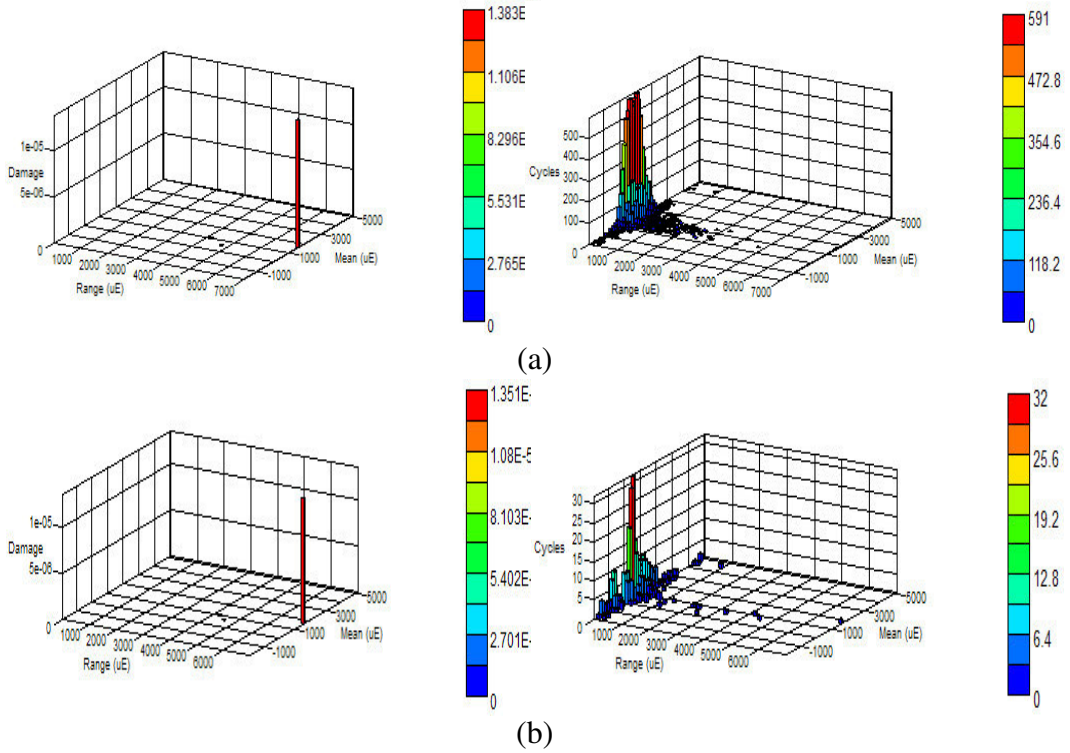

Figure 4.54 Distributions of fatigue damage and cycle range based on the Morrow model for the highway strain signal: (a) S1-original, (b) S7-edited

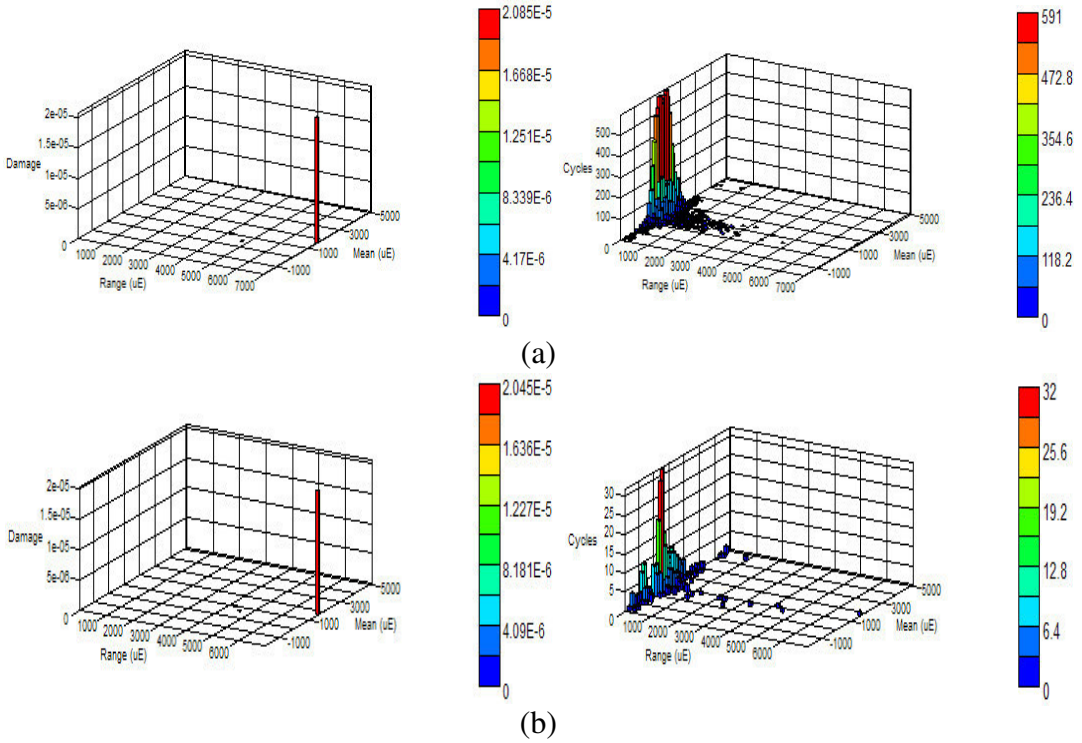

Figure 4.55 Distributions of fatigue damage and cycle range based on the SWT model for the highway strain signal: (a) S1-original, (b) S7-edited

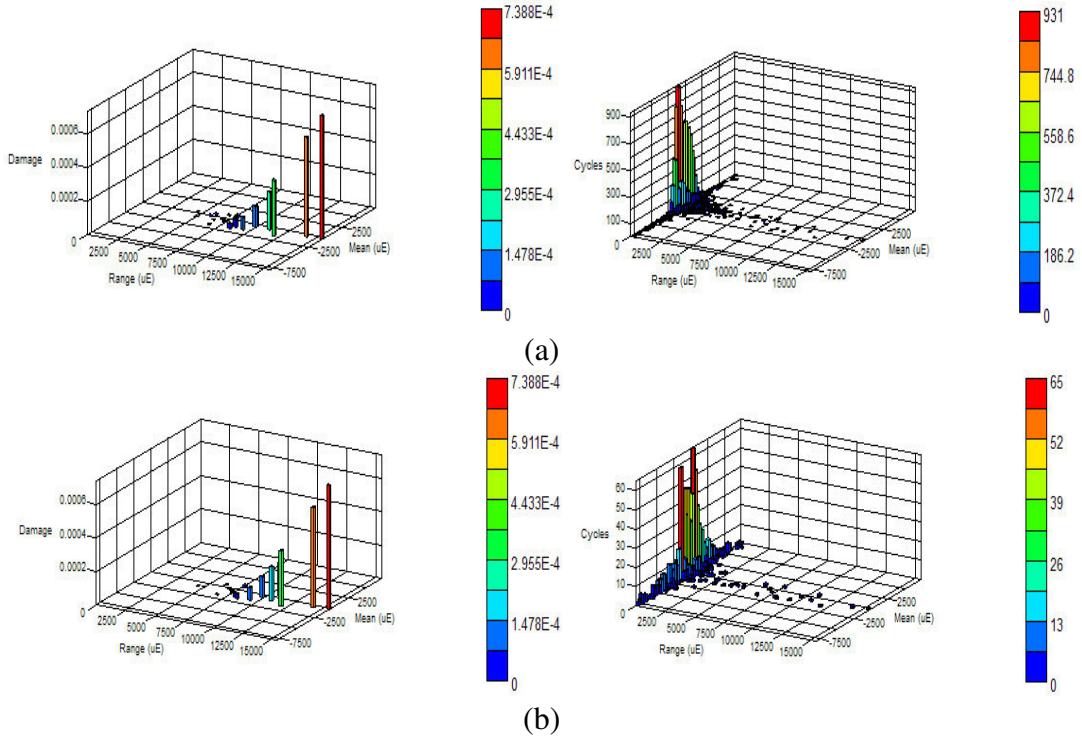

Figure 4.56 Distributions of fatigue damage and cycle range based on the Coffin-Manson model for the urban strain signal: (a) S2-original, (b) S8-edited

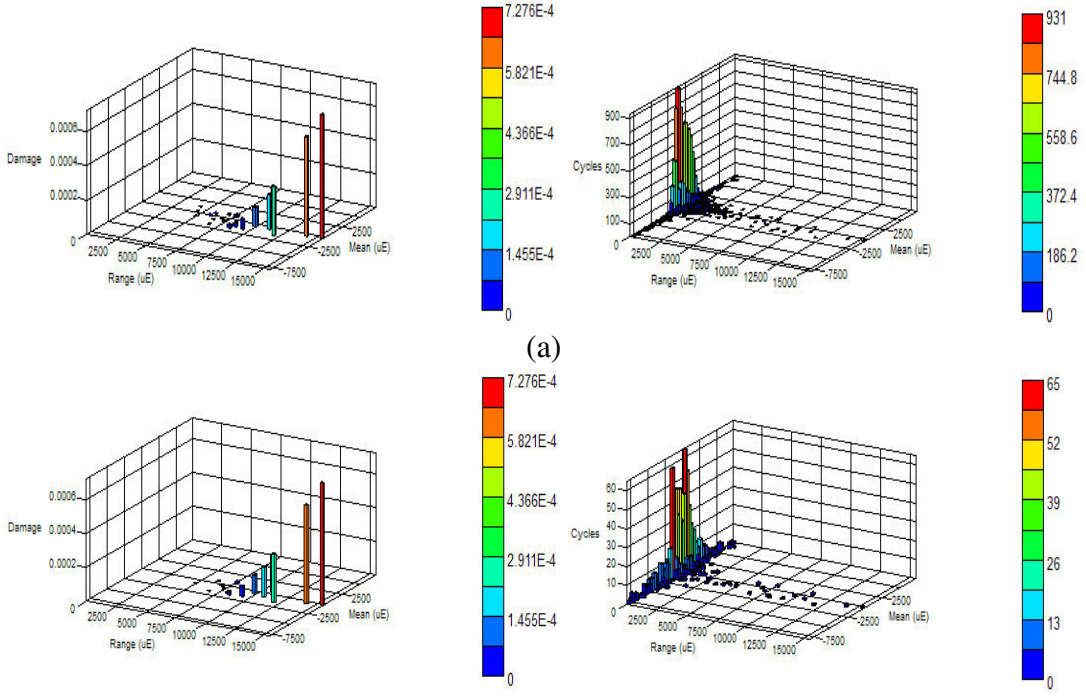

Figure 4.57 Distributions of fatigue damage and cycle range based on the Morrow model for the urban strain signal: (a) S2-original, (b) S8-edited

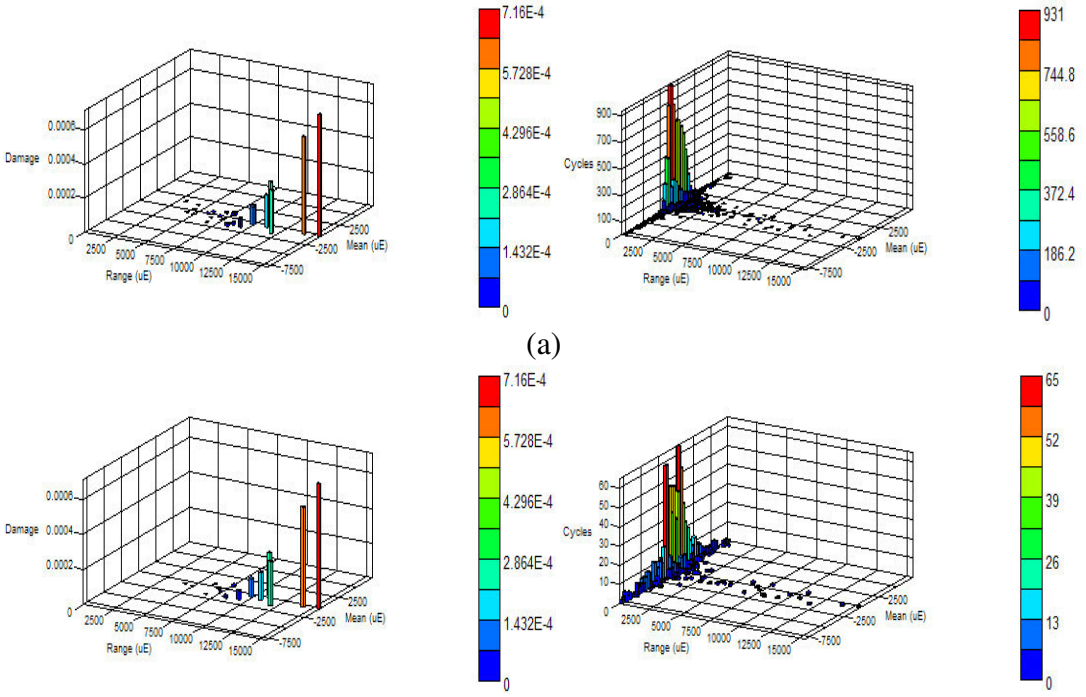

Figure 4.58 Distributions of fatigue damage and cycle range based on the SWT model for the urban strain signal: (a) S2-original, (b) S8-edited

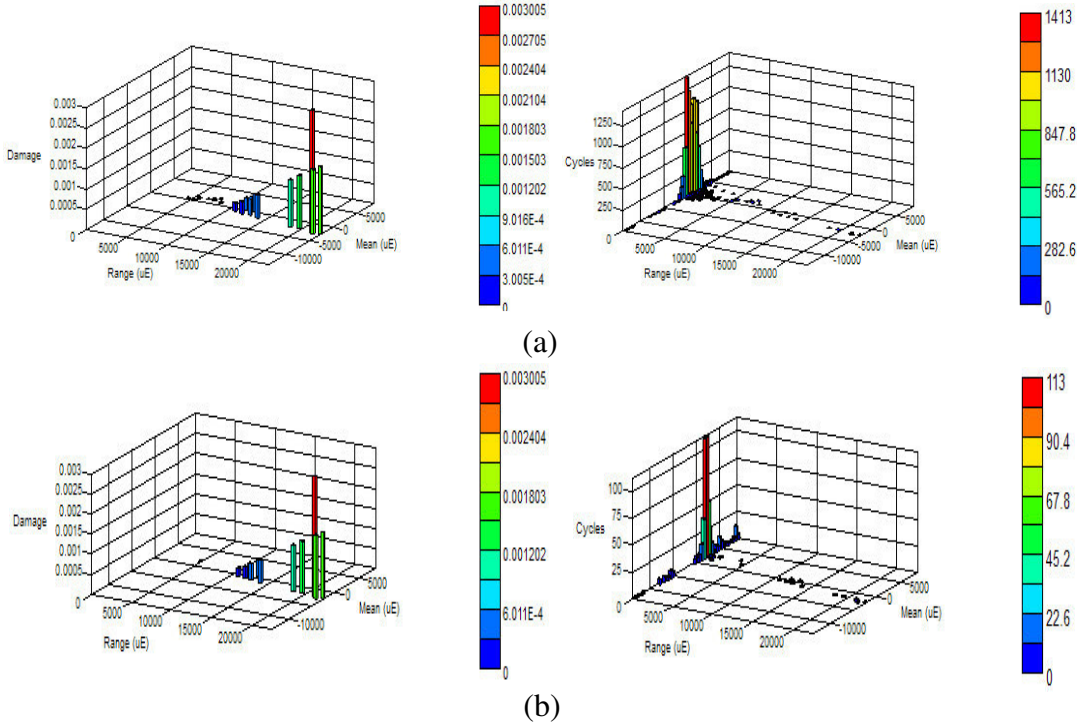

Figure 4.59 Distributions of fatigue damage and cycle range based on the Coffin-Manson model for the rural strain signal: (a) S3-original, (b) S9-edited

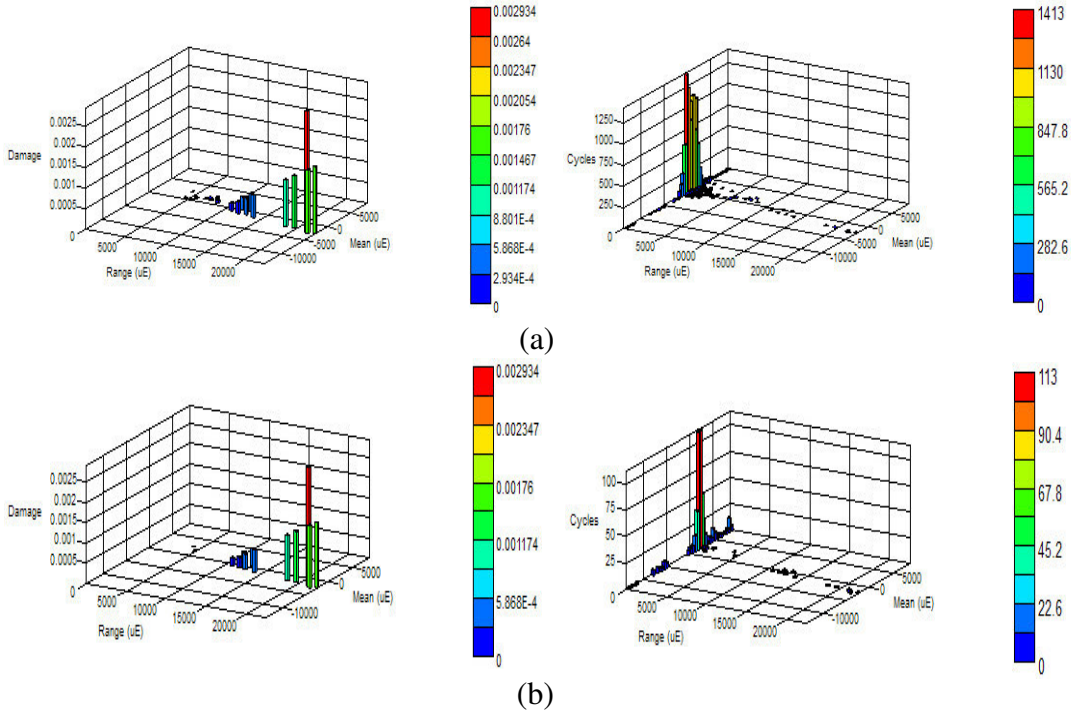

Figure 4.60 Distributions of fatigue damage and cycle range based on the Morrow model for the rural strain signal: (a) S3-original, (b) S9-edited

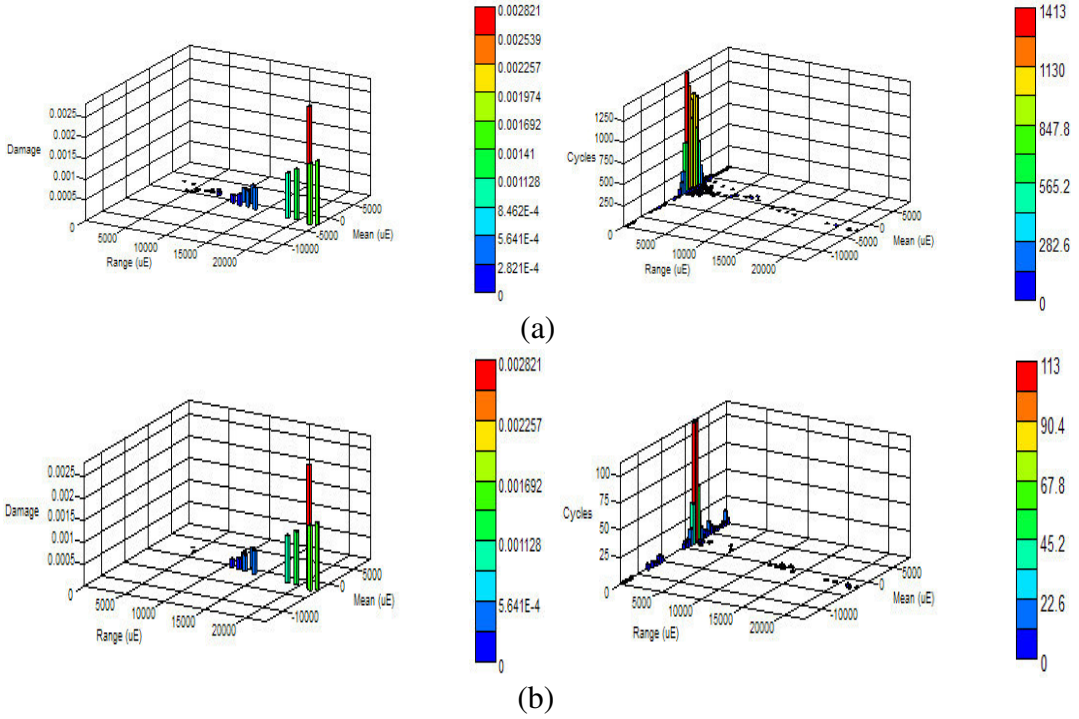

Figure 4.61 Distributions of fatigue damage and cycle range based on the SWT model for the rural strain signal: (a) S3-original, (b) S9-edited

the number of cycles in the strain signals. The Palmgren-Miner linear fatigue damage rule was then used to determine the overall fatigue damage of the strains applied. In the extraction process, all ranges that were less than the EGV were removed. When looking at each histogram, although the original strain signals were edited, the range and mean values in the mission strain signals remained unchanged compared to the original strain signals. The histograms demonstrate that at lower cycle ranges, the fatigue damage was found to be zero, or at a very minimum value, therefore, the removal of these cycles did not provide much effect to the total fatigue damage.

The modified strain signals were also validated using the PSD to see their effectiveness in maintaining the original characteristics of the strain signals, especially the energy they contain. The decreases of the PSD amplitude indicated the removal of lower energy located at a higher frequency region. However, the edited strain signals gave a similar PSD pattern as the original strain signals. This condition was very convenient for the PSD plots in Figure 4.62. The tidal components appeared as distinctive peaks at about 0 Hz and 5 Hz. The areas that were below the PSD graphs were calculated as well and the results are listed in Table 4.17. The energy for S7, S8

and S9 decreased by 96.4 %, 60.7 % and 77.2 %, respectively, as a result of the extraction process. The decreases in energy, as shown in Figure 4.63, were because r.m.s. for the modified strain signals was not controlled so the energy decreases were higher.

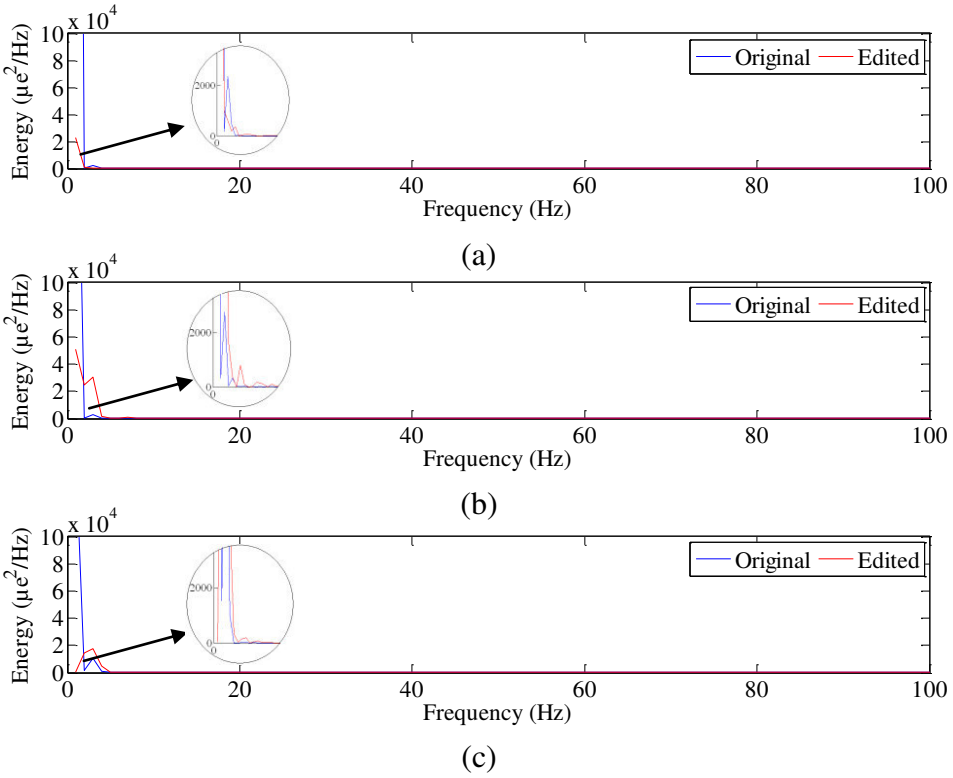

Figure 4.62 PSD comparisons between the original and edited strain signals: (a) highway, (b) urban, (c) rural

Table 4.17 PSD area differences between the original and edited strain signals

Strain signals	Original ($\mu\varepsilon^2$/Hz)	Edited ($\mu\varepsilon^2$/Hz)	Differences (%)
Highway	7.14 x 10^5	2.55 x 10^4	-96.4
Urban	2.81 x 10^5	1.10 x 10^5	-60.7
Rural	1.65 x 10^5	3.77 x 10^4	-77.2

Note: difference = (edited - original) / original x 100 %

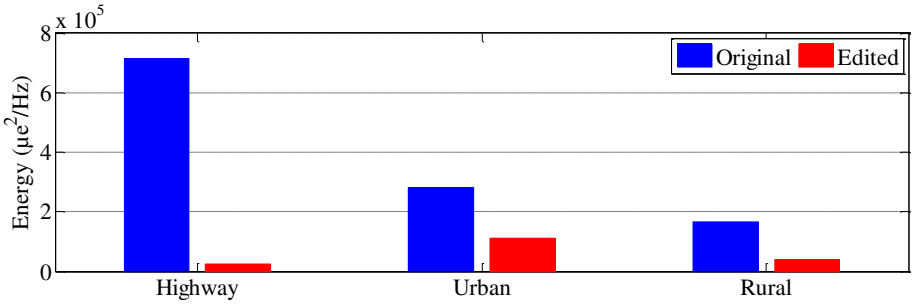

Figure 4.63 PSD differences for the original and edited strain signals

In the next task of the study, S4, S5 and S6 were edited as well. The wavelet coefficients for S4, S5 and S6 are shown in Figures 4.64b, 4.65b and 4.66b, respectively. The energy distributions of the simulated strain signals in Figures 4.64c, 4.65c and 4.66c, respectively, were similar to the energy distributions of the actual strain signals, as shown in Figures 4.37c, 4.38c and 4.39c, showing the accuracy of

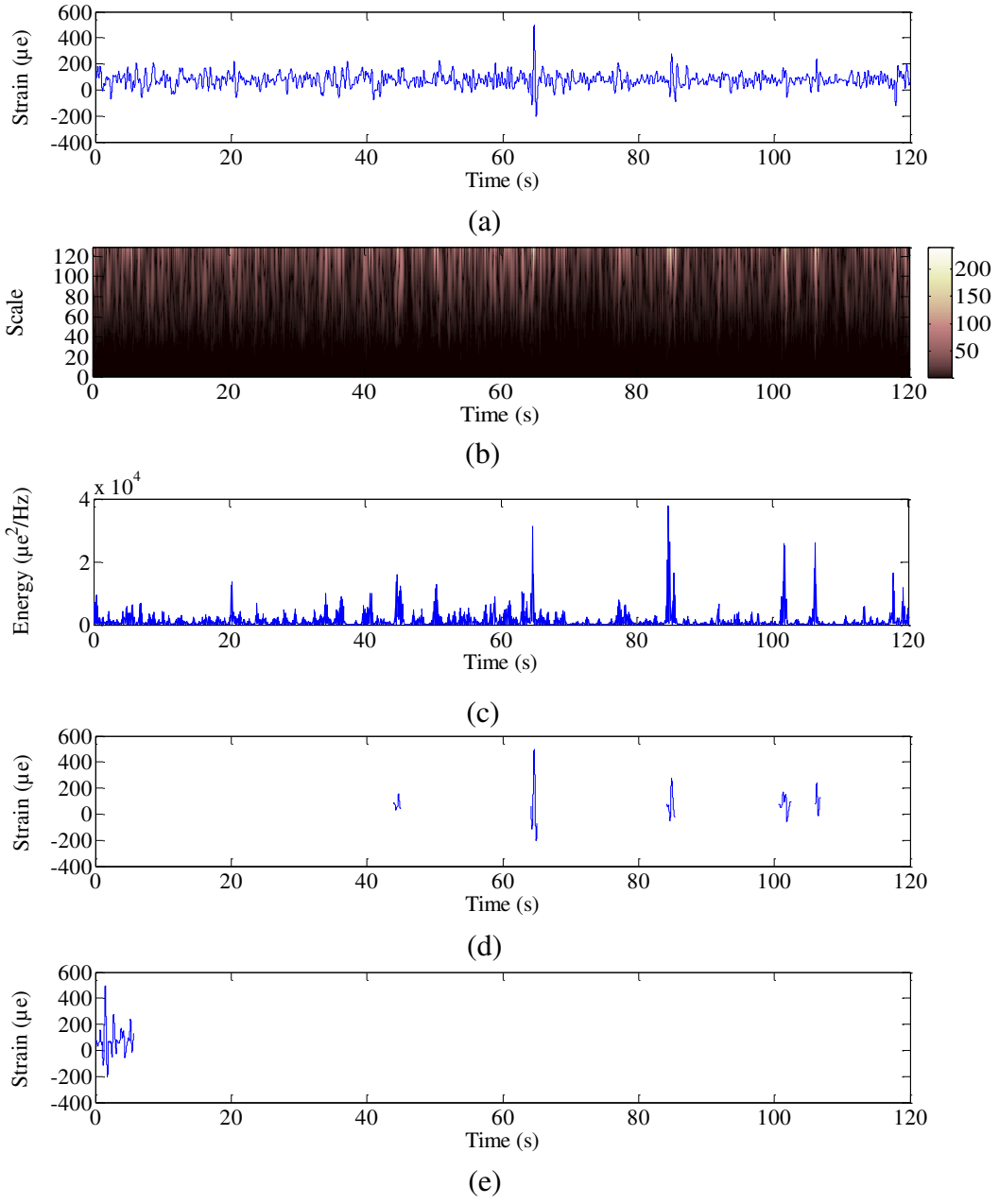

Figure 4.64 Fatigue feature extraction of the simulated highway strain signal: (a) time history strain signal, (b) wavelet coefficient, (c) energy distribution, (d) retained segments, (e) 5.7-second modified strain signal

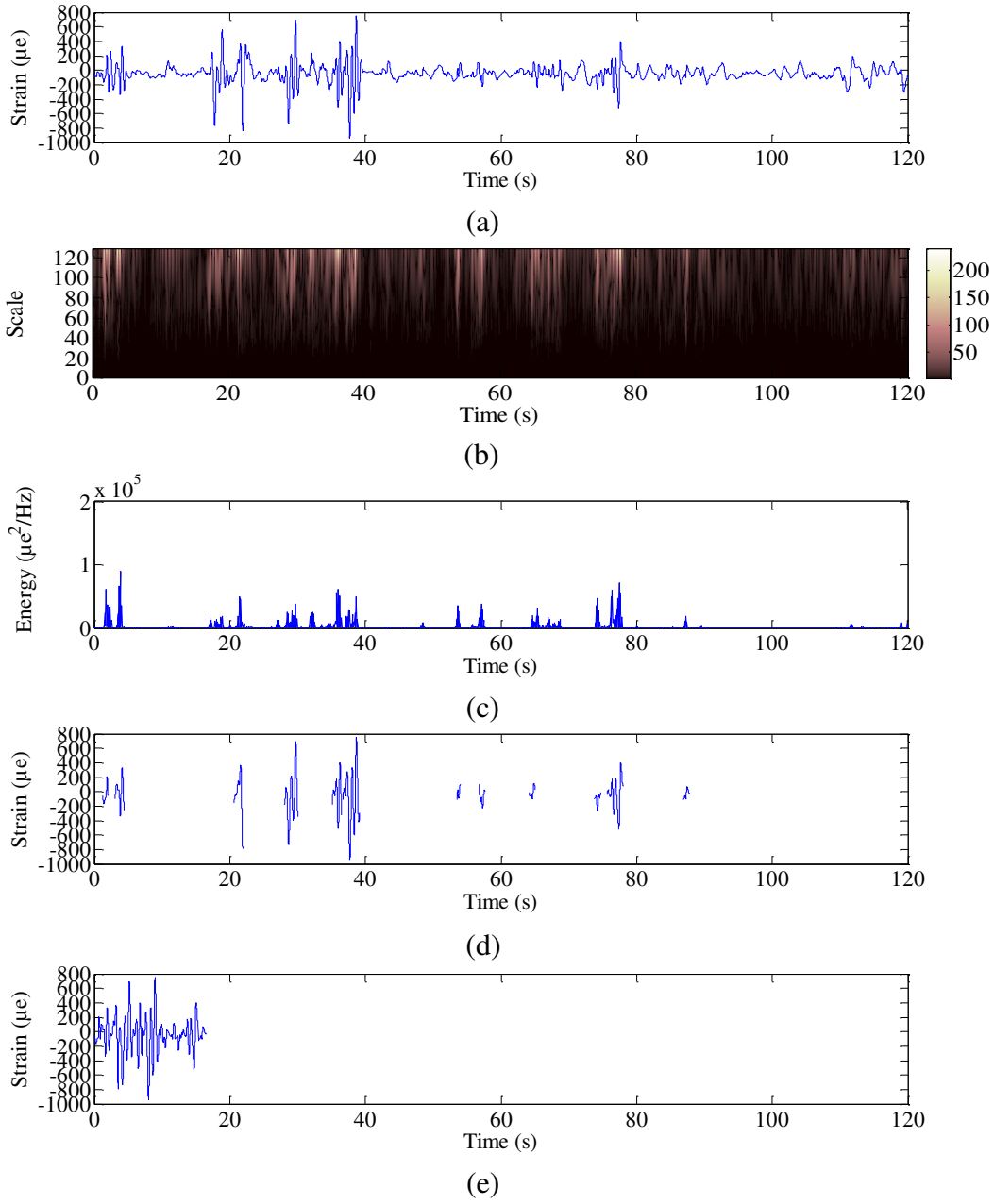

Figure 4.65 Fatigue feature extraction of the simulated urban strain signal: (a) time history strain signal, (b) wavelet coefficient, (c) energy distribution, (d) retained segments, (e) 16.5-second modified strain signal

the simulation. The extraction of S4, S5 and S6 was based on higher amplitude locations in S1, S2 and S3, respectively. Due to the actual and simulated strain signals being extracted at the same positions, the total of segments resulted from the extraction of S4, S5 and S6 was equivalent to the segments resulted from the extraction of S1, S2 and S3, respectively. The equivalent number of segments aimed to make the clustering processes in the next stage easier.

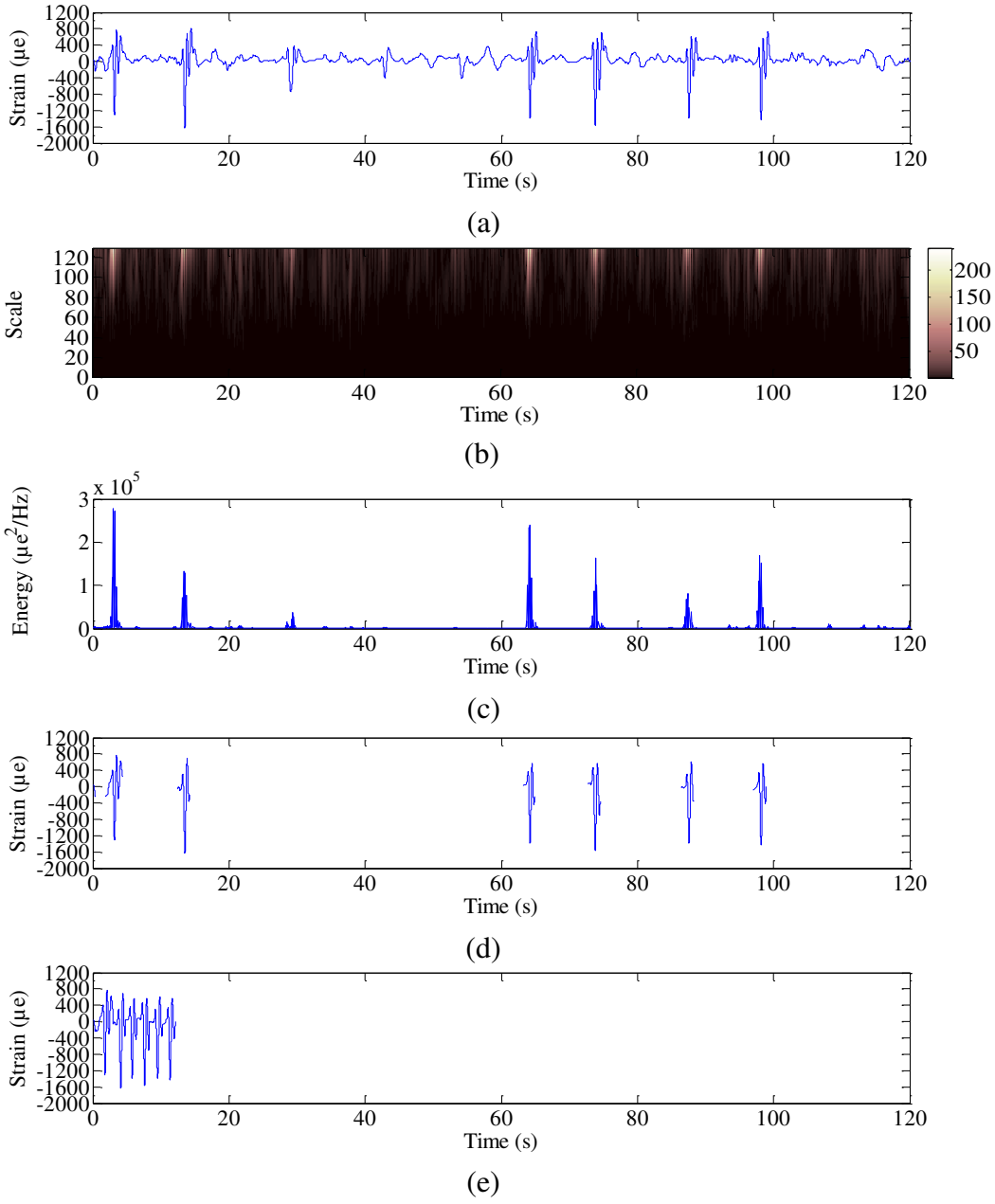

Figure 4.66 Fatigue feature extraction of the simulated rural strain signal: (a) time history strain signal, (b) wavelet coefficient, (c) energy distribution, (d) retained segments, (e) 12.1-second modified strain signal

Referring to Figure 4.43c, S1 extracted at the optimum EGV produced six non-damaging segments and five damaging segments. For S2, thirteen non-damaging segments and twelve damaging segments were obtained, as shown in Figure 4.44c. Furthermore, seven non-damaging and damaging segments were resulted in the S3 extraction, as shown in Figure 4.45c. The retained segments of S4, S5 and S6 are shown in Figures 4.64d, 4.65d and 4.66d, respectively. The damaging segments were

then assembled together to produce edited strain signals as well. The edited strain signals of S4, S5 and S6, called S10, S11 and S12, respectively, are shown in Figures 4.64e, 4.65e and 4.66e. S10, S11 and S12 had similar lengths as S7, S8 and S9, respectively, which were 5.7 seconds, 16.5 seconds and 12.1 seconds since they were extracted at the same positions.

The statistical and fatigue damage changes after extracting the simulated strain signals were observed. The statistical changes are listed in Table 4.18, while Tables 4.19 to 4.21 provide the fatigue damage changes for each strain signal. SD and r.m.s. increased by more than 95 % and 44 %, respectively, and the r.m.s. change almost reached 150 % for the rural strain signal. While kurtosis decreased by up to 81.8 % for the rural strain signal, as shown in Figure 4.67. There was no significant change in fatigue damage for the highway strain signal. However, a decrease of more than 16 % was resulted in for the urban and rural strain signals, as shown in Figure 4.68. Higher differences were because the simulated strain signals were extracted based on the energy locations of the actual strain signals, and were not based on their own energy.

Table 4.18 Statistical differences between the original and edited simulated strain signals

Parameters	Strain signals								
	S4	**S10**	**Diff. (%)**	**S5**	**S11**	**Diff. (%)**	**S6**	**S12**	**Diff. (%)**
SD (με)	50.4	108.2	114.6	125.8	246.2	95.7	202	490.8	143
r.m.s. (με)	92.1	132.8	44.1	134.6	242.1	79.9	204.9	502	144.9
Kurtosis	8.5	6.1	-28.2	13.8	5.1	-63.1	22.9	4.2	-81.8

Note: diff. = difference = (edited - original) / original x 100 %

Table 4.19 Fatigue damage differences between the original and edited simulated highway strain signals

Parameters	Strain signals		
	S4	**S10**	**Differences (%)**
Coffin-Manson (damage per block)	3.71×10^{-6}	3.71×10^{-6}	0
Morrow (damage per block)	1.29×10^{-5}	1.29×10^{-5}	0
SWT (damage per block)	1.93×10^{-5}	1.93×10^{-5}	-0.1

Note: difference = (edited - original) / original x 100 %

Table 4.20 Fatigue damage differences between the original and edited simulated urban strain signals

Parameters	Strain signals		
	S5	S11	Differences (%)
Coffin-Manson (damage per block)	2.56×10^{-3}	1.83×10^{-3}	-28.3
Morrow (damage per block)	2.42×10^{-3}	1.75×10^{-3}	-27.3
SWT (damage per block)	2.31×10^{-3}	1.70×10^{-3}	-26.3

Note: difference = (edited - original) / original x 100 %

Table 4.21 Fatigue damage differences between the original and edited simulated rural strain signals

Parameters	Strain signals		
	S6	S12	Differences (%)
Coffin-Manson (damage per block)	1.07×10^{-2}	8.92×10^{-3}	-16.5
Morrow (damage per block)	1.08×10^{-2}	8.67×10^{-3}	-19.8
SWT (damage per block)	1.06×10^{-2}	8.20×10^{-3}	-22.4

Note: difference = (edited - original) / original x 100 %

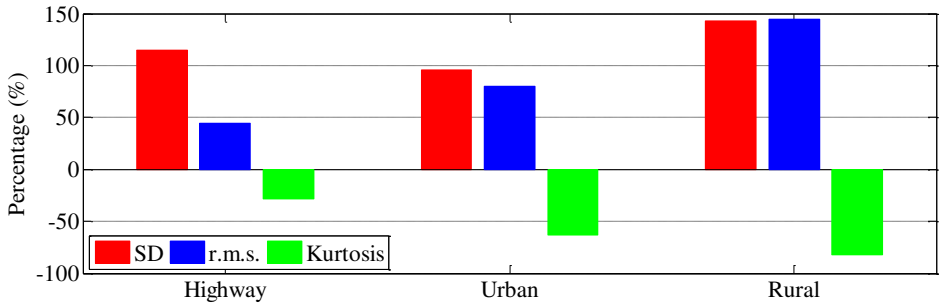

Figure 4.67 Percentage of the statistical parameter differences between the original and edited simulated strain signals

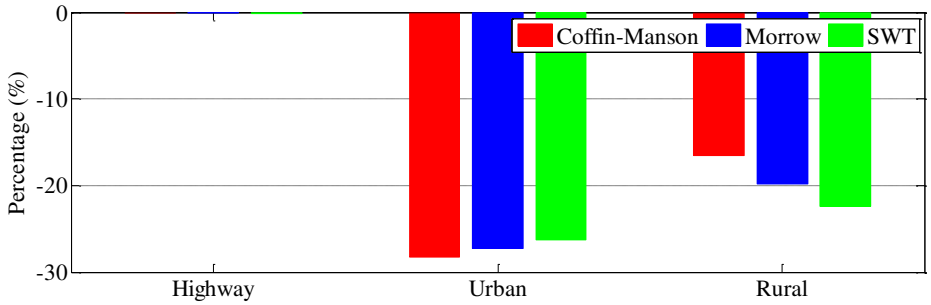

Figure 4.68 Percentage of the fatigue damage differences between the original and edited simulated strain signals

After extracting the actual and simulated strain signals, the acceleration signals in Figure 4.8 were also extracted for validation purposes. In order to validate the acceleration signals, some statistical analyses were performed. Figures 4.69 to 4.71 show the acceleration segments contributing to fatigue failure. The segments were the results of extraction based on the actual strain signals. Most the segments were concentrated in the range of 90 % confidence interval, as presented in Figure 4.72.

The coefficients of determination in terms of statistical parameters between the strain and acceleration segments are presented in Figures 4.73 to 4.75. In Figure 4.73, SD gave a coefficient of determination of 0.9546, 0.8132 and 0.9168 for the highway, urban and rural segments, respectively, described as a strong and significant correlation. A strong and significant correlation was also obtained in r.m.s. for the highway, urban and rural segments giving a coefficient of determination of 0.9117, 0.9033 and 0.9023, respectively, as shown in Figure 4.74. Although a coefficient of determination of 0.2084 was obtained for the rural segments, kurtosis gave a coefficient of determination of 0.9203 and 0.8899 for the highway and urban segments, respectively, as shown in Figure 4.75. A lower correlation in kurtosis for the rural segments was contributed by a segment having high kurtosis in the strain segment but low kurtosis in the acceleration segment, as the effect of the simplified simulated model.

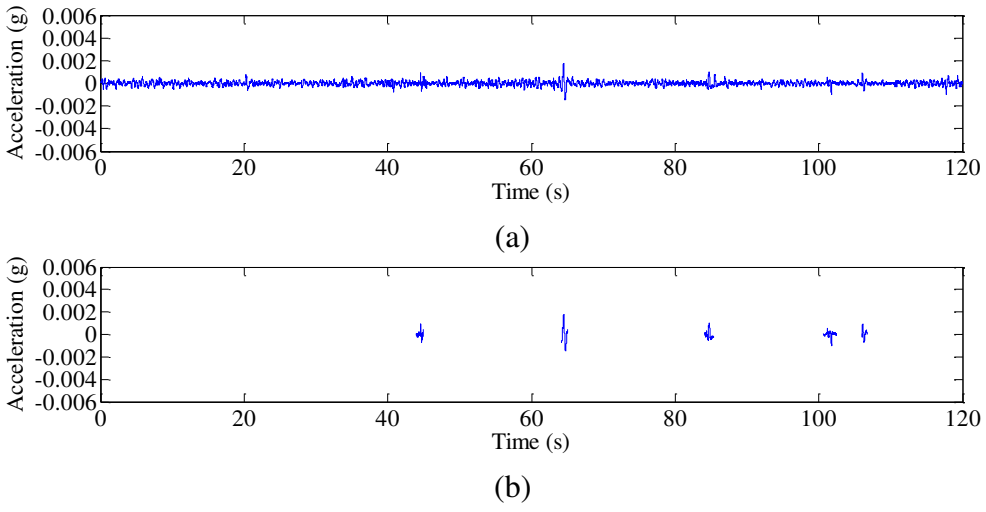

Figure 4.69 Damaging segments of the highway acceleration signal: (a) time series signal, (b) damaging segments

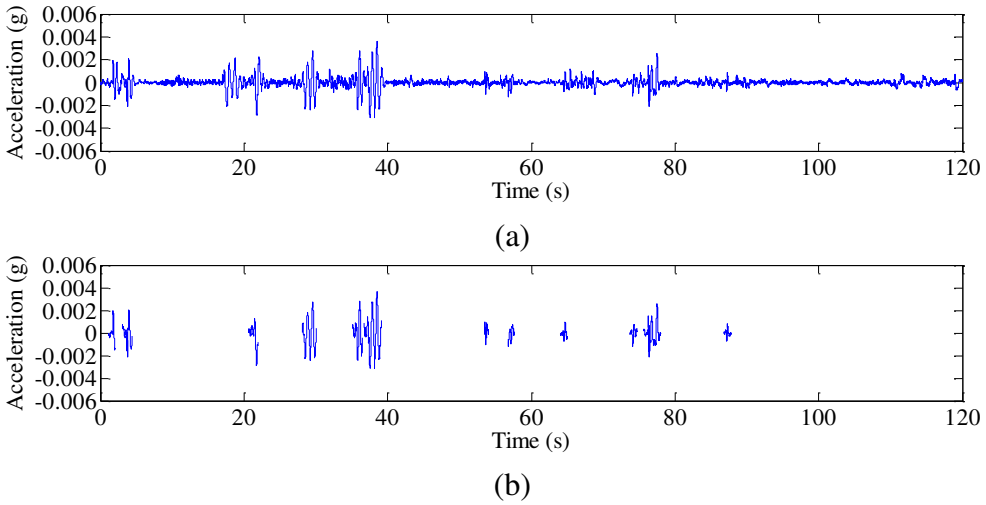

Figure 4.70 Damaging segments of the urban acceleration signal: (a) time series signal, (b) damaging segments

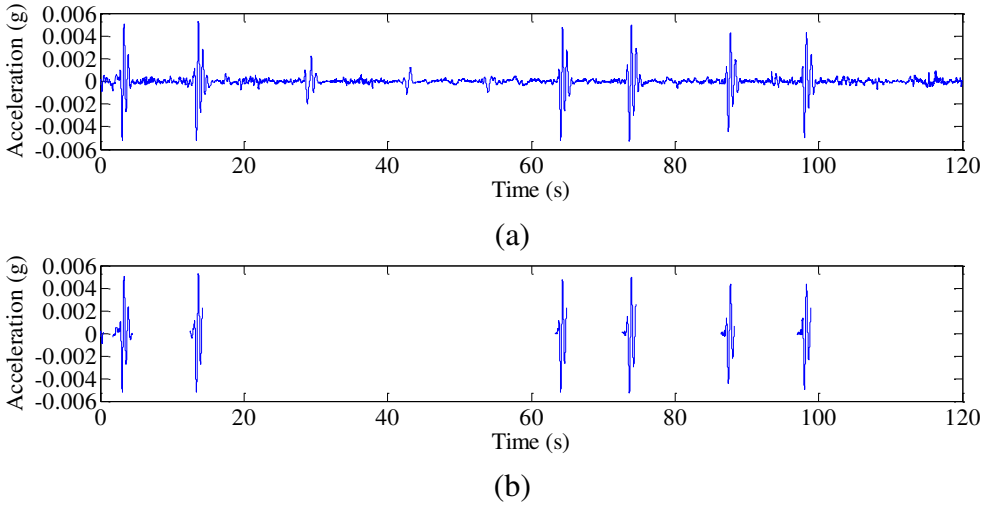

Figure 4.71 Damaging segments of the rural acceleration signal: (a) time series signal, (b) damaging segments

In addition, if all the segments were combined, the coefficients of determination resulted were 0.9294, 0.9284 and 0.7693 for SD, r.m.s. and kurtosis, respectively, with an error of 0.049 %, 0.019 % and 86.32 %. The strain and acceleration segments gave a perfect linear correlation, especially for SD and r.m.s. It shows that the strain-based model developed in Section 3.1.3 was suitable with a good correlation. In order to investigate the ability of the MBD simulation to generate a simulated strain signal, and to investigate the accuracy of the FDE technique in identifying amplitude changes to yield an optimum higher amplitude segment, it was decided to cluster the resulting segments from the extraction process. Thus, in the subsequence segment of the study, the correlations between SD, r.m.s., kurtosis and energy to fatigue damage were observed.

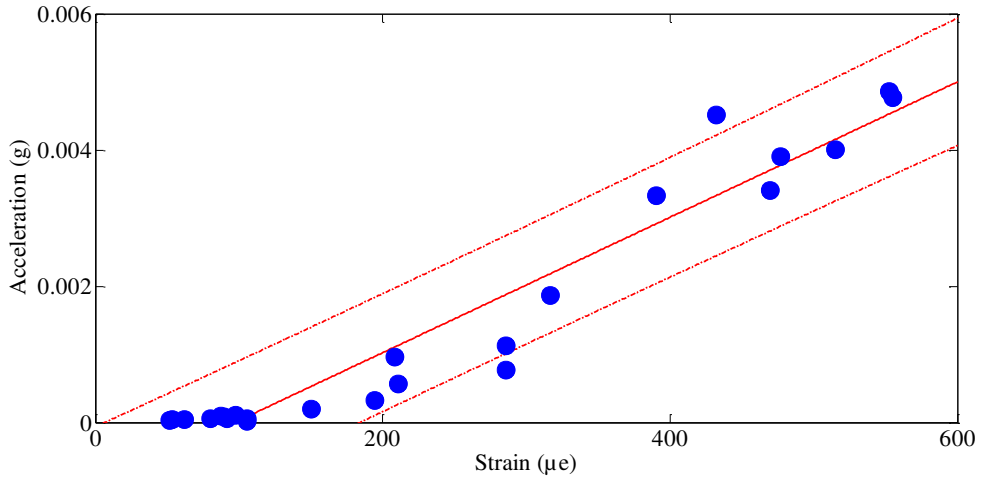

(a)

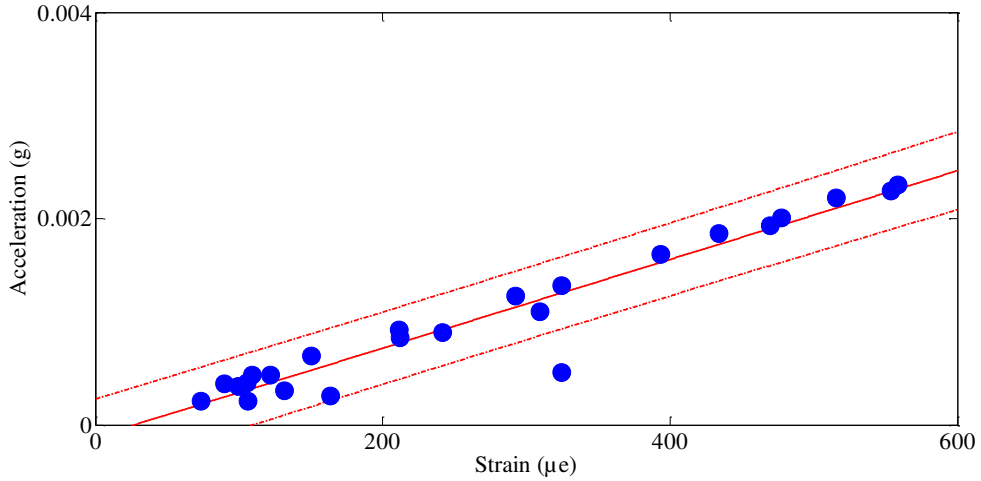

(b)

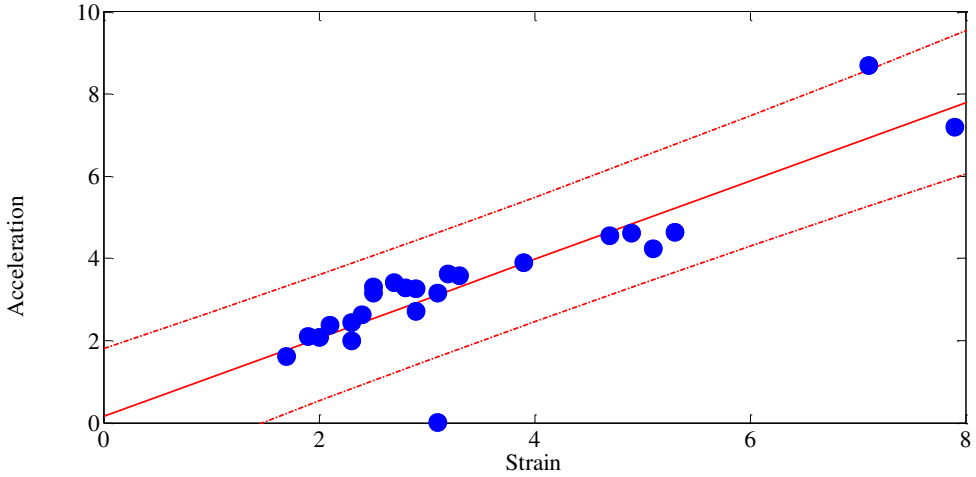

(c)

Figure 4.72 Acceleration and strain segment distributions in the 90 % confidence interval: (a) SD, (b) r.m.s., (c) kurtosis

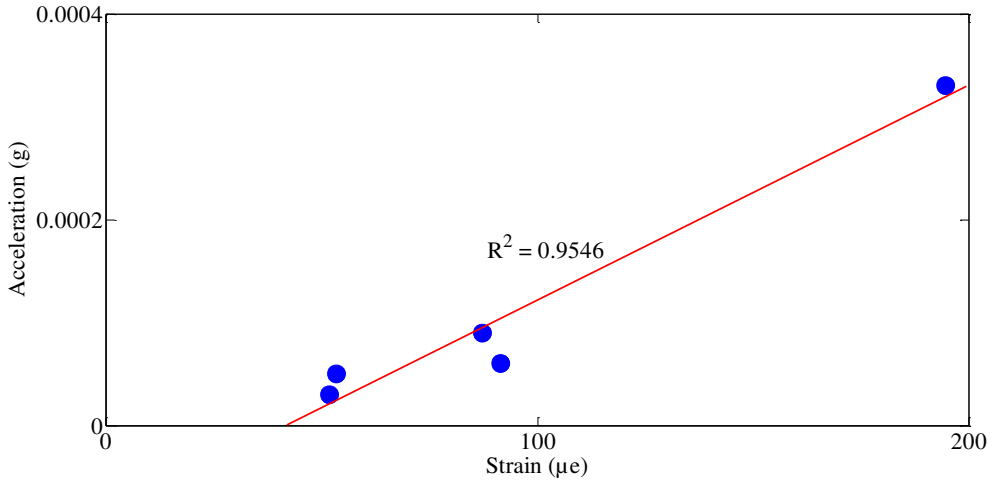

(a)

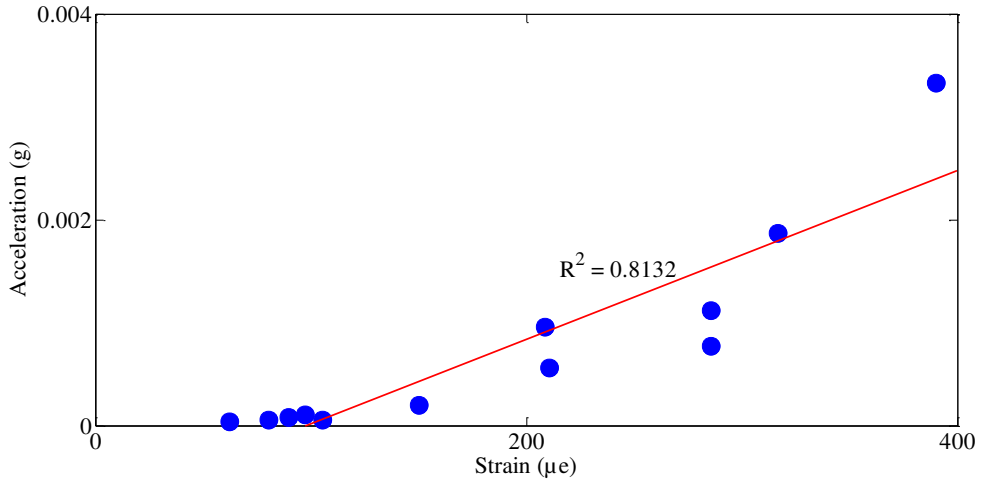

(b)

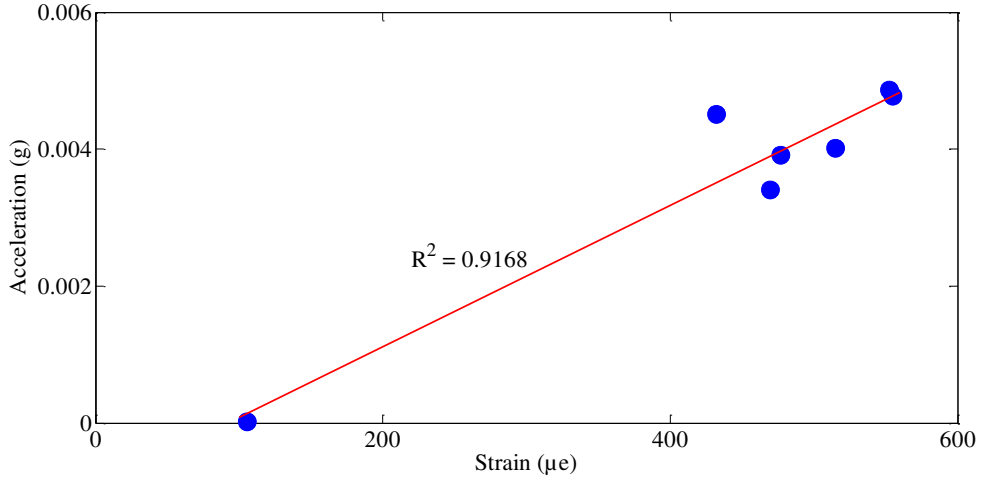

(c)

Figure 4.73 Coefficient of determination for SD between the acceleration and strain segments: (a) highway, (b) urban, (c) rural

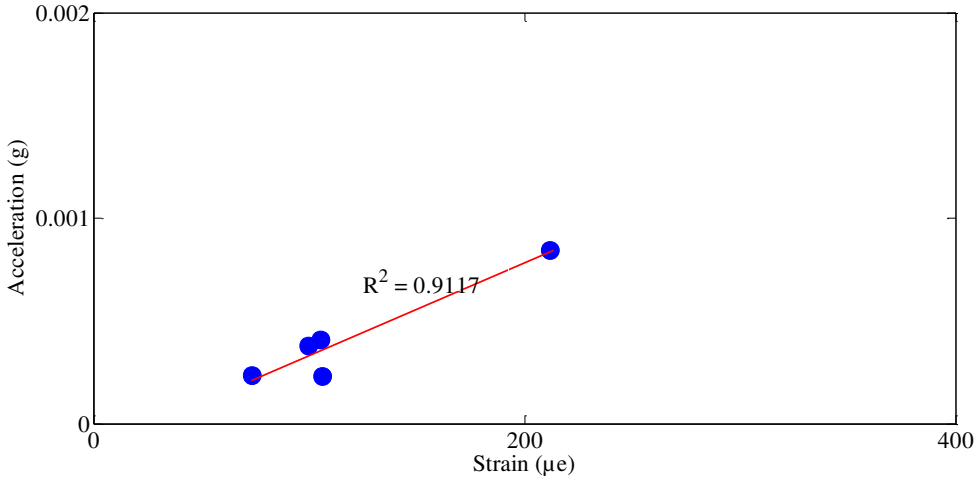

(a)

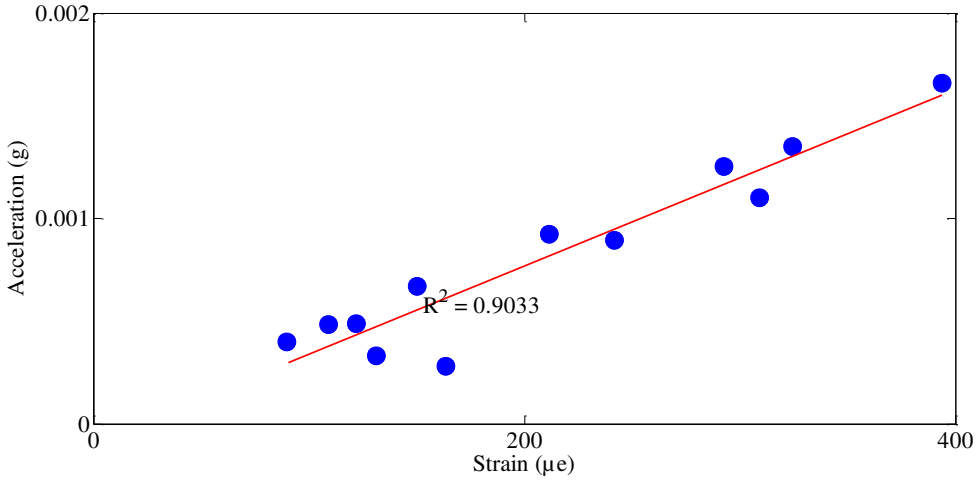

(b)

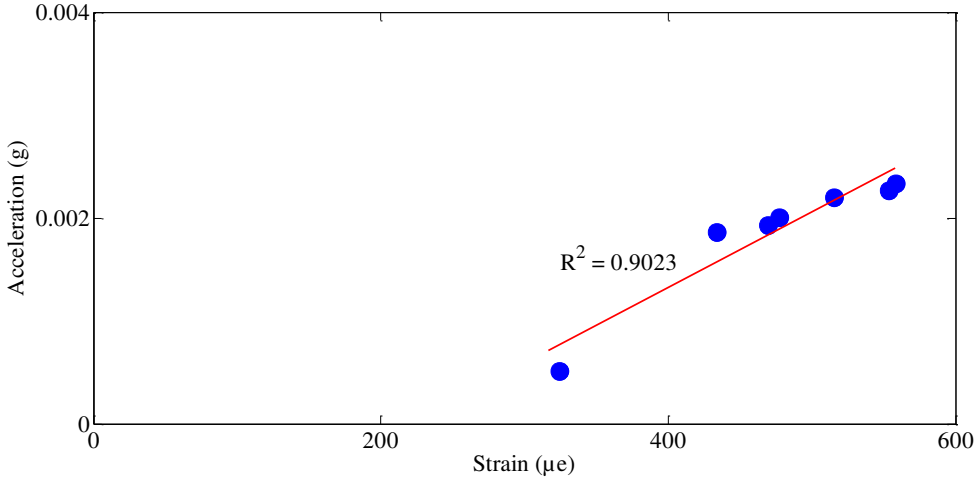

(c)

Figure 4.74 Coefficient of determination for r.m.s. between the acceleration and strain segments: (a) highway, (b) urban, (c) rural

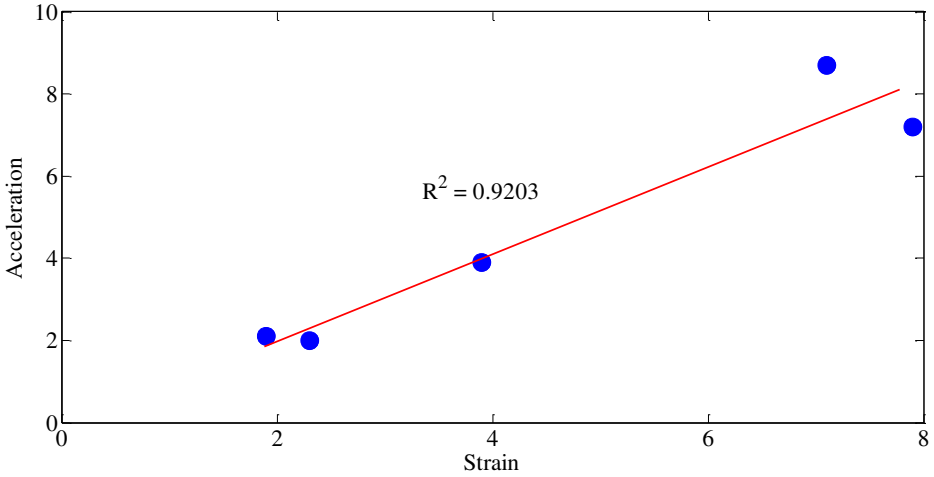

(a)

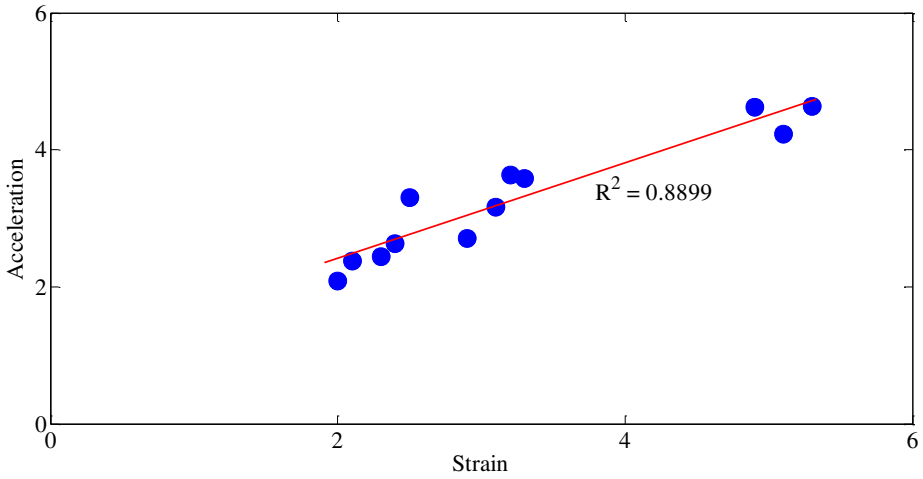

(b)

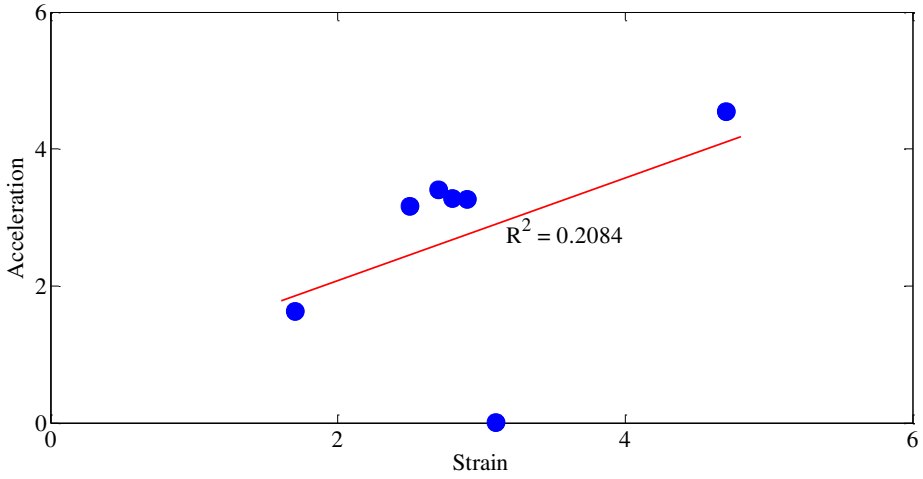

(c)

Figure 4.75 Coefficient of determination for kurtosis between the acceleration and strain segments: (a) highway, (b) urban, (c) rural

4.3.2 Strain Signal Correlation

A relationship pattern between the actual and simulated strain signals could be identified using the clustering method. In addition, the clustering also aimed to ensure that higher amplitude segments could be detected and extracted from the original strain signals, and at the same time maintained fatigue damage. For this purpose, the required data were segments drawn from the fatigue feature extraction. The extracted features, also known as non-damaging and damaging segments, were clustered in order to analyse the segment behaviour based on related findings. The clustering provided a base for strain signal scattering, enabling the observation of the strain signal behaviour.

Figures 4.76 to 4.78 represent the three-dimensional scatters of energy and fatigue damage related to SD, r.m.s. and kurtosis, respectively. All these parameters should be normalised to obtain parameter values in the same range since they had significant differences, using the following equations:

$$SD_{\text{normalised}} = \frac{SD}{SD_{\max}} \tag{4.2}$$

$$r.m.s._{\text{normalised}} = \frac{r.m.s.}{r.m.s._{\max}} \tag{4.3}$$

$$K_{\text{normalised}} = \frac{K}{K_{\max}} \tag{4.4}$$

$$\bar{e}_{\text{normalised}} = \frac{\bar{e}}{\bar{e}_{\max}} \tag{4.5}$$

$$D_{\text{normalised}} = \frac{D}{D_{\max}} \tag{4.6}$$

where $SD_{\text{normalised}}$ is the normalised SD, $SD_{\max}$ is the maximum SD, $r.m.s._{\text{normalised}}$ is the normalised r.m.s., $r.m.s._{\max}$ is the maximum r.m.s., $K_{\text{normalised}}$ is the normalised kurtosis, $K_{\max}$ is the maximum kurtosis, $\bar{e}_{\text{normalised}}$ is the normalised wavelet-based energy, $D_{\text{normalised}}$ is the normalised cumulative fatigue damage and $D_{\max}$ is the maximum cumulative fatigue damage.

Generally, lower, moderate and higher fatigue damage represented lower, moderate and higher energy, respectively (Darpe 2007), that were similar to results in Figure 4.50. The wavelet-based energy is suitable to be used as early indicator of fatigue damage since it could accurately detect the changing amplitudes in the strain signals. Meanwhile, the graphs of fatigue damage against statistical parameters provided inconsistent and irregular patterns. These findings were similar to results in Figure 4.49. Statistical parameters were accurate to identify fatigue damage when applying for the original strain signals, as shown in Tables 4.1 and 4.2, but when the strain signals were edited, statistical parameters were inaccurate. This was because the edited strain signals only contain mostly higher amplitudes that influencing the statistical results. From the scattering results, it was found that using only statistical parameters to predict fatigue damage, it produced a scattering containing certain strain signals that deviated from expectations.

In Figures 4.79 to 4.86, the segments were separately clustered for each parameter, depending on fatigue damage using the FCM. It aimed to measure how well the regression line did. For the actual SD clustering in Figure 4.79, it was found that the coefficients of determination were 0.4348, 0.4112 and 0.3784 for the Coffin-Manson, Morrow and SWT models, respectively. The coefficients of determination of 0.4594, 0.4506 and 0.4239 were resulted for the Coffin-Manson, Morrow and SWT models, for the simulated SD clustering, as shown in Figure 4.80. A lower coefficient of determination shows that statistical parameters cannot act as a single criterion for damaging segment identification and extraction. In addition, it was because the simulated strain signals were not extracted based on their own energy, but based on the actual strain energy.

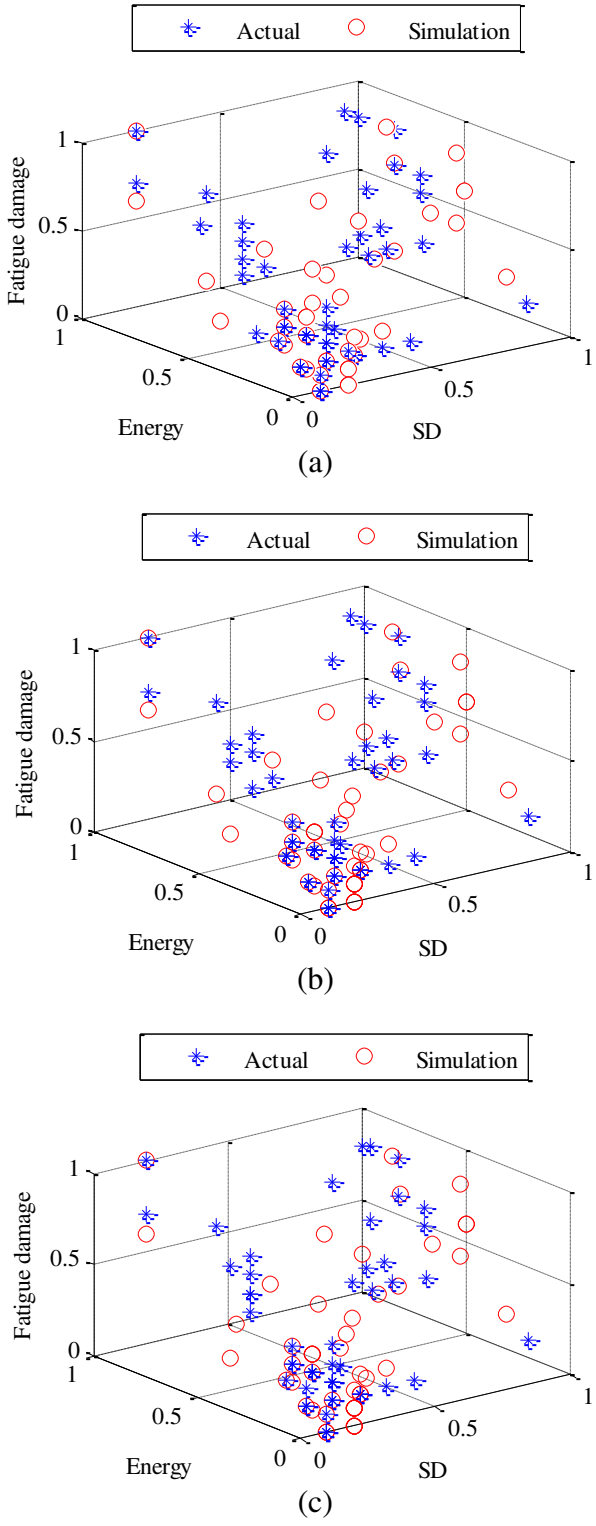

Figure 4.76 Scattering of SD against energy and fatigue damage: (a) Coffin-Manson, (b) Morrow, (c) SWT

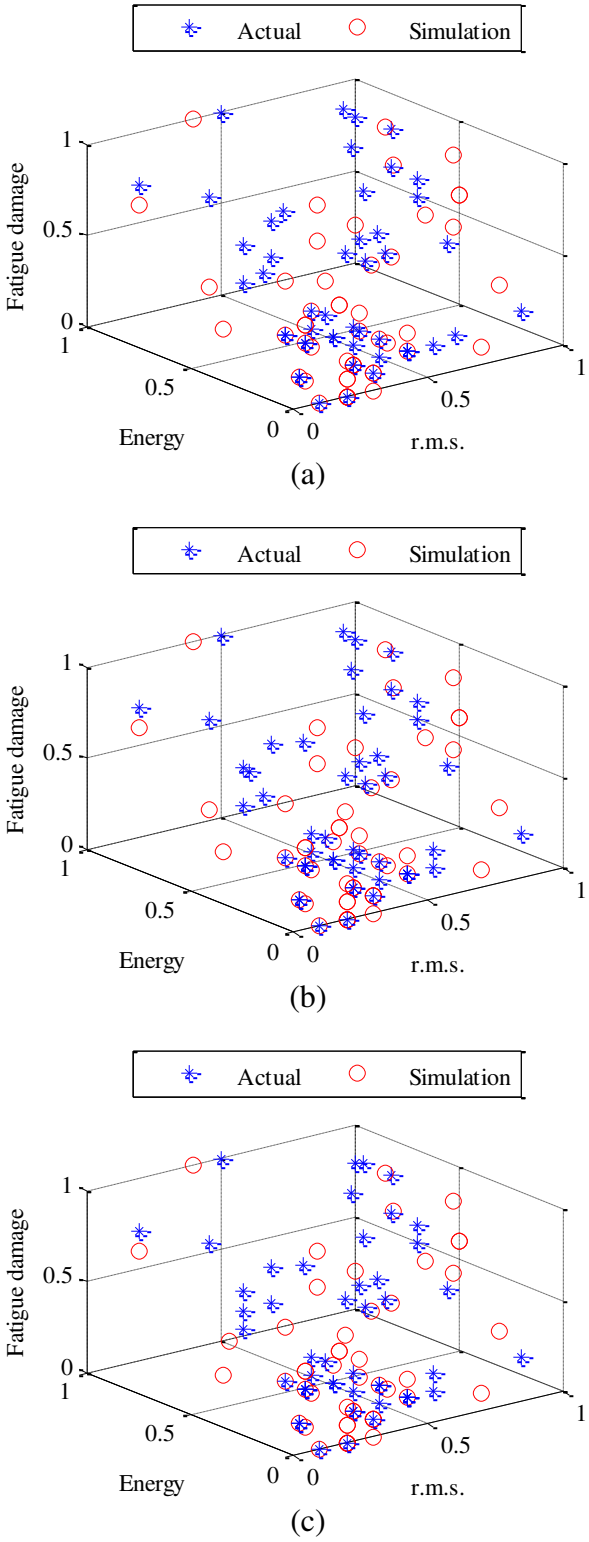

Figure 4.77 Scattering of r.m.s. against energy and fatigue damage: (a) Coffin-Manson, (b) Morrow, (c) SWT

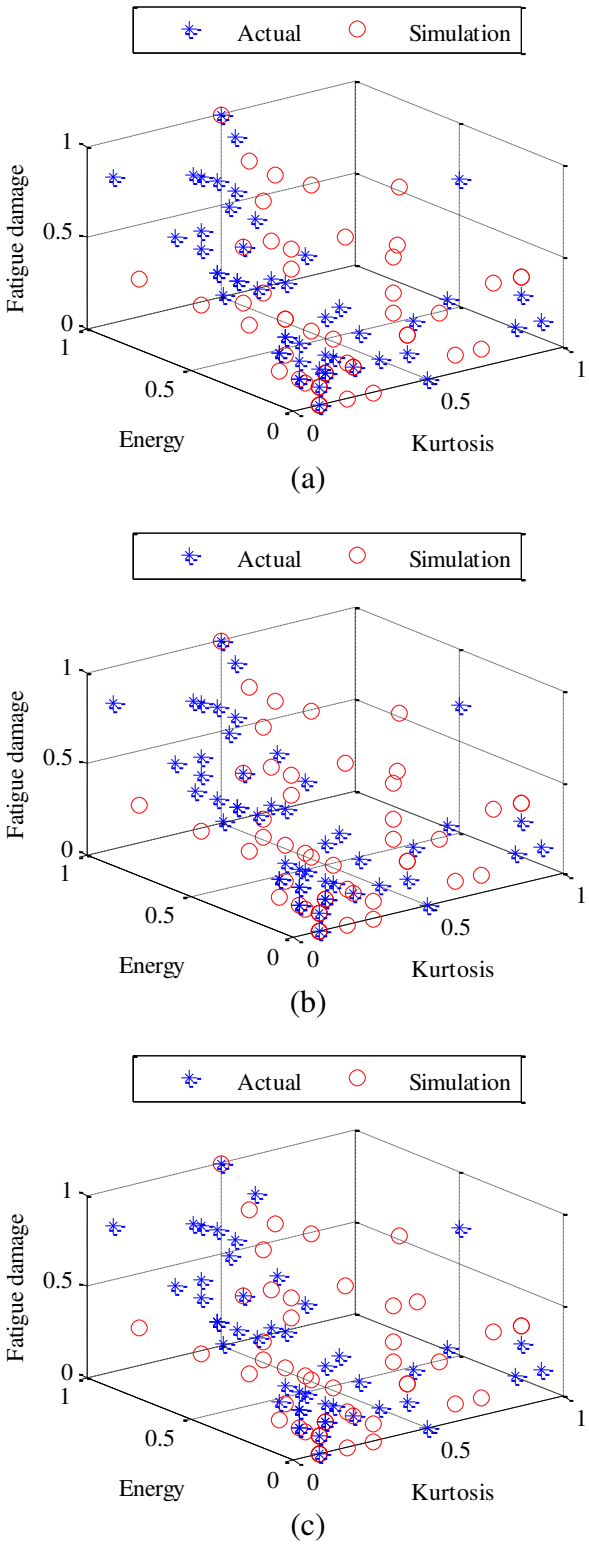

Figure 4.78 Scattering of kurtosis against energy and fatigue damage: (a) Coffin-Manson, (b) Morrow, (c) SWT

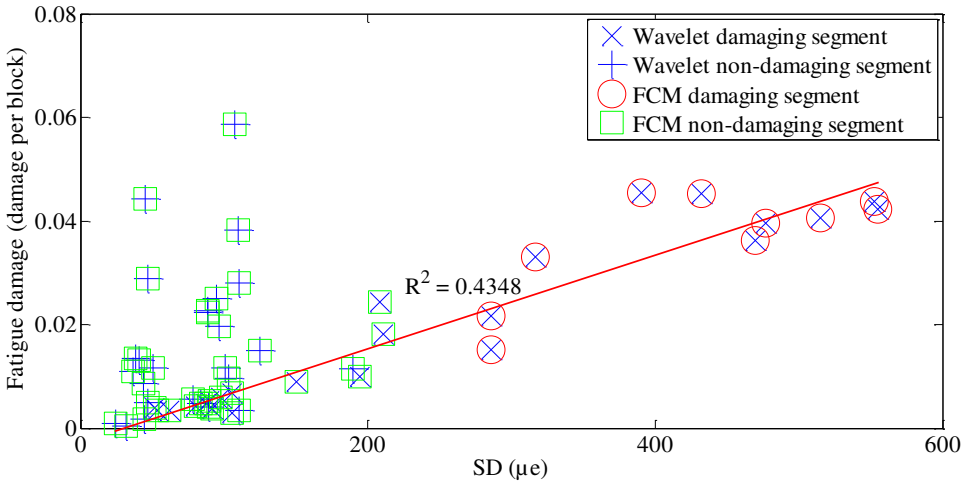

(a)

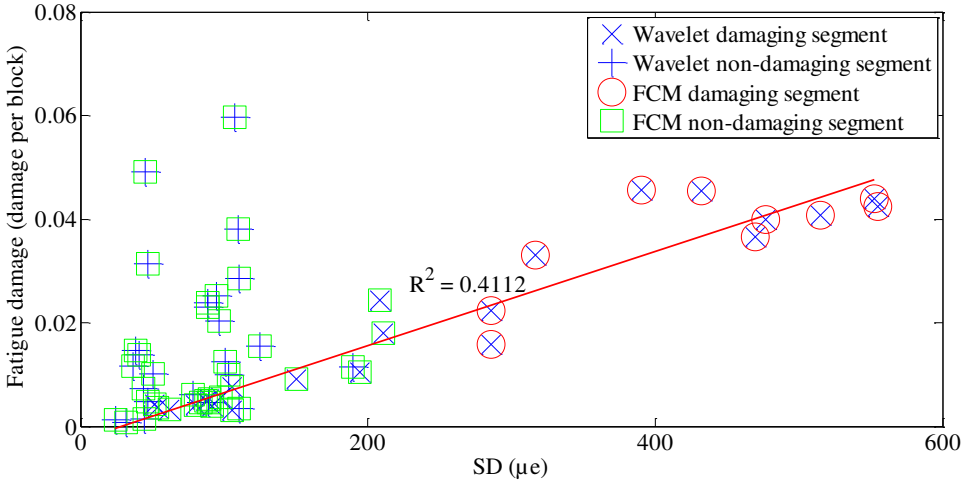

(b)

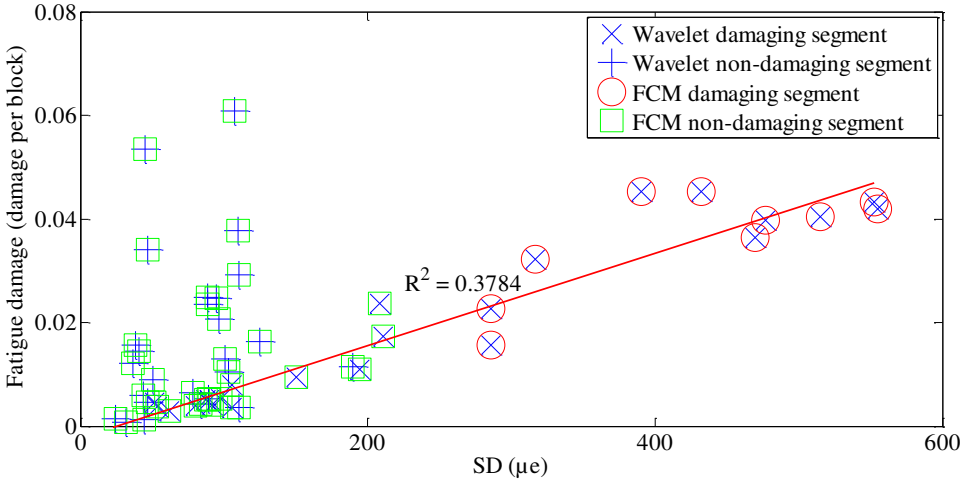

(c)

Figure 4.79 Coefficient of determination of the actual SD and fatigue damage: (a) Coffin-Manson, (b) Morrow, (c) SWT

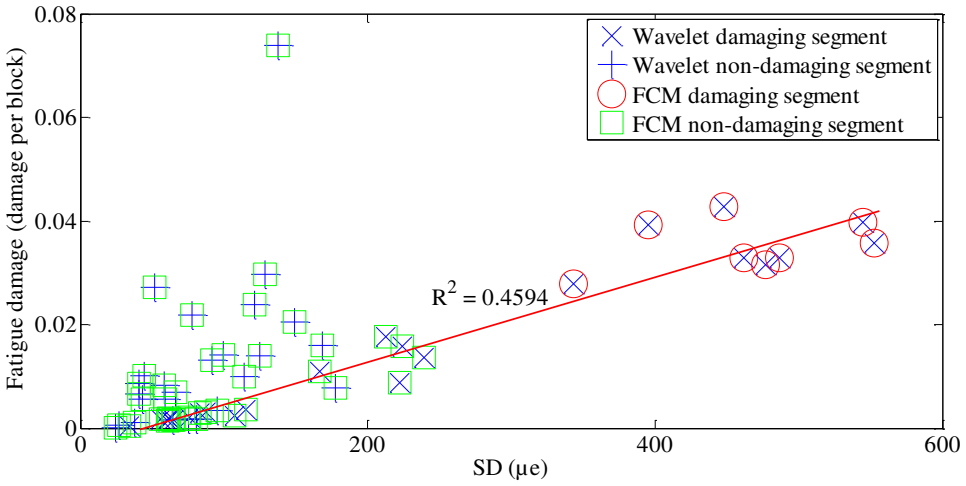

(a)

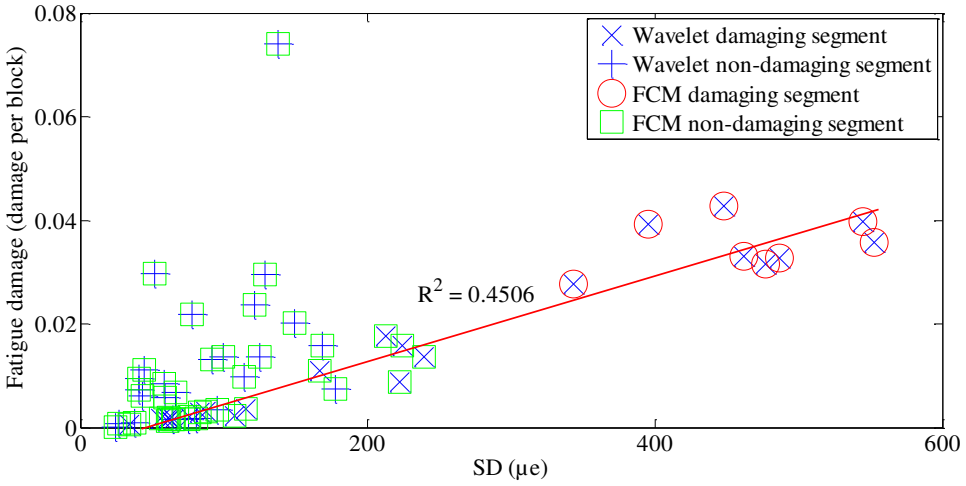

(b)

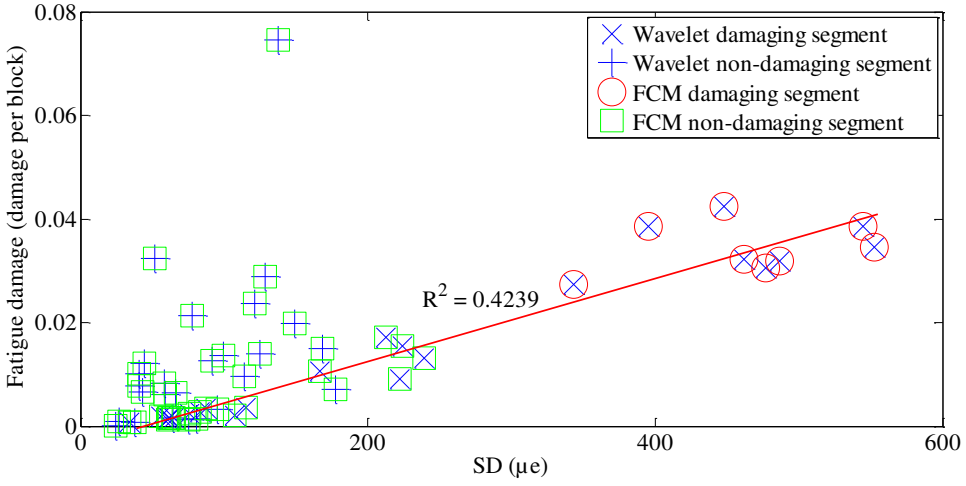

(c)

Figure 4.80 Coefficient of determination of the simulated SD and fatigue damage: (a) Coffin-Manson, (b) Morrow, (c) SWT

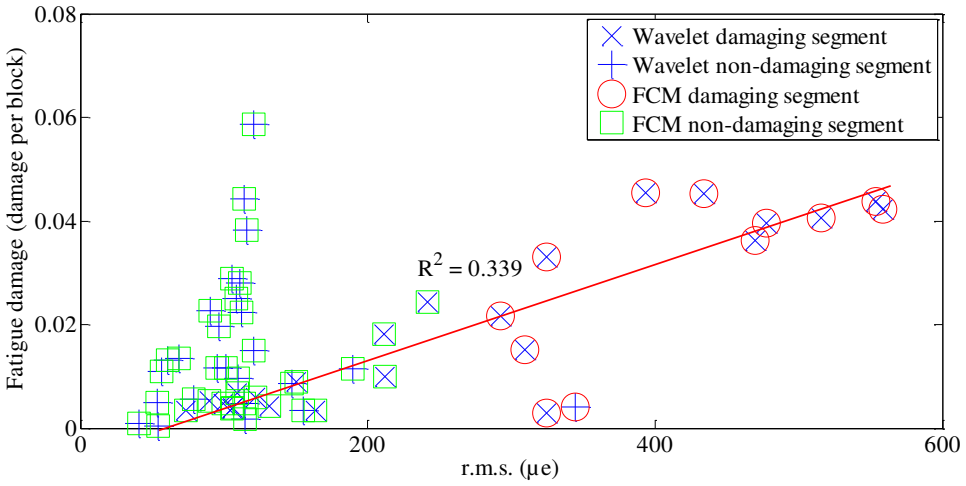

(a)

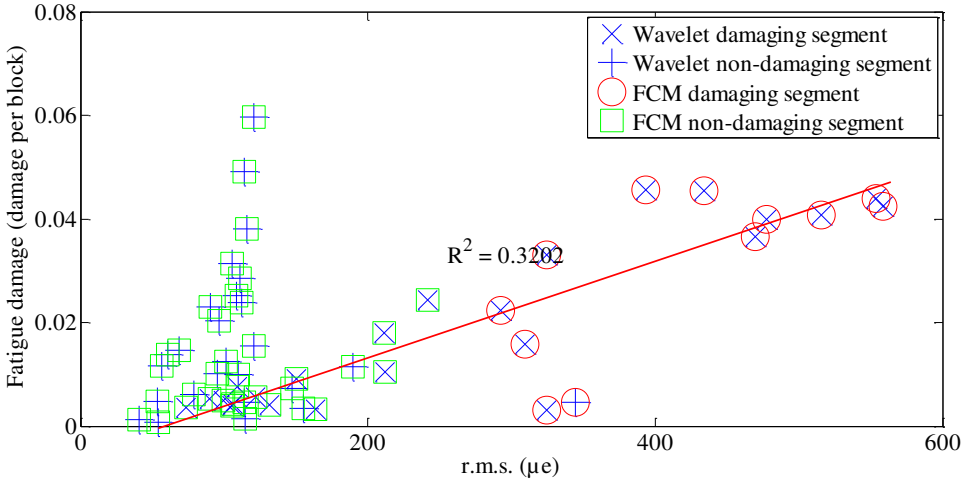

(b)

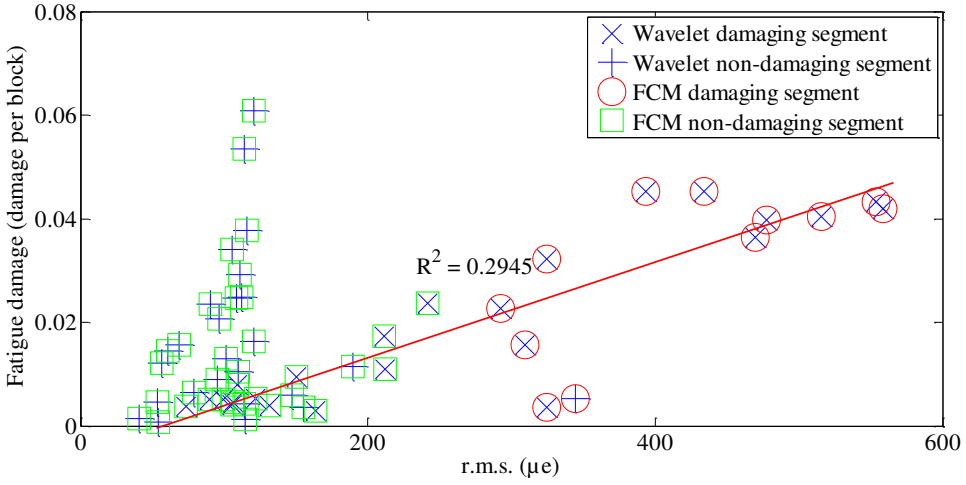

(c)

Figure 4.81 Coefficient of determination of the actual r.m.s. and fatigue damage: (a) Coffin-Manson, (b) Morrow, (c) SWT

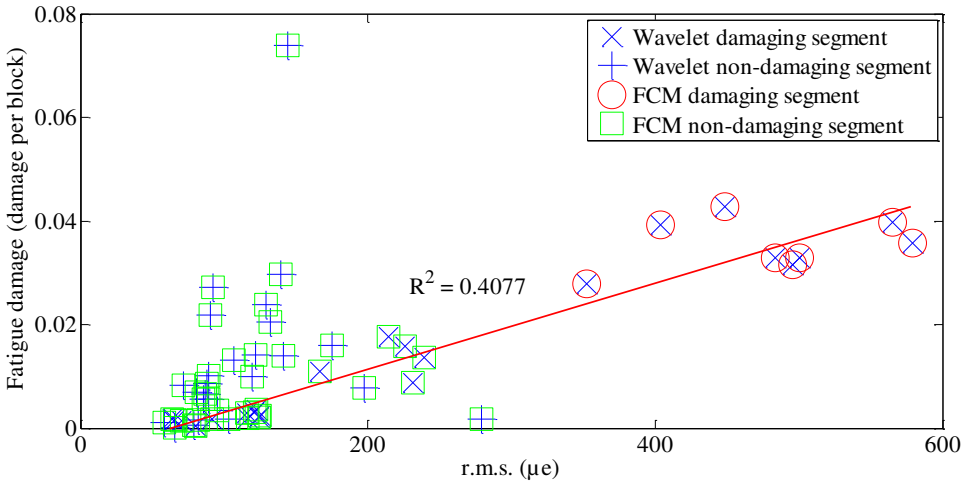

(a)

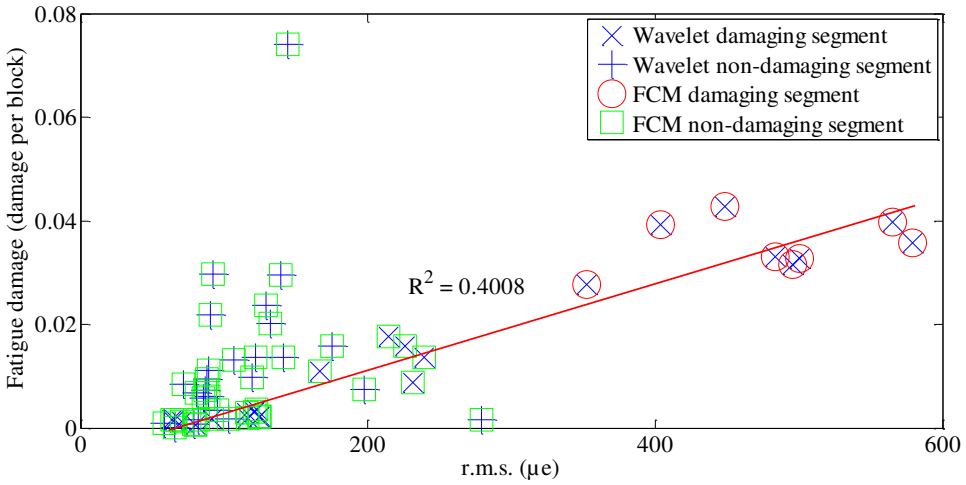

(b)

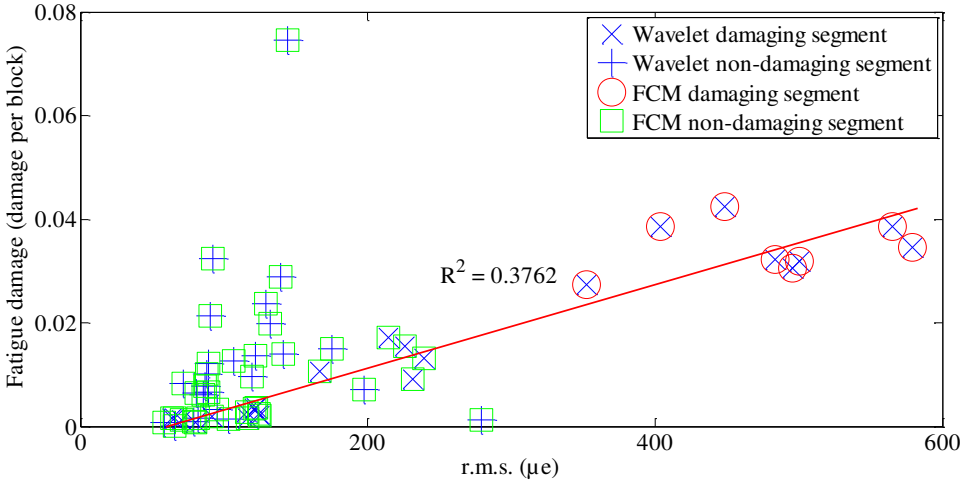

(c)

Figure 4.82 Coefficient of determination of the simulated r.m.s. and fatigue damage: (a) Coffin-Manson, (b) Morrow, (c) SWT

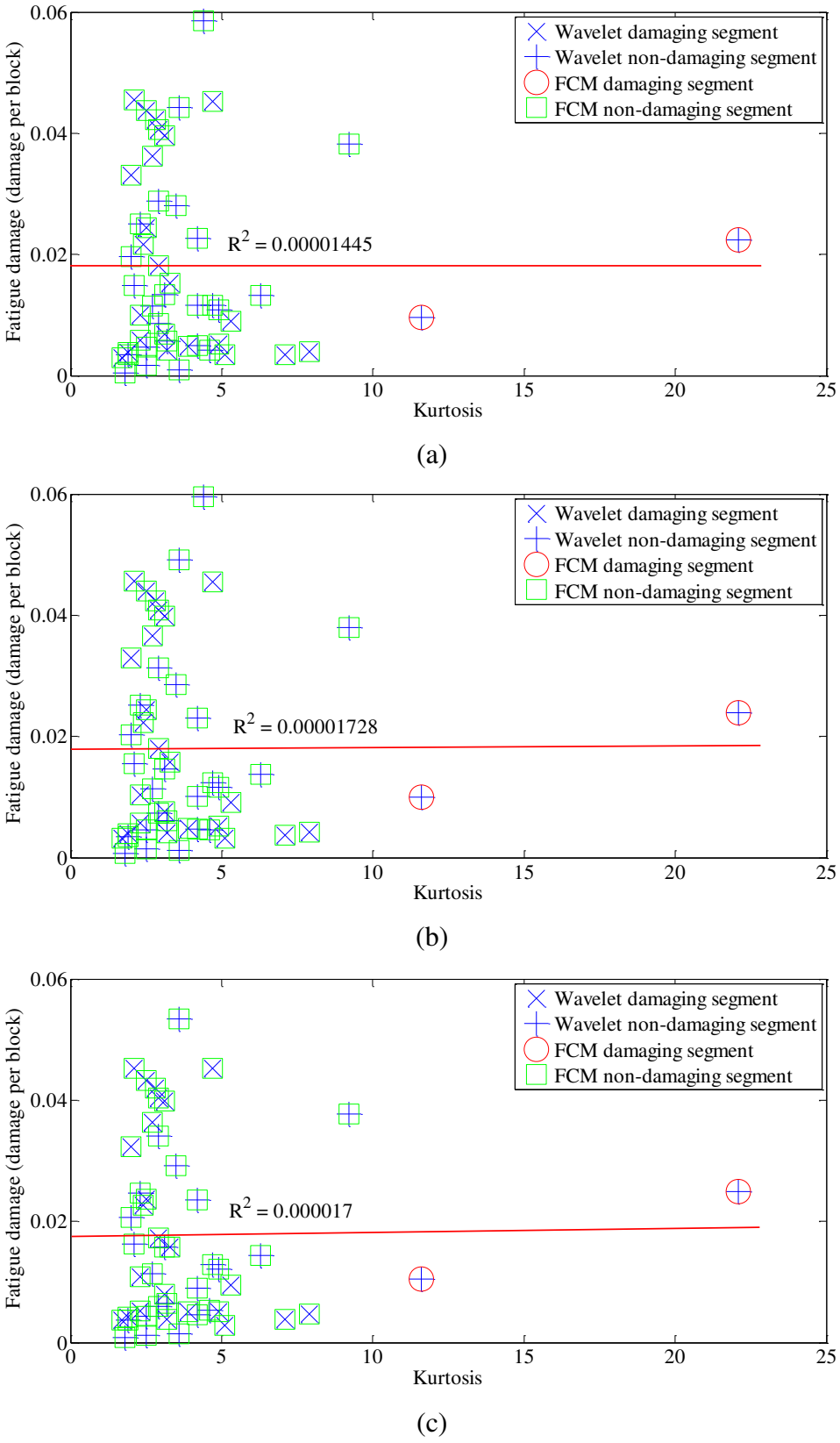

Figure 4.83 Coefficient of determination of the actual kurtosis and fatigue damage: (a) Coffin-Manson (b) Morrow, (c) SWT

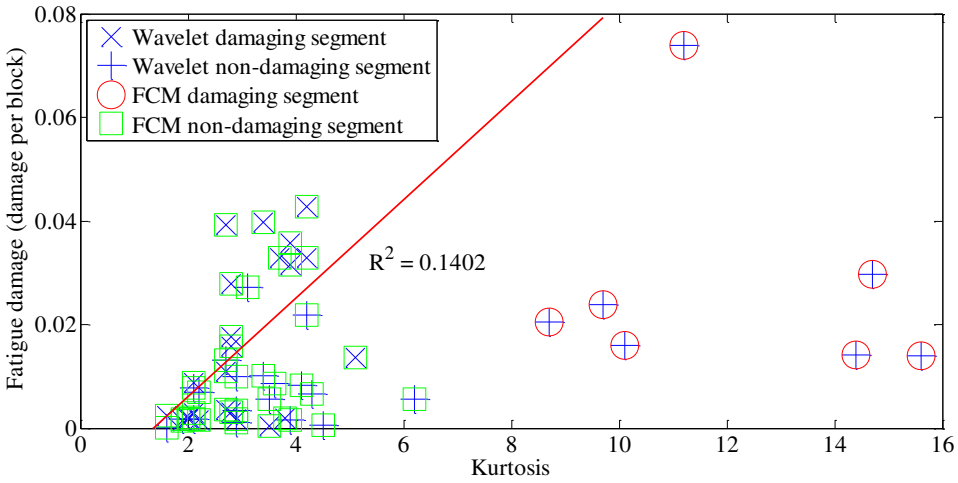

(a)

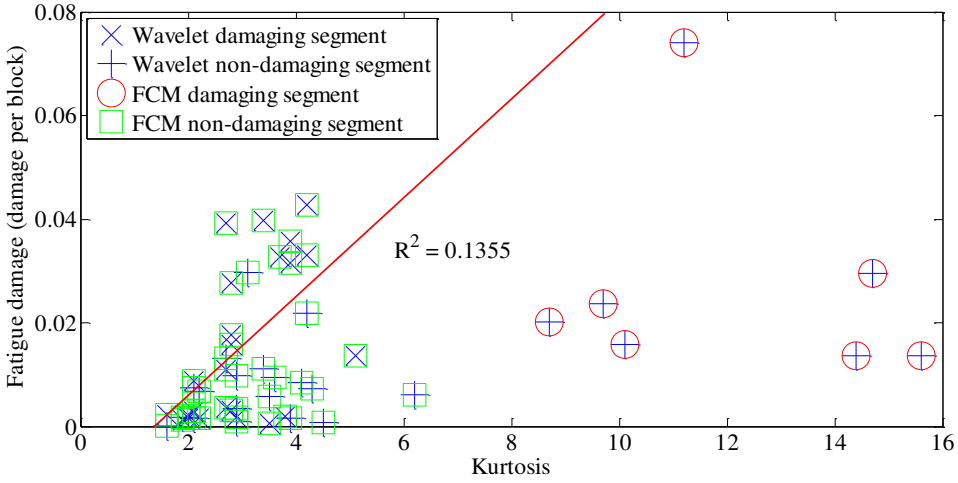

(b)

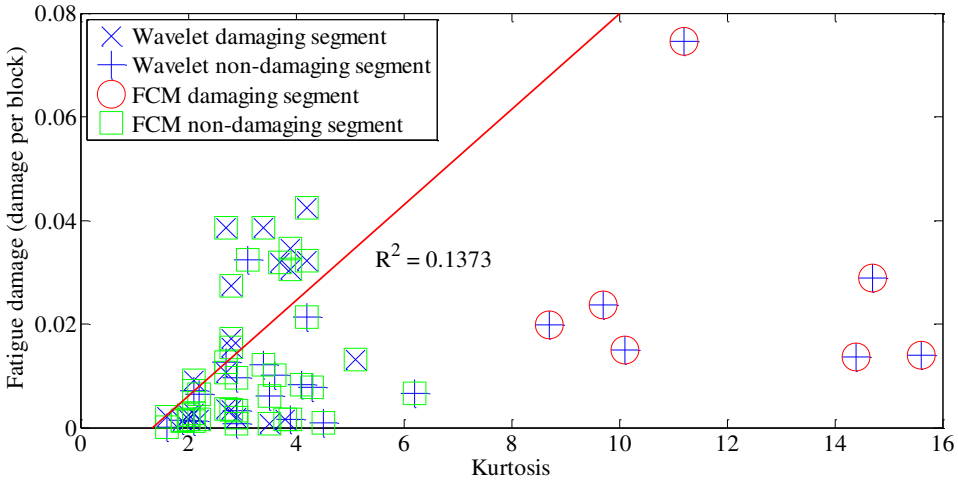

(c)

Figure 4.84 Coefficient of determination of the simulated kurtosis and fatigue damage: (a) Coffin-Manson, (b) Morrow, (c) SWT

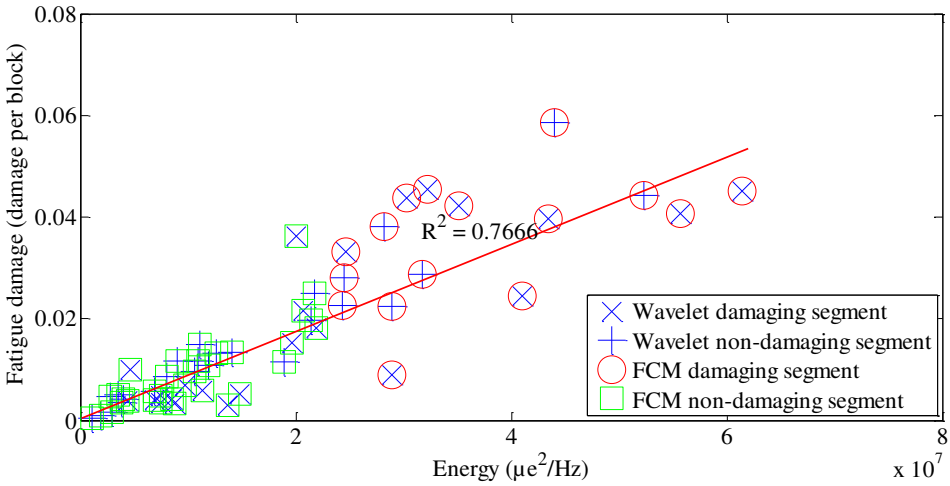

(a)

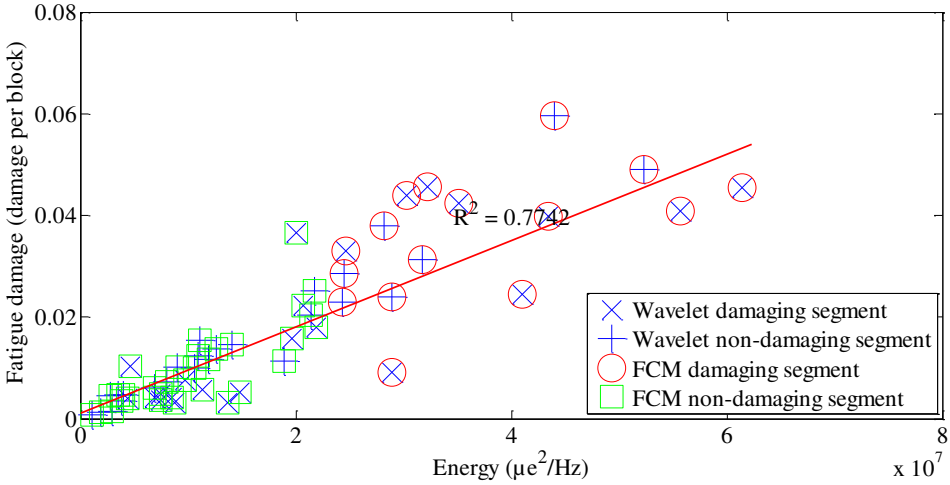

(b)

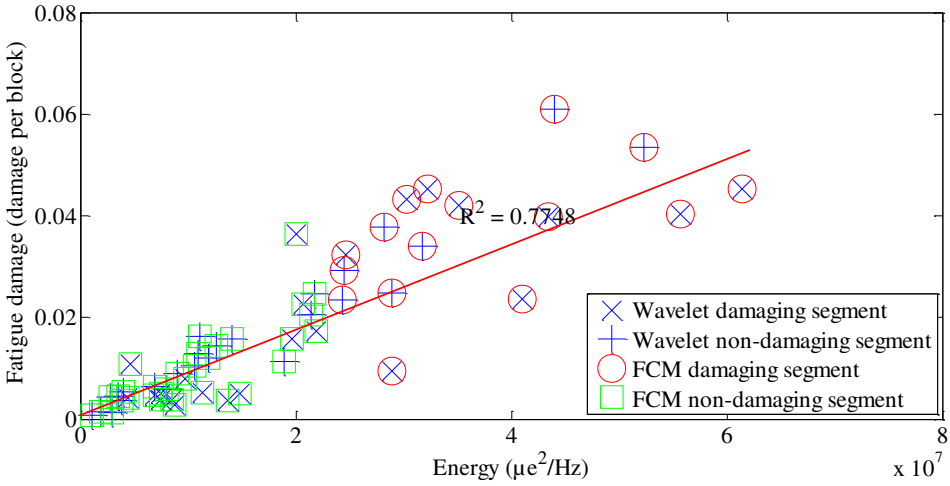

(c)

Figure 4.85 Coefficient of determination of the actual energy and fatigue damage: (a) Coffin-Manson, (b) Morrow, (c) SWT

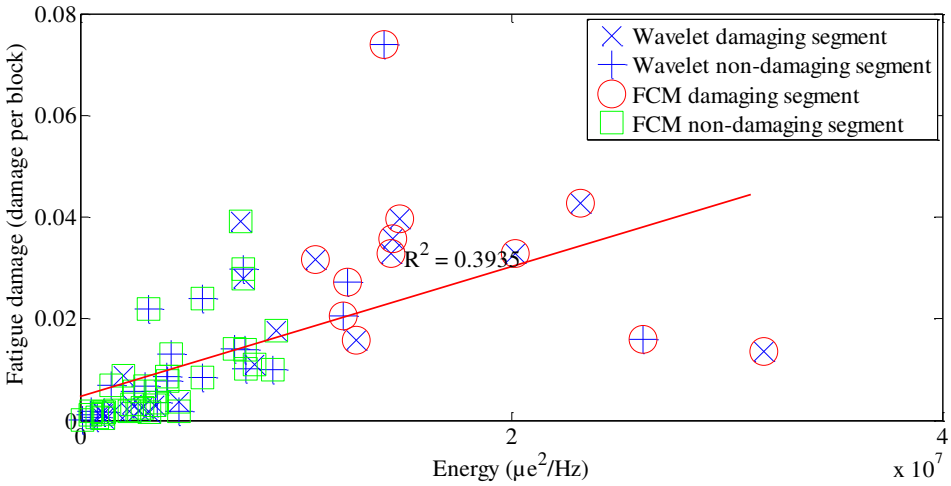

(a)

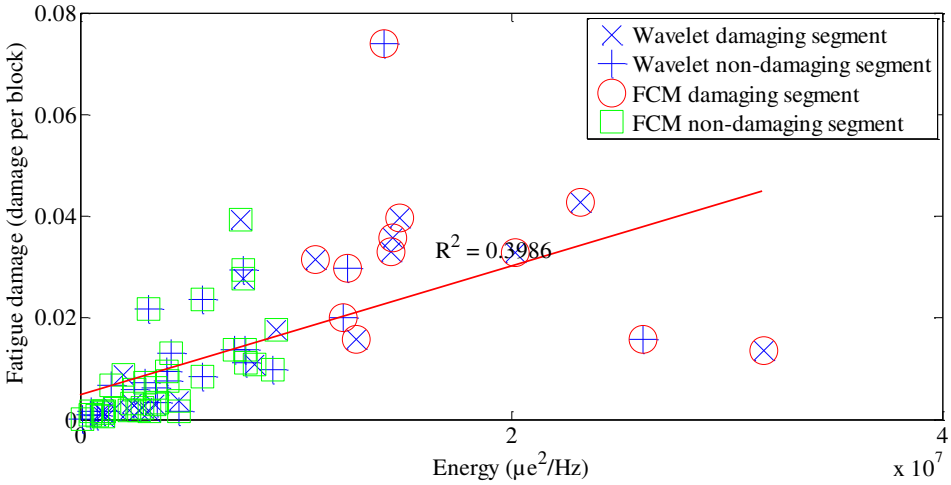

(b)

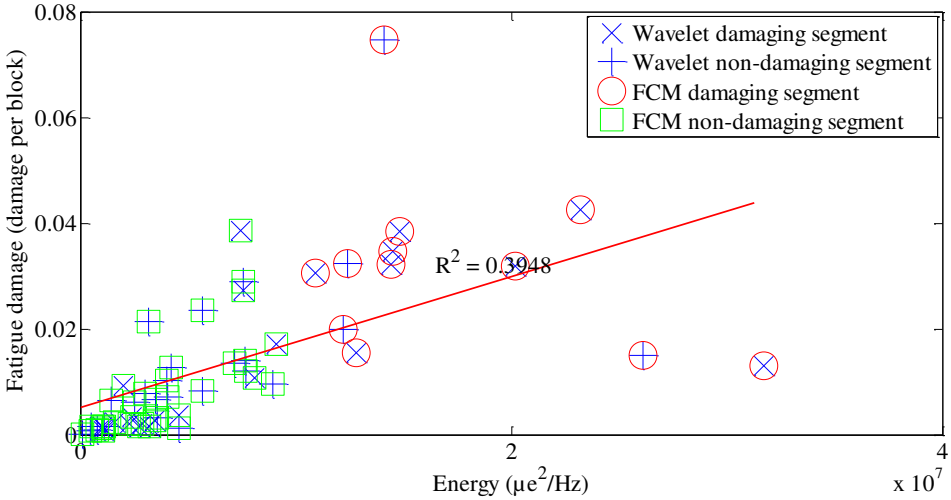

(c)

Figure 4.86 Coefficient of determination of the simulated energy and fatigue damage: (a) Coffin-Manson, (b) Morrow, (c) SWT

A similar situation could be seen in the distributions of r.m.s. and kurtosis. The weakness of statistical parameters in predicting fatigue damage was shown with a coefficient of determination of 0.339, 0.3202 and 0.2945 for the Coffin-Manson, Morrow and SWT models, respectively, for the actual r.m.s. clustering in Figure 4.81, while for the simulated r.m.s. clustering in Figure 4.82, the coefficients of determination were 0.4077, 0.4008 and 0.3762 for the Coffin-Manson, Morrow and SWT models. Furthermore, there was no significant correlation for kurtosis and fatigue damage in Figure 4.83. The coefficients of determination of 0.00001445, 0.00001728 and 0.000017 were obtained for the Coffin-Manson, Morrow and SWT models, respectively, for the actual kurtosis clustering. The coefficients of determination became 0.1402, 0.1355 and 0.1373 for the Coffin-Manson, Morrow and SWT models, for the simulated kurtosis clustering in Figure 4.84. Among statistical parameters, the results gave the highest coefficient of determination for SD, however, a correlation of less than 0.5 was generally described as weak (Sivák & Ostertagová 2012).

A different condition happened in distributions of energy and fatigue damage, in which both the parameters were more accurately correlated. In the correlation shown in Figure 4.85, the coefficients of determination of 0.7666, 0.7742 and 0.7748 were obtained for the Coffin-Manson, Morrow and SWT models, respectively, for the actual energy, which were higher than the correlations for statistical parameters, although the values were decreased to 0.3935, 0.3986 and 0.3948 for the Coffin-Manson, Morrow and SWT models, for the simulated energy clustering in Figure 4.86. A lower coefficient of determination for the simulated strain signals was because they were not extracted based on their own energy, but based on the actual strain energy.

The clustering plots, however, were produced based on proportional relationships between the fatigue damage and its corresponding energy. The pattern indicated that the fatigue damage was generally translated into the energy. Segments with higher energy presented higher fatigue damage, while segments with smaller energy presented smaller fatigue damage. With the loss of energy, fatigue damage decreased. This meant that the clustering graphs in fact reflected the hypothesised

correlation. Compared to statistical parameters, energy gave a more realistic correlation with fatigue damage. Energy could be used as a reference for determining fatigue damage because it produced data scattering that contained certain data as expected. Furthermore, the clustering results had proved that the simulated strain signals were close to the actual strain signals, giving a significant parallel correlation.

The FCM successfully detected segments with lower fatigue damage. From all segments, the FCM had categorised several non-damaging segments as damaging segments, and several damaging segments were categorised as non-damaging segments. This meant that the wavelet-based damaging segments were categorised as non-damaging segments by the FCM. The question arose as to why the FDE categorised the non-damaging segments as damaging segments. This is explained in Figure 3.13. As shown in the figure, the non-damaging segment is longer than the damaging segment. This condition is also seen in Figures 4.43 to 4.45, where most the maintained segments were shorter than the removed segments. This caused the energy of the non-damaging segments for several cases to be higher than the energy of the damaging segments. This was due to the FDE technique applying horizontal extraction. Although the FCM method is often used for noise and vibration signals and is new for fatigue studies, the current study succeeded in using the FCM method for a fatigue signal clustering. The approach was suggested as an alternative method for evaluating and clustering a strain signal. Introducing the extraction and the clustering of fatigue features, fatigue life assessments can be more accurate because each segment only contained one peak in overall.

Furthermore, based on the plots in Figures 4.87 to 4.90, most the strains were distributed in the range of 90 % confidence interval, although they had a lower coefficient of determination in Figures 4.91 to 4.94. It is seen that most SD, r.m.s., kurtosis and energy were located between the upper and lower bounds of the fitted curve. In Figure 4.91, the SD graphs gave a coefficient of determination of 0.4417, 0.4245 and 0.3937 for the Coffin-Manson, Morrow and SWT models, respectively, with an error of 1.14 %, 1.17 % and 1.21 %. In addition, in Figure 4.92, it was found that the coefficients of determination for the Coffin-Manson, Morrow and SWT models for r.m.s. were 0.3707, 0.3568 and 0.3307, respectively, with an error of

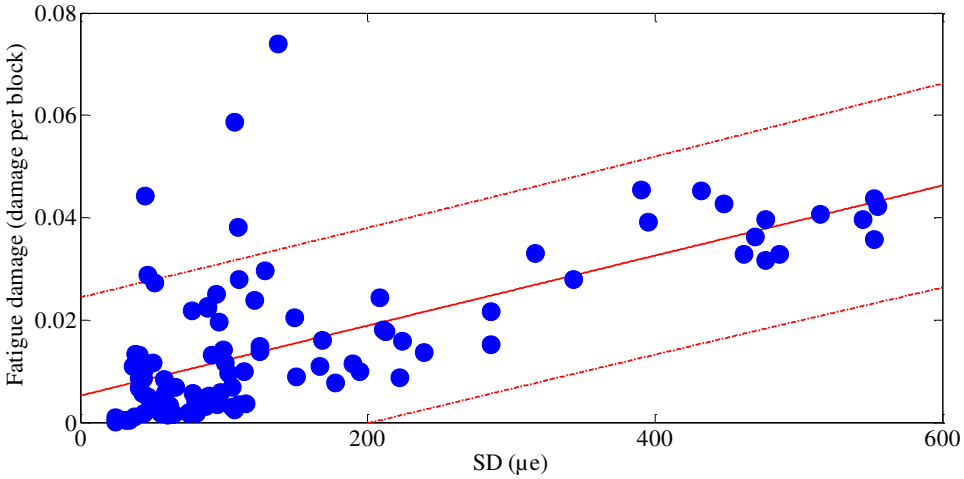

(a)

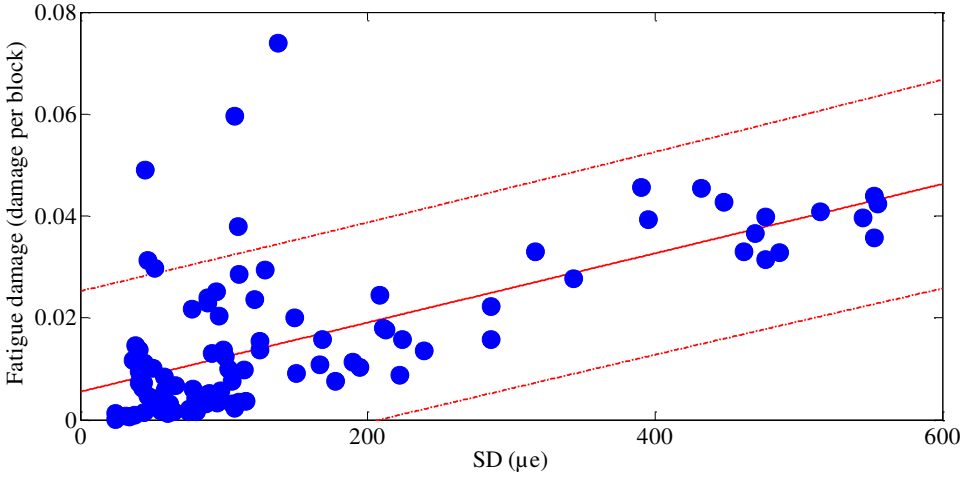

(b)

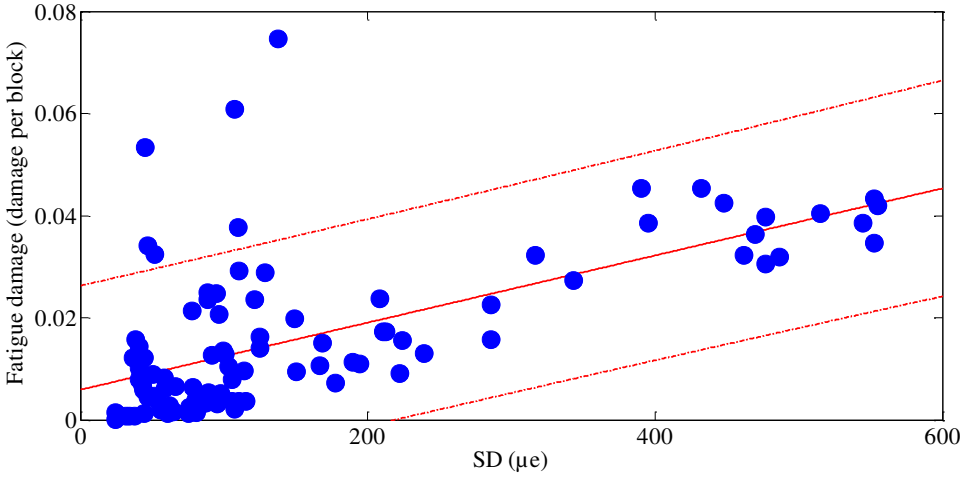

(c)

Figure 4.87 Distributions of SD against fatigue damage in the 90 % confidence interval: (a) Coffin-Manson, (b) Morrow, (c) SWT

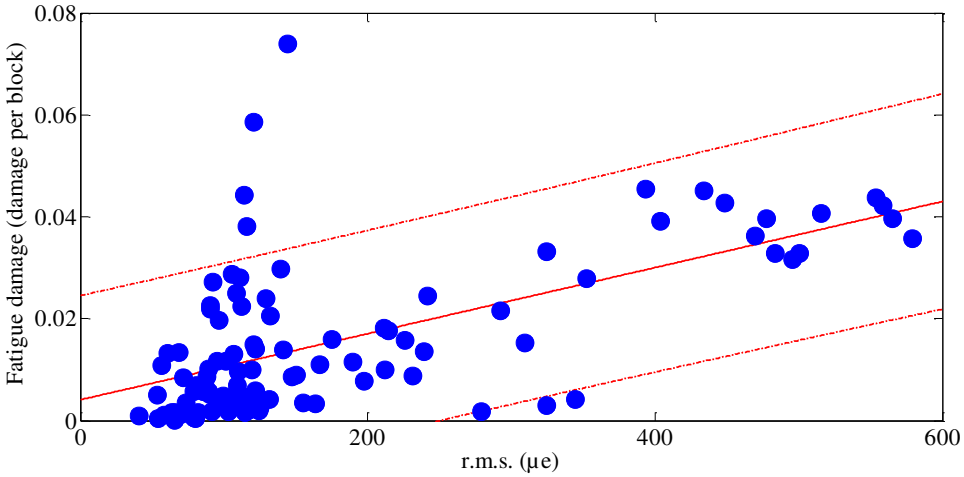

(a)

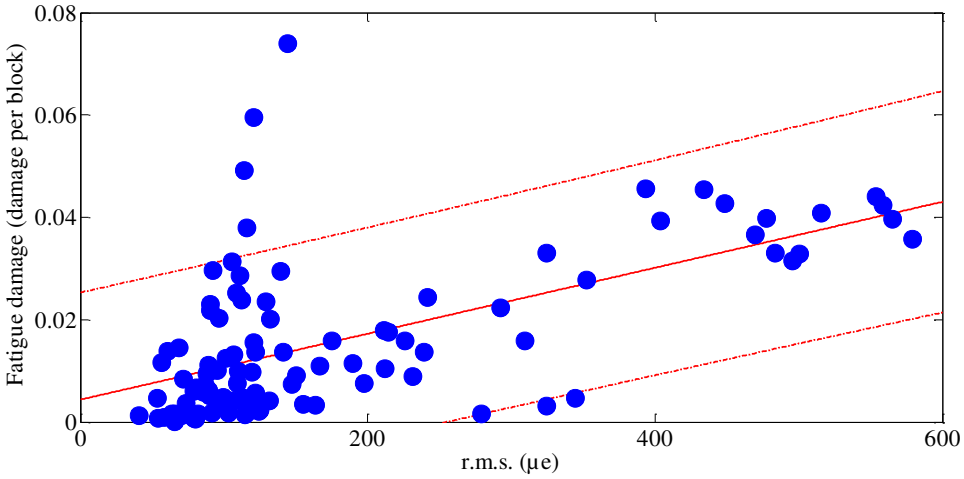

(b)

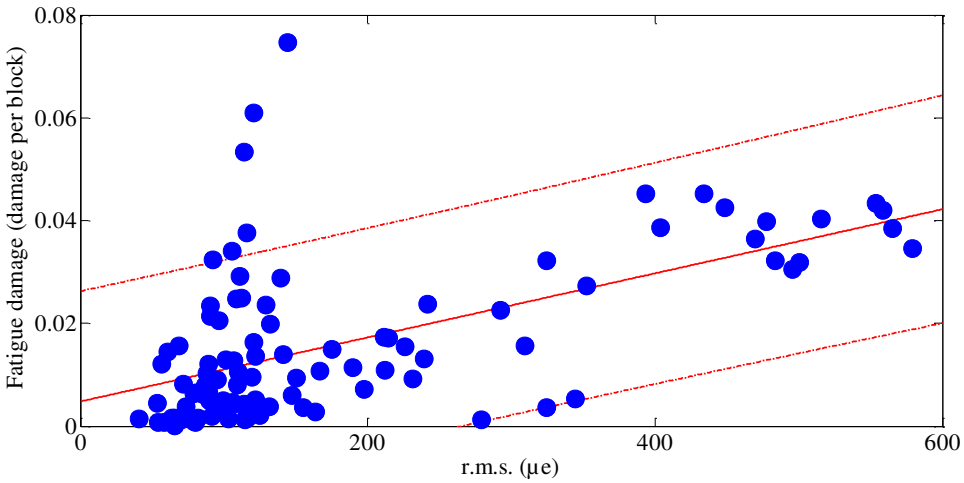

(c)

Figure 4.88 Distributions of r.m.s. against fatigue damage in the 90 % confidence interval: (a) Coffin-Manson, (b) Morrow, (c) SWT

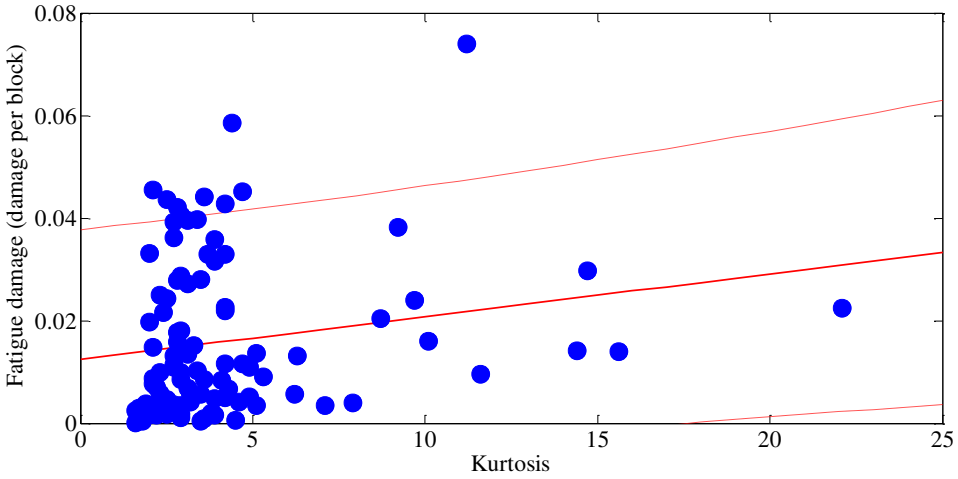

(a)

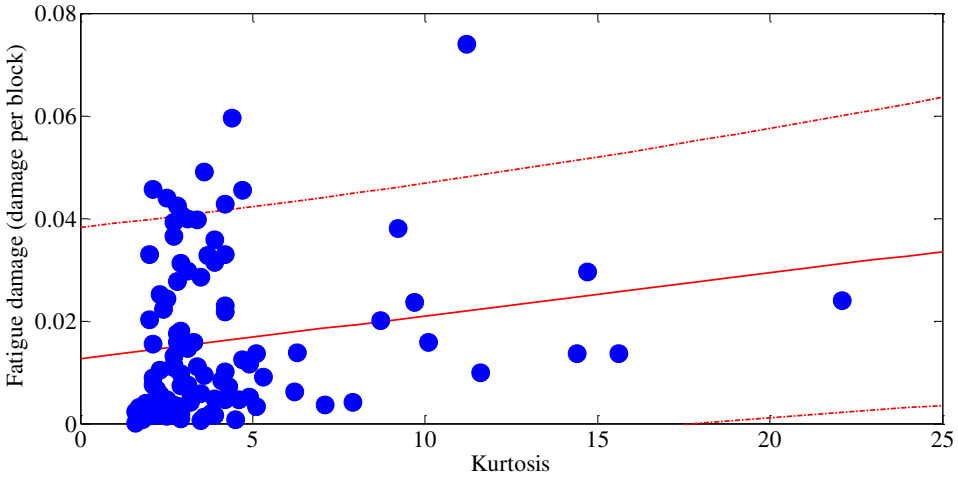

(b)

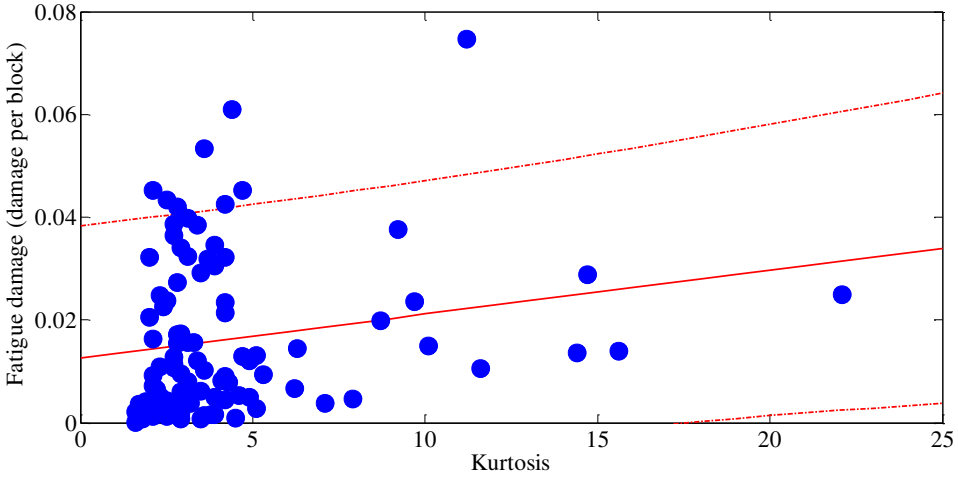

(c)

Figure 4.89 Distributions of kurtosis against fatigue damage in the 90 % confidence interval: (a) Coffin-Manson, (b) Morrow, (c) SWT

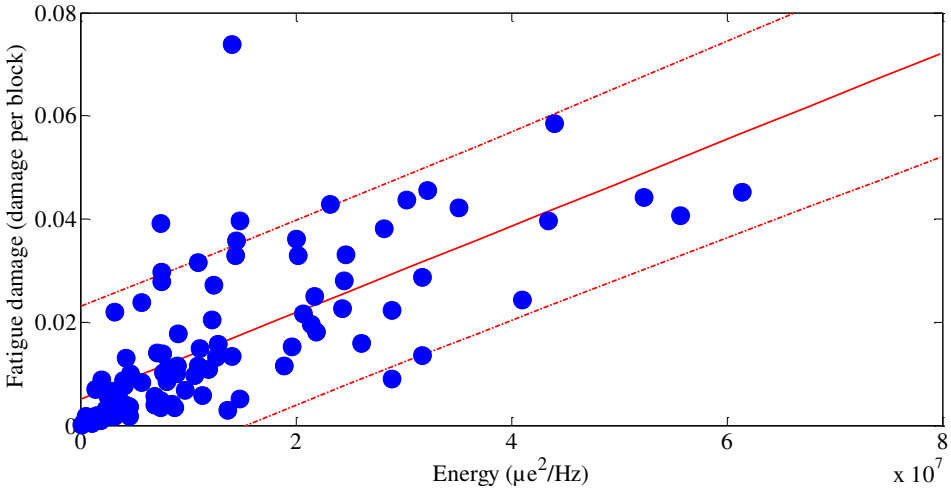

(a)

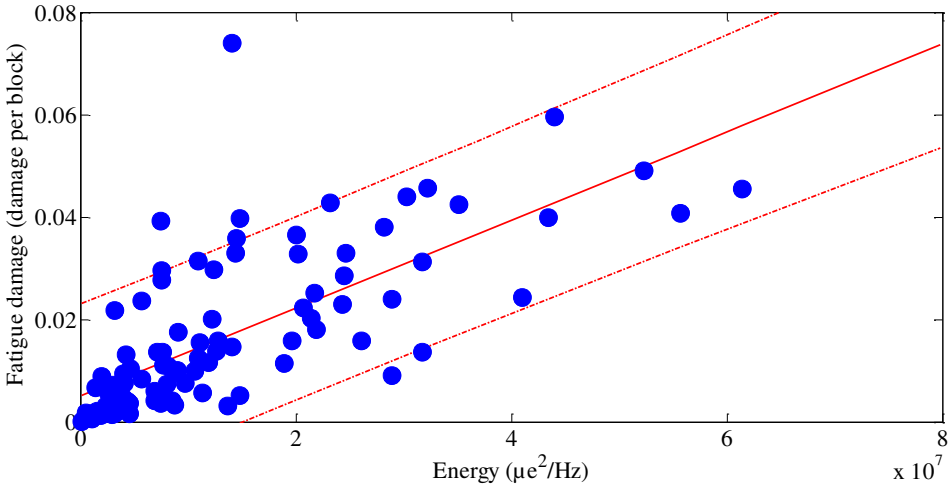

(b)

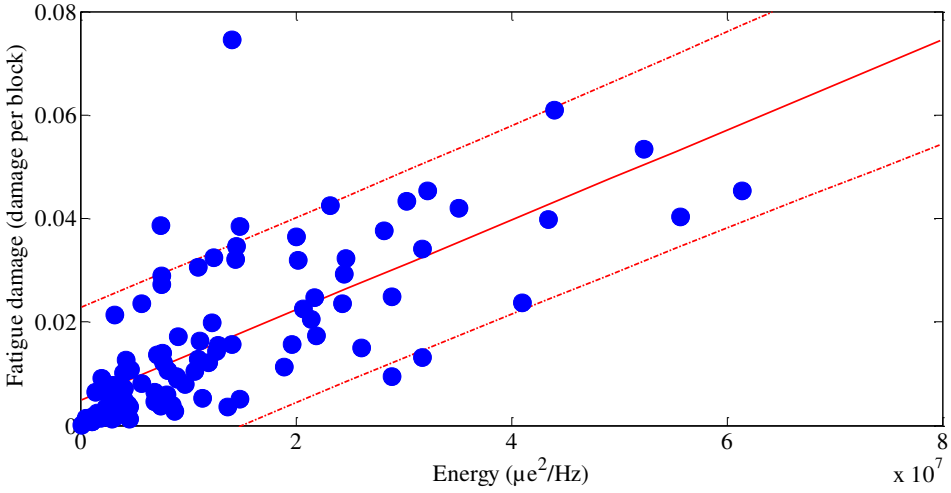

(c)

Figure 4.90 Distributions of energy against fatigue damage in the 90 % confidence interval: (a) Coffin-Manson, (b) Morrow, (c) SWT

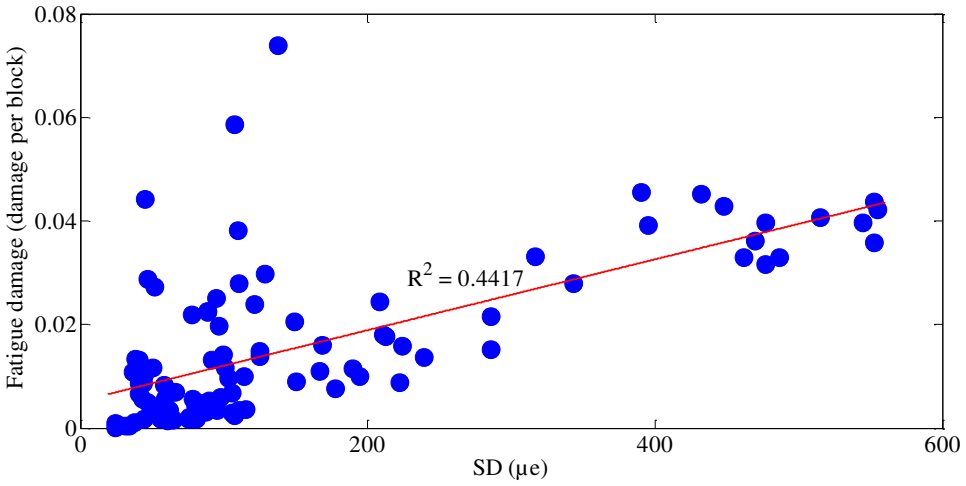

(a)

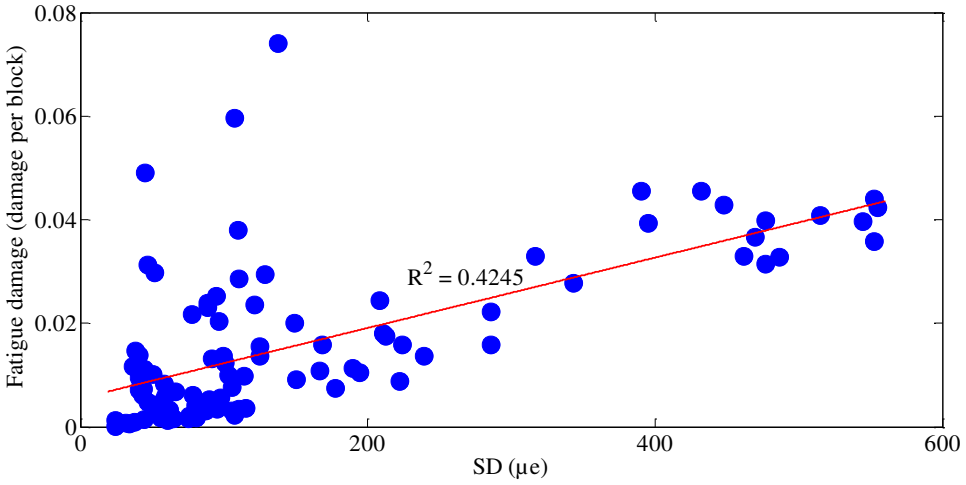

(b)

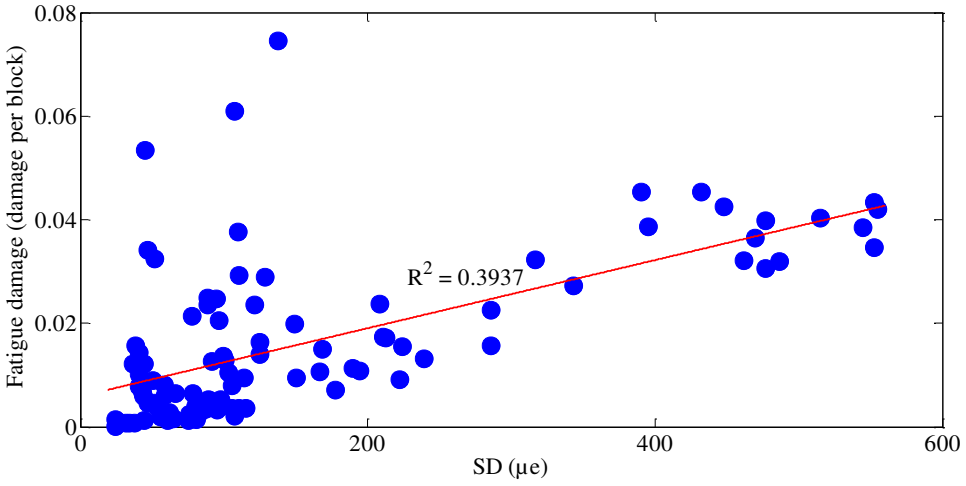

(c)

Figure 4.91 Coefficient of determination for SD and fatigue damage: (a) Coffin-Manson, (b) Morrow, (c) SWT

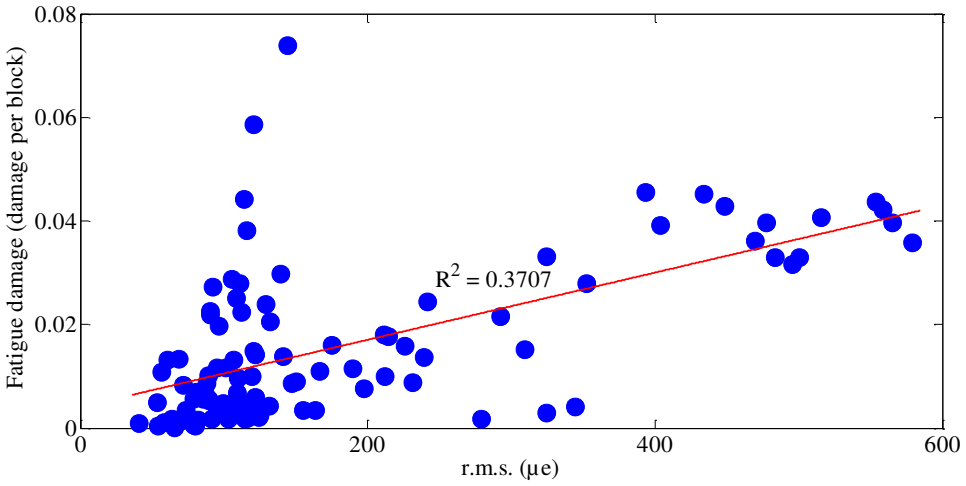

(a)

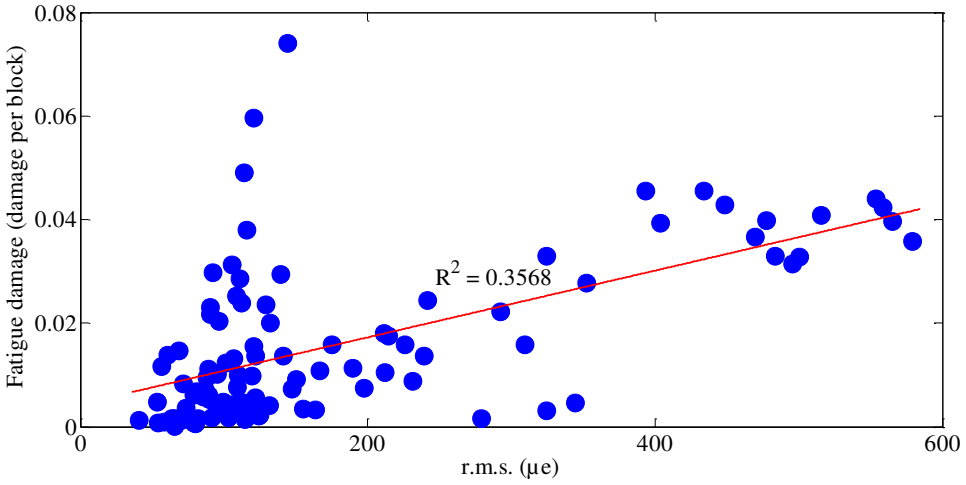

(b)

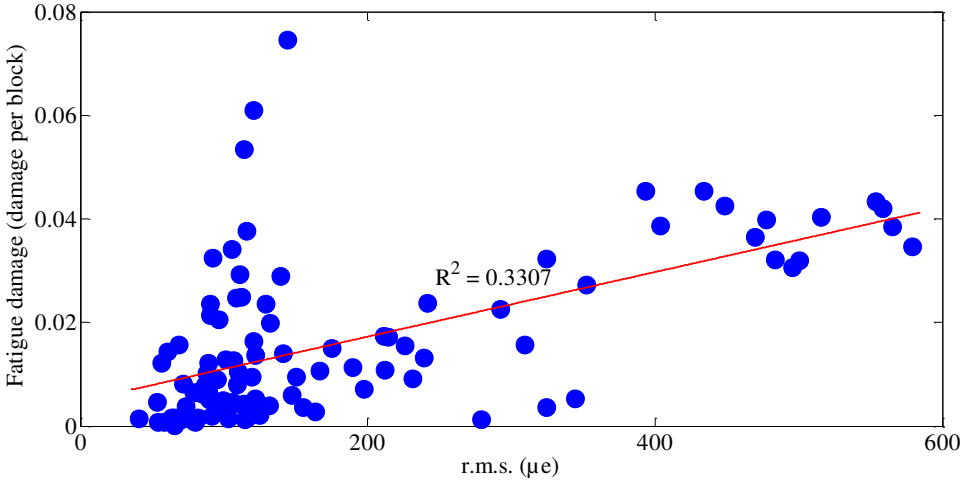

(c)

Figure 4.92 Coefficient of determination for r.m.s. and fatigue damage: (a) Coffin-Manson, (b) Morrow, (c) SWT

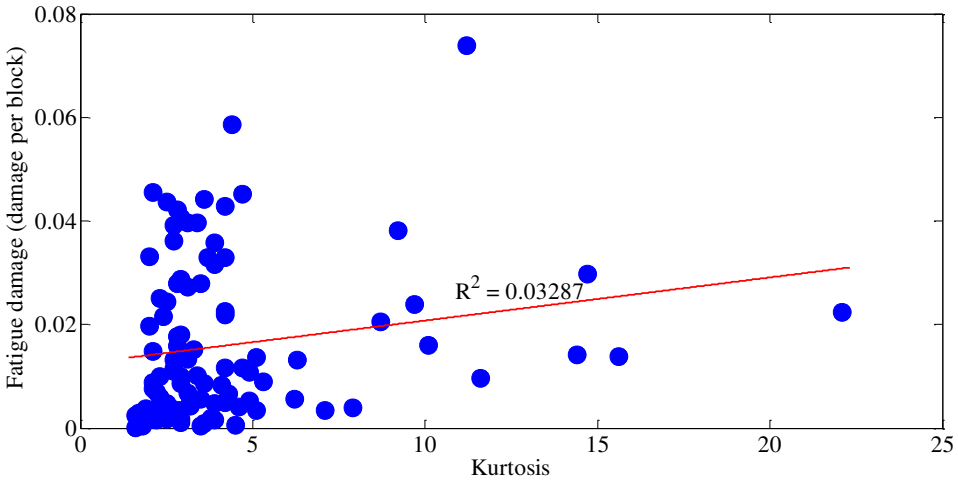

(a)

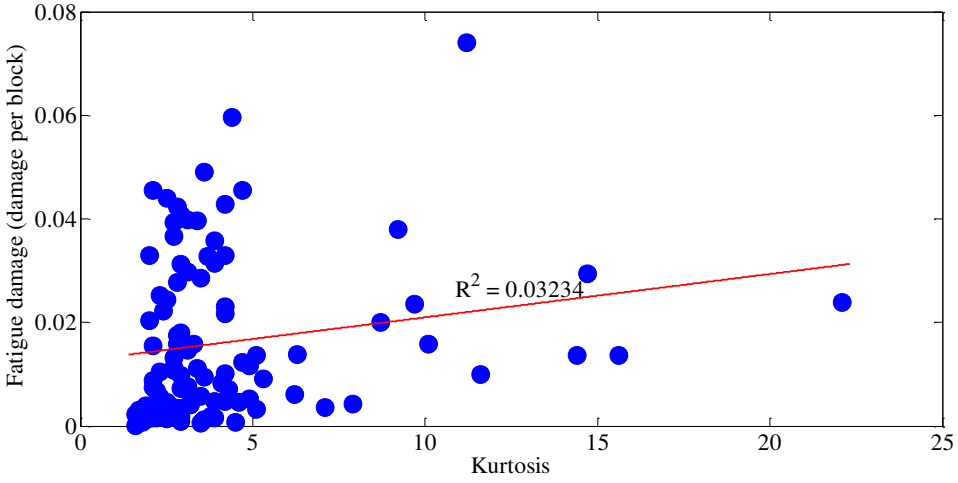

(b)

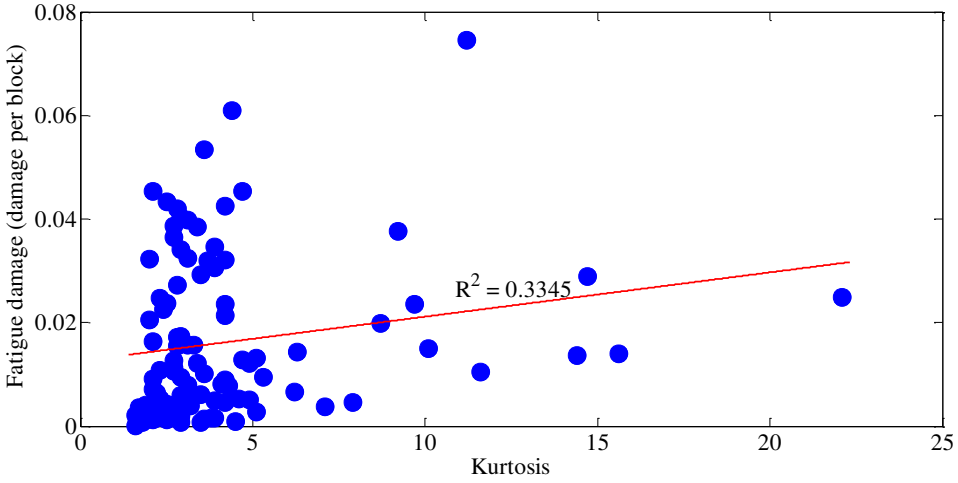

(c)

Figure 4.93 Coefficient of determination for kurtosis and fatigue damage: (a) Coffin-Manson, (b) Morrow, (c) SWT

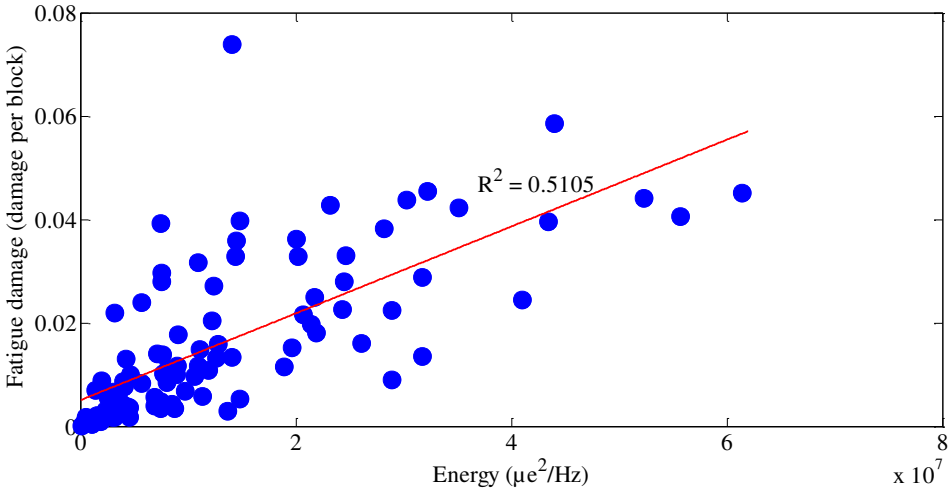

(a)

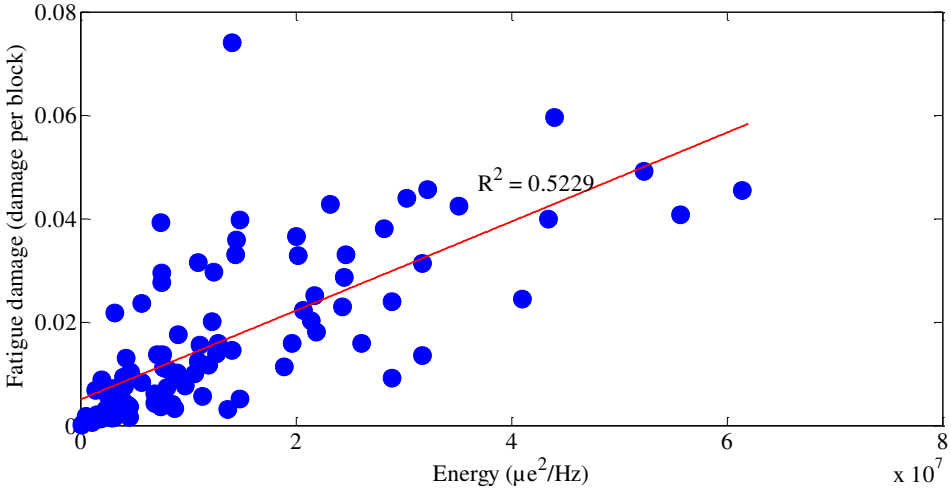

(b)

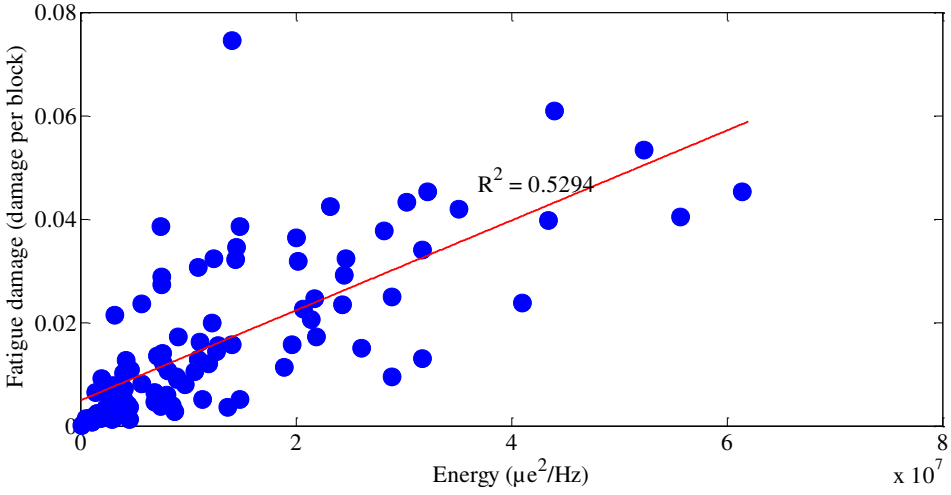

(c)

Figure 4.94 Coefficient of determination for energy and fatigue damage: (a) Coffin-Manson, (b) Morrow, (c) SWT

1.21 %, 1.24 % and 1.27 %. For kurtosis in Figure 4.93, the coefficients of determination for the Coffin-Manson, Morrow and SWT models were only 0.03287, 0.03234 and 0.03345, respectively, with an error of 1.5 % for all the strain-life models. Once more, it proved that statistical parameters cannot act as a single criterion for predicting fatigue damage. Compared to statistical parameters, the energy gave the highest correlation and the lowest error. It can be seen in Figure 4.94, where the energy gave a coefficient of determination of 0.5105, 0.5229 and 0.5294, respectively, for the Coffin-Manson, Morrow and SWT models, with an error of 1.07 % for all the strain-life models.

Each parameter in the actual strain signals was correlated to a parameter in the simulated strain signals. An energy correlation of 0.4723 for the actual and simulated strain signals was obtained in Figure 4.95. A lower coefficient of determination was because the simulated strain signals were not extracted based on their own energy, but based on the actual strain energy. Although it had a lower correlation, most the energies were distributed in the range of 90 % confidence interval, as shown in Figure 4.96. In terms of statistics shown in Figure 4.97, SD gave the highest coefficient of determination, which was 0.9724, followed by r.m.s. and kurtosis, which was 0.8396 and 0.2728, respectively. A lower coefficient of determination for kurtosis was because the simulated strain signals were not extracted based on their own energy. However, most statistical parameters were also distributed in the range of 90 % confidence interval in Figure 4.98.

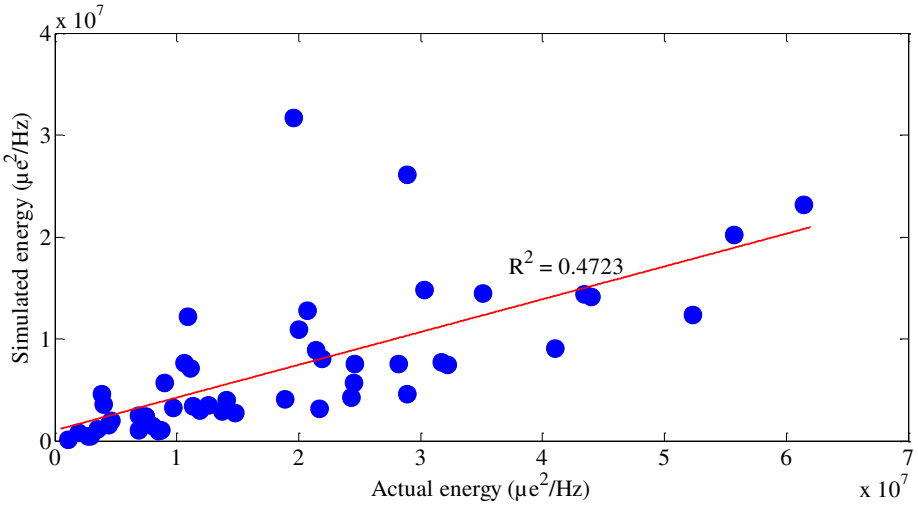

Figure 4.95 Coefficient of determination for energy between the actual and simulated strain signals

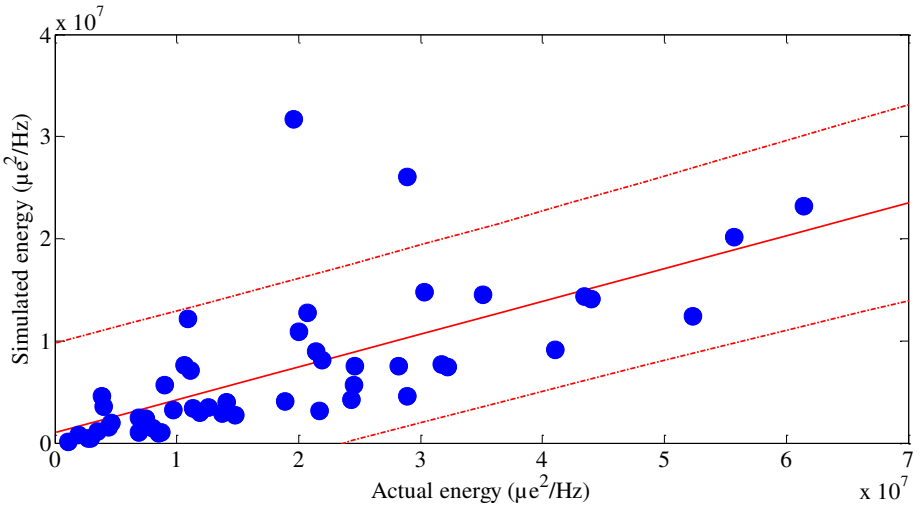

Figure 4.96 Actual and simulated energy distributions in the 90 % confidence interval

The coefficients of determination for fatigue damage between the actual and simulated segments were 0.8904, 0.8865 and 0.8788 for the Coffin-Manson, Morrow and SWT models, respectively, with an RMSE of 0.5 % for all the strain-life models, as shown in Figure 4.99. Based on the results, it strengthened the previous hypothesis where the simulation could produce the strain signals having equivalent fatigue damage to the actual strain signals. In the correlation graphs of fatigue damage shown in Figure 4.100, some of the segments gave higher energy causing the segments to be distributed out as 1:2 or 2:1 correlations. This was because the simulated strain signals were not extracted based on their own energy. For the next validation process, the fatigue life for each strain signal was estimated through experimental works.

4.3.3 Fatigue Life

The stress-strain curve obtained from the tensile test is shown in Figure 4.101. The test revealed some basic information, known as the monotonic mechanical properties. A line was drawn parallel to the straight-line portion of the original stress-strain curve at 0.2 % of strain, providing the yield strength. The yield strength was the stress at which the specimen strain changed from elastic deformation to plastic deformation, causing it to deform permanently. The UTS was the maximum stress on the stress-strain curve at which the specimen could withstand tension, compression or shearing before breaking or permanently deforming. Using the Hooke law in Equation (2.8), the material modulus of elasticity was determined, measuring how much the specimen bends under the given stress.

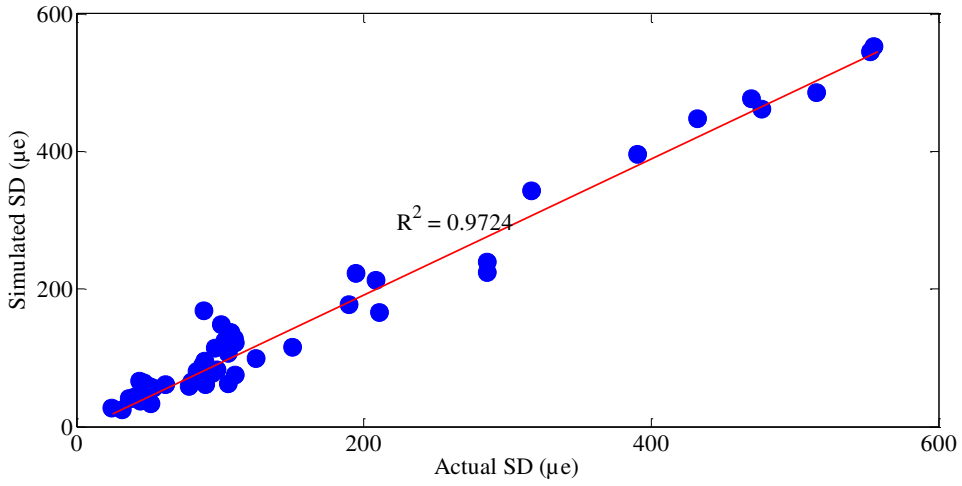

(a)

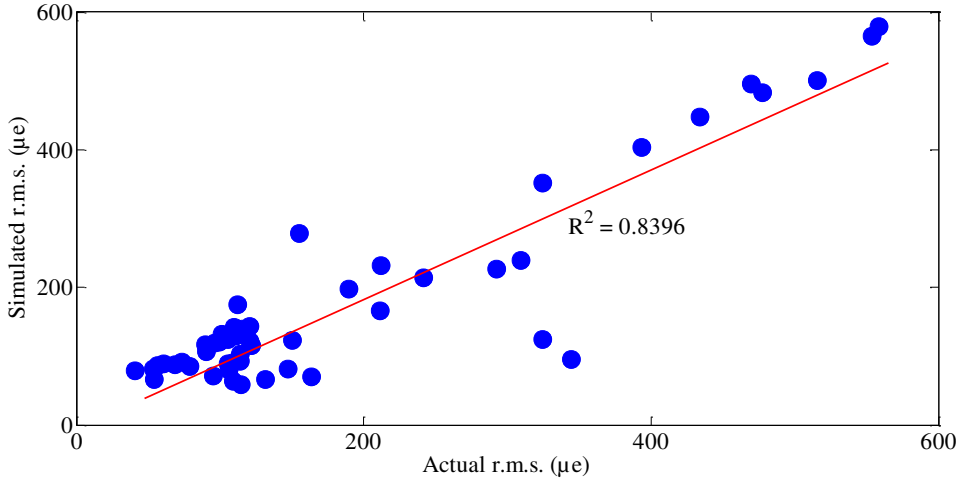

(b)

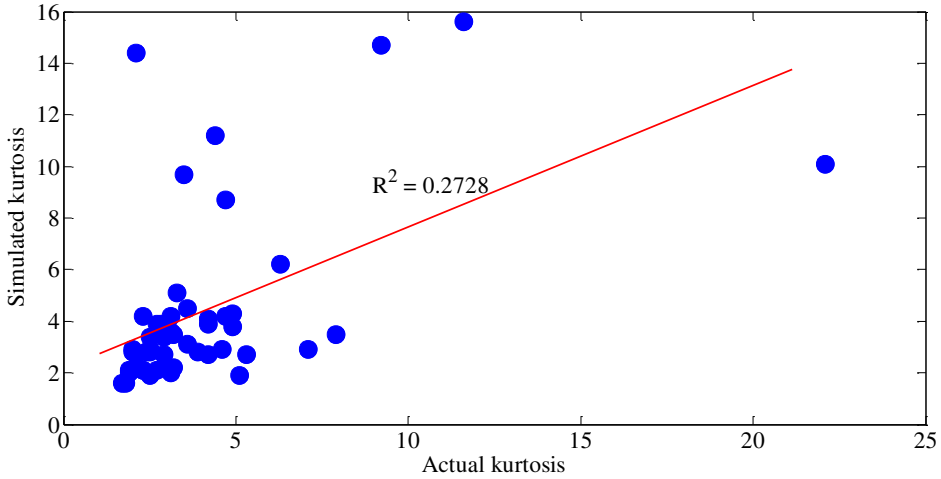

(c)

Figure 4.97 Coefficient of determination for statistical parameters between the actual and simulated strain signals: (a) SD, (b) r.m.s. (c) kurtosis

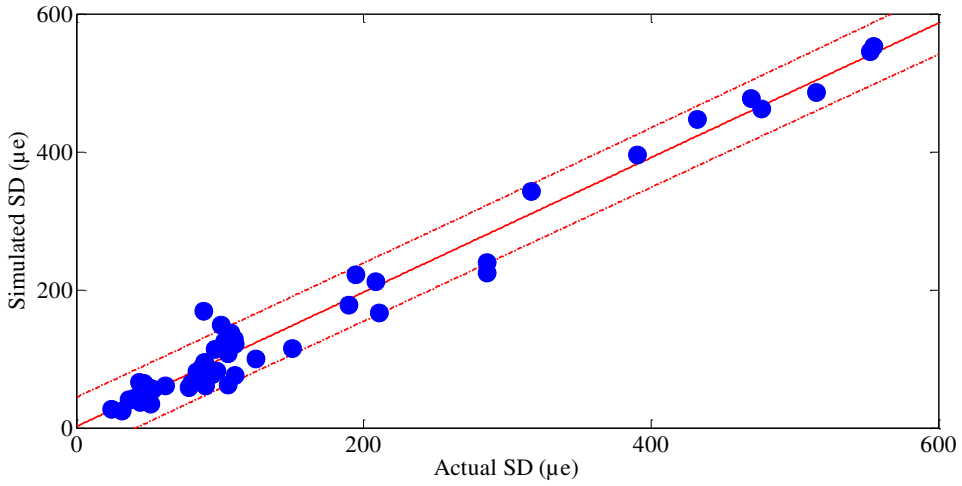

(a)

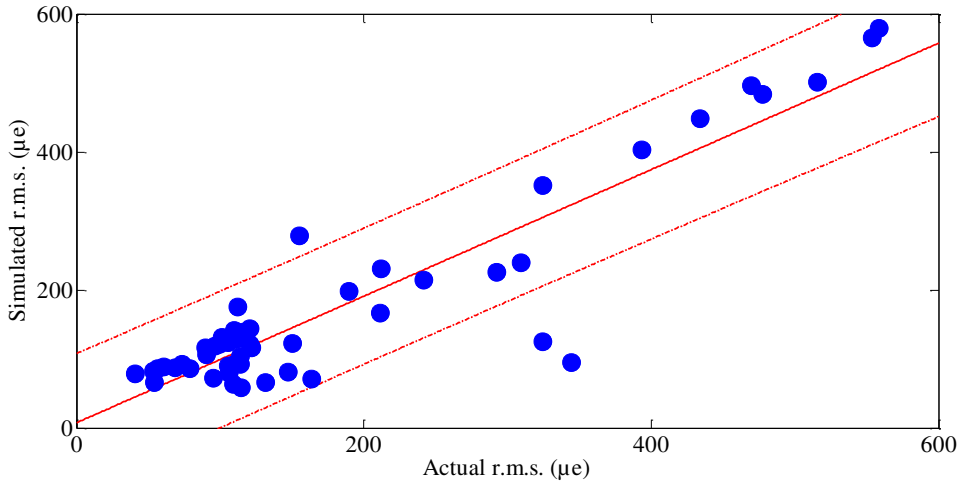

(b)

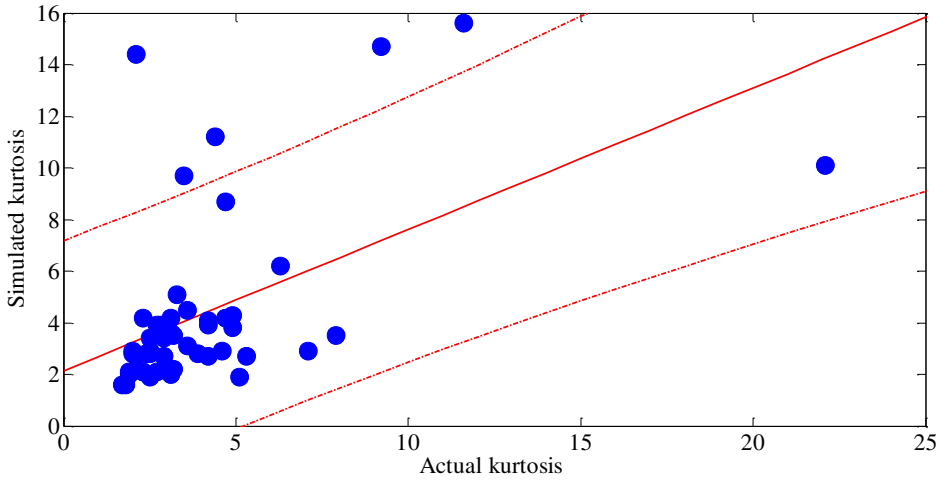

(c)

Figure 4.98 Actual and simulated statistical parameter distributions in the 90 % confidence interval: (a) SD, (b) r.m.s., (c) kurtosis

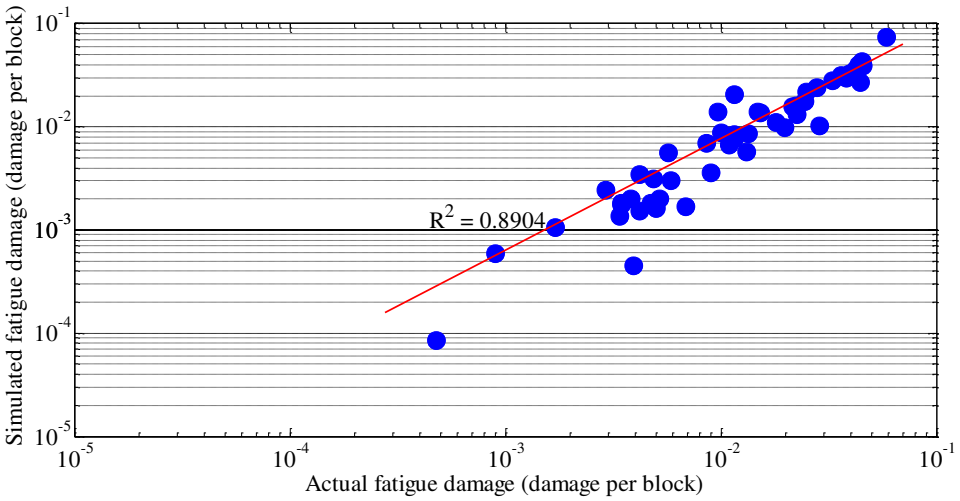

(a)

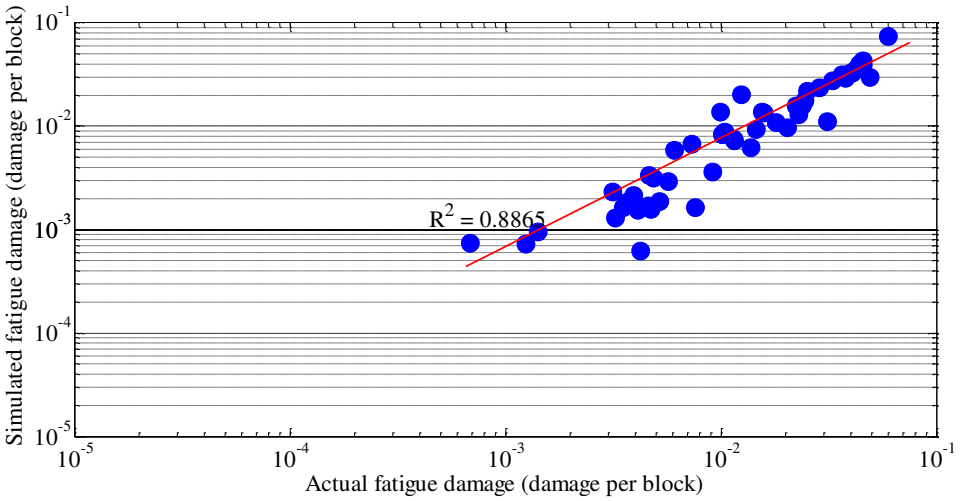

(b)

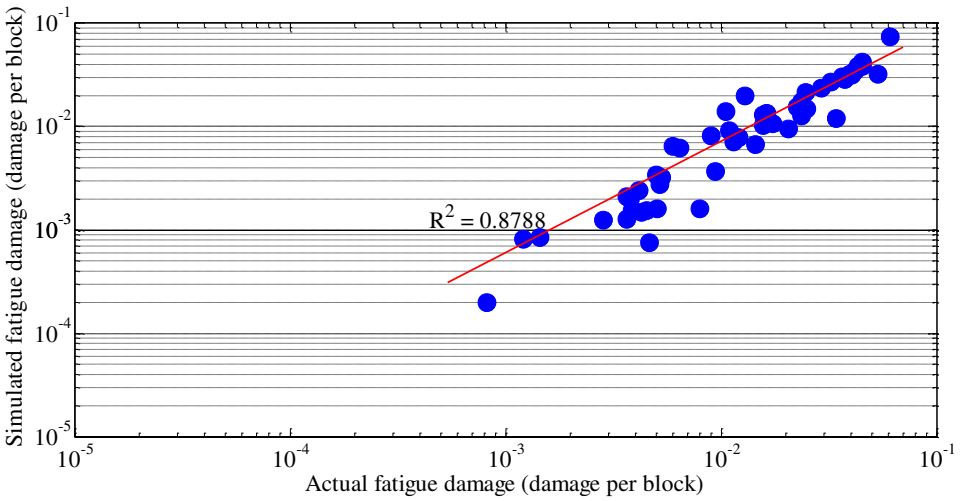

(c)

Figure 4.99 Coefficient of determination for fatigue damage between the actual and simulated strain signals: (a) Coffin-Manson, (b) Morrow, (c) SWT

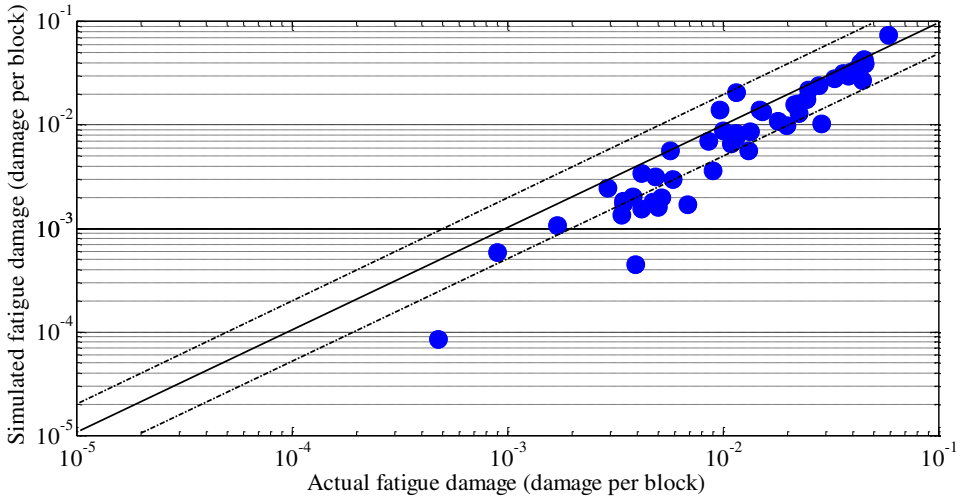

(a)

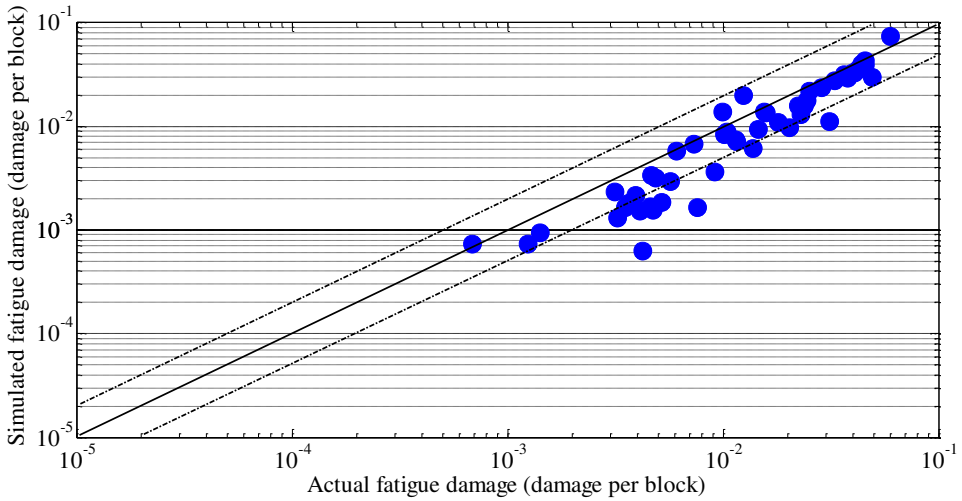

(b)

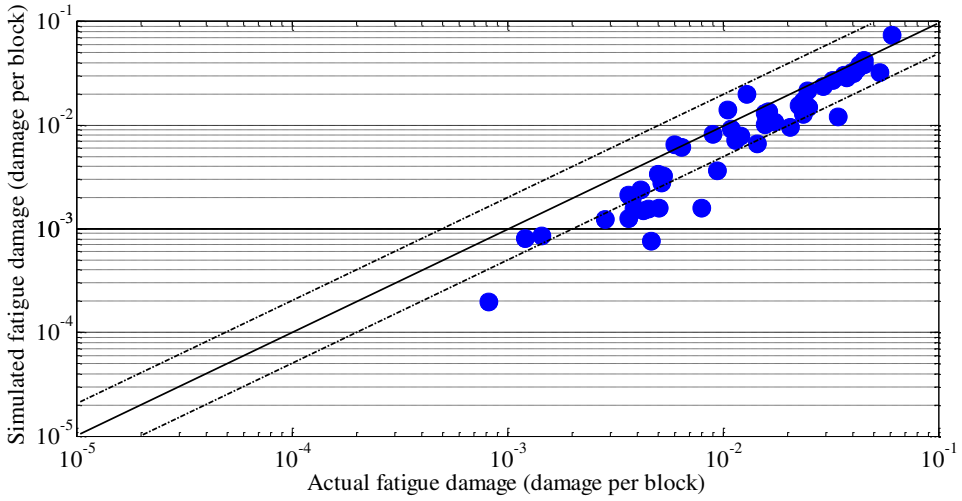

(c)

Figure 4.100 Actual and simulated fatigue damage distributions in the range of 1:2 or 2:1 correlation: (a) Coffin-Manson, (b) Morrow, (c) SWT

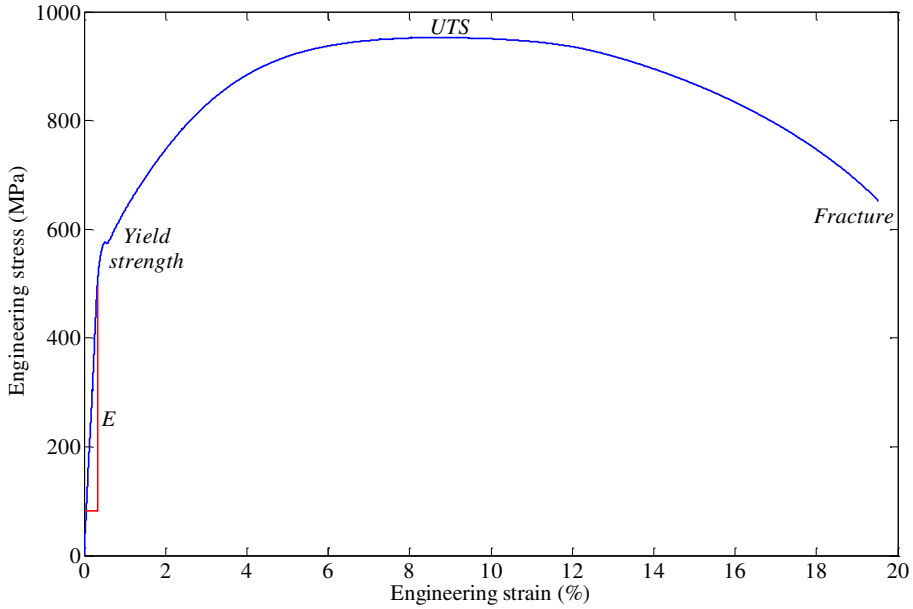

Figure 4.101 Stress-strain curve obtained for the SAE5160 carbon steel during the tensile test

The tensile test gave the elongation before failure of 19.5 %, providing 953 MPa and 572 MPa of the UTS and the 0.2 % yield strength, respectively. The UTS and the yield strength resulted were lower than the values listed in Table 3.3, giving 1,584 MPa and 1,487 MPa for the UTS and the yield strength. The test, however, gave a material modulus of elasticity of 208 GPa, which was equivalent to the value provided in the table.

A broken specimen of the fatigue test is shown in Figure 4.102. Tables 4.22 to 4.25 provide the fatigue life comparisons between the actual and simulated strain signals obtained from the strain-life approach and the fatigue tests. Most the strain-life models gave longer fatigue life for the simulated strain signals. Referring to the fatigue life based on the strain-life approach in Tables 4.22 to 4.24, the original strain signals gave the biggest increase of 8 % for the highway strain signal based on the SWT model. However, the edited simulated strain signals gave the highest deviations, which were more than 20 %. It was because the simulated strain signals were extracted based on the actual strain signals.

Figure 4.102 A broken specimen of the fatigue test

Table 4.22 Fatigue life comparisons between the actual and simulated strain signals based on the Coffin-Manson model

Strain signals		Actual (reversals of blocks)	Simulation (reversals of blocks)	Differences (%)
Highway	Original	267,100	269,400	1
	Edited	279,100	269,300	-4
Urban	Original	397	391	-2
	Edited	426	546	28
Rural	Original	91	94	3
	Edited	92	112	22

Note: difference = (simulation - actual) / actual x 100 %

Table 4.23 Fatigue life comparisons between the actual and simulated strain signals based on the Morrow model

Strain signals		Actual (reversals of blocks)	Simulation (reversals of blocks)	Differences (%)
Highway	Original	72,040	77,374	7
	Edited	73,860	77,370	5
Urban	Original	417	414	-1
	Edited	448	570	27
Rural	Original	92	93	0
	Edited	94	115	23

Note: difference = (simulation - actual) / actual x 100 %

Table 4.24 Fatigue life comparisons between the actual and simulated strain signals based on the SWT model

Strain signals		Actual (reversals of blocks)	Simulation (reversals of blocks)	Differences (%)
Highway	Original	47,800	51,690	8
	Edited	48,760	51,710	6
Urban	Original	430	433	1
	Edited	464	588	27
Rural	Original	95	95	0
	Edited	97	122	25

Note: difference = (simulation - actual) / actual x 100 %

Table 4.25 Fatigue life comparisons between the actual and simulated strain signals based on the fatigue tests

Strain signals		Actual (reversals of blocks)	Simulation (reversals of blocks)	Differences (%)
Highway	Original	3,080	1,802	-41
	Edited	3,276	3,188	-3
Urban	Original	352	345	-2
	Edited	383	285	-26
Rural	Original	80	78	-3
	Edited	82	65	-21

Note: difference = (simulation - actual) / actual x 100 %

Contrasting results were obtained from the fatigue tests. Based on the results in Table 4.25, the simulated strain signals provided shorter fatigue life compared to the actual strain signals. This showed that the simulated strain signals provided higher amplitudes, since the equation of motion used to develop the simulated model being simplified. The original highway strain signal gave a deviation of up to 41 %. This could be influenced by the presence of notches on the specimen surface (Solin et al. 2009). Except for the edited urban and rural strain signals giving more than 20 % deviation, other the strain signals gave a maximum difference of 3 %. The results showed that the simulated model was suitable, with differences mostly below 10 %.

The fatigue life comparisons between the original and edited strain signals obtained from the strain-life approach and the fatigue tests are provided in Tables 4.26 to 4.29. The fatigue life increased in almost all the edited strain signals either based on the strain-life approach or the fatigue tests. The increases were because lower strain

Table 4.26 Fatigue life comparisons between the original and edited strain signals based on the Coffin-Manson model

Strain signals		Original (reversals of blocks)	Edited (reversals of blocks)	Differences (%)
Highway	Actual	267,100	279,100	4
	Simulation	269,400	269,300	0
Urban	Actual	397	426	7
	Simulation	391	546	39
Rural	Actual	91	92	1
	Simulation	94	112	20

Note: difference = (edited - original) / original x 100 %

Table 4.27 Fatigue life comparisons between the original and edited strain signals based on the Morrow model

Strain signals		Original (reversals of blocks)	Edited (reversals of blocks)	Differences (%)
Highway	Actual	72,040	73,860	3
	Simulation	77,374	77,370	0
Urban	Actual	417	448	8
	Simulation	414	570	38
Rural	Actual	92	94	2
	Simulation	93	115	25

Note: difference = (edited - original) / original x 100 %

Table 4.28 Fatigue life comparisons between the original and edited strain signals based on the SWT model

Strain signals		Original (reversals of blocks)	Edited (reversals of blocks)	Differences (%)
Highway	Actual	47,800	48,760	2
	Simulation	51,690	51,710	0
Urban	Actual	430	464	8
	Simulation	433	588	36
Rural	Actual	95	97	2
	Simulation	95	122	29

Note: difference = (edited - original) / original x 100 %

Table 4.29 Fatigue life comparisons between the original and edited strain signals based on the fatigue tests

Strain signals		Original (reversals of blocks)	Edited (reversals of blocks)	Differences (%)
Highway	Actual	3,080	3,276	6
	Simulation	1,802	3,188	77
Urban	Actual	352	383	9
	Simulation	345	285	-17
Rural	Actual	80	82	3
	Simulation	78	65	-17

Note: difference = (edited - original) / original x 100 %

amplitudes removed in the extraction process actually contributed to a minimum fatigue damage. When the minimum fatigue damage in the original strain signals was eliminated, it gave additional lives for the edited strain signals before failure. The maximum increase was 77 % based on the fatigue test for the simulated highway strain signal. Higher increase was because the simulated strain signals were extracted based on the actual strain signals. The life for the edited actual strain signals, however,

was not significantly different compared to the life for the original actual strain signals, which was mostly below 10 %, showing the suitability of the simulated model.

In Figure 4.103, it was presented the fatigue life distributions based on the strain-life approach and the fatigue tests. All the fatigue lives, listed in Tables 4.22 to 4.25, were distributed in the range of 1:2 or 2:1 correlation. Figure 4.104 gave a coefficient of determination of 0.9993, 0.9998 and 0.9999 for the Coffin-Manson, Morrow and SWT models, respectively. In addition, the coefficient of determination indicated in Figure 4.105 for the fatigue tests was 0.9056. This indicated that the simulated fatigue life was almost linearly proportional to the actual fatigue life and the developed simulated model was correct with a good correlation. It strengthened the previous hypothesis where the simulation could produce the strain signals having similar behaviour to the actual strain signals.

In Figure 4.103, the fatigue tests gave shorter fatigue lives compared to the strain-life aproach. The results indicated that the approach predicted fatigue lives much longer than the actual spectrum loading testing life. These findings were

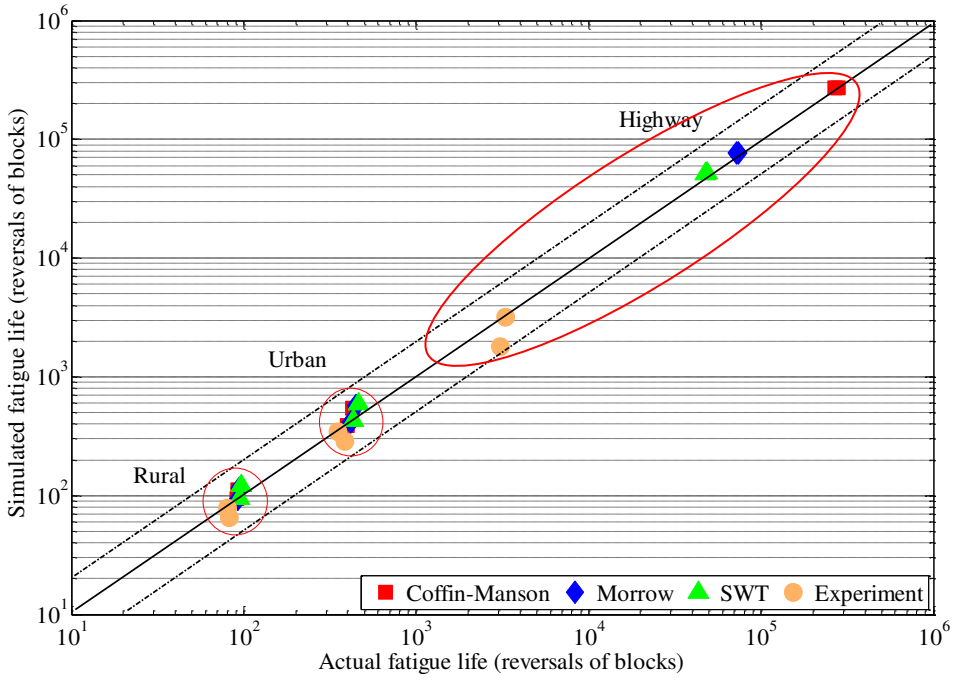

Figure 4.103 Fatigue life distributions for the actual, simulated and edited strain signals in the range of 1:2 or 2:1 correlation

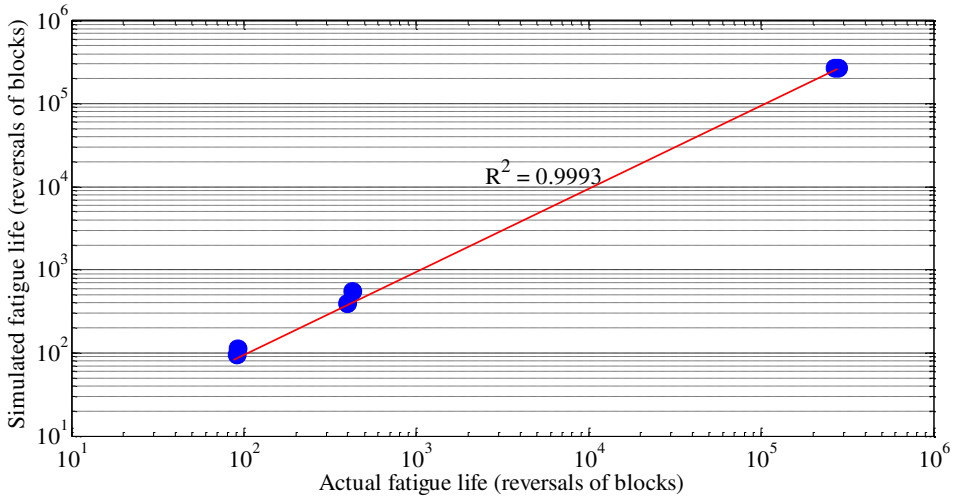

(a)

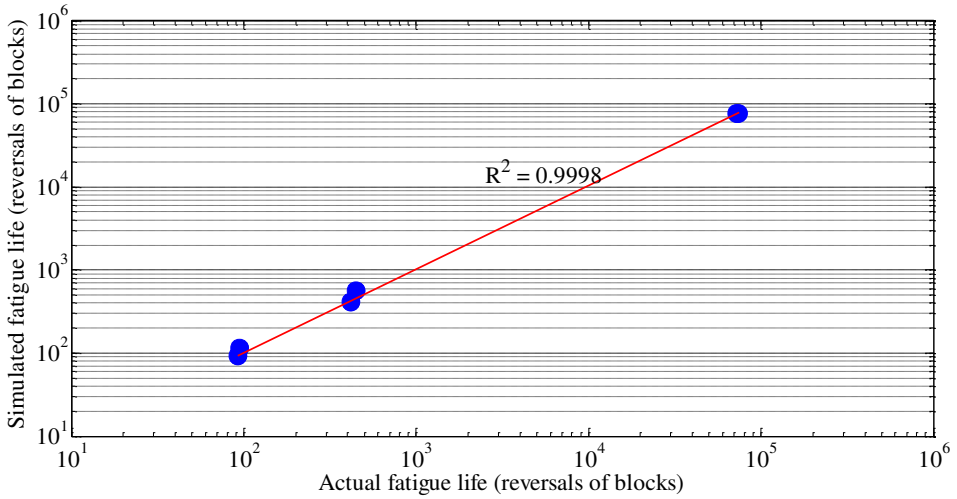

(b)

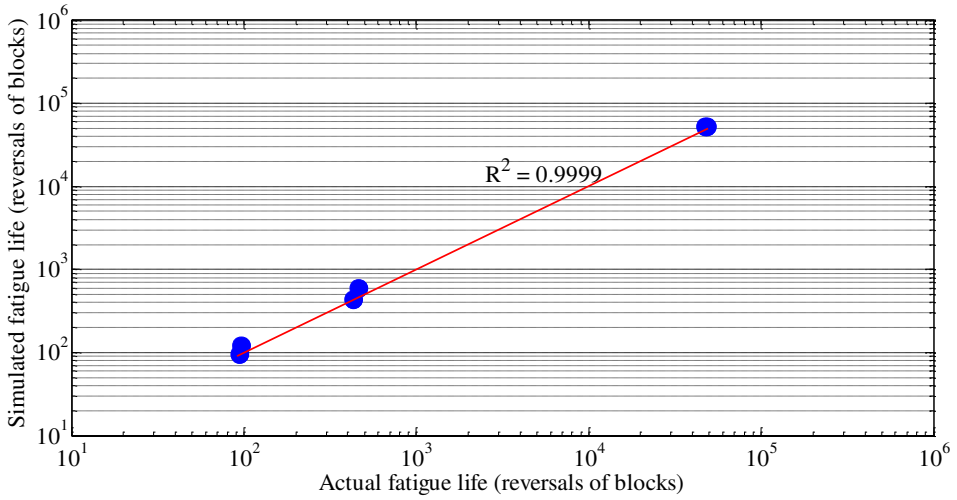

(c)

Figure 4.104 Fatigue life correlations based on the strain-life approach: (a) Coffin-Mason, (b) Morrow, (c) SWT

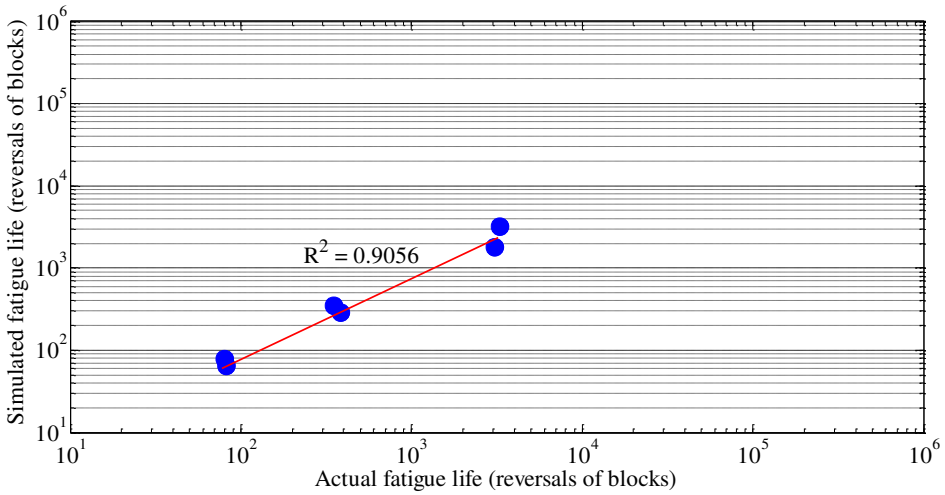

Figure 4.105 Fatigue life correlation based on the fatigue tests

equivalent to the results presented by Garcia et al. (2005), Mottitschka et al. (2010), Lipski & Mroziński (2012) and Bruchhausen et al. (2015). The SWT model gave the nearest fatigue life to the fatigue tests for the highway strain signal, followed by the Morrow and Coffin-Manson models, respectively. Meanwhile for the urban and rural strain signals, the Coffin-Manson model provided the nearest fatigue life, followed by the Morrow and SWT models, respectively. Thus, fatigue life assessments based on the strain-life approach were inaccurate to the fatigue tests. This statement was supported by Cui (2002) and Banvillet et al. (2004). There is no evidence to determine the best model for fatigue life assessments with mean stresses because the fatigue failure is analysed based on micro crack growth during the loading dominated by shear or tensile planes.

The fatigue life differences were a result of the durability being influenced by some factors (Cui 2002; Varvani-Farahani et al. 2005; Lei et al. 2010), namely stress or strain range, mean stress, time of load applied, extreme load, low cycles, surface finish and quality, as well as surface treatments and cycle sequence. The Palmgren-Miner linear cumulative fatigue damage rule applied to the strain-life approach depends on the assumption that sequence changes that occur in a non-uniform cycle do not affect fatigue life. However, the cycle sequence contributes substantially to fatigue life, and therefore, small cycles should not be ignored when predicting fatigue life for a VAL. Thus, results given by this rule were quite wide in the calculations of fatigue life.

This could be proven experimentally through the fatigue tests using low-high and high-low cycles. Referring to Table 4.2, the SWT model gave lower fatigue damage for S2 and S3, indicating that the model gave lower strain amplitudes. Thus, the model was selected to determine the fatigue damage for loading arrangements, as shown in Figures 3.18 to 3.20. The selection of lower strain amplitudes for developing the block loading was because fatigue tests usually give a shorter fatigue life. If higher strain amplitude was selected, it could have caused specimens to fail suddenly.

The fatigue tests had shown that the cycle sequences greatly influenced the fatigue life when the loads were changed from low cycles to high cycles. The fatigue life for high-low cycles was lower than low-high cycles, which was 29.6 %, 12.6 % and 21.5 %, respectively, for the highway, urban and rural strain signals, as shown in Table 4.30 and Figure 4.106. Since cycle sequences changed the results, this sequence effect should be considered and addressed in predicting fatigue life in order to achieve accurate results. These results were in line with the studies conducted by Carvalho et al. (2010), Ayoub et al. (2011), Taheri et al. (2013) and Nagode (2014), where one of the results is presented in Figure 4.107. Either increasing or decreasing block

Table 4.30 Fatigue life comparisons between the low-high and high-low cycle sequences

Strain signals	**Low-high cycles (reversals of blocks)**	**High-low cycles (reversals of blocks)**	**Differences (%)**
Highway	74,134	57,182	-29.6
Urban	2,053	1,823	-12.6
Rural	791	651	-21.5

Note: difference = (low-high - high-low) / high-low x 100 %

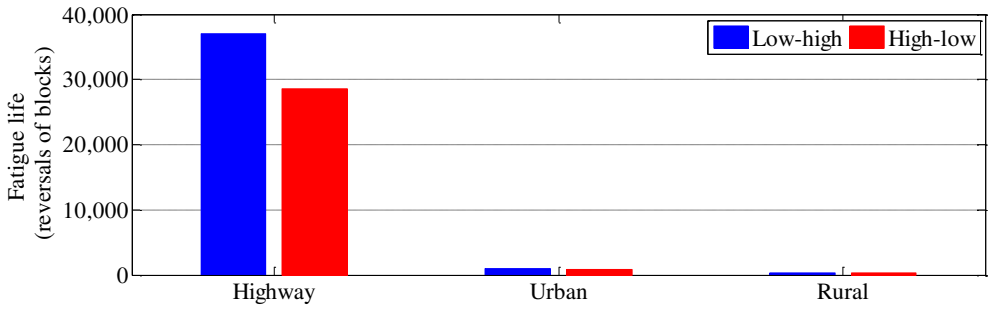

Figure 4.106 Cycle sequence effects for all the strain signals

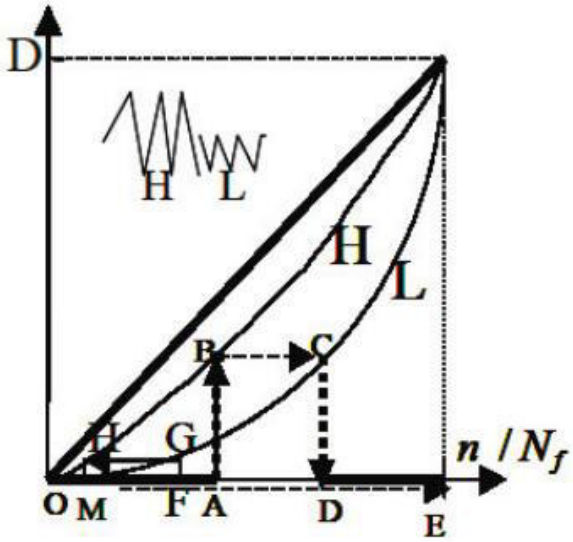

Figure 4.107 Non-linear damage modelling representing high-low cycles more damaging than low-high cycles

Source: Taheri et al. 2013

loadings, fatigue test results are below the predictions (Garcia et al. 2005; Rognin et al. 2009). Therefore, these weaknesses result in significant differences in predicting fatigue life between theory and experiment.

Although the edited strain signals provided a higher fatigue life compared to the original strain signals, as shown in Tables 4.26 to 4.29, the fatigue testing time were shorter because most lower amplitude cycles were removed. Testing time, however, is not necessarily proportional to strain amplitudes, since in a full-scale test small amplitudes usually have a shorter period (higher frequency) than large amplitudes. As listed in Table 4.31, the original actual strain signal of the highway road (S1) required at least 3,080 reversals of blocks until failure and the time required was more than 513.8 hours. The reduction of the time by 41.5 % or 300.5 hours was obtained using the original simulated strain signal (S4) providing 1,802 reversals of blocks, that could be caused by the presence of notches on the specimen surface (Solin et al. 2009). When the length of S1 could be reduced up to 95.3 % in the edited actual strain signal (S7) with 3,276 reversals of blocks without affecting the fatigue damage content, the time required to perform the fatigue test could be reduced up to 95 %, or about 25.8 hours. In S7, the lower strain amplitudes contained in S1 were removed, and thus, accelerated the fatigue test. The time could be reduced once more using the

edited simulated strain signal (S10) since the lower amplitudes contained in the strain signal were removed as well. The strain signal gave 3,188 reversals of blocks and just needed 25.1 hours until failure in the fatigue test. In total, the time could be reduced more than 95.1 %.

Table 4.31 Testing time required for the fatigue tests until specimens failure for each strain signal

Strain signals	Original actual (hours)	Original simulation (hours)	Diff. 1 (%)	Edited actual (hours)	Diff. 2 (%)	Edited simulation (hours)	Diff. 3 (%)
Highway	513.8	300.5	-41.5	25.8	-95.0	25.1	-95.1
Urban	58.7	57.6	-2.0	8.8	-85.1	6.5	-88.9
Rural	13.4	13.0	-2.5	1.4	-89.7	1.1	-91.8

Note: diff. 1 = difference = (original simulation - original actual) / original actual x 100 %
diff. 2 = difference = (edited actual - original actual) / original actual x 100 %
diff. 3 = difference = (edited simulation - original actual) / original actual x 100 %

A similar condition could be seen in two more strain signals. The time needed to perform the fatigue test for the original actual strain signal of the urban road (S2) was 58.7 hours, involving 352 reversals of blocks. The time was reduced by 2 % using the original simulated strain signal (S5) with 345 reversals of blocks. This was because the strain signal provided higher amplitudes. Only 8.8 hours and 6.5 hours were needed to perform the tests using the edited actual (S8) and simulated (S11) strain signals, involving 383 and 285 reversals of blocks, respectively, or 85.1 % and 88.9 % faster than the time needed for S2, because of the lower strain amplitude removal in the FDE technique. The rural strain signal provided the shortest testing time since it had the highest strain amplitudes. Only 13.4 hours and 13 hours were needed to perform the fatigue tests using the original actual (S3) and simulated (S6) strain signals, respectively, involving 80 and 78 reversals of blocks. The time could be reduced by 89.7 % and 91.8 % or only 1.4 hours and 1.1 hours, using the edited actual (S9) and simulated (S12) strain signals, respectively, involving 82 and 65 reversals of blocks. This was due to the effects of the FDE technique.

There are requirements that should be considered when generating a new fatigue random load history, such as (Xiong & Shenoi 2008): (1) sequence of load cycles should be maintained, (2) damage resulting from the new load history should be the same as the original load history, and (3) the new load history should be shorter in length than the original load history to decrease the testing time, by deleting small load cycles and merging smaller ones. Considering the requirements, the simulated strain signals were able to maintain the original cycle sequences, as shown in Figure 4.14, the actual and simulated strain signals had equivalent fatigue damage, as shown in Table 4.9 and Figures 4.34 to 4.35, and the simulated strain signals decreased the fatigue testing time, as shown in Table 4.31. Laboratory experiments involving the acceleration of the durability testing were conducted to show that the fatigue tests had shorter time than the original strain signals, but had similar potential fatigue damage. The required testing time became shorter because of the use of a shorter strain signal.

It was emphasised that retaining high loads is important and that cycles that less than half of the load limit can be eliminated without significantly affecting fatigue testing results. Fatigue damage does not display a significant difference as long as omitted amplitudes are not higher than 13 % of the largest load cycles (Yan et al. 2001). As a result, in many cases, lower amplitude cycles are edited from theses original histories so as to produce shortened loads consisting of higher amplitude cycles for an accelerated fatigue testing (Ko et al. 2005; Xiong & Shenoi 2008), however, their original characteristics are retained. Without editing service load before performing a fatigue test, testing time and cost can become prohibitive. It was suggested that the wavelet transform had successfully identified the higher amplitudes in the strain signals and created new mission strain signals which retained the majority of the original loading sequences in the time histories, i.e. within 10 % deviation. It clearly indicated that the FDE technique could be successfully applied to compress the original strain signals without changing the main histories as well. A comprehensive fatigue analysis can be developed based on the wavelet transform and is expected to be the best choice in the near future estimation of fatigue damage of strain signals.

4.4 SUMMARY

In this chapter, the results obtained from the simulations and experiments were presented. The simulation was able to produce the simulated strain signals. This was because the simulated strain signals were certified as accurate with the fatigue damage deviations below 7.5 % and most the fatigue life deviations below 10 %. There was a 90 % chance that the true values of strain can be generated. With the discovery of the past, the present and the future, a strain signal can be developed via simulation. The manual ways for measuring strain signals can be abandoned. More recently, it has also become possible to estimate strain amplitudes for a coil spring by means of MBD analysis. The economic effects may be reduced by applying current fatigue technologies. The results from this research bode well for increasing the connection between the virtual and real worlds of durability testing. These findings allow further fatigue analyses to be performed. Hence, the MBD simulation developed in the current study is suggested as an alternative method in fatigue-based strain signal acquisitions.

CHAPTER V

CONCLUSIONS AND RECOMENDATIONS

5.1 CONCLUSIONS

The study focused on the development of the simulated strain signals at a coil spring. The study proposed a computer-based simulation for generating strain signals with consideration of road surface profiles that may lead to a fatigue failure. This study was divided into three main stages, namely:

1. Investigation of the acceleration trends based on the strain signals measured at a coil spring on various types of road surfaces.
2. Determination of the strain signals via the MBD simulation considering the acceleration signals.
3. Validation of the simulated strain signals by involving various simulated and experimental tests.

The execution of these three stages produced the simulated strain signals having similar characteristics to the actual strain signals.

5.1.1 Investigation of the Acceleration Trend

The acceleration signals were generated based on the strain signals measured at a coil spring by utilising the equation of motion. Based on the acceleration trend obtained from the highway road, the data received by the component contained a lot of lower acceleration amplitudes, with uniform characteristics because the road had a similar surface. In the acceleration trend from the urban road, the acceleration signal revealed parts with higher amplitudes because the car was driven on a less flat surface. In the

rural acceleration signal, the trend was equal to the urban acceleration trend, but had more segments with higher amplitudes, indicating that the rural road had more rough surfaces, and thus, it caused stronger vibrations to the vehicle. The accelerations for the rural road were distributed between -0.00529 g and 0.00525 g, contributing to higher fatigue damage, which was 1.10×10^{-2}, 1.08×10^{-2} and 1.05×10^{-2} damage per block for the Coffin-Manson, Morrow and SWT models, respectively. This shows that the first objective of the research had been successfully achieved. The fatigue-based acceleration signals were then used as an input for the developed simulation for generating the simulated strain signals.

5.1.2 Determination of the Strain Signal

A further objective of the current study was to develop the MBD simulation to generate the simulated strain signals. The simulated strain signals led to fatigue damage affected by the road surfaces, because the acceleration signals as the input were resulted from the actual strain signals, collected at higher stress distribution giving higher fatigue damage. Generally, both the actual and simulated strain signals had similar patterns. It reflected the high uniformity indicating that the probability of similarity between both the strain signals was big. Based on the comparison between the actual and simulated strain signals, the deviations of fatigue damage were acceptable, which were below 7.5 %. It gave a minimum RMSE-based error of 0.011 %. However, there was a problem when generating the simulated strain signals. The model produced zero-mean strain signals since the acceleration signals had zero-mean values as well. Thus, modification of the simulated model is needed to improve its ability to generate a non-zero-mean strain signal.

5.1.3 Validation of the Simulated Strain Signal

Based on the FDE results, the wavelet transform was able to shorten the strain signal time up to 95.3 % and that 96.1 % of lower amplitude cycles were reduced. Thus, maintenance of fatigue damage by more than 92.7 % was produced. There was a specific correlation trend and regular pattern between fatigue damage against wavelet-based energy. This statement was shown by the consistent reduction of the values due to the extraction process. Based on the fatigue tests, the fatigue lives of all the strain

signals were distributed in the range of 1:2 or 2:1 correlation. In addition, the deviations of fatigue life were acceptable, with most the deviations at below 10 %. It was 90 % confident that the simulated strain signals are realistic. The fatigue testing time could be saved at least 85.1 % using the edited actual strain signals. The time could be reduced by more than 88.9 % using the edited simulated strain signals. Although the frequency was increased up to 100 Hz to accelerate the testing time, it did not affect the fatigue lives since all the strain signals were tested at the same frequency.

5.2 CONTRIBUTION TO KNOWLEDGE

Since the actual acquisition of a strain signal proves to be exorbitantly expensive, the study replicated this problem scenario using a simulator. Since such simulation is not yet found in previous works, an MBD simulation was developed in order to generate a simulated strain signal. Utilising an actual strain signal, an acceleration signal was generated based on the equation of motion for an automotive coil spring. The acceleration signal represents the road surface profile. The fatigue-based acceleration signal was considered as a disturbance for generating a simulated strain signal. Using the MBD simulation, a simulated strain signal was accurately measured. It is a guide to the discovery of the latest methods to measure a strain signal. Using the newly developed FDE technique, higher strain amplitudes causing the majority of fatigue damage were identified and extracted and thus only shortened loads which consisted of higher strain amplitudes were produced. Utilising the MBD simulation and the FDE technique, the integrity of a coil spring can be accurately predicted and a fatigue failure can be effectively detected at an early stage, thus saving the cost of maintenance and operation.

5.3 RECOMENDATIONS

There are some tasks that can be improved for the continuation of the work in the future, which are:

1. In real applications, machine components and structures are generally subjected to multi-axial fatigue loading conditions. Fatigue life evaluation of

mechanical components under complex loading conditions is of great importance to optimise structural designs and improve inspection and maintenance procedures. Therefore, a multi-axial fatigue test is good to be performed in order to investigate a better life assessment.

2. To improve the accuracy of the MBD simulation, external forces should be considered as well. Tyre effect, for example, could play an important role in the simulation.
3. Optimisation can be applied in generating a shorter edited strain signal. Thus, the FCM can be employed to detect damaging segments having lower energy and then remove them in order to further shorten the edited strain signal, especially for lower strain amplitude signals.
4. Optimisation can also be applied to determine the trim level for damage extraction using a mathematical model.
5. The developed simulation used nominal estimation of a road surface profile, which is difference compared to the actual situation. Thus, a mathematical model associating to a road surface profile should be developed in order to produce a better outcome in strain signal generation. The mathematical model can be combined with the simulated model in the current study. Thus, measurements of acceleration and strain signals are not needed anymore.

REFERENCES

Abaqus. 2008. *Getting Started with Abaqus*. Providence: Dassault Systèmes Simulia Corp.

Abdullah, S. 2005. Wavelet Bump Extraction (WBE) for Editing Variable Amplitude Fatigue Loadings. Ph.D. Thesis. The University of Sheffield.

Abdullah, S., Choi, J.C., Giacomin, J.A. & Yates, J.R. 2006. Bump Extraction Algorithm for Variable Amplitude Fatigue Loading. *International Journal of Fatigue*, 28: 675-691.

Abidin, M.I.Z., Mahmud, J., Latif, M.J.A. & Jumahat, A. 2013. Experimental and Numerical Investigation of SUP12 Steel Coil Spring. *Procedia Engineering*, 68: 251-257.

Abu-Mahfouz, I. & Banerjee, A. 2014. Drill Wear Feature Identification under Varying Cutting Conditions using Vibration and Cutting Force Signals and Data Mining Techniques. *Procedia Computer Science*, 36: 556-563.

Aid, A., Amrouche, A., Bouiadjra, B.B., Benguediab, M. & Mesmacque, G. 2011. Fatigue Life Prediction under Variable Loading based on a New Damage Model. *Materials and Design*, 32: 183-191.

Al-Asady, N.A., Abdullah, S., Ariffin, A.K., Beden, S.M. & Rahman, M.M. 2009. Comparison Between Experimental Road Data and Finite Element Analysis Data for the Automotive Lower Suspension Arm. *European Journal of Scientific Research*, 29: 557-571.

Alaoui, A.E.M., Thevenet, D. & Zeghloul, A. 2009. Short Surface Fatigue Cracks Growth under Constant and Variable Amplitude Loading. *Engineering Fracture Mechanics*, 76: 2359-2370.

Alvarez-Sánchez, E. 2013. A Quarter-Car Suspension System: Car Body Mass Estimator and Sliding Mode Control. *Procedia Technology*, 7: 208-214.

Antoni, J. 2006. The Spectral Kurtosis: a Useful Tool for Characterising non-Stationary Signals. *Mechanical Systems and Signal Processing*, 20: 282-307.

Asnaashari, E. & Sinha, J.K. 2014. Off-line Crack Detection in Rotors. *Proceedings of VETOMAC X*, 23: 129-137.

ASTM E8/E8M-11. 2012. *Standard Test Methods for Tension Testing of Metallic Materials*. West Conshohocken: ASTM International.

ASTM E112-96. 2004. *Standard Test Methods for Determining Average Grain Size*. West Conshohocken: ASTM International.

ASTM E606-92. 1998. *Standard Practice for Strain-Controlled Fatigue Testing*. West Conshohocken: ASTM International.

ASTM E739-91. 2004. *Standard Practice for Statistical Analysis of Linear or Linearized Stress-Life (S-N) and Strain-Life (ε-N) Fatigue Data.* West Conshohocken: ASTM International.

ASTM E1049-85. 1997. *Standard Practice for Cycle Counting in Fatigue Analysis.* West Conshohocken: ASTM International.

ASTM E1237-93. 2009. *Standard Guide for Installing Bonded Resistance Strain Gages*. West Conshohocken: ASTM International.

Aygül, M., Al-Emrani, M. & Urushadze, S. 2012. Modelling and Fatigue Life Assessment of Orthotropic Bridge Deck Details using FEM. *International Journal of Fatigue*, 40: 129-142.

Aygül, M., Bokesjö, M., Heshmati, M. & Al-Emrani, M. 2013. A Comparative Study of Different Fatigue Failure Assessments of Welded Bridge Details. *International Journal of Fatigue*, 49: 62-72.

Aykan, M. & Çelik, M. 2009. Vibration Fatigue Analysis and Multi-Axial Effect in Testing of Aerospace Structures. *Mechanical Systems and Signal Processing*, 23: 897-907.

Ayoub, G., Naït-Abdelaziz, M., Zaïri, F., Gloaguen, J.M. & Charrier, P. 2011. A Continuum Damage Model for the High-Cycle Fatigue Life Prediction of Styrene-Butadiene Rubber under Multiaxial Loading. *International Journal of Solids and Structures*, 48: 2458-2466.

Baek, S.H., Cho, S.S. & Joo, W.S. 2008. Fatigue Life Prediction based on the Rainflow Cycle Counting Method for the End Beam of a Freight Car Bogie. *International Journal of Automotive Technology*, 9: 95-101.

Ban, H., Shi, G., Shi, Y. & Wang, Y. 2012. Overall Buckling Behavior of 460 MPa High Strength Steel Columns: Experimental Investigation and Design Method. *Journal of Constructional Steel Research*, 74: 140-150.

Banvillet, A., Łagoda, T., Macha, E., Niesłony, A., Palin-Luc, T. & Vittori, J.-F. 2004. Fatigue Life under non-Gaussian Random Loading from Various Models. *International Journal of Fatigue*, 26: 349-363.

Beaurepaire, P. & Schuëller, G.I. 2011. Modeling of the Variability of Fatigue Crack Growth using Cohesive Zone Elements. *Engineering Fracture Mechanics*, 78: 2399-2413.

Benedetti, M., Fontanari, V. & Monelli, B.D. 2010. Plain Fatigue Resistance of Shot Peened High Strength Aluminium Alloys: Effect of Loading Ratio. *Procedia Engineering*, 2: 397-406.

Bezdek, J.C. 1981. *Pattern Recognition with Fuzzy Objective Function Algorithms*. New York: Plenum Press.

Bhagi, L.K., Gupta, P. & Rastogi, V. 2013. Fractographic Investigations of the Failure of L-1 Low Pressure Steam Turbine Blade. *Case Studies in Engineering Failure Analysis*, 1: 72-78.

Bhat, S. & Patibandla, R. 2011. Metal Fatigue and Basic Theoretical Models: a Review, Alloy Steel - Properties and Use. Chapter in Book. *Intech*, 203-236.

Bishop, N.W.M., Steinbeck, J. & Sherratt, F. 2000. Finite Element based Fatigue Calculations. *Proceedings of the International Association for the Engineering Analysis Community*.

Böhm, M. & Niesłony, A. 2015. Strain-based Multiaxial Fatigue Life Evaluation using Spectral Method. *Procedia Engineering*, 101: 52-60.

Brandt, S. 2014. *Data Analysis: Statistical and Computational Methods for Scientists and Engineers*, 4th Ed. Switzerland: Springer International Publishing.

Braccesi, C., Cianetti, F., Lori, G. & Pioli, D. 2009. The Frequency Domain Approach in Virtual Fatigue Estimation of non-Linear Systems: the Problem of non-Gaussian States of Stress. *International Journal of Fatigue*, 31: 766-775.

Bruchhausen, M., Fischer, B., Ruiz, A., González, S., Hähner, P. & Soller, S. 2015. Impact of Hydrogen on the High Cycle Fatigue Behaviour of Inconel 718 in Asymmetric Push–Pull Mode at Room Temperature. *International Journal of Fatigue*, 70: 137-145.

Brünnet, H., Lyubenova, N., Müller, M., Hoffmann, J.E. & Bähre, D. 2014. Verification and Application of a New 3D Finite Element Approach to Model the Residual Stress Depth Profile After Autofrettage and Consecutive Reaming. *Procedia CIRP*, 13: 72-77.

Buch, A. 1980. Effect of Some Aircraft Loading Program Modifications on the Fatigue Life of Open Hole Specimens. *Engineering Fracture Mechanics*, 13: 237-256.

Callister, W.D. & Rethwisch, D.G. 2012. *Fundamentals of Materials Science and Engineering: an Integrated Approach*, 4th Ed. New Jersey: John Wiley & Sons, Inc.

Carvalho, A.L.M., Martin, J.P. & Voorlwad, H.J.C. 2010. Fatigue Damage Accumulation in Aluminum 7050-T7451 Alloy Subjected to Block Programs Loading under Step-Down Sequence. *Procedia Engineering*, 2: 2037-2043.

Chapetti, M.D. & Jaureguizahar, L.F. 2012. Fatigue Behavior Prediction of Welded Joints by using an Integrated Fracture Mechanics Approach. *International Journal of Fatigue*, 43: 43-53.

Chen, T. 2007. Extremely Low Cycle Fatigue Assessment of Thick-Walled Steel Piers. Ph.D. Thesis. Nagoya University.

Chen, H., Zuo, M.J., Wang, X. & Hoseini, M.R. 2010. An Adaptive Morlet Wavelet Filter for Time-of-Fight Estimation in Ultrasonic Damage Assessment. *Measurement*, 43: 570-585.

Chen, N.-Z., Wang, G. & Soares, C.G. 2011. Palmgren-Miner's Rule and Fracture Mechanics-based Inspection Planning. *Engineering Fracture Mechanics*, 78: 3166-3182.

Chen, X. 2014. Analysis of Crosswind Fatigue of Wind-Excited Structures with Nonlinear Aerodynamic Damping. *Engineering Structures*, 74: 145-156.

Chikhale, S.J. & Deshmukh, S.P. 2013. Comparative Analysis of Vehicle Suspension System in Matlab-SIMULINK and MSc-ADAMS with the Help of Quarter Car Model. *International Journal of Innovative Research in Science, Engineering and Technology*, 2: 4074-4081.

Chiou, Y.-C. & Yang, J.-K. 2012. The Effects of Pre-Deformation on the Subsequent Fatigue Behaviors of SUS 430 Stainless Steel in Load-Control. *International Journal of Solids and Structures*, 49L: 3263-3268.

Chuliang, Y. & Kege, L. 2011. Theory of Economic Life Prediction and Reliability Assessment of Aircraft Structures. *Chinese Journal of Aeronautics*, 24: 164-170.

Cini, A. 2012. Scribe Marks at Fuselage Joints: Initiation and Propagation of Fatigue Cracks from Mechanical Defects in Aluminium Alloys. Ph.D. Thesis. Cranfield University.

Claeys, F. 2008. A Generic Software Framework for Modelling and Virtual Experimentation with Complex Environmental Systems. Ph.D. Thesis. Ghent University.

Combet, F. & Gelman, L. 2009. Optimal Filtering of Gear Signals for Early Damage Detection based on the Spectral Kurtosis. *Mechanical Systems and Signal Processing*, 23: 652-668.

Conle, A. & Topper, T.H. 1979. Evaluation of Small Cycle Omission Criteria for Shortening of Fatigue Service Histories. *International Journal of Fatigue*, 1: 23-28.

Conle, A. & Topper, T.H. 1980. Overstrain Effects during Variable Amplitude Service History Testing. *International Journal of Fatigue*, 2: 130-136.

Cooley, J.W. & Tukey, J.W. 1965. An Algorithm for the Machine Calculation of Complex Fourier Series. *Mathematics of Computation*, 19: 297-301.

Cui, W. 2002. A State-of-the-Art Review on Fatigue Life Prediction Methods for Metal Structures. *Journal Marine Science and Technology*, 7: 43-56.

Darpe, A.K. 2007. A Novel Way to Detect Transverse Surface Crack in a Rotating Shaft. *Journal of Sound and Vibration*, 305: 151-171.

Das, S.K., Mukhopadhyay, N.K., Kumar, B.R. & Bhattacharya, D.K. 2007. Failure Analysis of a Passenger Car Coil Spring. *Engineering Failure Analysis*, 14: 158-163.

Das, S. 2013. Pattern Recognition using the Fuzzy *C*-Means Technique. *International Journal of Energy, Information and Communications*, 4.

Daubechies, I. 1992. *Ten Lectures on Wavelets*. Philadelphia: Society for Industrial and Applied Mathematics.

de Jesus, A.M.P. & da Silva, A.L.L. 2010. Identification of the Net Effective Strain-Life Model for a Puddle Iron from the Portuguese Fão Riveted Road Bridge. *Procedia Engineering*, 2: 1181-1190.

Ditommaso, R., Mucciarelli, M. & Ponzo, F.C. 2012. Analysis of non-Stationary Structural Systems by using a Band-Variable Filter. *Bulletin of Earthquake Engineering*.

Donato, G.H.B. & Bianchi, M. 2012. Pressure Dependent Yield Criteria Applied for Improving Design Practices and Integrity Assessments against Yielding of Engineering Polymers. *Journal of Materials Research and Technology*.

dos Santos, H.A.F.A., Auricchio, F. & Conti, M. 2012. Fatigue Life Assessment of Cardiovascular Balloon-Expandable Stents: a Two-Scale Plasticity-Damage Model Approach. *Journal of the Mechanical Behavior of Biomedical Materials*, 15: 78-92.

Dunn, J.C. 1974. A Fuzzy Relative of the ISODATA Process and its Use in Detecting Compact Well-Separated Clusters. *Journal of Cybernetics*, 3: 32-57.

Dymola. 2011a. *Dymola User Manual*, vol. 1. Lund: Dassault Systèmes AB.

Dymola. 2011b. *Dymola User Manual*, vol. 2. Lund: Dassault Systèmes AB.

Elanchezhian, C., Ramnath, B.V., Venkatesan, P., Sathish, S., Vignesh, T., Siddharth, R.V., Vinay, B. & Gopinath, K. 2014. Parameter Optimization of Friction Stir Welding of AA8011-6062 using Mathematical Method. *Procedia Engineering*, 97: 775-782.

Elmqvist, H. 1978. A Structured Model Language for Large Continuous Systems. Ph.D. Thesis. Lund Institute of Technology.

Eski, İ. & Yildirim, Ş. 2009. Vibration Control of Vehicle Active Suspension System using a New Robust Neural Network Control System. *Simulation Modelling Practice and Theory*, 17: 778-793.

Fajdiga, G. & Sraml, M. 2009. Fatigue Crack Initiation and Propagation under Cyclic Contact Loading. *Engineering Fracture Mechanics*, 76: 1320-1335.

Ferreira, C., Ventura, P., Morais, R., Valente, A.L.G., Neves, C. & Reis, M.C. 2009. Sensing Methodologies to Determine Automotive Damper Condition under Vehicle Normal Operation. *Sensors and Actuators A: Physical*, 156: 237-244.

Figliola, R.S. & Beasley, D.E. 2011. *Theory and Design for Mechanical Measurements*, 5th Ed. New Jersey: John Wiley & Sons, Inc.

Fisher, R.A. 1918. The Correlation between Relatives on the Supposition of Mendelian Inheritance. *Philosophical Transactions of the Royal Society of Edinburgh*, 52: 399-433.

Fourier, J. 1878. *The Analytical Theory of Heat*. Cambridge: The University Press.

Fu, P., Li, W. & Guo, L. 2011. Fuzzy Clustering and Visualization Analysis of Tool Wear Status Recognition. *Procedia Engineering*, 23: 479-486.

Gabor, D. 1945. Theory of Communication. *Journal of the Institution of Electrical Engineers*, 93: 429-457.

Garcia, S., Amrouche, A., Mesmacque, G., Decoopman, X. & Rubio, C. 2005. Fatigue Damage Accumulation of Cold Expanded Hole in Aluminum Alloys Subjected to Block Loading. *International Journal of Fatigue*, 27: 1347-1353.

Georgiadis, K. 2003. Development, Implementation and Application of Partially Saturated Soil Models in Finite Element Analysis. Ph.D. Thesis. The University of London.

Ghafoori, E., Motavalli, M., Nussbaumer, A., Herwig, A., Prinz, G.S. & Fontana, M. 2015. Determination of Minimum CFRP Pre-Stress Levels for Fatigue Crack Prevention in Retrofitted Metallic Beams. *Engineering Structures*, 84: 29-41.

Giacomin, J., Steinwolf, A. & Staszewski, W.J. 2001. Application of Mildly Nonstationary Mission Synthesis (MNMS) to Automotive Road Data. *Proceedings of ATA 7th International Conference on the New Role of Experimentation in the Modern Automotive Product Development Process*.

Gocmez, T., Awarke, A. & Pischinger, S. 2010. A New Low Cycle Fatigue Criterion for Isothermal and Out-Of-Phase Thermomechanical Loading. *International Journal of Fatigue*, 32: 769-779.

Goga, V. & Kľúčik, M. 2012. Optimization of Vehicle Suspension Parameters with Use of Evolutionary Computation. *Procedia Engineering*, 48: 174-179.

Gonzales, M.A.C., Barrios, D.B., de Lima, N.B. & Gonçalves, E. 2010. Importance of Considering a Material Micro-Failure Criterion in the Numerical Modelling of the Shot Peening Process Applied to Parabolic Leaf Springs. *Latin American Journal of Solids and Structures*, 7: 21-40.

Goodman, J. 1914. *Mechanics Applied to Engineering*, 8th Ed. London: Longman, Green & Company.

Goupillaud, P., Grossman, A. & Morlet, J. 1984. Cycle-Octave and Related Transforms in Seismic Signal Analysis. *Geoexploration*, 23: 85-102.

Griffith, A.A. 1921. The Phenomena of Rupture and Flow in Solids. *Philosophical Transactions of the Royal Society of London*, A221: 163-198.

Guo, W., Tse, P.W. & Djordjevich, A. 2012. Faulty Bearing Signal Recovery from Large Noise using a Hybrid Method based on Spectral Kurtosis and Ensemble Empirical Mode Decomposition. *Measurement*, 45: 1308-1322.

Haar, A. 1910. On the Theory of Orthogonal Function Systems. *Mathematische Annalen*, 67: 76-113.

Haiba, M., Barton, D.C., Brooks, P.C. & Levesley, M.C. 2003. The Development of an Optimisation Algorithm based on Fatigue Life. *International Journal of Fatigue*, 25: 299-310.

Hamed, M., Tesfa, B., Gu, F. & Ball, A.D. 2014. Vehicle Suspension Performance Analysis based on Full Vehicle Model for Condition Monitoring Development. *Proceedings of VETOMAC X*, 23: 495-505.

Hardy, M. & Bryman, A. 2009. *The Handbook of Data Analysis*. London: SAGE Publications, Ltd.

He, B.-Y., Wang, S.-X. & Gao, F. 2010. Failure Analysis of an Automobile Damper Spring Tower. *Engineering Failure Analysis*, 17: 498-505.

Heuler, P. & Seeger, T. 1986. A Criterion for Omission of Variable Amplitude Loading Histories. *International Journal of Fatigue*, 8: 225-230.

Hosoi, A., Takamura, K., Sato, N. & Kawada, H. 2011. Quantitative Evaluation of Fatigue Damage Growth in CFRP Laminates that Changes due to Applied Stress Level. *International Journal of Fatigue*, 33: 781-787.

Ilic, S. 2006. Methodology of Evaluation of In-Service Load Applied to the Output Shafts of Automatic Transmissions. Ph.D. Thesis. The University of New South Wales.

Ince, A. & Glinka, G. 2011. A Modification of Morrow and Smith-Watson-Topper Mean Stress Correction Models. *Fatigue & Fracture of Engineering Materials & Structures*, 34: 854-867.

Ismail, N. 2010. Correlation Study of the Strain and Vibration Signals of the Automotive Suspension System. M.Sc. Thesis. Universiti Kebangsaan Malaysia.

Jiang, R. & Murthy, D.N.P. 2011. A Study of Weibull Shape Parameter: Properties and Significance. *Reliability Engineering and System Safety*, 96: 1619-1626.

Jiang, Y., Tang, B., Qin, Y. & Liu, W. 2011. Feature Extraction Method of Wind Turbine based on Adaptive Morlet Wavelet and SVD. *Renewable Energy*, 36: 2146-2153.

Jiang, J. & Zhao, M. 2012. Influence of Residual Stress on Stress Concentration Factor for High Strength Steel Welded Joints. *Journal of Constructional Steel Research*, 72: 20-28.

John, V.B. & Phillip, V.B. 2012. The Fatigue Damage Spectrum and Kurtosis Control. *Sound & Vibration Magazine*, 10-12.

Julien, B., Bertrand, F. & Thierry, Y. 2013. Probabilistic Random Vibration Fatigue. *Procedia Engineering*, 66: 522-529.

Juvinall, R.C. & Marshek, K.M. 2012. *Fundamentals of Machine Component Design*, 5th Ed. New Jersey: John Wiley & Sons, Inc.

Kang, H.T., Lee, Y.-L., Chen, J. & Fan, D. 2007. A Thermo-Mechanical Fatigue Damage Model for Variable Temperature and Loading Amplitude Conditions. *International Journal of Fatigue*, 29: 1797-1802.

Karthik, J.P., Chaitanya, K.L. & Sasanka, C.T. 2012a. Fatigue Life Prediction of a Parabolic Spring under non-Constant Amplitude Proportional Loading using Finite Element Method. *International Journal of Advanced Science and Technology*, 46: 143-156.

Karthik, J.P., Chaitanya, K.L. & Sasanka, C.T. 2012b. Life Assessment of a Parabolic Spring under Cyclic Stress and Cyclic Strain Loading using Finite Element Method. *International Journal of Mechanical Engineering*, 2: 36-43.

Karunananda, K., Ohga, M., Dissanayake, P.B.R. & Siriwardane, S. 2011. Effect of High Amplitude Loading on Fatigue Life Prediction of Steel Bridges. *Procedia Engineering*, 14: 521-528.

Kelly, S.G. 2012. *Mechanical Vibrations: Theory and Applications*. Stamford: Cengage Learning.

Khalil, M. & Topper, T.H. 2003. Prediction of Crack-Opening Stress Levels for 1045 As-Received Steel under Service Loading Spectra. *International Journal of Fatigue*, 25: 149-157.

Khan, S.M.A., Benyahia, F., Bouiadjra, B.B. & Albedah, A. 2014. Analysis and Repair of Crack Growth Emanating from V-Notch under Stepped Variable Fatigue Loading. *Procedia Engineering*, 74: 151-156.

Kihm, F. & Delaux, D. 2013. Vibration Fatigue and Simulation of Damage on Shaker Table Tests: the Influence of Clipping the Random Drive Signal. *Procedia Engineering*, 66: 549-564.

Kim, H. & Melhem, H. 2003. Fourier and Wavelet Analyses for Fatigue Assessment of Concrete Beams. *Experimental Mechanics*, 43: 131-140.

Kim, S.T., Tadjiev, D. & Yang, H.T. 2006. Fatigue Life Prediction under Random Loading Conditions in 7475–T7351 Aluminum Alloy using the RMS Model. *International Journal of Damage Mechanics*, 15: 89-102.

Kim, B.S., Lee, S.H., Lee, M.G., Ni, J., Song, J.Y. & Lee, C.W. 2007. A Comparative Study on Damage Detection in Speed-Up and Coast-Down Process of Grinding Spindle-Typed Rotor-Bearing System. *Journal of Materials Processing Technology*, 187-188: 30-36.

Kinloch, A.J., Lee, S.H. & Taylor, A.C. 2014. Improving the Fracture Toughness and the Cyclic-Fatigue Resistance of Epoxy-Polymer Blends. *Polymer*, 55: 6325-6334.

Klimkeit, B., Nadot, Y., Castagnet, S., Nadot-Martin, C., Dumas, C., Bergamo, S., Sonsino, C.M. & Büter, A. 2011. Multiaxial Fatigue Life Assessment for Reinforced Polymers. *International Journal of Fatigue*, 33: 766-780.

Ko, S.-G., Oh, C.-S. & Choi, B.-I. 2005. The Elucidation of Load History Editing Effect on Fatigue Crack Growth by Crack Closure Concept. *International Journal of Fatigue*, 27: 255-262.

Kogent Learning Solutions. 2011. *CATIA® Essentials*, 6th Ed. Sudbury: Jones and Bartlett Publishers.

Kovacs, S., Beck, T. & Singheiser, L. 2013. Influence of Mean Stresses on Fatigue Life and Damage of a Turbine Blade Steel in the VHCF-Regime. *International Journal of Fatigue*, 49: 90-99.

Krasovskyy, A. & Virta, A. 2014. Fracture Mechanics based Estimation of Fatigue Life of Welds. *Procedia Engineering*, 74: 27-32.

Kreyszig, E. 2011. *Advanced Engineering Mathematics*, 10th Ed. New Jersey: John Wiley & Sons, Inc.

Kumar, S.M. 2008. Analyzing Random Vibration Fatigue: Powerful ANSYS Workbench Tools Help Calculate the Damage of Vibrations that Lack Straightforward Cyclic Repetition. *ANSYS Advantage*, 2: 39-42.

Lajqi, S. & Pehan, S. 2012. Designs and Optimizations of Active and Semi-Active non-Linear Suspension Systems for a Terrain Vehicle. *Journal of Mechanical Engineering*, 58: 732-743.

Lanciotti, A. & Lazzeri, L. 1992. Effects of Spectrum Variations on Fatigue Crack Growth. *International Journal of Fatigue*, 14: 319-324.

Lee, Y.-L., Pan, J., Hathaway, R. & Barkey, M. 2005. *Fatigue Testing and Analysis: Theory and Practice*. Oxford: Elsevier Butterworth-Heinemann.

Lee, J. 2007. Free Vibration Analysis of Cylindrical Helical Springs by the Pseudospectral Method. *Journal of Sound and Vibration*, 302: 185-196.

Lee, Y.-L., Tjhung, T. & Jordan, A. 2007. A Life Prediction Model for Welded Joints under Multiaxial Variable Amplitude Loading Histories. *International Journal of Fatigue*, 29: 1162-1173.

Lee, J.-M. & Choi, B.-H. 2009. Experimental Observation and Modeling of the Retardation of Fatigue Crack Propagation under the Combination of Mixed-Mode Single Overload and Constant Amplitude Loads. *International Journal of Fatigue*, 31: 1848-1857.

Lei, Z., Xie, J., Zhao, A. & Hong, Y. 2010. A Simulation on Microstructure Sensitivity to Very-High-Cycle Fatigue Behavior of Metallic Materials. *Procedia Engineering*, 4: 225-232.

Leonowicz, Z., Łobos, T. & Woźniak, K. 2007. Analysis of Power Quality Disturbances using the S-Transform. *Proceedings of International Conference on Fundamentals of Electrotechnics and Circuit Theory*.

Li, H., Li, P. & Hu, S.-L.J. 2012. Modal Parameter Estimation for Jacket-Type Platforms using Noisy Free-Vibration Data: Sea Test Study. *Applied Ocean Research*, 37: 45-53.

Liao, T.W. 2005. Clustering of Time Series Data - a Survey. *Pattern Recognition*, 38: 1857-1874.

Liao, K.-C., Cian, Y.-A., & Lin, W.-C. 2009. Fatigue Life Assessment of an Innovative Laptop Hinge. *Materials and Design*, 30: 1497-1502.

Lin, J. & Zuo, M.J. 2003. Gearbox Fault Diagnosis using Adaptive Wavelet Filter. *Mechanical Systems and Signal Processing*, 17: 1259-1269.

Lipski, A. & Mroziński, S. 2012. Approximate Determination of a Strain-Controlled Fatigue Life Curve for Aluminum Alloy Sheets for Aircraft Structures. *International Journal of Fatigue*, 39: 2-7.

Liu, G.R. & Quek, S.S. 2003. *The Finite Element Method: a Practical Course*. Oxford: Elsevier Butterworth-Heinemann.

Liu, H., Huang, W., Wang, S. & Zhu, Z. 2014. Adaptive Spectral Kurtosis Filtering based on Morlet Wavelet and its Application for Signal Transients Detection. *Signal Processing*, 96: 118-124.

Llano-Vizcaya, L.D., Rubio-González, C., Mesmacque, G. & Cervantes-Hernández, T. 2006. Multiaxial Fatigue and Failure Analysis of Helical Compression Springs. *Engineering Failure Analysis*, 13: 1303-1313.

Longhurst, C. 1994. The Suspension Bible. http://www.carbibles.com/suspension_bible.html, accesed: 7th May 2012.

MacQueen, J.B. 1967. Some Methods for Classification and Analysis of Multivariate Observations. *Proceedings of 5th Berkeley Symposium on Mathematical Statistics and Probability*, 281-297.

Magrab, E.B. 2012. *Vibrations of Elastic Systems with Applications to MEMS and NEMS*. New York: Springer Science+Business Media B.V.

Mallat, S. 2009. *A Wavelet Tour of Signal Processing*, 3rd Ed. MA: Elsevier, Inc.

Manson, S.S. 1954. Behaviour of Materials under Conditions of Thermal Stress. *National Advisory Committee for Aeronautics*, 317-350.

Manson, S.S. & Halford, G.R. 2006. *Fatigue and Durability of Structural Materials.* West Conshohocken: ASTM International.

Maraini, D. & Nataraj, C. 2014. Freight Car Roller Bearing Fault Detection using Artificial Neural Networks and Support Vector Machines. *Proceedings of VETOMAC X*, 23: 663-672.

Martínez-Morales, J.D., Palacios, E. & Carrillo, G.A.V. 2012. Modeling of Internal Combustion Engine Emissions by LOLIMOT Algorithm. *Procedia Technology*, 3: 251-258.

MATLAB. 2008a. *Signal Processing Toolbox™ User's Guide*, 6th Ed. MA: The Math Works, Inc.

MATLAB. 2008b. *Statistics Toolbox™ User's Guide*, 6th Ed. MA: The Math Works, Inc.

MATLAB. 2008c. *Fuzzy Logic Toolbox™ User's Guide*, 2nd Ed. MA: The Math Works, Inc.

Memon, I.R., Zhang, X. & Cui, D. 2002. Fatigue Life Prediction of 3-D Problems by Damage Mechanics with Two-Block Loading. *International Journal of Fatigue*, 24: 29-37.

Mgdob, H.M., Torry, J.N., Vincent, R. & Al-Naami, B. 2003. Application of Morlet Transform Wavelet in the Detection of Paradoxical Splitting of the Second Heart Sound. *Computer in Cardiology*, 30: 323-326.

Miller, L.R. 1988. Tuning Passive, Semi-Active, and Fully Active Suspension Systems. *Proceedings of the 27th Conference on Decision and Control*, 2047-2053.

Misiti, M., Misiti, Y., Oppenheim, G. & Poggi, J.-M. 2008. *Wavelet Toolbox™ User's Guide*, 4th Ed. MA: The Math Works, Inc.

Mohd, S., Mutoh, Y., Otsuka, Y. & Miyashita, Y. 2013. Scatter Behavior of Fatigue Limit of a Die-Cast and Extruded Magnesium Alloys. *Procedia Engineering*, 68: 681-687.

Montgomery, D.C. 2013. *Design and Analysis of Experiments*, 8th Ed. New Jersey: John Wiley & Sons, Inc.

Morlet, J., Arens, G., Fourgeau, E. & Giard, D. 1982a. Wave Propagation and Sampling Theory - Part I: Complex Signal and Scattering in Multilayered Media. *Geophysics*, 47: 203-221.

Morlet, J., Arens, G., Fourgeau, E. & Giard, D. 1982b. Wave Propagation and Sampling Theory - Part II: Sampling Theory and Complex Waves. *Geophysics*, 47: 222-236.

Motra, H.B., Hildebrand, J. & Dimmig-Osburg, A. 2014. Assessment of Strain Measurement Techniques to Characterize Mechanical Properties of Structural Steel. *Engineering Science and Technology, an International Journal*, 17: 260-269.

Mottitschka, T., Pusch, G., Biermann, H., Zybell, L. & Kuna, M. 2010. Influence of Overloads on the Fatigue Crack Growth in Nodular Cast Iron: Experiments and Numerical Simulation. *Procedia Engineering*, 2: 1557-1567.

MSC NASTRAN. 2012. *Dynamic Analysis User's Guide*. Santa Ana: MSC Software Corporation.

Mulia, T.M., Kadam, S.J. & Kengar, V.S. 2012. Finite Element Analysis of Helical Coil Compression Spring for Three Wheeler Automotive Front Suspension. *International Journal of Mechanical and Industrial Engineering*, 2: 74-77.

Nascimento, M.P., Voorwald, H.J.C. & Filho, J.C.P. 2011. Fatigue Strength of Tungsten Inert Gas-Repaired Weld Joints in Airplane Critical Structures. *Journal of Materials Processing Technology*, 211: 1126-1135.

Nagode, M. 2014. Continuous Damage Parameter Calculation under Thermo-Mechanical Random Loading. *MethodsX*, 1: 81-89.

nCode. 2007. *ICE-flow 4.1: GlyphWorks Worked Examples*. Sheffield: nCode International, Ltd.

Neupauer, R.M. & Powell, K.L. 2005. A Fully-Anisotropic Morlet Wavelet to Identify Dominant Orientations in a Porous Medium. *Computers & Geosciences*, 31: 465-471.

Neyman, J. 1937. Outline of a Theory of Statistical Estimation based on the Classical Theory of Probability. *Philosophical Transactions of the Royal Society A*, 236: 333-380.

Niesłony, A., el Dsoki, C., Kaufmann, H. & Krug, P. 2008. New Method for Evaluation of the Manson-Coffin-Basquin and Ramberg-Osgood Equations with Respect to Compatibility. *International Journal of Fatigue*, 30: 1967-1977.

Niesłony, A. & Böhm, M. 2013. Mean Stress Effect Correction using Constant Stress Ratio *S-N* Curves. *International Journal of Fatigue*, 52: 49-56.

Norton, M.P. & Karczub, D.G. 2007. *Fundamentals of Noise and Vibration Analysis for Engineers*, 2nd Ed. UK: Cambridge University Press.

Nyman, T., Ansell, H. & Blom, A. 2000. Effects of Truncation and Elimination on Composite Fatigue Life. *Composite Structures*, 48: 275-286.

Oh, C.-S. 2001. Application of Wavelet Transform in Fatigue History Editing. *International Journal of Fatigue*, 23: 241-250.

Ossa, E.A., Palacio, C.C. & Paniagua, M.A. 2011. Failure Analysis of a Car Suspension System Ball Joint. *Engineering Failure Analysis*, 18: 1388-1394.

Ottosen, N.S., Stenström, R. & Ristinmaa, M. 2008. Continuum Approach to High-Cycle Fatigue Modeling. *International Journal of Fatigue*, 30: 996-1006.

Pantazopoulos, G., Vazdirvanidis, A., Rikos, A. & Toulfatzis, A. 2014. Analysis of Abnormal Fatigue Failure of Forklift Forks. *Case Studies in Engineering Failure Analysis*, 2: 9-14.

Papadogiannis, Y., Lakes, R.S., Palaghias, G., Helvatjoglu-Antoniades, M. & Papadogiannis, D. 2007. Fatigue of Packable Dental Composites. *Dental Materials*, 23: 235-242.

Paris, P.C., Gomez, M.P. & Anderson, W.E. 1961. A Rational Analytic Theory of Fatigue. *The Trend in Engineering*, 13: 9-14.

Pathak, A.Y. 2012. Computational Approach to Contact Fatigue Damage Initiation and Deformation Analysis of Gear Teeth Flanks. *International Journal of Research in Engineering and Technology*, 1: 564-570.

Pearson, K. 1900. On the Criterion that a Given System of Deviations from the Probable in the Case of a Correlated System of Variables is such that is can be Reasonably Supposed to have Arisen from Random Sampling. *Philosophical Magazine Series*, 550: 157-175.

Peng, X. & Yan, Z. 2014. Estimation and Application for a New Extended Weibull Distribution. *Reliability Engineering and System Safety*, 121: 34-42.

Pessoa, O.F., da Silva, J.M. & Gavini, G. 2013. Cyclic Fatigue Resistance of Rotary NiTi Instruments after Simulated Clinical Use in Curved Root Canals. *Brazilian Dental Journal*, 24: 117-120.

Petrenec, M., Tesařová, H., Beran, P., Šmíd, M. & Roupcová, P. 2010. Comparison of Low Cycle Fatigue of Ductile Cast Irons with Different Matrix Alloyed with Nickel. *Procedia Engineering*, 2: 2307-2316.

Phillips, E.P. 1979. Effects of Truncation of a Predominantly Compression Load Spectrum on the Life of a Notched Graphite / Epoxy Laminate. NASA Technical Memorandum. Langley Research Center.

Pinnegar, C.R. & Mansinha, L. 2003. A Method of Time-Time Analysis: the TT-Transform. *Digital Signal Processing*, 13: 588-603.

Praveen, K.V.U. & Singh, V. 2008. Effect of Heat Treatment on Coffin-Manson Relationship in LCF of Superalloy IN718. *Materials Science and Engineering A*, 485: 352-358.

Prawoto, Y., Ikeda, M., Manville, S.K. & Nishikawa, A. 2008. Design and Failure Modes of Automotive Suspension Springs. *Engineering Failure Analysis*, 15: 1155-1174.

Priyandoko, G., Mailah, M. & Jamaluddin, H. 2009. Vehicle Active Suspension System using Skyhook Adaptive Neuro Active Force Control. *Mechanical Systems and Signal Processing*, 23: 855-868.

Prokopowicz, P., Bednarek, T. & Sosnowski, W. 2009. Fuzzy Numbers Calculations as Help in Fatigue Reliability Estimation. *Proceedings of the International Multiconference on Computer Science and Information Technology*, 4: 99-104.

Purushotham, V., Narayanan, S. & Prasad, S.A.N. 2005. Multi-Fault Diagnosis of Rolling Bearing Elements using Wavelet Analysis and Hidden Markov Model based Fault Recognition. *NDT & E International*, 38: 654-664.

Putra, T.E. 2010. Fatigue Durability Features Clustering using the Morlet Wavelet Transform. M.Sc. Thesis. Universiti Kebangsaan Malaysia.

Qazi, A.J., Khan, A., Khan, M.T. & Noor, S. 2013. A Parametric Study on Performance of Semi-Active Suspension System with Variable Damping Coefficient Limit. *AASRI Procedia*, 4: 154-159.

Ramberg, W. & Osgood, W.R. 1943. Description of Stress-Strain Curves by Three Parameters. *National Advisory Committee for Aeronautics.*

Rao, S.J. 2009. Vehicle Modeling and ADAMS-Simulink Co-Simulation with Integrated Continuously Controlled Electronic Suspension (CES) and Electronic Stability Control (ESC) Models. M.Sc. Thesis. The Ohio State University.

Reytier, T., Bes, C., Marechal, P., Bianciardi, M. & Santgerma, A. 2012. Generation of Correlated Stress Time Histories from Continuous Turbulence Power Spectral Density for Fatigue Analysis of Aircraft Structures. *International Journal of Fatigue*, 42: 147-152.

Rognin, F., Abdi, F., Kunc, V., Lee, M. & Nikbin, K. 2009. Probabilistic Methods in Predicting Damage under Multi-Stage Fatigue of Composites using Load Block Sequences. *Procedia Engineering*, 1: 55-58.

Roman, L., Florea, A. & Cofaru, I.I. 2014. Software Application for Assessment the Reliability of Suspension System at OPEL Cars and of Road Profiles. *Fascicle of Management and Technological Engineering*, 1: 289-294.

Rösler, J., Harders, H. & Bäker, M. 2007. *Mechanical Behaviour of Engineering Materials*. Heidelberg: Springer-Verlag.

Ross, S. 2009. *Introduction to Probability and Statistics for Engineers and Scientists*, 4th Ed. MA: Elsevier, Inc.

Runciman, A., Xu, D., Pelton, A.R. & Ritchie, R.O. 2011. An Equivalent Strain / Coffin-Manson Approach to Multiaxial Fatigue and Life Prediction in Superelastic Nitinol Medical Devices. *Biomaterials*, 32: 4987-4993.

Ruspini, E.H. 1969. A New Approach to Clustering. *Information and Control*, 15: 22-32.

Sadananda, K., Vasudevan, A.K. & Phan, N. 2007. Analysis of Endurance Limits under Very High Cycle Fatigue using a Unified Damage Approach. *International Journal of Fatigue*, 29: 2060-2071.

Sakin, R. & Ay, İ. 2008. Statistical Analysis of Bending Fatigue Life Data using Weibull Distribution in Glass-Fiber Reinforced Polyester Composites. *Materials and Design*, 29: 1170-1181.

Schaumann, P. & Steppeler, S. 2013. Fatigue Tests of Axially Loaded Butt Welds Up to Very High Cycles. *Procedia Engineering*, 66: 88-97.

Schijve, J. 2004. *Fatigue of Structures and Materials.* Dordrecht: Kluwer Academic Publishers.

Scuracchio, B.G., de Lima, N.B. & Schön, C.G. 2013. Role of Residual Stresses Induced by Double Peening on Fatigue Durability of Automotive Leaf Springs. *Materials and Design*, 47: 672-676.

Sheen, Y.-T. 2009. On the Study of Applying Morlet Wavelet to the Hilbert Transform for the Envelope Detection of Bearing Vibrations. *Mechanical Systems and Signal Processing*, 23: 1518-1527.

Shimmel, M. & Gallart, J. 2005. The Inverse S-Transform in Filters with Time-Frequency Localization. *IEEE Transactions on Signal Processing*, 53: 4417-4422.

Simulink. 2013. *Simulink User's Guide*. MA: The MathWorks, Inc.

Singh, N. 2013. General Review of Mechanical Springs used in Automobiles Suspension System. *International Journal of Advanced Engineering Research and Studies*.

Sireteanu, T., Mitu, A.-M., Giuclea, M. & Solomon, O. 2014. A Comparative Study of the Dynamic Behavior of Ramberg-Osgood and Bouc-Wen Hysteresis Models with Application to Seismic Protection Devices. *Engineering Structures*, 76: 255-269.

Sivák, P. & Ostertagová, E. 2012. Evaluation of Fatigue Tests by Means of Mathematical Statistics. *Procedia Engineering*, 48: 636-642.

Sivapragash, M., Lakshminarayanan, P.R., Karthikeyan, R., Raghukandan, K. & Hanumantha, M. 2008. Fatigue Life Prediction of ZE41A Magnesium Alloy using Weibull Distribution. *Materials and Design*, 29: 1549-1553.

Smith, C., Akujuobi, C.M., Hamory, P. & Kloesel, K. 2007. An Approach to Vibration Analysis using Wavelets in an Application of Aircraft Health Monitoring. *Mechanical Systems and Signal Processing*, 21: 1255-1272.

Solin, J., Nagel, G. & Mayinger, W. 2009. Fatigue Curve and Stress Strain Response for Stainless Steel. *Proceedings of 20th International Conference on Structural Mechanics in Reactor Technology.*

SoMat. 2002. *eDAQ Manual*. Champaign: SoMat Corporation.

Sonsino, C.M. 2007. Fatigue Testing under Variable Amplitude Loading. *International Journal of Fatigue*, 29: 1080-1089.

Souza, R.C., dos Santos, C., Barboza, M.J.R., Bicalho, L.d.A., Baptista, C.A.R.P. & Elias, C.N. 2014. Fatigue Behavior of 3%Y2O3-Doped ZrO2 Ceramics. *Journal of Materials Research and Technology*, 3: 48-54.

Staninec, M., Kim, P., Marshall, G.W., Ritchie, R.O. & Marshall, S.J. 2008. Fatigue of Dentin - Composite Interfaces with Four-Point Bend. *Dental Materials*, 24: 799-803.

Stephens, R.I., Dindinger, P.M. & Gunger, J.E. 1997. Fatigue Damage Editing for Accelerated Durability Testing using Strain Range and SWT Parameter Criteria. *International Journal of Fatigue*, 19: 599-606.

Stephens, R.I., Fatemi, A., Stephens, R.R. & Fuchs, H.O. 2001. *Metal Fatigue in Engineering*, 2nd Ed. New York: John Wiley & Sons, Inc.

Stockwell, R.G., Mansinha, L. & Lowe, R.P. 1996. Localization of the Complex Spectrum: the S Transform. *IEEE Transactions on Signal Processing*, 44: 998-1001.

Stockwell, R.G. 2007. A Basis for Efficient Representation of the S-Transform. *Digital Signal Processing*, 17: 371-393.

Su, W., Wang, F., Zhu, H., Zhang, Z. & Guo, Z. 2010. Rolling Element Bearing Faults Diagnosis based on Optimal Morlet Wavelet Filter and Autocorrelation Enhancement. *Mechanical Systems and Signal Processing*, 24: 1458-1472.

Sum, W.S., Williams, E.J. & Leen, S.B. 2005. Finite Element, Critical-Plane, Fatigue Life Prediction of Simple and Complex Contact Configurations. *International Journal of Fatigue*, 27: 403-416.

Taheri, F., Trask, D. & Pegg, N. 2003. Experimental and Analytical Investigation of Fatigue Characteristics of 350WT Steel under Constant and Variable Amplitude Loadings. *Marine Structures*, 16: 69-91.

Taheri, S., Vincent, L. & Le-roux, J.-C. 2013. A New Model for Fatigue Damage Accumulation of Austenitic Stainless Steel under Variable Amplitude Loading. *Procedia Engineering*, 66: 575-586.

Tandel, A., Deshpande, A.R., Deshmukh, S.P. & Jagtap, K.R. 2014. Modeling, Analysis and PID Controller Implementation on Double Wishbone Suspension using SimMechanics and Simulink. *Procedia Engineering*, 97: 1274-1281.

Tang, B., Liu, W. & Song, T. 2010. Wind Turbine Fault Diagnosis based on Morlet Wavelet Transformation and Wigner-Ville Distribution. *Renewable Energy*, 35: 2862-2866.

Tao, G. & Xia, Z. 2007. Mean Stress / Strain Effect on Fatigue Behavior of an Epoxy Resin. *International Journal of Fatigue*, 29: 2180-2190.

Thite, A.N. 2012. Development of a Refined Quarter Car Model for the Analysis of Discomfort due to Vibration. *Advances in Acoustics and Vibration.*

Tong, W. & Guo, K.H. 2012. Simulation Testing Research on Ride Comfort of Vehicle with Global-Coupling Torsion-Elimination Suspension. *Physics Procedia*, 33: 1741-1748.

Upadhyaya, Y.S. & Sridhara, B.K. 2012. Fatigue Life Prediction: a Continuum Damage Mechanics and Fracture Mechanics Approach. *Materials and Design*, 35: 220-224.

Varvani-Farahani, A., Sharma, M. & Kianoush, M.R. 2005. Fatigue Damage Analysis and Life Assessment under Variable Amplitude Loading Conditions. *Materials Science and Engineering*, 403: 42-47.

Wang, B., Jalil, N.A.A. & Voon, W.S. 2012a. Prediction of Rotary Machinery Degradation Status based on Vibration Data using Back Propagation Neural Network. *Scientific Research and Essays*, 7: 1393-1404.

Wang, S., Yin, C. & Zhao, H. 2012b. Matching of Suspension Damping and Air Spring based on Multi-Body Dynamic Model. *IERI Procedia*, 3: 15-21.

Wang, R., Wei, J., Hu, D., Shen, X. & Fan, J. 2013a. Investigation on Experimental Load Spectrum for High and Low Cycle Combined Fatigue Test. *Propulsion and Power Research*, 2: 235-242.

Wang, D., Shen, C. & Tse, P.W. 2013b. A Novel Adaptive Wavelet Stripping Algorithm for Extracting the Transients caused by Bearing Localized Faults. *Journal of Sound and Vibration*, 332: 6871-6890.

Wei, D. & Elgindi, M.B.M. 2013. Finite Element Analysis of the Ramberg-Osgood Bar. *American Journal of Computational Mathematics*, 3: 211-216.

Weibull, W. 1951. A Statistical Distribution Function of Wide Applicability. *Journal of Applied Mechanics*, 18: 293-297.

Weiguo, H., Weifang, Z., Xiao, L., Zongren, W. & Meili, D. 2011. Failure Analysis of Aviation Torsional Springs. *Chinese Journal of Aeronautics*, 24: 527-532.

White, P., Barter, S.A. & Wright, C. 2009. Small Crack Growth Rates from Simple Sequences Containing Underloads in AA7050-T7451. *International Journal of Fatigue*, 31: 1865-1874.

Wijker, J. 2009. *Random Vibrations in Spacecraft Structures Design: Theory and Applications*. New York: Springer Science+Business Media B.V.

Williams, C.R., Lee, Y.-L. & Rilly, J.T. 2003. A Practical Method for Statistical Analysis of Strain-Life Fatigue Data. *International Journal of Fatigue*, 25: 427-436.

Wittenburg, J. 2008. *Dynamics of Multibody Systems*, 2nd Ed. Berlin: Springer-Verlag.

Wolfsteiner, P. & Breuer, W. 2013. Fatigue Assessment of Vibrating Rail Vehicle Bogie Components under non-Gaussian Random Excitations using Power Spectral Densities. *Journal of Sound and Vibration*, 332: 5867-5882.

Xia, H.W., Ni, Y.Q., Wong, K.Y. & Ko, J.M. 2012. Reliability-based Condition Assessment of In-Service Bridges using Mixture Distribution Models. *Computers and Structures*, 106-107: 204-213.

Xiong, J.J. & Shenoi, R.A. 2008. A Load History Generation Approach for Full-Scale Accelerated Fatigue Tests. *Engineering Fracture Mechanics*, 75: 3226-3243.

Xu, Y.-L., Chen, Z.-W. & Xia, Y. 2012. Fatigue Assessment of Multi-Loading Suspension Bridges using Continuum Damage Model. *International Journal of Fatigue*, 40: 27-35.

Yan, J.H., Zheng, X.L. & Zhao, K. 2001. Experimental Investigation on the Small-Load-Omitting Criterion. *International Journal of Fatigue*, 23: 403-415.

Yang, X., Wang, Z. & Peng, W. 2009. Coordinated Control of AFS and DYC for Vehicle Handling and Stability based on Optimal Guaranteed Cost Theory. *Vehicle System Dynamics*, 47: 57-79.

Ye, X.W., Ni, Y.Q., Wong, K.Y. & Ko, J.M. 2012a. A Statistical Analysis of Stress Spectra for Fatigue Life Assessment of Steel Bridges with Structural Health Monitoring Data. *Engineering Structures*, 45: 166-176.

Ye, X.W., Ni, Y.Q. & Ko, J.M. 2012b. Experimental Evaluation of Stress Concentration Factor of Welded Steel Bridge T-Joints. *Journal of Constructional Steel Research*, 70: 78-85.

Ye, X.W., Su, Y.H. & Han, J.P. 2014. A State-of-the-Art Review on Fatigue Life Assessment of Steel Bridges. *Mathematical Problems in Engineering.*

Zadeh, L.A. 1965. Fuzzy Sets. *Information and Control*, 8: 338-353.

Zambrano, O.A., Coronado, J.J. & Rodríguez, S.A. 2014. Failure Analysis of a Bridge Crane Shaft. *Case Studies in Engineering Failure Analysis*, 2: 25-32.

Zhang, L.-J., Lee, C.-M. & Wang, Y.S. 2002. A Study on Nonstationary Random Vibration of a Vehicle in Time and Frequency Domains. *International Journal of Automotive Technology*, 3: 101-109.

Zhang, Y., Guo, Z., Wang, W., He, S., Lee, T. & Loew, M. 2003. A Comparison of the Wavelet and Short-Time Fourier Transforms for Doppler Spectral Analysis. *Medical Engineering & Physics*, 25: 547-557.

Zhang, C.-J., Duanmu, C.-J. & Chen, H.-Y. 2007. Typhoon Image Segmentation by Combining Curvelet Transform with Continuous Wavelet Transform.

Proceedings of the 2007 International Conference on Wavelet Analysis and Pattern Recognition, 1512-1517.

Zhang, H., Zhang, X. & Wang, J. 2014. Robust Gain-Scheduling Energy-to-Peak Control of Vehicle Lateral Dynamics Stabilization. *Vehicle System Dynamics*, 52: 309-340.

Zhu, Y., Wang, Y. & Huang, Y. 2014. Failure Analysis of a Helical Compression Spring for a Heavy Vehicle's Suspension System. *Case Studies in Engineering Failure Analysis*, 2: 169-173.

APPENDIX A

MAPS OF THE MEASURING TRACK AREAS

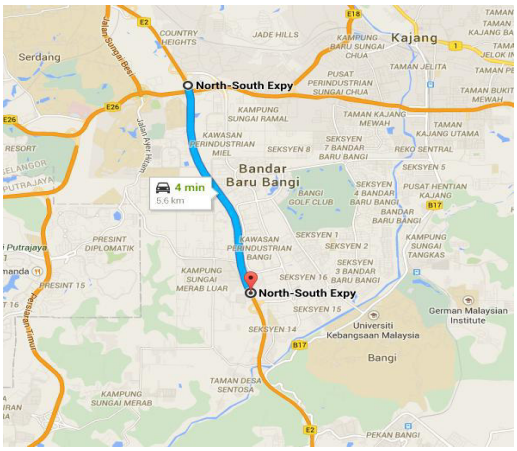

Highway track area

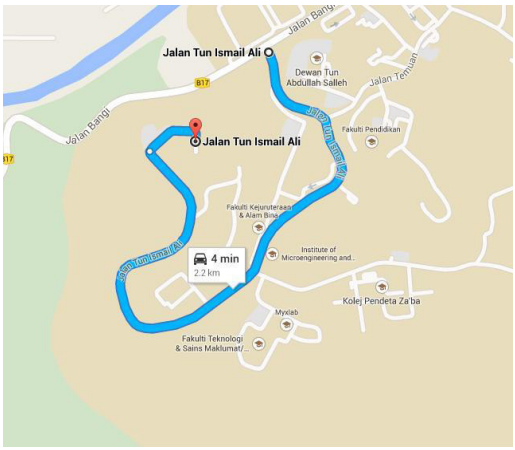

Urban track area

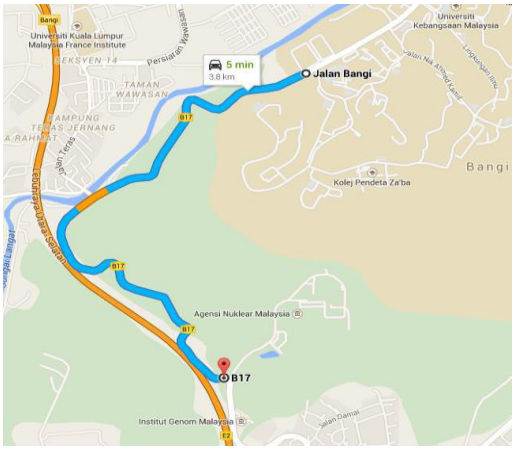

Rural track area

APPENDIX B

CHI SQUARE DISTRIBUTION TABLE

Table entry for p is the critical value $(\chi^2)^*$ with probability p lying to its right.

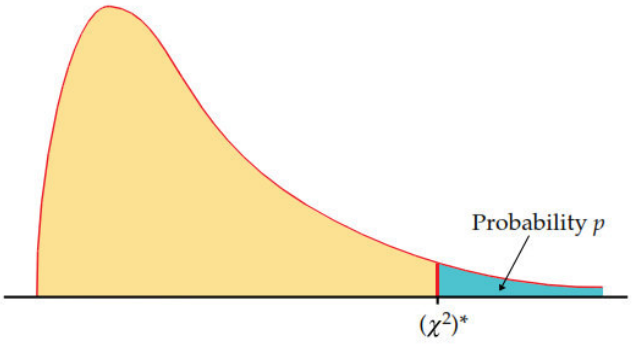

DF	*P*-value											
	0.25	0.20	0.15	0.10	0.05	0.025	0.02	0.01	0.005	0.0025	0.001	0.0005
1	1.32	1.64	2.07	2.71	3.84	5.02	5.41	6.63	7.88	9.14	10.83	12.12
2	2.77	3.22	3.79	4.61	5.99	7.38	7.82	9.21	10.60	11.98	13.82	15.20
3	4.11	4.64	5.32	6.25	7.81	9.35	9.84	11.34	12.84	14.32	16.27	17.73
4	5.39	5.99	6.74	7.78	9.49	11.14	11.67	13.28	14.86	16.42	18.47	20.00
5	6.63	7.29	8.12	9.24	11.07	12.83	13.39	15.09	16.75	18.39	20.51	22.11
6	7.84	8.56	9.45	10.64	12.59	14.45	15.03	16.81	18.55	20.25	22.46	24.10
7	9.04	9.80	10.75	12.02	14.07	16.01	16.62	18.48	20.28	22.04	24.32	26.02
8	10.22	11.03	12.03	13.36	15.51	17.53	18.17	20.09	21.95	23.77	26.12	27.87
9	11.39	12.24	13.29	14.68	16.92	19.02	19.68	21.67	23.59	25.46	27.88	29.67
10	12.55	13.44	14.53	15.99	18.31	20.48	21.16	23.21	25.19	27.11	29.59	31.42
11	13.70	14.63	15.77	17.28	19.68	21.92	22.62	24.72	26.76	28.73	31.26	33.14
12	14.85	15.81	16.99	18.55	21.03	23.34	24.05	26.22	28.30	30.32	32.91	34.82
13	15.98	16.98	18.20	19.81	22.36	24.74	25.47	27.69	29.82	31.88	34.53	36.48
14	17.12	18.15	19.41	21.06	23.68	26.12	26.87	29.14	31.32	33.43	36.12	38.11
15	18.25	19.31	20.60	22.31	25.00	27.49	28.26	30.58	32.80	34.95	37.70	39.72
16	19.37	20.47	21.79	23.54	26.30	28.85	29.63	32.00	34.27	36.46	39.25	41.31
17	20.49	21.61	22.98	24.77	27.59	30.19	31.00	33.41	35.72	37.95	40.79	42.88
18	21.60	22.76	24.16	25.99	28.87	31.53	32.35	34.81	37.16	39.42	42.31	44.43
19	22.72	23.90	25.33	27.20	30.14	32.85	33.69	36.19	38.58	40.88	43.82	45.97
20	23.83	25.04	26.50	28.41	31.41	34.17	35.02	37.57	40.00	42.34	45.31	47.50
21	24.93	26.17	27.66	29.62	32.67	35.48	36.34	38.93	41.40	43.78	46.80	49.01
22	26.04	27.30	28.82	30.81	33.92	36.78	37.66	40.29	42.80	45.20	48.27	50.51
23	27.14	28.43	29.98	32.01	35.17	38.08	38.97	41.64	44.18	46.62	49.73	52.00
24	28.24	29.55	31.13	33.20	36.42	39.36	40.27	42.98	45.56	48.03	51.18	53.48
25	29.34	30.68	32.28	34.38	37.65	40.65	41.57	44.31	46.93	49.44	52.62	54.95
26	30.43	31.79	33.43	35.56	38.89	41.92	42.86	45.64	48.29	50.83	54.05	56.41
27	31.53	32.91	34.57	36.74	40.11	43.19	44.14	46.96	49.64	52.22	55.48	57.86
28	32.62	34.03	35.71	37.92	41.34	44.46	45.42	48.28	50.99	53.59	56.89	59.30
29	33.71	35.14	36.85	39.09	42.56	45.72	46.69	49.59	52.34	54.97	58.30	60.73
30	34.80	36.25	37.99	40.26	43.77	46.98	47.96	50.89	53.67	56.33	59.70	62.16
40	45.62	47.27	49.24	51.81	55.76	59.34	60.44	63.69	66.77	69.70	73.40	76.09
50	56.33	58.16	60.35	63.17	67.50	71.42	72.61	76.15	79.49	82.66	86.66	89.56
60	66.98	68.97	71.34	74.40	79.08	83.30	84.58	88.38	91.95	95.34	99.61	102.7
80	88.13	90.41	93.11	96.58	101.9	106.6	108.1	112.3	116.3	120.1	124.8	128.3
100	109.1	111.7	114.7	118.5	124.3	129.6	131.1	135.8	140.2	144.3	149.4	153.2

APPENDIX C
LIST OF PUBLICATIONS

A. Chapter in Book

A1 S. Abdullah, **T. E. Putra**, D. Schramm, M. Z. Nuawi. The wavelet transform for extracting chaotic acceleration data, *New Trends in Chaotic Modeling and Simulation*, accepted.

B. Journal Papers

B1 **T. E. Putra**, S. Abdullah, D. Schramm, M. Z. Nuawi, T. Bruckmann. 2015. Generating strain signals under consideration of road surface profiles, *Mechanical Systems and Signal Processing*, 60-61: 485-497. **ISI-Q1.**

B2 **T. E. Putra**, S. Abdullah, D. Schramm, M. Z. Nuawi, T. Bruckmann, M. F. M. Yunoh. 2014. Time-frequency-based fatigue data editing for automotive applications, *Australian Journal of Basic and Applied Sciences*, 8: 88-91.

B3 S. Abdullah, **T. E. Putra**, D. Schramm, M. Z. Nuawi. 2014. Acceleration data extraction associating to the peak-valley segmentation approach using the Morlet wavelet transform, *Chaotic Modeling and Simulation*, 1: 69-77.

C. International Conference Papers

C1 **T. E. Putra**, S. Abdullah, D. Schramm, M. Z. Nuawi, T. Bruckmann. 2014. Application of the wavelet transforms for compressing lower suspension arm strain data, *Applied Mechanics and Materials*, 663: 78-82. **SCOPUS.**

C2 S. Abdullah, **T. E. Putra**, D. Schramm, M. Z. Nuawi, T. Bruckmann. 2014. Generation of simulated acceleration and strain signals as the responses of a car coil spring, *International Journal of Fracture Fatigue and Wear*, 2: 189-194.

C3 **T. E. Putra**, S. Abdullah, D. Schramm, M. Z. Nuawi, T. Bruckmann. 2014. FCM-based optimisation to enhance the Morlet wavelet ability for compressing suspension strain data, *Procedia Materials Science*, 3: 288-294.

C4 **T. E. Putra**, S. Abdullah, D. Schramm, M. Z. Nuawi, T. Bruckmann. 2014. Wavelet-based feature extraction algorithm for fatigue strain data associated with the *k*-means clustering technique, *Advanced Materials Research,* 891-892: 1717-1722. **SCOPUS.**

C5 **T. E. Putra**, S. Abdullah, M. Z. Nuawi, M. F. M. Yunoh. 2014. The Morlet and Daubechies wavelet transforms for fatigue strain signal analysis, *Applied Mechanics and Materials*, 471: 197-202. **SCOPUS.**

C6 **T. E. Putra**, S. Abdullah, D. Schramm, M. Z. Nuawi, T. Bruckmann. 2013. The Morlet wavelet-based features extraction for compressing automotive fatigue strain data, *7th International Conference on Low Cycle Fatigue* (LCF7), 133-138, Aachen, Germany, 9th - 11th September 2013.